Interfacial Properties of Fibre Reinforced Ceramic Matrix Composites

by

Adrian M. Daniel

Submitted for the Degree of Doctor of Philosophy,

Centre for Advanced Materials Technology,

Department of Physics,
University of Warwick.

November 1994.

To Mum and Dad

ABSTRACT

A review of ceramic matrix composites development over the past thirty years is presented, with emphasis placed on their application in gas turbine engine components.

The fracture mechanics of brittle solids are outlined and the toughening mechanisms operating within continuous fibre reinforced ceramic matrix composites are discussed. The importance of the fibre-matrix interface in governing the overall mechanical properties of a composite is highlighted with respect to the micromechanical properties of interface debond fracture surface energy G_i and frictional shear stress τ.

Current techniques for measuring G_i and τ are listed, together with their inherent disadvantages. The requirement for a micro-indentation system that can be used to measure interfacial properties via individual fibre pushing experiments across a wide range of composite systems, is discussed.

The development of a unique Scanning Electron Microscope (SEM) based microindentation system is described in detail. It enables dynamic, high magnification imaging of the indentor tip and specimen contact point, and continuously records applied load and tip displacement throughout the indentation cycle. A piezoelectric load cell, coupled to a specifically developed amplifier, enables load resolution of 2mN measured up to the maximum possible of 20N. Novel capacitance displacement gauge design gives a resolution of 10nm over a 100μm range.

The instrument has been used successfully to measure the interface micromechanical properties across a wide range of silicon carbide fibre reinforced glass and glass ceramic matrix composites. This data has been correlated with interface structural information obtained via Transmission Electron Microscopy (TEM) and SEM. Effects of oxidation, fatigue testing and interface pre-synthesis via fibre coating, have been measured. Fibres with diameters ranging from 7μm to 150μm have been tested to demonstrate the versatility of the device for interfacial property measurement across the full range of modern ceramic matrix composites. Successful attempts have been made to correlate changes in the interfacial G_i and τ to changes in overall composite mechanical behaviour. Theoretical requirements for values of G_i that introduce toughness to composites have been discussed and compared to those determined by experiment. Variation of τ and its effect on matrix micro-cracking and the tough/brittle property transition of a composite has been measured.

Other applications that exploit the instrument's high resolution and imaging capability have been demonstrated. They include hardness and modulus measurement of individual phases in heterogeneous materials, and direct observation of controlled crack growth in ceramic composites.

Ideas for the development of the instrument into a more versatile SEM based mechanical test facility are proposed.

CONTENTS

ACKNOWLEDGEMENTS ..... *(vii)*

DECLARATION ..... *(viii)*

CHAPTER ONE: INTRODUCTION 1

1.1 Gas Turbine Material Requirements 1
1.2 Ceramic Matrix Composites 2
1.2.1 Historical development 4
1.2.2 Whisker and short fibre reinforced ceramic matrices 6
1.2.3 Continuous fibre reinforced ceramic matrices 7

CHAPTER TWO: CONTINUOUS FIBRE REINFORCED CERAMIC MATRIX COMPOSITES 9

2.1 Fracture Mechanics 9
2.1.1 Brittle failure of Ceramics 9
2.1.2 Fibre reinforced composite mechanical behaviour 13
2.1.2.1 Fibre - matrix interface debonding at matrix crack front 15
2.1.2.2 Matrix microcracking 19
2.1.2.3 Fibre failure and pull out 23
2.1.2.4 Ultimate tensile strength 25
2.1.2.5 Transition to brittle failure 26
2.1.2.6 Residual stresses 27
2.1.2.7 Summary of CMC mechanical behaviour 29
2.2 Ceramic Matrix Composite Materials 30
2.2.1 Ceramic matrices 31
2.2.2 Fibre reinforcements 32
2.2.3 CMC systems 34
2.2.4 Interface pre-synthesis 36
2.2.5 Glass and glass ceramic matrix composites 38

CHAPTER THREE: INTERFACIAL MICROMECHANICS 41

3.1 Importance of Interfacial Micromechanics 41
3.2 Techniques for Measurement of Interfacial Micromechanical Properties 43
3.2.1 Summary of tests 43
3.2.2 Individual fibre push or pull tests 44
3.3 Programme Objectives 49
3.3.1 Development of micromechanical measurement instrumentation 49
3.3.2 Fibre-matrix interface characterisation 50
3.3.3 Correlation of micromechanical and macromechanical behaviour 50

CHAPTER FOUR: THE SCANNING ELECTRON MICROSCOPE BASED MICROINDENTATION SYSTEM **51**

4.1 Overview 52
4.2 System development 52
4.2.1 Initial development 52
4.2.2 Load measurement 56
4.2.3 Indentor tip development and alignment 61
4.2.4 Displacement measurement 67
4.2.5 Instrumentation 72
4.2.6 Instrument considerations 78
4.2.7 Interfacing to microcomputer 80
4.2.8 Software development 85
4.3 Instrument Operation 86
4.3.1 Specimen preparation 86
4.3.2 Microindentor installation 86
4.3.3 Indentation sequence 87
4.3.4 Specimen exchange and system dismantling 89
4.4 Data Analysis 89
4.4.1 Dynamic, high magnification imaging 89
4.4.2 Load and displacement data processing 91

CHAPTER FIVE: INTERFACE CHARACTERISATION **96**

5.1 Determination of Interface Micromechanical Properties 96
5.1.1 Frictional sliding 96
5.1.2 Interface debonding and frictional sliding 98
5.1.3 Push-through test 100
5.1.4 Experimental procedure 102
5.2 Glass Ceramic Matrix Composites 106
5.2.1 As processed glass ceramic matrix composites 106
5.2.2 Heat treatment of glass ceramic matrix composites 115
5.2.2.1 Interface modification under oxidising conditions 115
5.2.2.2 Fibre strength degradation 123
5.2.3 Interface pre-synthesis via fibre coating 123
5.2.3.1 Chemical Vapour Deposition of bi-layer interface 124
5.2.3.2 Carbon coated Nicalon 127
5.2.4 Effects of fatigue on interfacial properties 130
5.3 Glass Matrix Composites 132
5.3.1 Structural characterisation of Borosilicate/Nicalon interfaces 132
5.3.2 Interfacial micromechanics and composite mechanical performance 140
5.4 Large diameter fibre reinforcements 144

CHAPTER SIX: DISCUSSION ON INTERFACE CHARACTERISATION **147**

6.1 Modelling of fibre push-down 147
6.1.1 Frictional shear stress τ 147
6.1.2 Debond fracture surface energy G_i 151
6.1.2.1 Models to determine G_i 151
6.1.2.2 Mixed mode crack deflection 154
6.1.2.3 Fracture energy of fibre reinforcement 156
6.1.2.4 Summary 157

6.2 Correlation of micromechanical behaviour to macromechanical performance 158
6.2.1 Comparison of interface structure to micromechanical behaviour 158
6.2.2 Matrix microcracking dependence on τ 163
6.2.3 Transition to brittle failure 165
6.2.4 Summary 166

CHAPTER SEVEN: ALTERNATIVE INDENTOR APPLICATIONS AND FURTHER DEVELOPMENT 167

7.1 Controlled crack propagation 167
7.2 Hardness and Modulus measurement 171
7.2.1 Hardness testing 171
7.2.2 Measurement of elastic modulus 175
7.2.3 Syalon 101 177
7.2.4 TiB_2 particulate reinforced sialon 181
7.2.5 Summary 184
7.3 Future development and applications 184
7.3.1 Improvement in indentation performance 185
7.3.2 Possible applications 187

CHAPTER EIGHT: CONCLUSIONS 190

8.1 The SEM based Microindentation System 190
8.2 Fibre Reinforced Ceramic Matrix Composite Interface Properties 191
8.3 Future developments 193

REFERENCES 194

APPENDIX I 202
APPENDIX II 211
APPENDIX III 215

ACKNOWLEDGEMENTS

I am indebted to Prof. Mike Lewis for giving me the opportunity to pursue this PhD, and thank him for the continuous encouragement and expert guidance he has given throughout. Thanks to the CMC group at Rolls Royce plc for their sponsorship and to Dr. Stuart Smith for help and advice on the development of instrumentation.

Within the Centre for Advanced Materials Technology, Warwick, I thank the two people whose combination of technical skills and experience in the world of electron microscopy is exceptional; Gerry Smith (experience) and Steve York (skills). I am grateful to Adrian Lovejoy and Ben Ackerman, and young Steve Carpenter for his photographic expertise and efficiency. I acknowledge Tony Chamberlain, Tony Razzell, Olwen Pullum, Nicole Frety, Markys Cain, Kevin Plucknett, Mark Pharaoh, John Lumby, F.Hong, Chris Wiffen, Stefan Bjorkert and Csaba Rappensburger, for their contributions both to work and to the more light hearted side of life on Floor 4. Thanks go to the Physics Department personnel in general.

I am grateful to Shirley, Noel and Sarah for looking after me during the majority of the time I have been writing. I may have had one or two more "specials" than were necessary to get me writing in the evenings, but I did enjoy them.

To Fiona, thank you for showing me there are more important things in life than ceramics and Aston Villa. Putting up with me and the PhD has not been easy, but I can promise you that good times are on their way - Olé, Viva España!

Most of all, I wish to thank my mother and father, Shirley and Thomas Daniel, for their continuous support, encouragement and understanding. They have given my brothers (Nicholas and Christopher) and I everything. I dedicate this work to them.

DECLARATION

This thesis is an account of my own independent research carried out between October 1990 and October 1993, at the Physics Department, University of Warwick. It has been prepared following the guidelines set out in document (PHYS/PG/3). Any contributions from other sources have been specifically acknowledged in the text. No part of this work has been submitted to this or any other institution toward the award of any other degree or qualification. Material has been presented at various international conferences and the following scientific articles have been published;

1) A.M.Daniel and M.H.Lewis "Measurement of interfacial micromechanics in fibre reinforced ceramic matrix composites" *Ceram. Eng. and Sci. Proc.*, **14** (7- 8), p131-138, (1993).

2) A.M.Daniel, S.T.Smith and M.H.Lewis,"A Scanning electron microscope based microindentation system." *Rev. Sci. Instrum.*, **65**, No.3, p 632-640, (1994).

3) A.M.Daniel and M.H.Lewis "Measurement of interfacial micromechanics in ceramic matrix composites" *Brit. Ceram. Trans.*, **93**, No.3, p108-113, (1994).

4) M.W. Pharaoh, A.M.Daniel and M.H.Lewis. "Stability of interfaces in CAS matrix /nicalon SiC fibre composites." *J. Mater. Sci. Lett.* **12**, p 998-1001, (1993).

5) M.H.Lewis, A.M. Daniel, A.Chamberlain, M.W.Pharaoh and M.G.Cain. "Microstructure - property relationships in silicate-matrix composites." *J.Microscopy*, **169**, 2, p109-118, (1993).

6) M.G.Cain, A.M.Daniel and M.H.Lewis. "Presynthesised interfaces for ceramic matrix composites via fibre coating." *Mater. Lett.*, **17**, p 246-252,(1993).

7) M.H.Lewis, A.Chamberlain, A.M. Daniel, M.W.Pharaoh, A.G. Razzell and S.Sutherland. "Microstructure and macromechanical behaviour of CMC's." *Proc. AGARD / NATO workshop on Introduction of Ceramics into Aerospace Structural Composites, Antalya, Turkey, 1993.* AGARD-R-**795**, ref. 10, (1993). *Defence Reasearch Information Centre, 65 Brown Street, Glasgow.*

8) A.Chamberlain, A.M.Daniel, M.W.Pharaoh and M.H.Lewis. "Fracture mechanical behaviour and interface properties in glass and glass-ceramic matrix composites." *Published in "HT-CMC 1", p321-328, ed. R.Naslain, J.Lamon, D.Doumeinats. Woodhead Publ. (1994).*

9) K.P.Plucknett, G.West, D.M.R. Taplin, A.M.Daniel, S.Sutherland, R.L.Cain and M.H.Lewis. "Continuous fibre reinforced glass-ceramic matrix composites:microstructure, mechanical behaviour and environmental stability." *Published in "Advances in Fracture and Structural Integrity" Pergamon Press, Oxford. 1994.*

10) R.F.Allen, A.M.Daniel, M.H.Lewis and P.Bowen. "The effect of cyclic loading on the interfacial shear stress in a SiC/CAS glass ceramic matrix composite." *Scripta Metall. (in press).*

11) K.P.Plucknett, S.Sutherland, A.M.Daniel, R.L.Cain, G.West, D.M.R.Taplin, and M.H.Lewis. "Environmental ageing effects in a silicon carbide fibre reinforced glass-ceramic matrix composite." *J. Microscopy. (submitted June 1994).*

12) M.H.Lewis, A.M.Daniel and M.G.Cain."Interfacial characterisation using an SEM based microindentor ." *Proc MRS symposium (M) on "CMCs /Advanced High Temperature Structural Materials", 28Nov.- 2Dec. 1994, Boston, USA. MRS, Pittsburgh, Pennsylvania 15237, USA.*

CHAPTER ONE
INTRODUCTION

1.1 Gas Turbine Material Requirements

The highly competitive aerospace industry is responsible for an ever increasing drive towards improvement of aero-engine performance and efficiency. Engine thrust, weight, fuel efficiency and cost are primary factors that determine a gas turbine's performance and their relative importance differs depending on the engine's use. For military applications, high thrust and low weight are the major design priorities whereas fuel efficiency and cost are given greater consideration when designing engines for civil aircraft. Over the past 50 years, military driven developments have increased thrust to weight ratios more than three fold and take off thrusts from 1,000 lbs to over 50,000 lbs [1].

Current turbines are reaching their optimum aerodynamic design. The application of nickel based superalloys in critical components is only possible by using up to 20% of the air intake of the engine to cool them, reducing the efficiency of the engine. A decrease in the proportion of cooling air used will produce a proportional increase in the power output of the engine and so great performance gains can be made if the amount of air required for cooling can be dramatically reduced. This can only be done by using component materials that have higher temperature capabilities than the current metal alloys. Cooling of components such as turbine blades and nozzles, currently allows a maximum turbine entry temperature (temperature of the gas stream as it enters the turbine) of 1800°C that is 700°C higher than the softening point of the component material. As with any heat engine, its efficiency is increased if its operating temperature can be increased. Therefore, if materials can be developed that can operate at temperatures approaching 2000°C (the stoichiometric combustion temperature of

kerosine) with minimal cooling, then maximum thermal efficiency would be achieved [1].

Over the past 25 years this requirement for structural components with high temperature capability has been the subject of world-wide materials development programs. Initially driven by the military markets [2], since the ending of the cold war fundamental research has necessarily become a collaboration between both civil and military organisations. An example is the U.S. policy of "Dual Use" funding where Government funds are split between co-operating civil and military aerospace agencies [3]. Whereas previously new technology was developed primarily to increase thrust to weight ratios and reduce physical engine size for military combat applications, priorities are now turning to development of fuel efficient engines for civil aircraft that have lower operating costs and are less damaging to the environment.

The possible economic gains to be made in the civil market are enormous. Recognition of this by western governments is evidenced by the long term research programs set up in the U.S.A., Japan and the E.C. [4]. Current estimates suggest that if Europe can maintain its current share of the world civil aero-engine market over the next 20 years, the business will be worth 80 billion ECU [5]. To do this, the product must remain competitive and this requires the development of engines that operate at higher temperatures than at present.

1.2 Ceramic Matrix Composites

The materials targeted as being the solution to achieving the higher temperature gas turbine are ceramics. Ceramics have been used for thousands of years in refractory applications such as furnace linings and kiln ware but it is only relatively very recently that processing techniques have progressed to a state where materials can be fabricated with a critical control over composition, microstructure and properties that can raise their performance limits. A ceramic can be defined as an inorganic, non-metallic solid and is often fabricated at high temperatures as the high energy bonding

(that can be covalent, ionic or mixed) between its atoms produce high melting or dissociation temperatures. The strong bonding gives ceramics the properties that make them potentially useful for high temperature structural applications. In particular, the advantages that ceramics have over metal alloys are ;

i) A much higher temperature capability.

ii) Better environmental resistance.

iii) Lower density (and high specific strength and stiffness).

However, they are not currently in large scale use because single phase or monolithic ceramics are brittle and susceptible to catastrophic failure. Such a property is unacceptable for components in high risk applications such as aero-engines. Introducing toughness into these materials, whilst maintaining their useful properties, has therefore been the goal of material scientists.

In a single crystal ceramic, a crack typically propagates through the material without resistance once a critical stress at the crack tip has been reached. In the same, but now polycrystalline ceramic, the force required to drive an equivalent sized crack through the solid is higher. This is due to microstructural features of grain boundaries, grains, inclusions and porosity reducing stresses in the material near the crack tip, thus increasing the applied force required to cause crack motion. Reduction in crack tip stresses is due in this case to the microstructure deflecting the crack so that it no longer lies in the optimum plane for stress concentration but can also, in a multi-phase material, be due to compressive internal stresses being applied across the crack tip by mechanisms involving microstructural aspects such as thermal expansion anisotropy, grain or fibre bridging and pull-out, and phase transformations. This influence that microstructural size and scale effects have on mechanical properties is the basis for increasing the strength and toughness of ceramics either by tailoring the microstructure of monolithics or by incorporating extra phases, producing Ceramic Matrix Composites (CMCs) [6].

1.2.1 Historical development

It was in the 1950's when the development of high strength ceramic composites got under way with a view to final application in aero-engine components [7]. The manufacture of glass fibres with strengths that approached the theoretical limit [8] and the production of vapour-grown whiskers of materials that had extremely high strength [9] became possible. It was realised that these whiskers and fibres when aligned correctly within a matrix could increase greatly the strength and toughness of a material, whether it be polymeric, metal or ceramic. For CMC manufacture however, the perfection of the fibres were seriously limited by their growth conditions and the scarcity and expense of vapour-grown whiskers restricted interest in these reinforcements to a minimum. In some cases aligned whiskers within a matrix could be obtained economically by growing them in-situ, via solidification from a near eutectic composition. However, the volume fraction and composition of whiskers and matrix were restricted by phase equilibria and significant increases in toughness were generally not achieved because the strong interface between matrix and reinforcement, resulting from the growth process, allowed matrix cracks to propagate through non-yielding whiskers or restricted the plastic elongation that a yielding whisker could sustain.

Work was carried out in the 1960's incorporating ductile phases into ceramic matrices [10]. However, the use of metal wire reinforcement was not a success as the ductile yielding of the metal facilitated matrix cracking with little resistance.

The first example of a ceramic composite displaying a significant increase in toughness compared to its monolithic matrix behaviour was produced by Crivelli-Visconti and Cooper in 1969 [11]. They produced a carbon fibre reinforced vitreous silica with a work of fracture of 11kJm^{-2} that compared to only 4Jm^{-2} for the matrix alone. It maintained its strength at temperatures up to 800°C. Other early work placed carbon fibre and silicon carbide monofilament reinforcements in different ceramic matrices resulting in work of fracture reaching 20 kJm^{-2} [12-16]. This initial activity on

fabrication was accompanied by theoretical modelling of the mechanical properties and failure behaviour of unidirectional fibre reinforced CMC's. Aveston, Cooper and Kelly, in what today is considered the fundamental model, attributed the high work of fracture of these materials to the energy lost to friction at the fibre-matrix interface as the fibres are pulled out from the matrix [17]. The so called 'ACK model' will be discussed in Chapter 2.

Interest in these fibre reinforced CMC's soon subsided however. The widely used carbon fibre reinforcement oxidised when the composites were held at high temperatures and mechanical properties suffered drastically. Concurrently, in the mid 1970's, a lot of promise was being shown by the monolithic SiC, Si_3N_4 and Sialon systems. By careful processing control it was thought they could provide the material requirements for gas turbine components and as they were monolithic, forming the complex shapes required would be far easier than doing so with fibre reinforced structures. The unusually high fracture toughness of the Si_3N_4 monolithic was due to the microstructural development of elongated grains during liquid phase sintering. A solution-precipitation mechanism results in elongated β-phase Si_3N_4 grains that introduce toughness via crack bridging and pull-out mechanisms. However, the residual glassy phase present at grain boundaries limits good mechanical properties to temperatures below 1200°C. To reduce the amount of liquid phase present for sintering and so reduce the amount of residual glass, the more complex Si-Al-O-N system has been extensively investigated. Although now realised to be an unsuccessful material for high temperature gas turbine use, it has achieved moderate success in lower temperature applications where the liquid phase content can be increased to enable processing by pressureless sintering. Sialon cutting tools have cut down machining times of current metal alloy turbine discs by over 75%, sialon die inserts used in the hot and cold extrusion of metals give improved dimensional accuracy and extrusion speeds, and sialon diesel engine components have been successfully manufactured and tested [18-22].

By the early 1980's the development of transformation toughened ceramics

helped even more to concentrate work on monolithic sinterable ceramics. The martensitic transformation of ZrO_2 from its high temperature tetragonal structure to the room temperature monoclinic structure is accompanied by a ~4% volume increase. Particles of ZrO_2 below a critical size can be held at room temperature in the high temperature tetragonal state if constrained by a stiff matrix. An applied tensile stress can then induce transformation from this metastable state to the monoclinic structure. Toughening relies on this stress induced transformation occurring in particles within a limited zone of stress concentration near a crack tip. The accompanying increase in volume of the particles produces compressive strains that reduce the stresses at the crack tip. The toughening mechanism is dependent on the degree of undercooling of the metastable structure and so the size of the effect diminishes as the temperature of the composite approaches the thermodynamic equilibrium temperature of the transformation and disappears above this temperature. Thus, the use of zirconia additions has produced a family of exceptionally strong and tough ceramics for ambient temperature application that are unsuitable for use at elevated temperatures.

Towards the latter half of the 1980s it was realised that development of the Si_3N_4 and Sialon monolithics had reached limits of refinement that fell below original expectations and the severe temperature limitations of the zirconia toughened composites prevented use in gas turbine components. As a result, interest swung back to the development of whisker and fibre reinforced ceramic matrices. This was possible because of the discovery of methods of producing SiC whiskers in large quantities [23,24], and the development of fibres [25] that were more stable at higher temperatures and in oxidising environments, than carbon fibre.

1.2.2 Whisker and short fibre reinforced ceramic matrices

Short fibre and whisker reinforcements offer advantages in the production of complex shapes with sharp corners or doubly curved surfaces as they have greater freedom to adjust to matrix reconfiguration during processing such as occurs during

sintering. To achieve maximum strength and toughness, the whiskers or fibres should be well aligned. Although a minor alignment of the reinforcements is usually unavoidable due to material flow during processing, to orient the large majority of whiskers, in an originally random jumble, is not easy. They also have the problem that only low concentrations can be incorporated successfully into matrices as their random orientation geometrically inhibits efficient packing. The most successful SiC whisker reinforced matrix to date is Al_2O_3 [26,27]. It has a work of fracture four-fold that of the monolithic matrix material and has found commercial application in, for example, the ceramic cutting tool market. The increase in toughness obtained with this type of reinforcement is significantly less than that of continuous fibre reinforced ceramics. An example is the almost 3000-fold increase in work of fracture of Crivelli-Visconti and Cooper's original composite over the monolithic matrix material [11] compared to the above 4-fold increase for a high performance whisker reinforced Al_2O_3 . Faber and Evans [28] have shown that the theoretically maximum increase in work of fracture from rod shaped reinforcements such as whiskers/chopped fibres, due to the toughening mechanism of crack deflection, is by a factor of 16 - still much less than 3000. (Other mechanisms such as crack bridging and grain pull-out do contribute extra, but often not as much).

1.2.3 Continuous fibre reinforced ceramic matrices

As stated above, the recent (mid 80's to present day) concentration on fibre reinforced ceramic matrices is due to the shortfall of monolithics in reaching their once perceived potential and to the development of fibres that are stable up to the same temperatures as their potential matrices.

Yajima et al's [25] development of a polycarbosilane resin that could be spun and pyrolysed to form a 12-18 μm diameter silicon-oxy-carbide fibre (Nicalon®, Nippon Carbon, Japan) that was stable at temperatures up to 1200°C in air, meant that there was a way of producing high strength, high temperature capability fibres in

quantity. Although developed in the 70's, it was not extensively used until the early to mid 80's. Prewo and Brennan, in conjunction with Chyung produced Nicalon reinforced glass-ceramic matrices with exceptional properties and performed extensive compositional and mechanical characterisation [29-32]. Since then, CMC development has been driven by the availability of suitable fibres. There are currently four types being used for high temperature composite development. They are a) carbon fibres that can operate up to 2200°C but may oxidise as early as 500°C, b) silicon carbide and silicon nitride yarns that are limited to a maximum of 1200°C-1400°C, c) SiC monofilaments that are produced via Chemical Vapour Deposition (CVD) and, d) polycrystalline and single crystal alumina fibres. Cases (c) and (d, single crystal) have large diameters of 120 - 150 μm which means they are not weavable into 2- or 3-dimensional structures but they do have the highest temperature capabilities in oxidising environments. The current classes of matrix under investigation and their operating temperatures are i) glass-ceramics (up to 1200°C), ii) oxides (in excess of 1500°C), iii) silicon carbide or silicon nitride (up to 1700°C) and, iv) carbon (potentially in excess of 2000°C when reinforced with carbon fibre).

This thesis is concerned with the investigation of continuous fibre reinforced ceramic matrix composites. Details of the mechanisms that increase the strength and toughness of ceramics via continuous fibre reinforcement will be discussed in Chapter 2 as well as a review of current composite development.

CHAPTER TWO

CONTINUOUS FIBRE REINFORCED CERAMIC MATRIX COMPOSITES

2.1 Fracture Mechanics

The toughening mechanisms present in continuous fibre reinforced ceramics differ from those of other composite systems mentioned in Chapter 1. In this section a brief review of brittle fracture mechanics will be given, followed by a full description of the mechanical behaviour and fracture mechanics of fibre reinforced CMCs.

2.1.1 Brittle failure of ceramics

The theoretical tensile strength of a solid is the stress required to break the atomic bonds at a cleavage plane and pull the structure apart. Considering the energy required to break these bonds, the theoretical strength σ_{th} can be shown to be

$$\sigma_{th} = \left[\frac{E\gamma}{a_0}\right]^{1/2} \tag{2.1}$$

where E is Young's modulus, γ is the fracture surface energy and a_0 is the interatomic spacing [33]. In reality, the measured strength of most ceramics is often 100 - 1000 times lower than σ_{th}. This was recognised by Inglis [34] and Griffith [35] to be due to the presence of microscopic flaws caused by fabrication routes or structural imperfections.

Inglis considered such small flaws or cracks to act as local stress concentrators within the material that magnify the applied stress at the tip of a crack and when this localised stress exceeds the theoretical strength σ_{th}, the crack propagates

and failure occurs. For an idealised flaw, he showed the stress at the tip σ, to be

$$\sigma = 2\sigma_a \left[\frac{c}{\rho}\right]^{1/2} \tag{2.2}$$

where σ_a is the applied stress, c is the crack length and ρ is the crack tip radius. In ceramic materials, crack lengths are typically 10 - 100 μm and crack tip radii of the same order of the interatomic spacing, 0.3 - 1 nm. Stress magnification factors up to 1000 thus result and these correlate with the measured tensile strengths of $\sigma_{th}/1000$ already mentioned [6].

Griffith's approach was to consider the the mechanical energy of crack stability. He equated the energy required to form two areas of new surface to the mechanical energy lost as the crack propagated. This resulted in the relationship for the applied stress at which failure occurs σ_f,

$$\sigma_f = \left[\frac{2E\gamma}{\pi c}\right]^{1/2} \tag{2.3}$$

where E is the Young's modulus, c is the crack length and γ is the surface energy of the solid.

As with Inglis' model, the strength of the solid is inversely proportional to the square root of the crack length and indeed these models are equivalent when the crack tip radius is of the order three times the lattice spacing of a brittle solid.

Irwin [36] extended these ideas to form the discipline of linear elastic fracture mechanics. He introduced the parameter of energy release rate, G, defined as the total mechanical energy release of the system, U, per unit surface area, A, that is formed for an infinitesimal crack extension,

$$G = \delta U / \delta A \tag{2.4}$$

When G reaches a critical value G_C, equal to (or greater than) twice the surface energy of the ceramic 2γ, fracture occurs. From equation (2.3),

$$2\gamma = \pi \sigma^2 c / E \tag{2.5}$$

and so with $G_C = 2\gamma$,

$$G_C = \pi \sigma_c^2 c / E \tag{2.6}$$

where σ_c is the stress applied to fracture brittle material with crack size c. The critical value G_C for particular materials can be determined by measuring the σ_c required to fracture a plate with a crack of known size in it. This modification to Griffith's theory can include a plastic term for consideration of metal fracture but even so, the energy balance approach still relies on the crack tip being atomically sharp and so is impracticable for many applications.

This lead Irwin to develop the stress intensity approach which describes the stresses in the vicinity of a crack tip σ_{ij} as

$$\sigma_{ij} = K / \sqrt{(2\pi r)} . f_{ij}(\theta) \tag{2.7}$$

where r, θ are the cylindrical polar coordinates of a point with respect to the crack tip, K is a parameter known as the stress intensity factor, and $f_{ij}(\theta)$ is a function of angle θ. K gives the magnitude of the elastic stress field and is defined as

$$K = \sigma Y c^{1/2} \tag{2.8}$$

with Y a dimensionless constant that is determined by the geometries of crack and specimen. As for G_C, for a particular crack length there is a critical K_C determined by

measuring the stress applied to a specimen for it to fail. Both G_C and K_C are alternative measurements of the fracture toughness of a brittle material and are simply related. For a crack opening under tension, it can be shown

$$K^2 = E\,G \tag{2.9}$$

under plane stress conditions, thus showing that the stress and the energy approaches to fracture are equivalent.

Brittle failure can be resolved into three distinct modes (see figure 2.1) ;

mode 1 - crack opening,

mode 2 - crack shearing,

mode 3 - crack tearing.

When giving K_C and G_C values for specific modes of fracture, the terms are suffixed for clarity, e.g. K_{1C} and G_{1C} for mode 1 critical intensity factor and mode 1 critical energy release rate.

Thus equation (2.9) becomes $K_1 = E\,G_1$ and for fracture, $K_{1C} = E\,G_{1C}$.

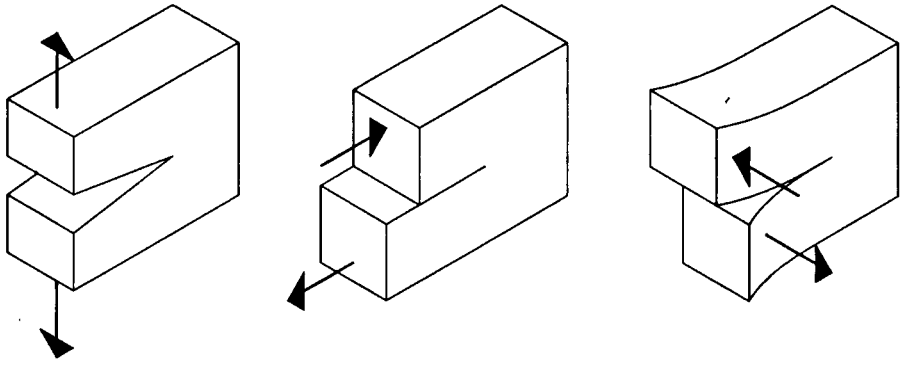

Figure 2.1. The three modes of brittle fracture.

In real ceramics, the flaws are randomly distributed and have varying sizes. As a result, prediction of and designing for fracture has to be treated via a probabilistic

approach. The most frequently used technique is that devised by Weibull [37]. Based on a weakest link theory, it assumes that a given volume of material under uniform stress will fail at the most severe flaw. A Weibull analysis gives the probability of failure P_f as a function of the applied stress σ, and the volume V under stress. For completely brittle ceramics,

$$P_f = 1 - \exp\left[-\int_V \left[\frac{\sigma - \sigma_u}{\sigma_o} \right]^m dV \right] \tag{2.10}$$

where σ_u is the threshold stress below which the probability of failure is zero, σ_0 is a normalising term and m is the Weibull modulus. The latter two parameters are a measure of the homogeneity of the size and distribution of flaws.

It is this statistical nature of the brittle fracture of monolithic ceramics that make them unsuitable for use in the high risk applications of aerospace. In CMCs, toughening mechanisms are introduced not only to increase the strength and toughness of materials but also to reduce the statistical spread in these properties, so that component designers can use them with confidence. The toughening mechanisms operating in continuous fibre reinforced ceramics are described below.

2.1.2 Fibre reinforced composite mechanical behaviour

Most practical fibre reinforced CMC's will undergo stresses that are multiaxial and will require 2- and 3- dimensional reinforcement structures (i.e. cross plied and woven fibres). The rigorous examination of the failure mechanisms of such complex reinforced systems is currently the subject of considerable effort but the fundamental toughening and failure processes that operate can be illustrated by considering a uniaxially reinforced composite system.

For the successful production of a tough CMC of higher modulus than a monolithic of pure matrix material, the elastic modulus of the fibre needs to be greater

than that of the matrix. This enables the fibres to reinforce the matrix by effectively sharing the applied stress. The elastic modulus of the composite is then given by the rule of mixtures,

$$E_c = E_f V_f + E_m V_m \tag{2.11}$$

where E_c, E_f and E_m are the elastic moduli of the composite, fibre and matrix respectively, and V_f, V_m the volume fractions of fibre and matrix. An example of the typical stress-strain behaviour of a tough, uniaxially reinforced material with fibre direction parallel to the tensile force is shown in figure 2.2(b). The stress-strain curve is very non linear and comprises three notable regions A, B and C.

Region A is the elastic region where the response of the material is governed by equation (2.11). As the composite is stressed, both fibre and matrix are subject to the same strain. Conventionally, the fibre is chosen to have a greater failure strain and strength than that of the matrix, and so at a certain strain (dependent on many material

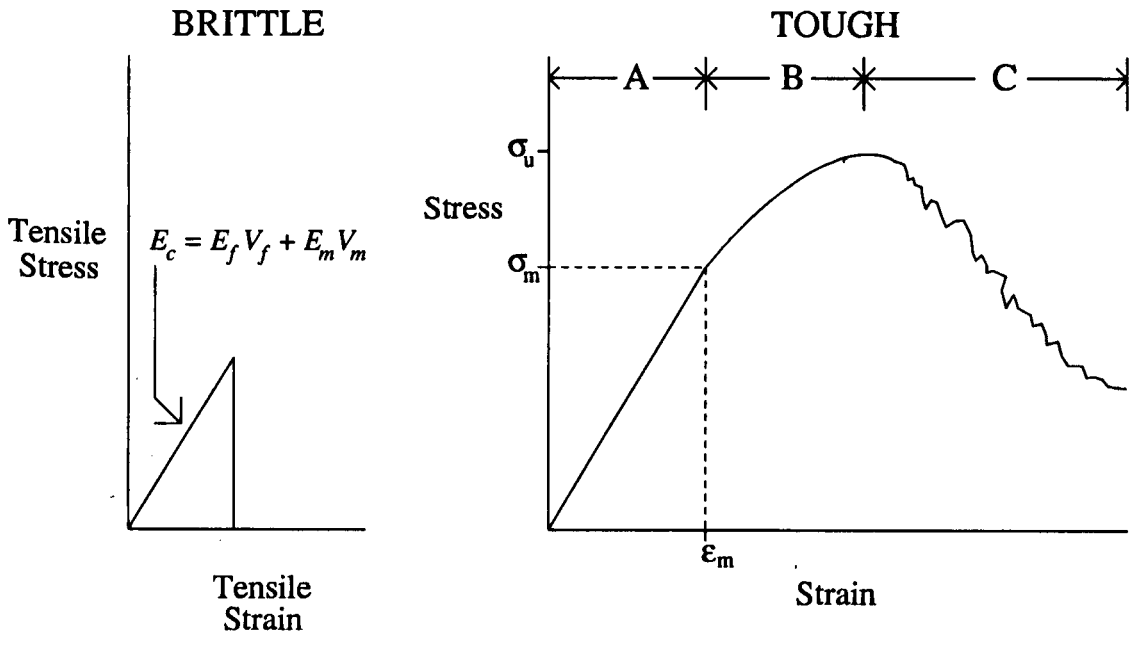

Figure 2.2. Composite Tensile Behaviour a) Brittle due to strong interface bond and b) Tough due to weak interface bond.

parameters), the matrix will fail before the fibres. As a result, two possible paths to complete composite failure are possible ;

i) If the fibres are well bonded to the matrix then a propagating matrix crack may pass straight through the fibre - matrix interfaces and continue through the fibres, resulting in brittle failure of the material, see figure 2.2(a). The fibres improve the material's performance (e.g. higher elastic modulus) but they do not eliminate its brittle nature.

ii) If the fibres are weakly bonded to the matrix, the advancing matrix cracks are deflected at the fibre-matrix interface, around the fibre, preventing fibre failure. The fibres are able to bear the load after the matrix has cracked. A stress-strain curve similar to that of figure 2.2(b) results where failure is not catastrophic, the composite material is not brittle.

Debonding of the matrix from the fibre at a crack front is the necessary condition for a composite to be tough. After the first matrix crack propagates, the stress strain curve is dominated by multiple matrix microcracking (region B in figure 2.2(b)), where the intact fibres bear the applied load by bridging an increasing number of regularly spaced matrix cracks. Under increasing load the composite strains until region C of figure 2.2(b) where multiple fibre failure occurs followed by their "pull out" of the matrix at the fracture plane.

2.1.2.1 Fibre - matrix interface debonding at matrix crack front

A crack impinging on an interface joining two dissimilar materials may arrest or may advance by either penetrating the interface or deflecting into the interface. For a fibre reinforced CMC to be tough, a matrix crack must be deflected into the interface. The typical mode 1 matrix crack propagating under tensile load impinges on an interface and has to deflect along the interface in a shear manner i.e. with mode 2 component. This mechanism was modelled by He and Hutchinson [38] for both singly

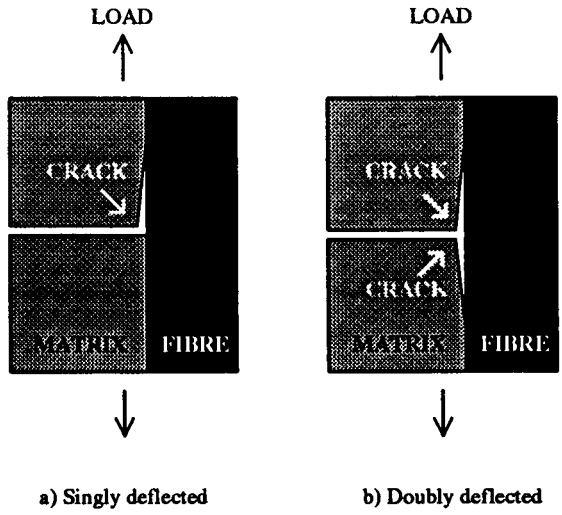

Figure 2.3 Crack deflection at an interface.

and doubly deflected cracks, see figure (2.3). By considering the ratios of energy release rate for a penetrating crack and a deflected crack, the requirement for deflection was determined to be

$$G_i / G_f < G_d / G_p \tag{2.12}$$

where G_i = the interface fracture surface energy, G_f = the fibre fracture surface energy, G_d = the energy release rate for a deflected crack and G_p = the energy release rate for a penetrating crack. In general, G_i is dependent on the ratio of shear to opening stresses for the propagating crack, i.e. ratio of mode 2 to mode 1 failure, and is a function of ψ,

$$\psi = \tan^{-1} (K_2 / K_1) \tag{2.13}$$

where K_2 and K_1 are the stress intensity factors for the respective fracture modes. The crack branching to one side generally controls the condition for deflection at the interface as it corresponds to the highest ratio of G_d / G_p . This is shown in figure (2.4), taken from [38], where G_d / G_p is plotted against elastic modulus mismatch of matrix and fibre, α_E,

$$\alpha_E = (\hat{E}_f - \hat{E}_m) / (\hat{E}_f + \hat{E}_m) \tag{2.14}$$

where

$$\hat{E} = E / (1 - \nu^2) \tag{2.15}$$

and ν is the Poisson's ratio. As can be seen, for α_E approximately equal to zero, the critical ratio is $G_d / G_p = 1 / 4$, but if the modulus of the fibre reinforcement approaches three times that of the matrix, $\alpha_E = 1 / 2$ and $G_d / G_p \sim 1 / 2$. Thus, depending on the elastic mismatch, the condition for cracks to be deflected around fibres, leaving them intact and bridging the cracks, is

$$G_i / G_f < 1 / 4 \rightarrow 1 / 2 \tag{2.16}$$

i.e. the fracture surface energy (or fracture energy release rate) of the interface has to

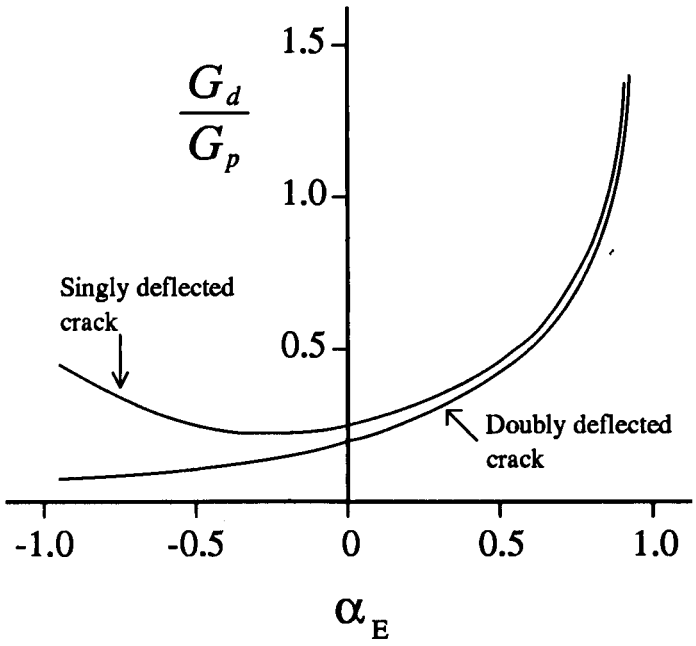

Figure 2.4. Ratio of energy release rate of deflected crack to penetrating crack as a function of elastic mismatch of fibre and matrix.

(From reference [38]).

be less than or equal to 1/4 →1/2 that of the fibre.

Deflection of a crack is necessarily a mixed mode failure mechanism, exemplified by the above examples where pure, tensile mode 1 cracks impinging on an interface at 90° are deflected to shear mode 2 along the interface. The relative contributions of K_1 and K_2 at the deflected crack tip can be illustrated by plotting ψ as a function of α, see figure (2.5). The trace shows that the mode 2 / mode 1 ratio is greater for a singly deflected crack than a doubly deflected one and that it can vary considerably for $\alpha_E = 0$ to $\alpha_E = 1/2$.

He and Hutchinson also considered the cases of cracks approaching interfaces at an oblique angle and found that the tendency to deflect increases the more oblique the crack. It was concluded that if an interface is to be designed to deflect cracks of any orientation, the 90° impinging crack should be taken as the required

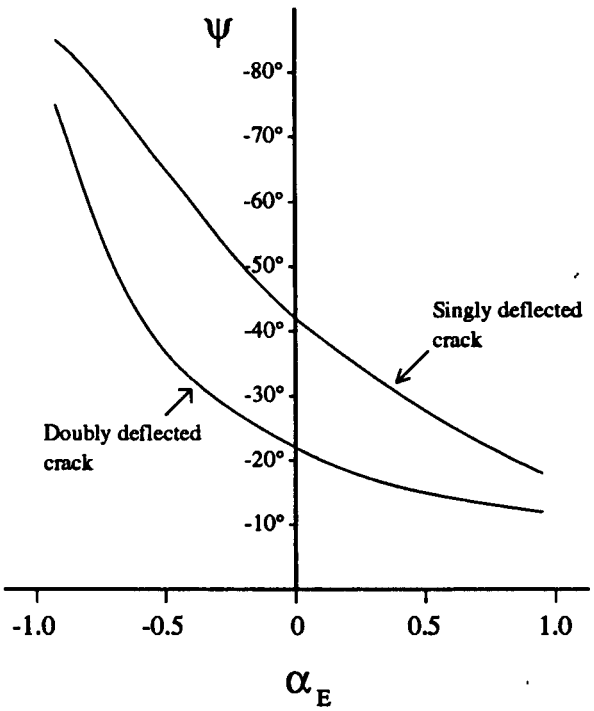

Figure 2.5. Combination of stress intensity factors at tip of deflected crack.

(From reference [38]).

condition to be satisfied. Thus the interface should be tailored to satisfy the conditions of figure 2.4.

It must be noted that although this condition is generally accepted as the necessary condition for fibre-matrix debonding at a matrix crack front and thus tough behaviour of a fibre reinforced composite, it has not to date been proven experimentally. This is due to the difficulty in measuring the interface fracture surface energies in a real composite. Current techniques used for measuring interface properties will be discussed in Chapter 3.

2.1.2.2 Matrix microcracking

Once stress/strain increase until the first matrix cracks propagate across the CMC, with the fibres left bridging them, the mechanical response of the material enters the matrix microcracking region (region B of figure 2.2(b)). The matrix microcracking region is typified by the further development of a series of cracks across the matrix that occur at regularly spaced intervals. It is a characteristic of all brittle matrix composites, occurring in such examples as fibre reinforced cements and reinforced concrete.

Although a complicated phenomenon, influenced by many parameters, a basic understanding is gained by the model first proposed to explain it, developed by Aveston, Cooper and Kelly [17]. Simplistically, the statistical flaw dependency of fracture strength of brittle ceramics (mentioned above in section 2.1.1) is ignored and it assumed that each material (fibre and matrix) has a well defined fracture stress and strain. The so called ACK theory also assumes the interface sustains purely frictional shear stresses i.e. there is no physical bonding between fibre and matrix to overcome - the interface fracture surface energy is zero.

Under stress the tensile strain is the same in the matrix and fibre until the first crack forms. As the failure strain of the fibre is conventionally greater than that of the matrix, the crack initiates and advances across the matrix, at a normal to the stress-

fibre axis. If the volume fraction of the fibres is large enough, the load is transferred to the fibres and they are left bridging the crack. The stress in the matrix immediately adjacent to the crack is now zero but will increase with distance from the crack, in the direction of the tensile force, at a rate determined by the frictional shear stress of the interface τ. It will eventually reach the matrix failure stress at a distance X from the crack and so another crack will traverse the matrix. Thus cracking proceeds, with no increase in load, until there are approximately uniform cracks spaced between X and $2X$ apart, normal to the stress-fibre axis (see figure 2.6), where

$$X = (V_m / V_f).(\sigma_m r / 2\tau) \tag{2.17}$$

and σ_m is the stress in the matrix at which cracks form (matrix microcracking stress), τ is the shear stress at the interface, r is the fibre radius and V_m , V_f are the matrix and fibre volume fractions.

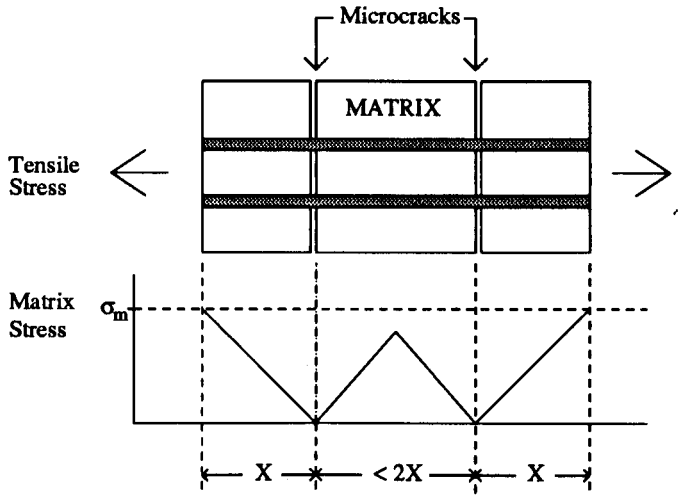

Figure 2.6 ACK modelling of matrix microcracking.

The ACK model is based on an energy balance argument. For the cracking to start, the work done by the applied stress in straining the composite (ΔW), plus the

release of strain energy by relaxation of the matrix on either side of the crack (ΔU_m), must be greater than or equal to the sum of the increase in strain energy of the fibres (ΔU_f), the frictional energy loss due to the relative sliding of the matrix and fibres near the crack (U_s), and the fracture surface energy of the matrix ($G_m V_m$), i.e.

$$\Delta W + \Delta U_m > \Delta U_f + U_s + G_m V_m \tag{2.18}$$

It can then be shown that the stress at which microcracking starts is,

$$\sigma_m = \left[\frac{6 \tau G_m E_f E_c^2 V_f^2}{r (1-V_f) E_m^2} \right]^{1/3} \tag{2.19}$$

Hence by decreasing the fibre radius, increasing the fibre volume fraction or increasing the interfacial shear stress, the microcracking stress can be increased.

The idealised stress - strain behaviour predicted by the model is shown in figure 2.7. At the point of multiple microcracking there is an increase in strain with no increase in stress that is due to the crack openings. The elastic modulus of the composite immediately after matrix microcracking is determined by the modulus of the

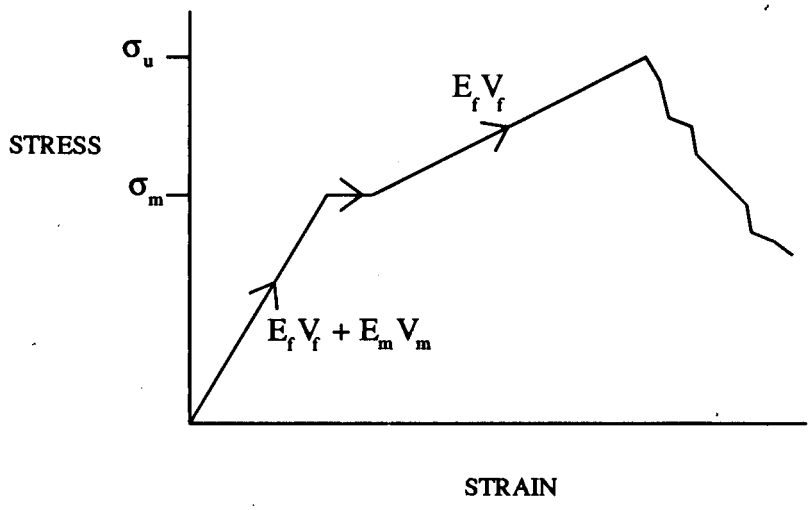

Figure 2.7 Idealised ACK model of CMC mechanical behaviour.

reinforcing fibres and their volume fraction. Each fibre now holds $1/V_f$ times the stress applied to the composite.

Applied stress and strain then increase until V_f times the fracture stress of the fibres is reached. At this point, according to ACK, all the fibres fail and are pulled out of the matrix, giving an ultimate composite strength of

$$\sigma_u = V_f S \tag{2.20}$$

where S is the fibre fracture stress. Fibre pull out requires work to be done against the frictional shear stresses of the interfaces and so the stress-strain plot does not drop immediately to zero but tails off gradually, introducing toughness.

In reality however, ceramics do not have well defined fracture stresses and strains. The statistical nature of failure strengths result in a CMC mechanical behaviour that is not as idealised as the ACK theory describes. Multiple matrix microcracking occurs in a progressive manner with increasing stress as is evidenced by region B of figure 2.2(b). The onset of microcracking is shown by the deviation from linearity at stress σ_m where the first microcrack forms. With increasing stress, more cracks develop and the modulus of the composite as a whole decreases. The fibres debond and slip relative to the matrix, absorbing applied work.

The increase in composite toughness due to the steady state microcracking mechanism ΔG_c (increase in fracture energy release rate), can be estimated as [39],

$$\Delta G_c = \frac{S^3 r V_f (1-V_f)^2 E_m^2}{6 \tau E_f E_c^2} \tag{2.21}$$

where S is the strength of the fibres (taken as a single value, ignoring statistical spread). However, this increases typical toughness values only by a factor of 3 [39]. The orders of magnitude increase found in CMCs are due to additional contributions to toughness from unbroken fibres bridging the crack wakes and slipping relative to the matrix and

from fibre pull-out, caused by fibre failure away from the matrix crack plane. Analysis of unbroken fibres slipping in a matrix crack wake [39] shows

$$\Delta G_b \propto [\, r^{m-5} / \tau^{m-2} \,]^{1/(m-1)} \qquad (2.22)$$

where ΔG_b is the component of increase in toughness due to unbroken fibres and m is the Weibull modulus that describes the statistical spread of fibre failure strengths within the composite.

2.1.2.3 Fibre failure and pull out.

In the microcracking region, as applied stress increases, the load is taken by the fibres and the interfaces. As the ultimate tensile strength σ_u is approached, individual fibres start to fracture and are pulled out of the matrix. This is not catastrophic as would be expected if all the fibres had the same strength. The random flaws in the fibres result in a statistical nature of failure that is described by a Weibull distribution. The fibres fail at points where applied stress is large enough to activate these pre-existing flaws.

After σ_u, the mechanical response enters region C of figure 2.2(b) that is dominated by the fracture and pull out of all the reinforcing fibres. The fibre-matrix interfacial frictional shear stress τ resists this pull out with the work done against it being dissipated as heat and producing a significant contribution towards the total work required to fracture the composite.

One would initially expect a high value of τ to contribute to a high work of fracture in region C of figure 2.2(b). However, for a large τ , the linear decrease in fibre stress with distance from a matrix microcrack plane is steep and so the volume of fibre under large stress is small [40,41]. Consequently, fibre failure occurs near the microcrack plane, resulting in a short fibre pull out length and little contribution to the

work of fracture through pull-out. A small τ produces large pull out lengths due to the shallow decrease in fibre stress with distance from a crack plane, causing fracture at fibre flaws a greater distance from the matrix crack. This is illustrated in figure 2.8. Large fibre pull out lengths require more work to pull them out and are characteristic of good fibre reinforced CMCs.

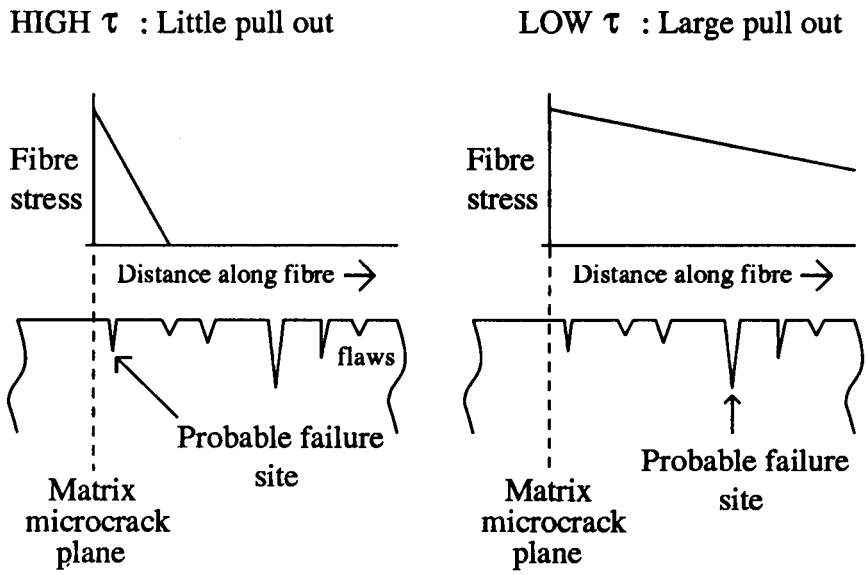

Figure 2.8 Probable fibre failure site - dependency on τ and effect on pull out lengths.

The contribution to the increased toughness due to broken fibre pull out is of the form [39],

$$\Delta G_b \sim \langle h \rangle^2 (\tau / r) \tag{2.23}$$

where $\langle h \rangle$ is the average fibre pull out length. Consideration of h in terms of fibre strengths and their Weibull distribution gives [39],

$$\Delta G_b \propto [\, r^{m-3} / \tau^{m-1} \,]^{1/(m+1)} \tag{2.24}$$

Comparing (2.22) and (2.24) above, it is seen that there are inversions of toughening trends with respect to r and τ , depending on the statistical spread of fibre strengths. When $m > 5$, the toughness increases with increasing r, but decreases when $m < 3$. It increases with increasing τ when $m \leq 1$ and decreases when $m > 2$. These limits arise because of the competing contributions towards toughening from the intact fibres bridging cracks and the failed fibres that experience pull out. The value of m is thus a crucial parameter to be considered when designing a composite.

Currently, the choice of fibres for reinforcement of high temperature CMCs is limited (see section 2.2) and as such the radius r is not a fully controllable parameter. Generally, for incorporation within a particular matrix, the available fibres do not have a range of radii to choose from and r is therefore not a true design variable. It is only τ, the interfacial frictional shear stress that can be varied (see Chapter 3).

2.1.2.4 Ultimate tensile strength

The ultimate tensile strength σ_u of a CMC is necessarily dependent on the fibre volume fraction V_f, fibre mean strength S, Weibull distribution of fibre strengths m, fibre radius r and interfacial frictional shear stress τ,

$$\sigma_u = V_f \, S \, f(\tau, r, m) \tag{2.25}$$

where f is a function of τ, r, m. If there were no statistical spread (i.e. $m = \infty$) the ultimate strength would simply be the product of fibre volume fraction and fibre strength, $\sigma_u = V_f S$, from ACK theory (equation 2.20 above). As $m \neq \infty$, typically $m < 5$ [41], then the mechanisms of toughening that come into play after the onset of matrix microcracking combine to produce an ultimate strength. A lower bound on the value of σ_u can be deduced by ignoring any load bearing capability of fractured fibres undergoing pull out [39],

$$\sigma_u = V_f S \exp\left[- \frac{\left[1 - (1-\tau X / rS)^{m+1}\right]}{(m+1)\left[1 - (1-\tau X / rS)^{m}\right]} \right] \qquad (2.26)$$

where X is the matrix microcrack spacing from equation (2.17), and S, in this case, is a fibre bundle strength.

2.1.2.5 Transition to brittle failure

The above expressions describing the behaviour of a fibre reinforced CMC, suggest it is possible to optimise the properties of a composite's constituent materials to achieve maximum mechanical performance.

In particular, the microcracking stress can be increased by increasing τ (equation 2.19). However, overall toughness decreases with increasing τ, from equations (2.21), (2.22) and (2.24), (assuming $m > 2$), as does the ultimate tensile strength (from equation 2.26). For a CMC comprising particular matrix and fibre materials and with a fixed fibre volume fraction, the properties can be tailored by changing the interfacial frictional shear stress τ.

For low τ values, a CMC will have very high toughness but inelastic behaviour over almost all of its load range as the microcracking level will be very low. If τ is increased, the toughness of the material will decrease as will the ultimate tensile strength but elastic behaviour will be introduced as long as the normal operating stresses do not exceed the now increased microcracking stress. The behaviour would be as that in figure 2.2(b). If τ were further increased, contributions to toughening would continue to decrease until the rising microcracking stress equalled the falling ultimate strength. At this point the tough composite would revert to brittle behaviour and suffer catastrophic failure as in figure 2.2(a).

Maximum performance is not achieved by making the value of τ very low.

This would result in inefficient load transferral to the reinforcing fibres in the elastic region of CMC response - producing low ultimate strength, and negligible work done against interfacial friction on fibre pull out - producing low toughness.

2.1.2.6 Residual stresses

In all practical CMCs where the coefficient of thermal expansion α of the matrix (α_m) and fibre (α_f) differ there will be residual stresses present within the composite caused by its cooling down from the high temperatures required for manufacture. These have not been considered as yet, but at room temperature and any operating temperature below that of manufacture, they affect composite properties.

The residual stresses manifest themselves both parallel to and normal to fibre direction. If the matrix contracts more than the fibre on cooling ($\alpha_m > \alpha_f$) then a residual axial compression of fibre is produced (figure 2.9 (a)) and a radial compression (figure 2.10(a)). Conversely, for $\alpha_m < \alpha_f$, the residual state is of axial and radial tension in the fibre (figures 2.9(b) and 2.10(b)). If $\alpha_m >> \alpha_f$, then spontaneous matrix

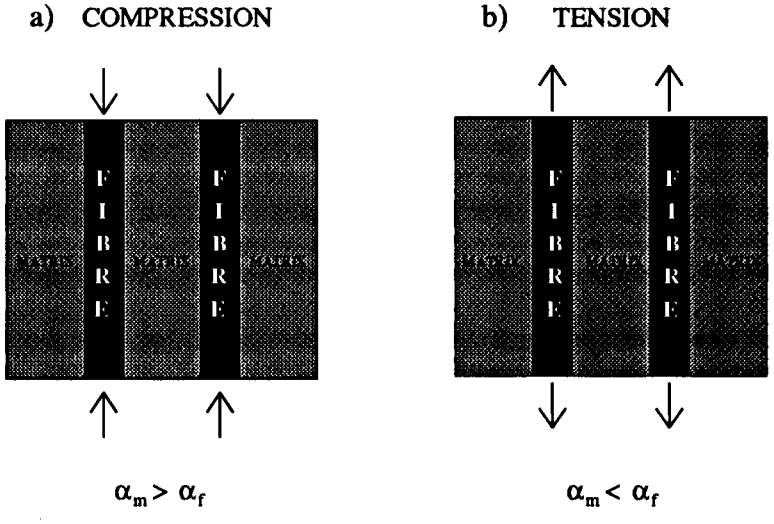

Figure 2.9. The axial residual stresses acting on the fibre due to thermal mismatch of fibre and matrix, a) for $\alpha_m > \alpha_f$ the fibre is compressed and b) for $\alpha_m < \alpha_f$ the fibre is under tension.

cracking will occur on cool down from manufacture and thus impair material performance. For $\alpha_m << \alpha_f$, the matrix may pull away from the fibres, if the fibre-matrix bond is small or non-existent, leaving a gap at the interface (figure 2.10(b)), and negating the influence of the reinforcement. Thus comparable values of α_m and α_f are required for production of a successful CMC.

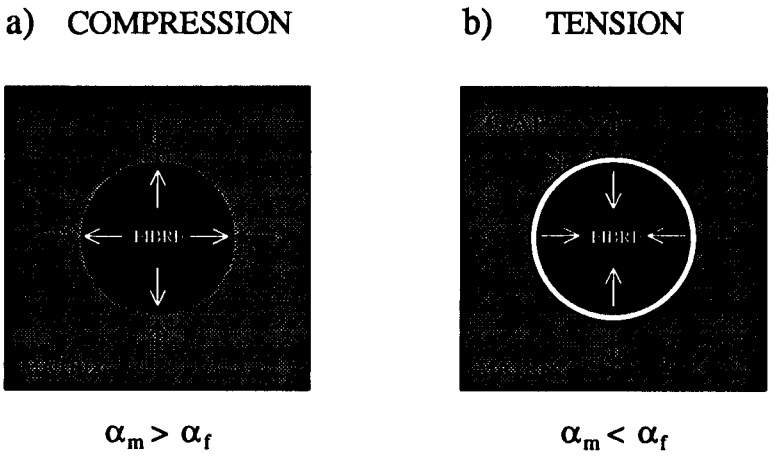

Figure 2.10. The radial residual stresses acting across the interface due to thermal mismatch of fibre and matrix, a) for $\alpha_m > \alpha_f$ the interface is compressed and b) for $\alpha_m < \alpha_f$ the interface is under tension.

The residual stress influences the matrix microcracking stress, the interfacial shear stress and the ultimate strength [39, 42, 43, 44]. A uniaxially reinforced CMC, under tension applied in the direction of the fibre reinforcement, will begin to microcrack at a stress given by equation (2.19) but offset by an axial residual stress term, i.e.

$$\sigma_m^* = \sigma_m - q E_c / E_m \qquad (2.27)$$

where σ_m^* is the matrix cracking stress including residual stress effects, σ_m is the ACK microcracking stress given by equation (2.19) and q is the residual axial stress in the matrix. The value of q is proportional to the thermal mismatch strain ε,

$$\varepsilon = (\alpha_f - \alpha_m) \Delta T \tag{2.28}$$

where ΔT is the difference between ambient and the elevated processing temperatures (and is thus negative). For a matrix under residual tension, q is positive and therefore the matrix microcracking stress is lower than the stress free state. Conversely, a CMC with residually compressed matrix will produce a higher microcracking level (negative q). The residual stress normal to the fibre-matrix interface p, is also proportional to ε. Precise derivations of p and q are illustrated in Budiansky, Hutchinson and Evans [42].

If the interfacial frictional shear stress is assumed to follow a Coulombic friction law, then it can be represented as

$$\tau = \mu p \tag{2.29}$$

where μ is the coefficient of friction [39, 42]. Therefore an increase in compressive residual stress across the interface will increase τ and reduce fibre pull out length at fracture. Toughness of the CMC will be reduced (see above) and ultimate strength affected.

However, if the major contribution to τ is from interface roughness, the assumption of (2.29) is not valid as the asperities on the debonded interface produce a discrete sliding shear stress τ [39, 42].

2.1.2.7 Summary of CMC mechanical behaviour

The fracture mechanics of fibre reinforced ceramic composites have been discussed and the various parameters that describe the mechanical behaviour and the variables that control them illustrated. It is important to realise that apart from the inherent material properties that a matrix or fibre may have e.g. modulus, and the relative volume fractions, there are other variables to be considered when manufacturing a CMC.

Matrix microcracking stress is significantly influenced by the matrix fracture energy G_m (equations (2.19) and (2.27)). Fibre strength within a composite S, and statistical scatter, measured by its Weibull modulus m, plays an important role in determining ultimate strength and toughness (equations 2.20 - 2.26), as does the radius r.

The nature of the fibre-matrix interface is critical to the tensile characteristics of a CMC. Without a sufficiently low interface fracture surface energy G_i , a composite will be brittle (section 2.1.2.1). A suitable frictional shear sliding stress τ, is required for optimum microcracking level, strength or toughness (sections 2.1.2.2 $\rightarrow$ 2.1.2.6). Although the theory on fracture toughness of CMCs is generally accepted, the optimum ranges for G_i and τ have not, to date, been experimentally proven.

The following section describes briefly current fibres, matrices and interfaces used in continuous fibre reinforced ceramic development.

2.2 Ceramic Matrix Composite Materials

Choice of the fibre and matrix used in a CMC is dependent on them being compatible in three respects;

i) They should have similar thermal expansion coefficients to avoid residual stresses causing cracking during processing (see above).

ii) Elastic modulus of the fibre should be larger so that the composite modulus is higher than that of the monolithic matrix (rule of mixtures, equation 2.11).

iii) Fibre and matrix must be chemically compatible. No strength degrading reactions should occur between them at the temperatures and environments present during fabrication and operation.

2.2.1 Ceramic matrices

There are currently 4 types of CMC under development for high temperature, structural applications. Classified in terms of the matrix material used and its temperature capability, they are illustrated in figure 2.11.

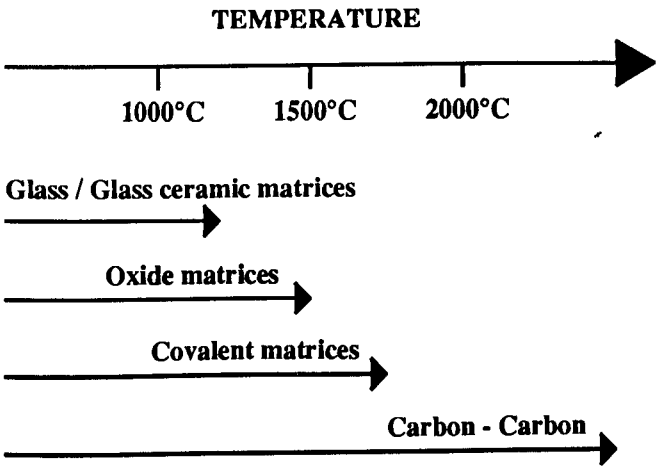

Figure 2.11. Main CMC matrices available today according to their ultimate operating temperatures (taken from [45]).

Glass and glass ceramic matrix composites were the original continuous fibre reinforced CMC to be studied, initially reinforced with carbon fibre [11-16], and are still the most widely investigated class of matrix. They have upper temperature limits in the range of 1000°C - 1200°C and offer particular advantages in that there is a range of possible systems with different mechanical properties to choose from, individual glass ceramic properties can be tailored by altering initial glass composition, and viscous flow of glass near the liquidus temperature aids processing. Section 2.2.5 below describes these CMCs in more detail.

Oxide matrices are only now receiving a great deal of attention. Materials such as alumina and mullite can operate at temperatures up to ~1600°C. Their biggest advantage is that they are inherently oxidation resistant, a pre-requisite for potential gas turbine use. Difficulties of processing have previously inhibited their use.

Si_3N_4 and SiC are covalently bonded matrices, capable of operation at 1700°C. The covalent bonding of these materials results in the oxygen impermeability and oxidation resistance required at high temperatures, as well as high strength and stiffness.

Carbon reinforced carbon has potentially the highest operating temperature capability of 2500°C. Graphitisation of fibre and matrix results in creep resistance superior to that of alternative systems. However, carbon does suffer from oxidation at temperatures as low as 500°C and can only achieve the expected high temperature performance in inert atmospheres.

2.2.2 Fibre reinforcements

CMCs will undergo three dimensional stress patterns in normal operation and so require a three dimensional reinforcing fibre architecture. The fibre has to be capable of being woven into such shapes and for this smaller diameters are preferred as they have a smaller radius of curvature [46]. Fibres should also retain their strength and

resist creep under high loading at high temperatures and in oxidising environments.

Original CMC development utilised carbon fibre as the reinforcement [11-15]. Today, its major use is in the reinforcement of low temperature, polymer matrix composites, as it is unable to withstand oxidising environments at temperatures above 500°C [47,48]. However, it is used to reinforce carbon matrices where under inert conditions, high strength can be retained for short periods of time up to ~2500°C [49,50]. The fibre can be fabricated by several routes that involve drawing a polymer (polyacrylonitrile, pitch or rayon) through a die and then applying a pyrolysing heat treatment to produce carbon. Its properties are typically anisotropic as the hexagonal carbon rings of graphite are highly aligned with fibre direction.

Carbon fibres were the only small diameter fibre capable of withstanding matrix fabrication temperatures until the development of silicon carbide based fibres produced by a polymer pyrolysis route [25]. Nicalon® (Nippon Carbon Co., Japan) has a nanocrystalline, silicon-oxy-carbide microstructure containing SiC, SiO_2 and free carbon [51]. It can retain its strength (~ 2.7 GPa) and modulus (~ 200 GPa) to 1000°C in air or inert environments. Typical diameter of 10-20μm has resulted in it becoming the most successful reinforcement used in CMC development because it is easily woven into 2 & 3 dimensional shapes. Tyranno® (Ube Industries, Japan) is fabricated in a similar way but from a polymer containing a small amount of titanium. It has similar properties to Nicalon.

Monofilaments of Silicon Carbide are available, produced by chemical vapour deposition of a SiC onto a carbon core. Originally produced for metal matrix composite use, Textron SCS-6® (Textron, USA) can hold its strength (3.9 GPa) and modulus (400 GPa) to higher temperatures than Nicalon and Tyranno [52] and can be used to reinforce matrices such as Si_3N_4 that require high fabrication temperatures (typically 1700°C). The large diameter (~150 μm) of the monofilaments does restrict its general use as a reinforcement as it cannot be easily incorporated into a textile structure [46].

Recent developments have produced fibres based on Si-C-N-O, manufactured by pyrolysis of melt spun polymer precursors [51]. They are approximately 15μm in diameter and retain their strength up to 1400°C. Fiberamic® (Rhone Poulenc, France) and HPZ® (Dow Corning/Celanese, USA) have not as yet been extensively studied as CMC reinforcement.

High alumina content, polycrystalline fibres have been available for many years. Although of small diameter (10-20μm), they suffer from grain growth and poor creep resistance at temperatures as low as 850°C [51]. Incorporation within an oxide matrix also requires the prior application of a protective coating to the fibres to prevent reaction and strong bonding [51]. As a result they have not found much use in CMC development, unlike in metal matrix composites where they are used extensively.

Saphikon Al_2O_3® (Saphikon Inc. USA) is an exceptional alumina fibre. It is a single crystal, grown preferentially in the c-axis direction of the hexagonal crystal and as such is creep resistant, strong (2.1 - 3.4 GPa) and stiff (414 GPa) [45]. As it is stoichiometric Al_2O_3, it is inherently oxidation resistant and is capable of operating at 1600°C [45]. Its diameter however is 120μm and so it cannot be easily woven. Reducing the diameter is currently the subject of considerable effort. Experimental batches have been produced with a diameter of ~50μm but these are not yet commercially available [53].

Saphikon has great potential for use in oxide matrix/oxide fibre CMCs. This and other classes of CMC system are described below, together with their fabrication techniques.

2.2.3 CMC systems

Various classes of CMC are under development. The largest is that of glass and glass ceramic matrix composites and these are dealt with in section 2.2.5.

Novel processing techniques are required for CMC matrices as conventional

sintering techniques used for monolithics and particulate reinforced composites are not generally applicable. This is because;

i) the limited thermal stability of the fibres prevent the prolonged holds at high temperatures required for sintering cycles (1500°C - 2100°C),

ii) the constraining of matrix shrinkage due to the presence of the fibres leads to matrix cracking and/or porosity.

CMC fabrication of an actual component involves preparation of a fibre preform and infiltration of it by matrix material, be it via decomposition of a gas phase, pyrolysis of a transformed liquid phase or viscous flow of a glassy phase.

Chemical Vapour Infiltration (CVI) is the most common process used for production of SiC fibre reinforced SiC. SiC fibre structures (typically Nicalon) are supported in a reaction chamber and heated to ~1100°C. Reactant gases are then passed through the chamber, infiltrating the preform, depositing matrix material (SiC) onto the fibres. The process is continued until the pores between fibres close up and prevent further densification. The technique can take weeks to manufacture a single component [54] but a faster "Forced CVI" technique has been developed that increases production times to less than 24 hours by applying a temperature gradient to the component [55]. SiC/SiC composites produced this way are typically brittle if they have not had a fibre coating applied prior to matrix infiltration to prevent bonding between matrix and fibre [54 - 58]. The CMCs are inherently porous (~10% - 20%) and suffer from interface and fibre oxidation at temperatures > 1000°C that reduce performance.

Carbon/carbon CMCs are produced by the infiltration of a fibre preform with a polymeric precursor, followed by pyrolysation to produce the carbon. The process is cycled a number of times to achieve maximum density. For extended use in aggressive environments, various technologies are being employed to apply oxidation resistant coatings to the components [50].

Silicon nitride has the ideal quality for a matrix material in that it is oxidation resistant at high temperature. Developmental work has however, only

produced uniaxially reinforced CMCs as the SiC fibre has to be the large diameter, Textron type mentioned above to withstand the high processing temperatures. CMCs can be processed via reaction bonded Si_3N_4 (RBSN) [59], hot-pressed Si_3N_4 (HPSN) [60], pressureless sintered Si_3N_4 (SSN) and sintered reaction bonded Si_3N_4 (SRBSN) [61]. Matrix shrinkage associated with sintering occurs to varying degrees with each technique.

Oxide matrix / oxide fibre composites are currently the focus of much attention as it is perceived the inherent oxidation resistance of matrix and fibre (oxides are already oxidised) can overcome the problems that SiC/SiC, C/C and glass and glass ceramic matrix (see section 2.2.5) CMCs have in high temperature, oxidising environments. Although fibres with the ideal properties are not as yet available, developments towards matrix consolidation techniques and interface production are progressing. Oxide matrices can be deposited via the sol-gel route that has the advantages of enhanced infiltration, particularly if adapted to pressure forming techniques, and lower processing temperatures (by hundreds of °C) compared to conventional sintering [62]. As mentioned above (section 2.2.2), oxide fibres and matrices bond strongly when processed under high temperatures if there is not a protective coating applied to the fibres beforehand. Pre-synthesis of the fibre-matrix interface is an accepted requirement for many CMCs including SiC/SiC and glass ceramic matrix composites that often, but not always, requires an extra processing step.

2.2.4 Interface pre-synthesis

Interface design involves the pre-synthesis of the fibre-matrix interface by coating the fibres before their incorporation within the matrix. The choice of coating depends on its functional requirement. It may be required to [63],

i) prevent cross diffusion and reaction between fibre and matrix that could reduce fibre strength or cause bonding,

ii) tailor the interfacial shear sliding stress τ and produce high mechanical performance,

iii) both the above.

For a coating to prevent fibre-matrix reactions during processing and operation, it must be stable at the temperatures encountered and be a diffusion barrier to the reactive species. For it to have the ideal properties for good composite mechanical performance, it must not strongly bond the fibre to the matrix, it must have a low fracture surface energy G_i (section 2.1.2.1), and provide a low interfacial frictional shear stress τ (sections 2.1.2.2 - 2.1.2.7).

Van der Waals type structures such as graphitic C and hexagonal BN are ideal for producing the required low τ interfaces and have been shown to increase toughness in SiC/SiC composites when applied to fibres prior to matrix infiltration [57,58]. They do however suffer from poor oxidation resistance and as such are likely to degrade when attacked by oxygen infiltrating from a matrix microcrack. It may be necessary to apply further coatings to protect the low τ interface from degradation [64].

As mentioned previously, oxide/oxide CMCs require a pre-synthesised interface to prevent fibre and matrix bonding during fabrication. One possible candidate is the application of a porous ZrO_2 to the fibre [65,66]. Although it may bond to fibre and matrix, any matrix crack that impinges on it will be deflected by the porosity, along the interface, thus introducing toughness to the material. Other possibilities for oxide/oxide interfaces are fibre coatings of refractory metals [67,68].

There are many coating techniques available for ceramic fibres. They include Chemical Vapour Deposition (CVD), Physical Vapour Deposition (PVD) and sol-gel or polymer precursor "wet" techniques.

CVD is by far the most versatile as many different compounds can be deposited in different morphologies. Fibres are placed in a chamber at high temperature where reactant gases deposit the relevant species on the fibre surface [69,70]. Coating composition and structure is controlled by varying chamber temperature and gas

concentrations. It is the major fibre coating technique not only because of its versatility but also because it is not "line of sight", fibres are simultaneously coated over the whole of their surface.

PVD techniques include sputtering and evaporating of species that are then deposited on target fibres. The major drawback of these techniques is that deposition is directional, the fibres or the material source have to be rotated around the other to achieve a complete surface coating.

Sol-gel organometallic precursor or polymer precursor techniques involve the dipping of fibres into the wet "gel" followed by pyrolysis to form the ceramic coating. C and SiC can be produced from polymer precursors and oxide coatings from organometallic precursors [71].

2.2.5 Glass and glass ceramic matrix composites

The use of glasses and glass ceramics as matrices provides various advantages over other ceramics for CMC production [29,31,72,73],

i) there is a range of different systems that have operating temperatures in excess of 1000°C, enabling different properties such as coefficient of thermal expansion α and elastic modulus to be selected for a particular application by choosing the suitable matrix system (see Table 2.1),

ii) production of a crystalline ceramic from a glass precursor is particularly beneficial as :

a) The process of densification of the matrix can be accomplished by viscous glass flow at temperatures near the liquidus.

b) Initial glass composition can be altered to tailor the final matrix properties. It can be chosen to be away from the stoichiometric position of a phase (i.e. nearer to a eutectic) so that its liquidus is lowered, reducing the required processing temperature. It can be chosen to produce particular concentrations of different phases

and so control α and the amount of residual glass in the final matrix [74]. The presence of residual glass impairs mechanical properties and effects oxygen diffusion rate through the matrix at high temperatures.

MATRIX	Major constituents	Major Phase	Elastic Modulus GPa	α .10^{-6} C^{-1}	Maximum use temp °C
LAS	$Li_2O, Al_2O_3, MgO, SiO_2$	β-Spodumene	88	1.5	1200
MAS	MgO, Al_2O_3, SiO_2	Cordierite	90	5.5	1200
CAS	CaO, Al_2O_3, SiO_2	Anorthite	88	4.5	1200
BMAS	BaO, MgO, Al_2O_3, SiO_2	Barium osumilite	106	2.7	1250
BAS	BaO, Al_2O_3, SiO_2	Celcian	~90	3.0	1500
BAS	BaO, Al_2O_3, SiO_2	Hexacelcian	~90	8.0	1700
Borosilicate Glass	B_2O_3, SiO_2	N/A	68	3.3	600

Table 2.1 Various glass ceramics suitable for matrix materials in CMCs.

The flow characteristics of glass at high temperature make it possible to adapt techniques that are used for resin matrix composite manufacture, such as hot matrix transfer moulding for complex 3D structures, and hot pressing of impregnated tape for uniaxial or cross-ply tiles [29]. Hot pressing is most commonly used for research purposes.

Tiles are fabricated by first passing the fibre (Nicalon or Tyranno) through a low temperature furnace to remove its protective, organic sizing. Impregnation with glass, by passing it through a slurry of organic binder, solvent and glass frit, is then required before it is wound on to a drum, dried and removed as plates of unidirectional fibre in glass frit. These are cut and stacked in a graphite die and hot pressed. To avoid damaging the fibres, the load is applied only after the softening temperature of the glass

is reached. The method was developed by Sambell et al. [13] in the early 70's.

During hot pressing, and as the specimen cools down, partial crystallisation of phases occurs. A further heat treatment to achieve maximum crystallinity is often required but not always necessary. For a monolithic glass ceramic, this heat treatment would be easily determined by considering the growth kinetics of phases involved. However, with siliconoxycarbide fibres such as Nicalon as reinforcement, the fibre-matrix reaction needs to be considered [64,75].

The silicate matrices and non-stoichiometric SiC fibres (Nicalon, Tyranno) react during processing to produce a carbon rich interface of low fracture energy G_i and low frictional shear stress τ which gives the typical mechanical behaviour of a tough composite i.e. matrix microcracking and fibre pull out. The SiC at the fibre surface is oxidised to form carbon [32],

$$SiC_{(s)} + O_{2(g)} \rightarrow SiO_{2\,(s,l)} + C_{\,(s)} \qquad (2.30)$$

Carbon rich interfaces were originally noted in the LAS (Li_2O-Al_2O_3-SiO_2) / Nicalon system [30-32,76] and have since been identified in MAS (MgO-Al_2O_3-SiO_2), CAS (CaO-Al_2O_3-SiO_2), BAS (BaO-Al_2O_3-SiO_2) and borosilicate glass systems reinforced with Tyranno as well as Nicalon [64,75,77,78].

Initially regarded as a major processing advantage due to the high composite performance produced at low temperatures, the in-situ formed carbon rich interfaces are not however stable at high temperatures. Prolonged exposure to air at elevated temperatures causes oxidation of the interface and SiO_2 formation, bonding fibre to matrix and causing brittleness [30,76,79,80].

As they currently stand, these CMCs are not useful in high temperature, oxidative applications. If they are going to be used in actual components, fibre coatings that produce the low cohesive interface will have to be applied first and then protected by another coating that prevents its degradation at high temperatures.

CHAPTER THREE
INTERFACIAL MICROMECHANICS

3.1 Importance of Interfacial Micromechanics

As discussed above, the interfacial micromechanics (mechanical properties of the fibre-matrix interface) are critical to the mechanical properties of the composite.

The essential interface properties required for a tough CMC are;

1) The debond fracture surface energy of the interface G_i has to be considerably lower than the fibre fracture surface energy G_f. This is a necessary condition for a composite to be non-brittle. Theoretically, it is expected that G_i requires to be less than one quarter to one half the value of G_f, depending on the relative fibre and matrix elastic moduli.

2) The interfacial shear sliding stress τ should be optimised. If it is too high, matrix microcracking level approaches ultimate tensile strength, fibre pull out lengths shorten and the CMC becomes brittle. If τ is too low, load transferral from matrix to fibre is low, resulting in a low microcracking stress, low ultimate strength and little work being required on fibre pull out.

Different CMC components will have different design criteria. Many applications will require a high work of fracture to prevent brittle failure and therefore require a low τ. This will give a low matrix microcracking stress σ_m. However, most components will require the design limit to be σ_m so that under normal loading conditions the material response is elastic but in the event of an abnormally high load being applied, catastrophic failure is avoided due to the toughening from microcracking and pull out. This analogous behaviour to a metal passing its yield point i.e. non-catastrophic failure through inelastic response, requires a higher interfacial τ.

Also, if normal operational stresses were above σ_m, matrix cracks would be

present throughout the component's lifetime. These would allow ingress of any aggressive environment to the fibres and interfaces, possibly reacting with them and causing strength degradation and embrittlement - obviously not acceptable.

Therefore in any CMC component the optimum interface for its application should be present. The absolute values required for σ_m and σ_u and their ratio σ_m / σ_u will be different for particular applications. Within a system (specific fibre and matrix) they can only be realistically changed by tailoring the micromechanics of the interface. Practically this can be done in two ways ;

i) The development of interfaces from matrix-fibre reaction during fabrication.

ii) The coating of fibres before they are incorporated into the matrix.

Method i) can only be used in such systems where reaction forms a favourable interface structure e.g. carbon in the glass ceramic / Nicalon-SiC fibre CMCs. In cases where favourable interface structures are not formed during fabrication, e.g. oxide matrices and oxide fibres, the only way to stop such reactions and introduce favourable properties is by fibre coating, method ii), i.e. interface pre-synthesis, see section 2.2.4.

Fibre coating can, in principal, be applied to any CMC system. The different coating techniques available mean a large number of compounds can be deposited to obtain the required micromechanical response (section 2.2.4).

The required micromechanical response is not however known to absolute values. Numerical limits have been given for τ of 2 MPa $< \tau <$ 40 MPa [81], but they are not appropriate as the optimum value will vary from system to system and the upper limit for tough behaviour, where microcracking stress equals ultimate strength, depends on τ / r and m, not solely on τ [39]. Optimum values for G_i and τ have not yet been experimentally determined.

With CMC research and development focussing on the tailoring of interfaces by fibre coating when the requirements are only qualitatively known, a technique for measuring interface micromechanical properties is required to quantitatively correlate different interface structures and behaviour to macromechanical

CMC performance and help empirically formulate the required interface behaviour for specific fibre and matrix types.

3.2 Techniques for Measurement of Interfacial Micromechanical Properties

For an interfacial micromechanical measurement technique to be successful in composite development it must :

i) measure interfacial frictional shear sliding stress τ ,

ii) measure fibre-matrix interface fracture surface energy G_i ,

iii) be applicable to a large range of fibre and matrix types,

iv) have minimal, non-specialised, specimen preparation,

v) have potential to work at high temperature.

Many techniques are currently available but they all have inherent disadvantages and none of them satisfy all the above requirements.

A number of methods rely on the tensile loading of a bar and measuring various parameters. They are not ideal as specially shaped test pieces have to be used, meaning parts of real CMC components cannot be easily tested. Other techniques can use small samples that could possibly be cut from actual components but do not measure all the required parameters. A final group of tests involve the pushing or pulling of individual fibres within the matrix, measuring the applied load and fibre displacement.

3.2.1 Summary of tests

The original technique of interfacial shear stress measurement comes directly from the ACK model [17] where a test bar is loaded past the microcracking stress, microcrack spacing is measured and equations (2.17) and (2.27) used to determine τ. It has been widely used but it is not possible to measure G_i with this

method.

Microcrack opening hysteresis [82,39] gives information on τ and residual stress across the interface but relates to crack opening displacements beyond those that dictate formation of microcracks. The crack opening displacements are measured as a function of the load applied to a tensile specimen. Again, a special test bar geometry is required for tensile testing and the technique cannot measure G_i.

There is a recently developed technique that can measure both τ and G_i from tensile testing. If a test piece is taken above the tensile microcracking stress and the applied load cycled up and down, the width at half height and permanent strain at zero load of the stress/strain hysteresis loop can give τ and G_i respectively [83,66]. Special test bar manufacture is however required and large errors are encountered as hysteresis loops are often small.

The Slice Compression Test [84-86], is a novel technique which involves compressing a specimen of unidirectional fibre composite, parallel to the fibre direction, between a hard Si_3N_4 base plate and soft Aluminium top plate. At the base, fibre and matrix strain are equal while at the top their stresses are the same. The elastic mismatch is relieved by debonding from the top surface downwards. The fibres protrude into the Aluminium leaving impressions. When their depth is measured, shear stress τ can be determined. The test is simple to perform, independent of fibre dimensions and can be used at elevated temperatures. However, it cannot determine G_i and there are shortcomings in modelling the mechanics of the test as its results for τ are orders of magnitude different to other tests.

3.2.2 Individual fibre push or pull tests

All the above tests are "macro-tests" in that the measured parameters are influenced by many reinforcing fibres. The group of interfacial tests that use fibre pushing or pulling is different in that individual fibres and therefore individual interfaces are tested. By measuring the load required to displace a fibre relative to the

matrix, whether by pulling or pushing, it is, in principle, possible to determine interfacial fracture surface energy G_i and frictional shear stress τ.

Single fibre pull out testing requires specialised specimen fabrication to mount a fibre in a block of matrix material with one end protruding. It is then mechanically pulled out with load and displacement continuously recorded. It has been used successfully for monofilament reinforcements (diameter 140μm) [87] but for smaller diameters of ~15μm it is difficult to mount and pull the fibres. Also, as test specimen fabrication is necessarily different to that of the composite, results cannot be confidently applied to the bulk material - an important consideration when in-situ interfaces are formed as with the glass ceramic matrix systems.

The difficulty in pulling small fibres such as Nicalon in glass ceramic matrices, has lead to fibre pushing becoming a more popular and successful technique. The original application of a microhardness tester to pushing on fibres within a CMC was made by Marshall [88]. Using a Vickers diamond to push on the individual fibres, frictional shear stress τ is calculated by measuring the force applied to the fibre and the total amount of slip between fibre and matrix. Force is determined by knowing the fibre hardness and measuring fibre indent size, and total slip by the difference in matrix and fibre indent size. However, the technique does not account for any fibre-matrix bonding, it can only be accurately applied to CMCs with $G_i = 0$. For information to be gained on G_i , dynamic recording of load and fibre displacement is required during the pushing process.

There are two techniques used to determine both interfacial parameters from fibre pushing, called "push-down" [89] and "push-through"[90]. They rely on indenting a fibre, pushing it down into the bulk or through a thin slice of matrix. Figure 3.1 shows, schematically, the geometry of the tests. Essentially, load is applied to the fibre end until it debonds at the top surface. The crack then propagates down the interface as load is increased and the fibre slips relative to the matrix behind this crack front, see figure 3.2. Continuously measuring fibre displacement and applied load enables G_i and τ to be determined. In fibre push-down the interface crack propagates

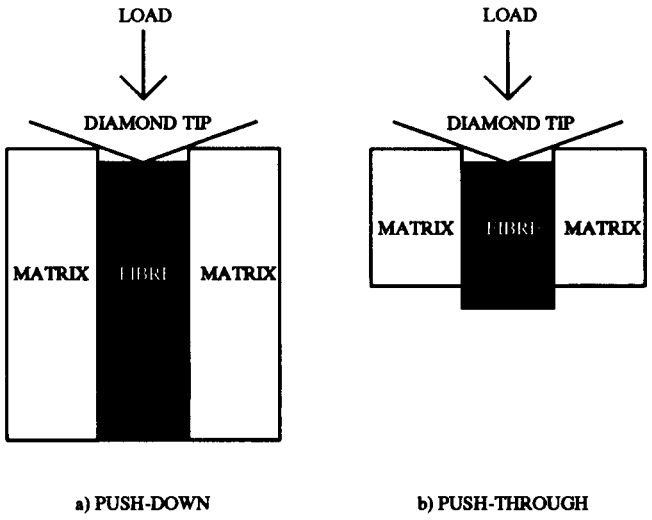

Figure 3.1 Schematic illustration of a) fibre push-down test and b) push-through test.

further into the bulk material with increased load but with push-through, the crack can only propagate to the underside of the composite slice after which the whole fibre moves, resisted only by the interfacial shear stress τ. Details of data interpretation are discussed in Chapter 4.

Sample preparation is simple. A slice of composite of the order 0.2 mm or 5mm thick, containing aligned, unidirectional fibres, is required for push-through testing of 15μm or 150μm diameter fibres respectively. Push-down tests of 15μm diameter fibres need typically 5 mm deep samples to make sure the interface crack does not propagate to the underside. Both these types of specimen can, if needed, be cut from actual components, making the tests useful for component lifetime studies.

Apparatus based on universal testing machines has been used to investigate large diameter (~150μm, such as Textron SCS-6) reinforcements using the push-through test [91-93]. Large loads (~10N) are required to push monofilaments because of the high interface surface area per fibre.

For fibre diameters ≤ 20 μm such as Nicalon, nanoindentation systems have

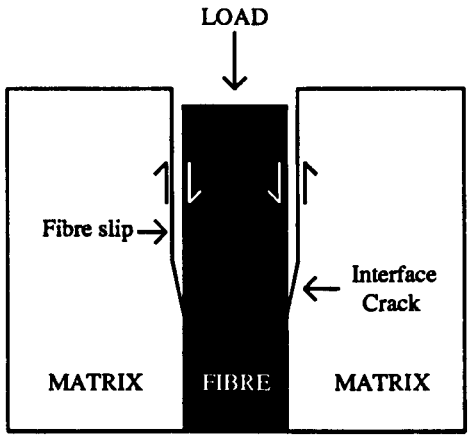

Figure 3.2 Interface crack progression and subsequent fibre slip in fibre pushing tests.

been used to develop the techniques [89,90]. With a load resolution of 0.3μN and displacement resolution of 0.16nm [94], the instruments are capable of precisely measuring the variables required. However, they have until recently had a maximum load capability of only 0.12N that has greatly restricted the number of composite systems that can be studied. In the area of SiC fibre reinforced glass ceramics, the only consistent results obtained have been with the Nicalon / LAS system where both G_i and τ are very small [89,90]. Using a microhardness tester, work performed by the author on other Nicalon / glass ceramic systems, has shown that loads of up to 1N are often required to push the fibres of a tough composite [95].

Nanoindentors have other major disadvantages that limit the amount of information they can deliver in fibre pushing tests.

The obtuse Berkovich or Vickers diamond geometries that are typically used to indent specimens, result in minimal fibre displacements beneath the surface before the diamond touches the matrix. This results in a small interface crack and little fibre slip and therefore a minimal area of interface that has been tested. The larger the sampled area of interface, the more relevant are the results to the real CMC.

Alignment of the fibres to be pushed is made by centering them with the cross-hairs of an optical microscope and then specimen stage translation to beneath the indenting diamond tip. The limited magnification of an optical microscope and stage resolution of ~1μm means the centre of a 10μm fibre is not always hit, making the process more labour intensive. The actual process of fibre pushing is not observed when, for multi-coated fibres, it would be invaluable to see at which interface debonding and slip occurs, as it happens.

Nanoindentors were originally designed for ultra-low load hardness measurement where a known indentation load is applied to a specimen surface i.e. the indentation cycle is load controlled with tip displacement measured as a function of load. This is a disadvantage for fibre pushing as at events where a load drop would normally occur, such as when the interface crack reaches the underside of the specimen in a push-through test [90], unstable, rapid fibre movement occurs as the applied load is greater than that required to push the fibre steadily. In the push-through test this means that only an upper bound for interfacial shear stress τ can be given, it cannot be accurately determined. If indentation were displacement controlled then fibre slip would be controlled, interface crack growth would be stable and the load required for each process would be measured.

Of all the available interfacial tests, fibre pushing satisfies more of the required parameters than the rest. It can measure both G_i and τ, with specimens easily prepared from real components. It can be applied to large and small diameter reinforcements although for small fibres, current instrumentation limits the possible range of CMCs that can be studied. Adaptation of equipment by incorporating hot stages, as has been done with microhardness testers [96], should allow high temperature measurements to be possible.

3.3 Programme Objectives

The objectives of the research programme were to study the interfacial properties of ceramic matrix composites by designing, building and implementing instrumentation to measure interfacial micromechanics and to correlate results to interface structure and, via the models of failure outlined in Chapter 2, to the mechanical properties of CMCs.

3.3.1 Development of micromechanical measurement instrumentation

As outlined above, the techniques of fibre pushing are potentially the best for measurement of interfacial micromechanics. An objective of this work was to manufacture a single instrument to overcome the disadvantages of current nanoindentors and universal testing machines, by its ability to test all types of fibre reinforcement and matrix composites.

From Marshall & Oliver [89] it was seen that such an instrument would need to have load and displacement resolutions of at least 0.01N and 0.05μm respectively to determine the parameters for small fibres such as Nicalon, but would also, from [91-93], need to apply loads in excess of 10N to be able to push 150μm diameter fibres.

To overcome the other disadvantages that nanoindentation systems have for fibre pushing, discussed in section 3.2, the system was to ;

i) be housed within a Scanning Electron Microscope (SEM), to allow dynamic, high magnification imaging of a fibre as it is pushed and reduce the need for specimen stage translation between indentor-fibre alignment and actual indenting,

ii) have a displacement controlled indentation cycle to enable controlled, stable interface crack growth,

iii) use novel indenting tips that were not restricted to Vickers and Berkovich geometries.

It was realised that such an instrument would have other applications in surface engineering and materials science as it would bridge a "resolution gap" between current nano- and micro-indentation systems. Some of these other applications were to be investigated.

3.3.2 Fibre-matrix interface characterisation

Interfacial characterisation across a range of CMCs was to be carried out. Micromechanical measurements were to be correlated to structural investigations of the interfaces made primarily by transmission and scanning electron microscopies.

Concentrating on glass and glass ceramic matrix composites, processing, environmental and fatigue effects were to be studied. The influence of interface pre-synthesis on structure and micromechanical response was to be investigated and compared to the in-situ formed interfaces.

Investigation of large diameter reinforced systems, such as Textron SCS-6, was an objective.

3.3.3 Correlation of micromechanical and macromechanical behaviour.

The values of τ and G_i measured for the composites studied, together with interface structure information, would be correlated to the CMC mechanical behaviour via the fracture theory outlined in Chapter 2.

Values for G_i would be compared to the fibre fracture energies, to try and validate the requirement of $G_i / G_f < 1/4 \rightarrow 1/2$ (equation 2.16). Ranges of τ that produce tough behaviour would be classified. Across the range of CMCs and within particular systems, changes in τ would be compared to changes in matrix microcracking stresses and ultimate strengths.

In general, a tool was to be developed to measure the critical interfacial mechanical properties and experimentally investigate CMC fracture theory.

CHAPTER FOUR

THE SCANNING ELECTRON MICROSCOPE BASED MICROINDENTATION SYSTEM

Indentation testing at the micrometre scale using a diamond probe has been performed for many years, a comprehensive survey being presented in 1956 by Mott [97]. Instrumentation developed for this purpose almost invariably required the operator to examine with an optical microscope the resultant indentation of a known applied load. However, as the probe load is reduced the conventional optical microscope becomes inadequate for the assessment of indentation area. This limitation was obviated by the arrival and subsequent development of the electron microscope and in 1970 Gane presented results of indentation hardness tests with sub-micrometre indentation depths [98,99]. However, relying solely on imaging of an indent only gives information on the material's plastic deformation. Modern indentation systems are being used to simultaneously and continuously measure applied load and indentor displacement, thus obtaining the full elastic - plastic behaviour of the indentation [100]. Today there are three basic types of instrument available for performing tests. For application of loads up to ~ 0.1N nanoindentors are used [101,102], loads between 0.1N and ~10N are applied by microindentors (that generally measure load only) and loads in excess of 10N are generally applied by adapted universal testing machines. Nano- and micro- indentors operate using load controlled testing cycles.

A Scanning Electron Microscope (SEM) based microindentor has been developed to continuously measure indentor displacement and applied load over the respective ranges required for CMC fibre pushing tests. The microscope enables dynamic, high magnification imaging of the indentor-specimen contact zone and applied load is measured continuously as a function of indentor tip displacement. It has

a maximum load capability of 20N measured to a resolution of ±2mN and indentor displacement is measured over a range of 100 μm to a possible 10 nm resolution.

4.1 Overview

A schematic diagram of the system positioned within the SEM is shown in figure 4.1. A piezoelectric motor is used to drive the indentor. It is sufficiently compact to fit in the chamber and as it is not a mechanical lead-screw type of system, there is no need for mechanical vacuum feed-throughs. The indentor tip is connected to the end of the stainless steel shaft. The motor is mounted perpendicularly to the sample stage and both motor and stage tilted 45° to the incident electron beam. Specimens are mounted on the SEM's *x-y* stage at a critical height so that the tip, specimen surface and incident electron beam intersect to within ~30 μm of the point that enables high magnification imaging of the indentor-specimen contact zone. For fibre pushing, a novel, conical diamond tip of apex angle ~75° and tip radius ~5 μm, is used.

Load measurement is via a piezoelectric load cell positioned on the shaft, immediately behind the tip mounting. A capacitance displacement gauge is also positioned on the shaft to measure tip displacement with reference to the specimen surface (not shown in figure 4.1).

The system is interfaced to a personal computer. Software has been developed to fully control motor speed and direction during indentation and automatically record load and displacement data. Processing of the data is performed on the same computer with another, specifically developed software package.

4.2 System development

4.2.1 Initial development

The major obstacle to overcome in placing an indentation device inside the

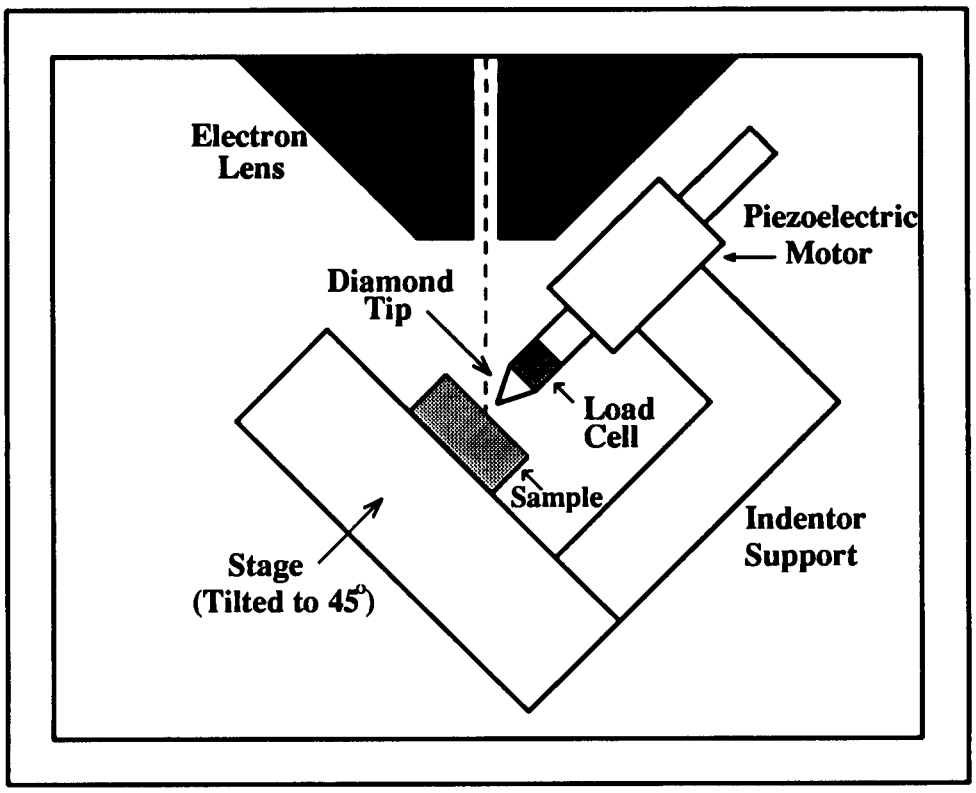

Figure 4.1 Schematic diagram of microindentation system within the SEM vacuum chamber (displacement gauge not shown).

restricted space of an SEM chamber was to find or develop a load applicator compact enough to fit. Designs that required mechanical feed-throughs were avoided as they would be too bulky and intricate to build into the JEOL-6100 SEM chamber that already had a Secondary Electron Detector, a Back Scattered Electron Detector and an X-Ray Energy Dispersive Spectrometer fitted. Alternatives such as piezoelectric motors were investigated. Most, although having the required load capability and mechanical resolution (specified as better than 0.1μm) e.g. Queensgate piezo drives [103], have a limited maximum translation and body dimensions that are too large for the chamber. The exception is the "Inchworm motor" from Burleigh Instruments, UK [104]. It is compact, vacuum compatible, has a mechanical resolution of 4nm [104], a total traverse length of 25 mm with linear motion, maximum load capability of 15N, and is controlled by simple electric cable connection to an interface control module.

Its principal of operation is different to that of motors that have piezoelectric slices stacked on top of each other that expand or contract when a voltage is applied across each of them simultaneously. Instead, it consists of a stainless steel shaft that is translated by three piezoelectric ceramics housed in a barrel around it. Two annular shaped ceramics clamp on and off the shaft when activated and a third expands and contracts between them, in the direction of shaft travel. With the expansion, clamping, contraction and clamping sequenced correctly, the shaft can be moved in either direction, at speeds up to 2 mms^{-1} or as low as 4 nms^{-1}. The nature of this motion is not however "truly linear" as the manufacturer's specification suggests. There is a slight discontinuity every 2-3 μm of travel caused by the change from contraction to expansion, and vice versa, of the central piezoelectric ceramic - this is discussed later in section 4.4.2.

An aluminium model of the motor was made, with slightly larger dimensions than those of the real motor. It was used to verify that the motor could fit in the SEM and that a high magnification, secondary electron image could be obtained even though the main body of the device would partly shadow the secondary electron detector. An Inchworm motor was then purchased with the proviso that it would operate under the conditions that were required of it. To confirm its operation within the SEM, a temporary stand was made for it that bolted on to the *x-y* stage of the SEM. It was planned throughout to incorporate the *x-y* specimen holder of the SEM in the system design as it was rated as having a load capability of 2 kg, acceptable for the indent loads that would be applied. The stand was therefore fitted onto the rear of the "tray" that the specimen stage traversed, see figure 4.2. Its dimensions were measured to within 0.5 mm in *x* and *y* directions (see figure 4.2) of that required for the centre of the motor shaft to intersect with the electron beam and specimen surface. The *x* dimension was not critical, and the *y* dimension could be precisely altered at a later stage by brass shim being place between stand and tray at the fixing point. The stage was tilted to precisely 47° for the whole arrangement to slide in to position, without knocking any pre-fixed instrumentation inside the chamber, as the door was closed.

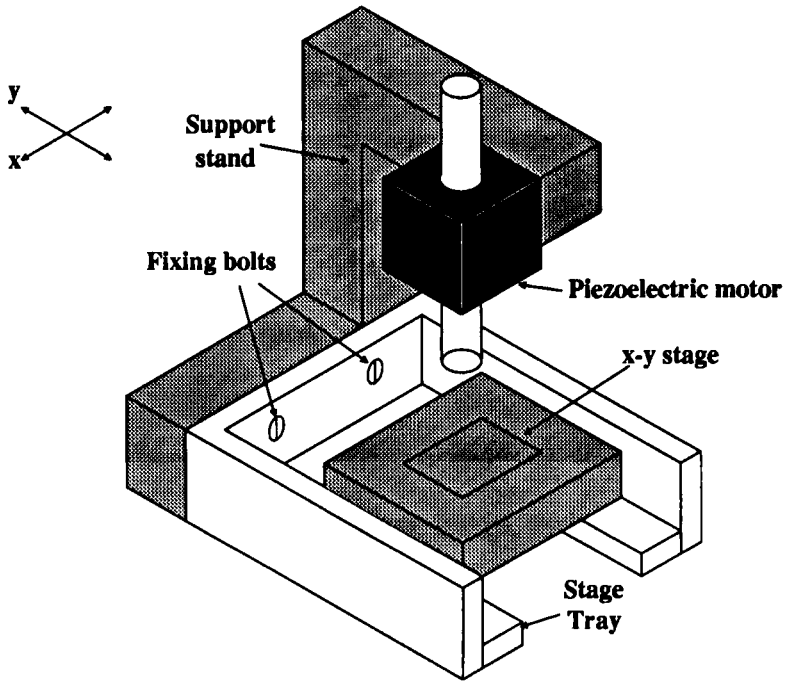

Figure 4.2 Schematic showing geometry of support stand for Inchworm motor and how it is fixed to the SEM x-y stage. (The tray is not tilted to 45°, and the chamber door is not shown.)

A 9-pin D type plug and socket vacuum feed through was machined into a side panel blanking plate for the motor's control cable (see figure 4.19). With an analogue controller on loan from Burleigh Instruments, the Inchworm was operated in the vacuum environment and an image obtained without difficulty. It must be noted that the piezoelectric motor, although it can operate at atmospheric pressure and vacuum, has to be switched off during pump down of the vacuum or venting as the high voltages that would otherwise be present cause arc discharging as the air pressure passes through the corona region (0.001 to 100 Torr).

At high magnifications (~ x5000), the secondary electron image was shifted dramatically as the voltages on the piezoelectric ceramics were ramped up and down. This was expected as the highest voltage applied is 600V and the motor sits close to the electron lens (less than 5mm away, as illustrated in figure 4.1). Total image shift was of

the order ±40μm with an electron beam accelerating potential of 5kV, that reduced to ±10μm as the accelerating voltage was increased to 20kV. The reduction in the image shift as the electron energy was increased proved that the electric fields produced by the voltages of the motor were deflecting the electron beam and that it was not due to some other electronic interference from the motor such as an earth loop. A Faraday shield made of a μ-metal casing connected to earth was placed around the motor and the image shift was dramatically reduced to much less than 1μm with a 10kV electron beam acceleration.

Although the electron beam shift was reduced, there was a slight contrast change still observable in the secondary electron image, that varied with applied motor voltage. This was not noticeable in Back Scattered Electron (BSE) image mode which suggested the close proximity of the motor to the secondary electron detector was attracting and repelling the secondary electrons to and from the detector. The attracting voltage on the front of a secondary electron detector is 1kV, which compares to 600V maximum on the motor. It was deduced that the motor was not shielded enough to prevent the changing applied voltages causing the contrast change.

4.2.2 Load Measurement

The applied load is continuously measured by a piezoelectric load cell positioned directly behind, and co-linear with, the indentor tip and Inchworm shaft. It was chosen because it has a high stiffness of 10^9 Nm^{-1}. A typical strain gauge based load cell has a stiffness of ~250.10^3 Nm^{-1} (i.e. it compresses 1μm under 0.25N load) and is far too compliant for microindentation applications where this may be double the measured tip displacement with reference to the specimen surface. The piezoelectric load cell is a factor of 4000 times stiffer and thus will have a negligible effect on displacement measurements if they are taken with reference to the indentor fixture.

Specimen surface height is critical as its intersection with indentor tip and incident electron beam has to be within a ~30 μm tolerance for the image shift on the

SEM to be used to direct the electron beam to within the 1μm tolerance required for high magnification imaging. Having the load cell behind the indentor tip rather than beneath the specimen enables quick and easy exchange of samples that are not restricted in size (sample mounting is discussed in sections 4.2.3 and 4.3.4). The piezoelectric load cell, Kistler Load Washer 9001 [105], has the same diameter as that of the Inchworm motor shaft, 10mm, and a depth of only 6.5mm, causing no space restriction problems.

The disadvantage in using a piezo-load cell is that under normal circumstances charge leakage from leads connecting it to a charge amplifier, and within the amplifier itself, causes drift in the output signal. Hence it is not normally suitable for load measurement over long periods of time. Indeed, the amplifier supplied by the manufacturer for use with the particular load cell had such a high level of drift that the signal from a fibre push experiment was barely measurable. For a measurement time of 1 minute, the signal could drift the equivalent of 0.5 N. This is not acceptable for the required application.

A charge amplifier was specifically built to minimise the drift caused by charge leakage and so increase the time span over which measurements could be made. It has an extremely high input impedance and is mounted directly on to the exterior wall of the SEM vacuum chamber, reducing to a minimum the length of cable connecting it to the load cell. The circuit diagram is illustrated in figure 4.3.

Principal of operation relies on the load cell output being fed directly to the gate of a low leakage JFET device. The amplifier circuit has an extremely high (almost infinite) impedance and as the load cell is a capacitive device that has no internal resistance, the circuit will not drain the charge developed across the load cell when the load is changed. This means that an applied load on the cell will produce a rise in the output that will remain constant until the load changes again; thus the output of the amplifier is proportional to the load placed upon the cell. As the device is a low leakage JFET, there is very little signal drift. Over typical indentation time scales it is negligible, at worst linear, and is easily compensated for with subsequent data

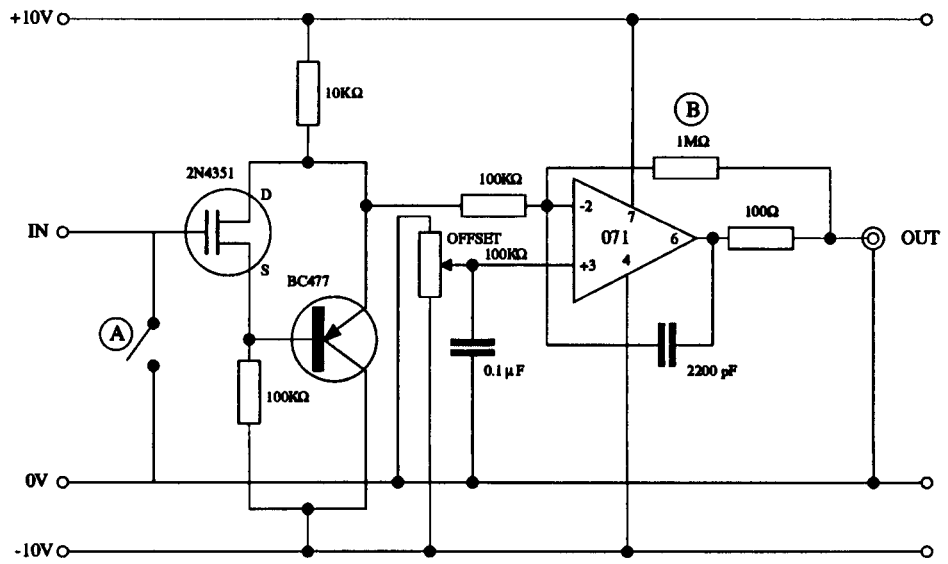

Figure 4.3 Circuit diagram of specifically developed, high input impedance, load cell charge amplifier.

processing (see section 4.4). Drift over extended periods of time between indents may occur to an extent where the signal rises to the supply rail level. To reset the level to the zero applied load level, a short circuit is required (switch "A" in figure 4.3) between the zero voltage line and input from the load cell. It is also necessary to keep switch "A" closed when the amplifier is disconnected from the load cell, to prevent any static charges damaging the JFET device during apparatus assembly and storage. The offset potentiometer is present to adjust the zero load voltage to an acceptable level for the Analogue to Digital Converter (ADC) of the personal computer interface board to read.

The amplifier is connected directly to the SEM wall, with a standard TNC connector to TNC vacuum feed through that connects to the shielded wire from the load cell. Figure 4.4 shows the amplifier connected to the chamber wall, on the blanking plate positioned below the Back Scattered Detector fixture (see section 4.2.5 for a picture of the blanking plate). The figure shows the output line to ADC, potentiometer offset and short circuit switch.

Calibration of the load cell was necessarily performed at atmospheric

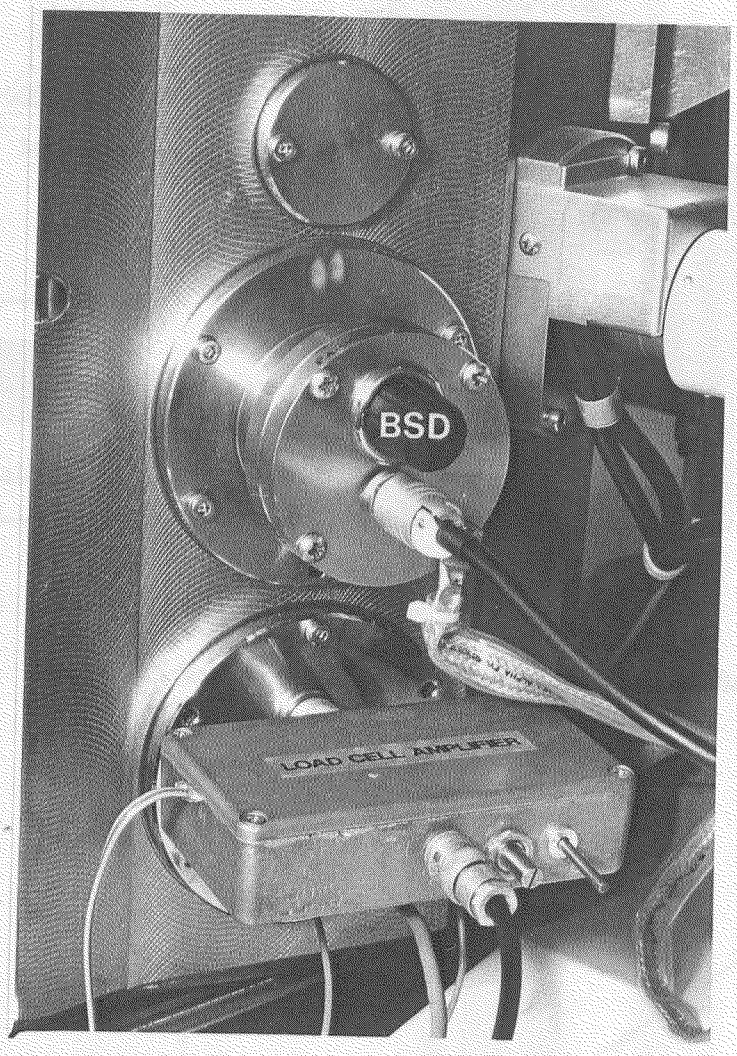

Figure 4.4 Load cell amplifier attached to SEM chamber wall.

pressure in a temperature controlled laboratory (20 ± 1°C). A calibration jig was fabricated onto which the Inchworm motor was attached. With diamond tip removed from the brass mounting that sandwiches the load cell to the motor shaft, the motor shaft was driven down onto the cantilever load beam of a standard "Sartorius" laboratory balance, range 0-100N, that had been partly disassembled (see figure 4.5). As the motor shaft depressed the beam down, the output voltage of the load cell was calibrated against the reading of the balance. Typical calibration data is shown in figure

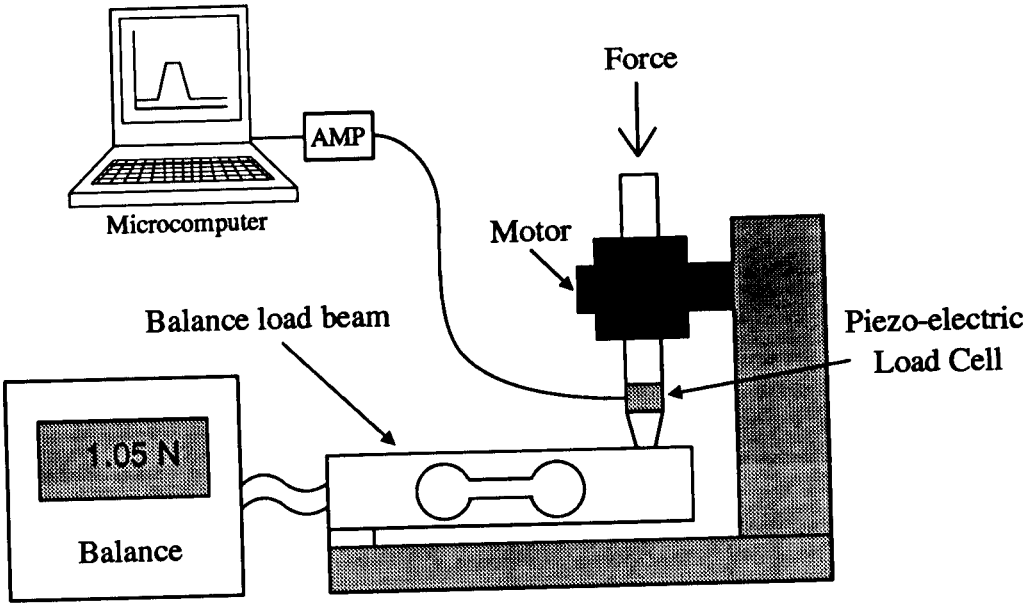

Figure 4.5 Schematic of load cell calibration apparatus.

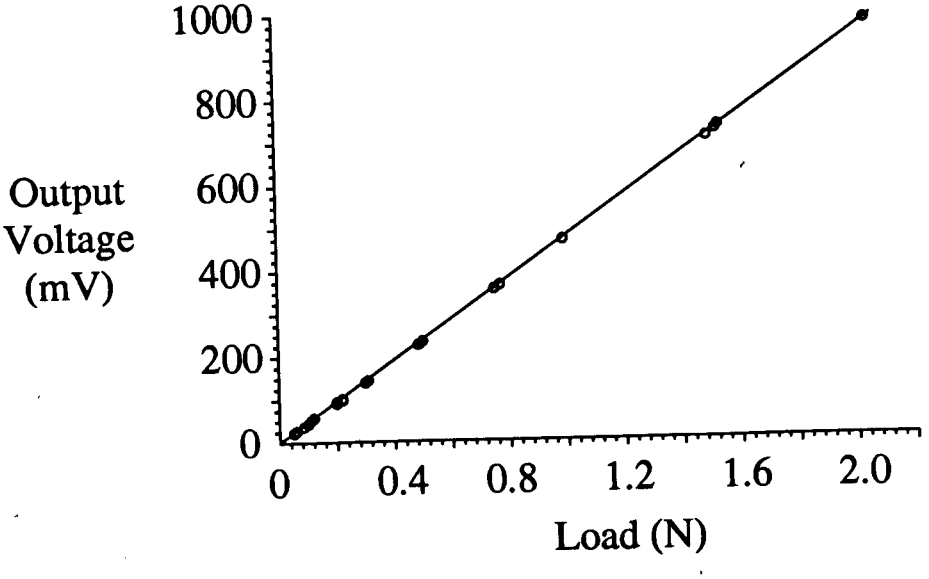

Figure 4.6 Typical calibration data for load cell.

4.6 and is linear. No change in the calibration of the load cell could be detected over the 18 months that it was in use.

Special software was written to control the motor and measure load cell amplifier readings through the ADC. A linear curve ($y = m\,x + c$) was fitted to the data and the numerical values for m and c recorded for use in data logging and processing software (see section 4.2.6 and 4.2.7). In figure 4.6, the load calibration goes up to approximately 2 N which is ample load for pushing small fibres like Nicalon. For the larger diameter fibres (150 μm) that require higher loads, the load cell was recalibrated with the amplifier gain reduced from 9 to 1 by replacing the 1MΩ resistor at position "B" in the amplifier circuit (figure 4.3) with a 100kΩ resistor. This was necessary to prevent the output voltage rising above the 1.8V maximum that the ADC could read (see 4.2.6).

The resolution in load measurement was measured as ±2mN, by recording signal noise with a constant load applied.

4.2.3 Indentor tip development and alignment

For the pushing of a fibre as small as 7 μm diameter to be observed at high magnification, the indentor tip needs to have a particular geometry and its point of contact with the specimen surface has to be aligned to within approximately 30 μm of the point where the electron beam impinges upon the specimen.

The ideal geometry for the diamond indentor would be a cone with total apex angle of approximately 75° (it must be less than 90°) but with its tip "cut off" to leave a flat surface of radius 5 μm. This would enable the electron beam to impinge upon the specimen and tip at the contact point at a stage angle of 47°, and also permit many microns of fibre displacement beneath the specimen surface. The flat end is to reduce the stresses produced in the fibre surface that could cause fracture at low loads.

Initially, this specification was given to a specialist indentor tip manufacturing company to fabricate a diamond tip. Using purely polishing and lapping

techniques they could not produce the required shape. The best attempt they made is shown in figure 4.7(a). The conical shape has become faceted and the flat end is chipped and irregularly shaped with dimensions of 10μm width and 20μm length. This is too large to be able to push down a 15μm fibre without indenting the matrix at the same time.

Ion beam machining can be used to mill diamond tips to specific shapes [106]. An attempt was made to shape the tip of figure 4.7(a) to a more suitable geometry by placing it in an "Ion Tech" ion beam miller used for the preparation of Transmission Electron Microscope (TEM) specimens. With the ion beam aligned so that it was incident "head on" to the diamond tip, an accelerating potential of 4kV and beam current of 4 mA, the tip shape was modified after only 2 hours. Further milling for 6 and 9 hours duration, produced a sharp faceted point to the diamond, see figure 4.7(b,c,d).

However, this was not the geometry required. A further unsuccessful attempt to mill this tip to the correct shape was made using an ion beam milling facility purpose built for fine tip and probe fabrication, belonging to the Nanotechnology and Microengineering Centre, University of Warwick. Discussions with Dr. S.T. Davies of the centre led to the generous donation of a selection of conical diamond tips, a number of which proved acceptable for use. They were not of the exact geometry specified above but did have apex angles of ~ 75° and a blunted end with tip radius of ~ 5μm. Figure 4.8 is an SEM image of the tip used for the fibre pushing experiments reported in Chapter 5.

The tips were set in threaded mounts and for easy installation, a brass mounting was fabricated that sandwiched the load cell to the Inchworm shaft on a semi-permanent basis but enabled the diamond tips to be screwed on and off when required. The brass mounting was again conical in shape to allow imaging of the indentation point, see figure 4.9.

Reproducible alignment of the indentor with specimen surface and electron beam is critical to consistently obtaining a high magnification image. It was achieved

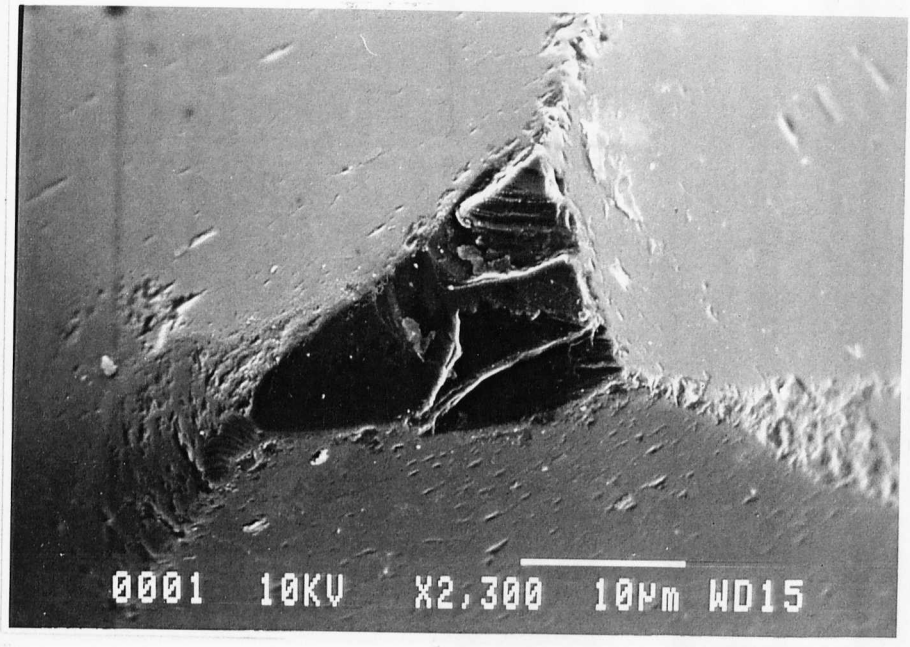

(a) as received,

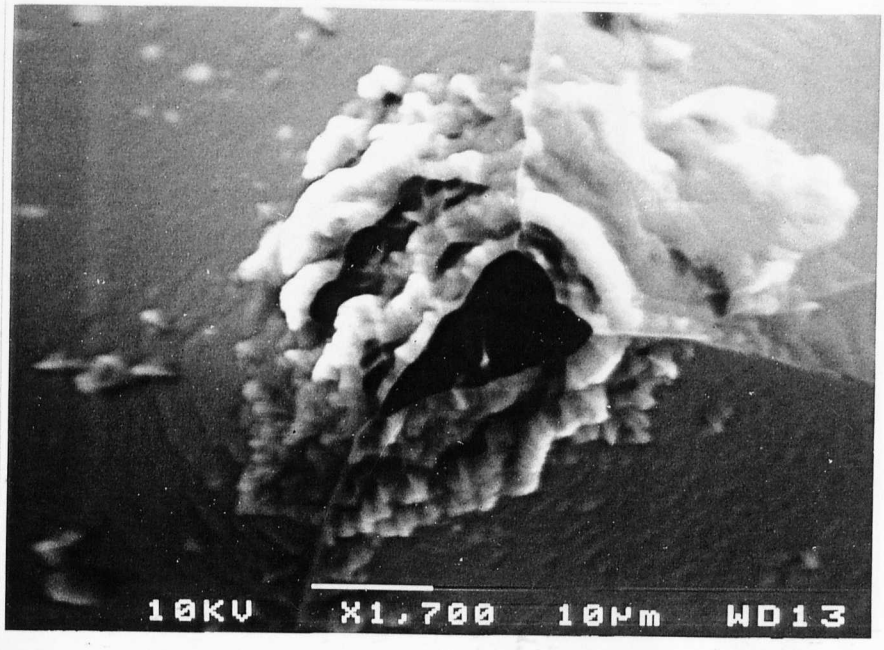

(b) after 2 hours ion milling,

Figure 4.7 SEM images of diamond tip supplied by manufacturer.

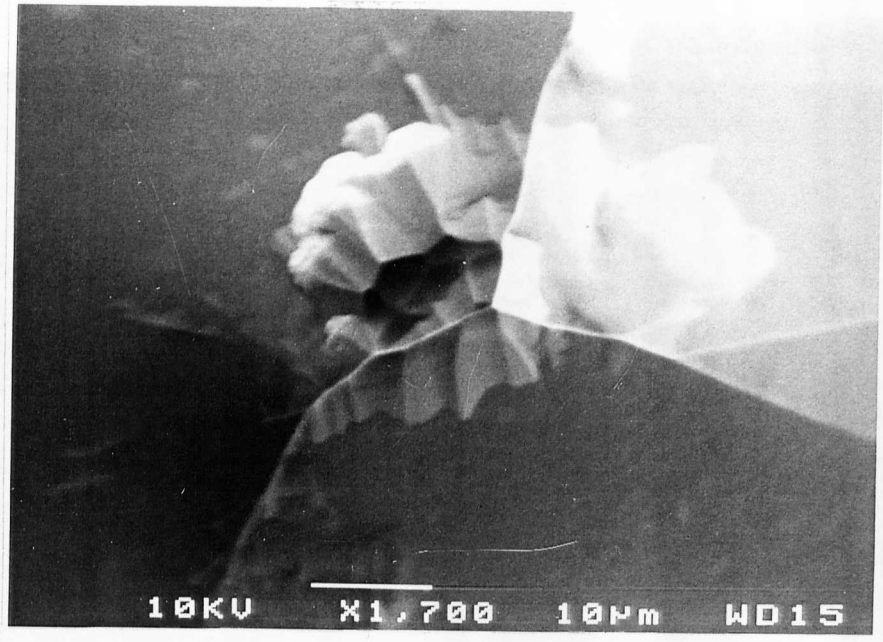

(c) after 6 hours ion milling,

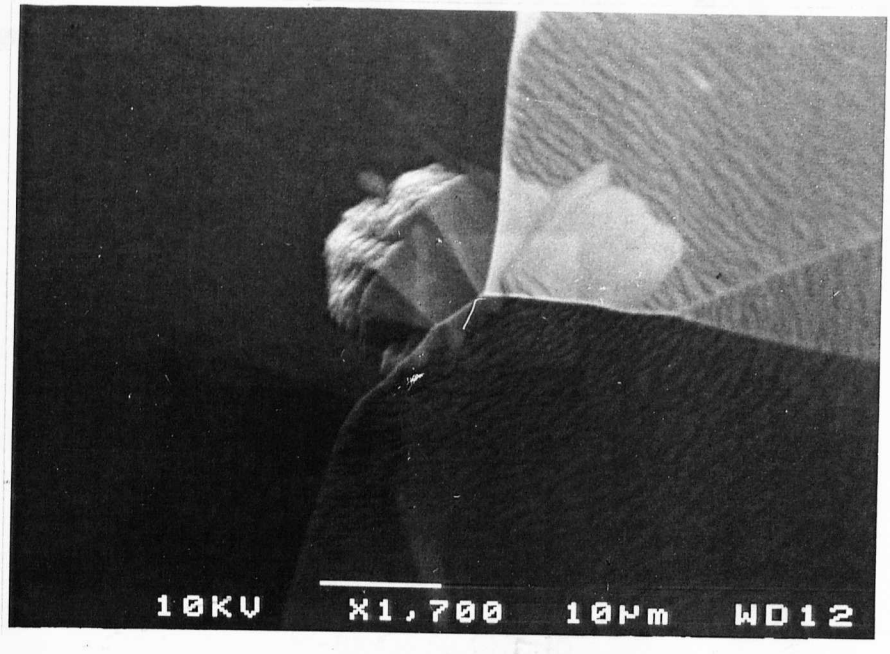

(d) after 9 hours ion milling.

Figure 4.7 (cont'd) SEM images of diamond tip supplied by manufacturer.

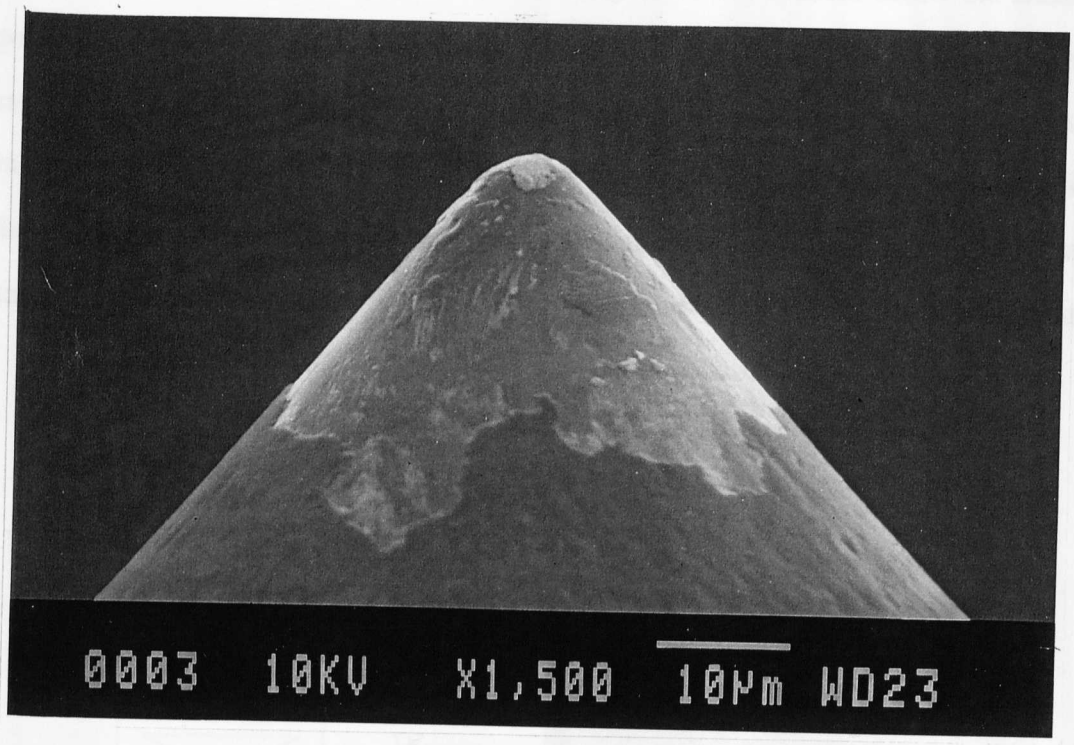

Figure 4.8 SEM image of the diamond tip used for fibre pushing experiments.

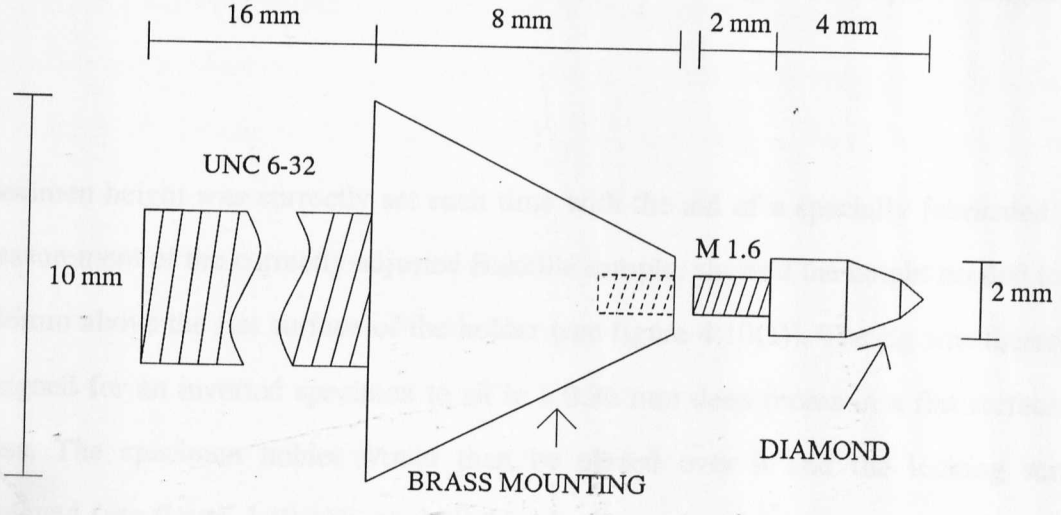

Figure 4.9 Schematic of the diamond tip mounting arrangement.

by setting up the system with a flat sample of Bakelite in the SEM's specimen holder and placing brass shim in between the indentor support stand and the stage tray to alter y-direction alignment (see figure 4.2), and using shim and spacers below the Bakelite specimen to alter its height, effectively adjusting the x-alignment. Correct alignment was accomplished when the indentor tip was just touching the specimen surface and it was imaged in the centre of field of view on the SEM at up to x5000 magnification. The shim between stand and stage was always used and locating washers were machined to help in correct positioning of the stand when setting up the apparatus.

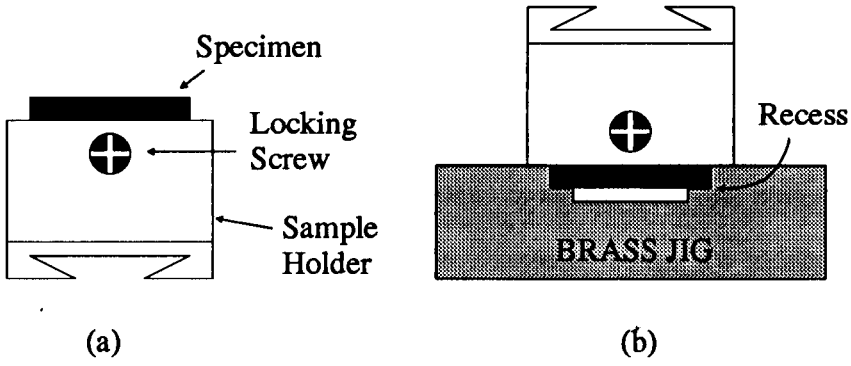

Figure 4.10, (a) Specimen holder, and (b) jig for mounting at the required height.

Specimen height was correctly set each time with the aid of a specially fabricated jig. Measurement of the correctly adjusted Bakelite sample, showed the height needed to be 0.86mm above the flat surface of the holder (see figure 4.10(a)). The jig was therefore designed for an inverted specimen to sit in a 0.86 mm deep recess in a flat surface of brass. The specimen holder would then be placed over it and the locking screw tightened (see figure 4.10(b)), resulting in a level specimen at the correct height. This arrangement meant that any flat specimen that had a diameter less than 30 mm and depth less than 20.3 mm could be used for indentation work.

4.2.4 Displacement measurement

Due to the restricted space within the SEM vacuum chamber, it was not possible to construct a massive and stiff instrument frame. The original support stand shown in figure 4.2 was used throughout. Thus displacement measurement devices such as LVDT's (linear variable differential transformers) and optical encoders that would measure Inchworm shaft displacement relative to the motor's fixing were not acceptable as the resultant measurement would be the sum of indentation depth and considerable instrumentation deflection under load. Also, the typical resolution of such devices (0.1 μm) was recognised as unacceptable for work in the nano/micro-indentation range (section 3.3.1).

A novel capacitance displacement gauge was developed to overcome the above problems by directly measuring tip displacement with respect to the specimen surface. Effectively, the gauge is a parallel plate capacitor with one plate fixed and the other deposited on the rear face of a flexible cantilever beam. To reduce temperature effects, the base was machined out of "Zerodur" glass ceramic that has a zero coefficient of thermal expansion. The front face of this base was polished optically flat to provide a reference surface for bonding the cantilever beam. Electrode separation was achieved by then masking a portion of the surface and removing the exposed area to a depth of 50 μm with a concentrated 2 HF : 1 HCl etchant. Aluminium was evaporated onto the etched surface to form one electrode and a strip of glass 1.5mm x 14mm x100 μm thick, cut from a cover slide and also coated with aluminium, was fixed with conducting silver glue over the edge of the step to form the capacitor. A hemispherical sapphire stylus (diameter 1.5 mm) was fixed on to the cantilever to contact the specimen surface. Figure 4.11 illustrates the construction.

The position of the gauge with respect to the indentor tip and load cell is shown in figure 4.12. The gauge is mounted on a threaded support that enables fine height adjustment by the locking nuts. Operation involves the sapphire stylus touching and pressing against the flat specimen surface just before the indenting tip touches, the

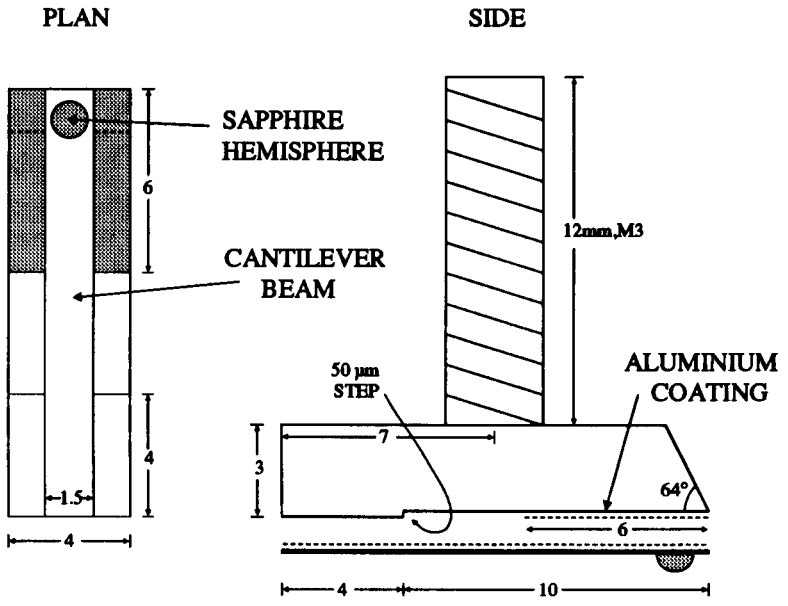

Figure 4.11 Capacitance gauge construction.

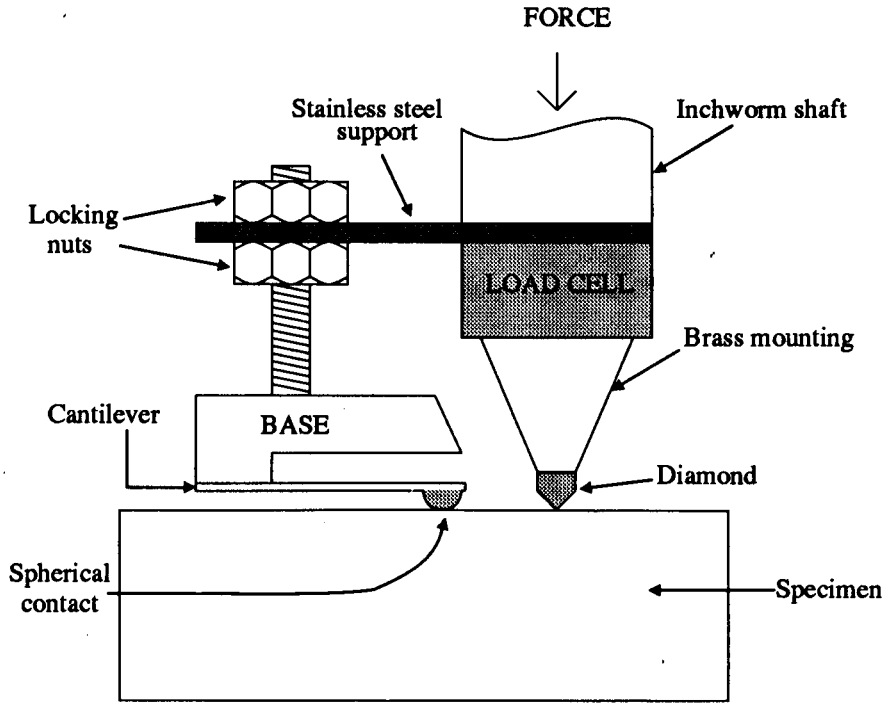

Figure 4.12 Indentor head (not to scale).

gap between the plates closing and increasing the capacitance.

The change in capacitance is measured using the "Nanosensor 2000" amplifier (Queensgate Instruments, U.K.) [103], connected via vacuum feed-through to the gauge. It compares the changing capacitance of the gauge C_g to a reference capacitor C_{ref}. Its output voltage V_{out} is proportional to C_{ref} / C_g,

$$V_{out} \propto (C_{ref} / C_g - 1) \tag{4.1}$$

For a parallel plate capacitor,

$$C = \varepsilon_0 \varepsilon_r A / z \tag{4.2}$$

where C is the capacitance, ε_0 is the permittivity of a vacuum, ε_r is the relative permittivity, A is the common area of the plates and z is the spacing between them. Thus by combining equations 4.1 and 4.2, it is seen that the output of the Nanosensor amplifier is proportional to the distance between the plates if they remain parallel,

$$V_{out} \propto (C_{ref} / \varepsilon_0 \varepsilon_r A_g) z_g - 1 \tag{4.3}$$

with A_g the gauge plate area and z_g the spacing between them. Operation of the gauge did not however involve measuring the capacitance between two consistently parallel plates. As soon as the flexing lever moved, the plates would not be parallel to each other. Amplifier output was therefore expected to be non-linear and had to be calibrated against lever deflection.

The reference capacitor had a value of 2 pF and so the gauge capacitance was designed to equal this and give zero voltage out at zero tip deflection. This required a plate spacing of approximately 50 μm and a common area given by the 1.5mm wide flexible plate opposite a 6mm long strip of aluminium deposited on the base, see figure 4.11. The 50 μm maximum deflection that would result was ample for

the indentation applications envisaged but in use, a range of over 100μm was obtained due to the cantilever not sitting flush on the flat base.

Calibration of the sensor was performed in a temperature controlled metrology facility maintained at a nominal value of 20°C with a diurnal fluctuation of ±1°C. Figure 4.13 shows a schematic diagram of the experimental calibration apparatus. In this, both the capacitance probe and a Rank Taylor Hobson Talysurf 4 inductive stylus probe were contacted against the flat surface of a non-rotating differential micrometer with a separation of approximately 3mm. The capacitance gauge was mounted on the Inchworm motor fixed to the support stand, while the transducer and micrometer were mounted on relatively large steel mounts. All three components rested on a large granite surface plate. Manual alignment of the sensors was used to achieve colinearity of the measurement axes to better than 0.1 radians resulting in a cosine error of less than 0.5%.

Calibration was achieved by manually rotating the micrometer while simultaneously measuring the outputs from both sensors over a displacement of 100μm. Because both sensors reference to the front face, the measurement loop does not pass through the micrometer. Consequently, for a typical experimental duration of 100 seconds, the calibration procedure was found to be relatively insensitive to the thermal disturbance due to manual operation. Figure 4.14 shows the output from a typical calibration test. The bending of the cantilever results in a non-linear response that is clearly seen. This was fitted to a third order polynomial giving the displacement of the sensor, δ, as a function of the output voltage V_{out},

$$\delta = a(V_{out})^3 + b(V_{out})^2 + cV_{out} + d \tag{4.4}$$

where a, b, c and d are constants. This formula was incorporated within the data processing software. Calibration was carried out each time the capacitance gauge was adjusted on the indentor shaft, for example when indenting tips were exchanged. The polynomial fitted the calibration data to ± 0.02 μm over the 100 μm range. Although

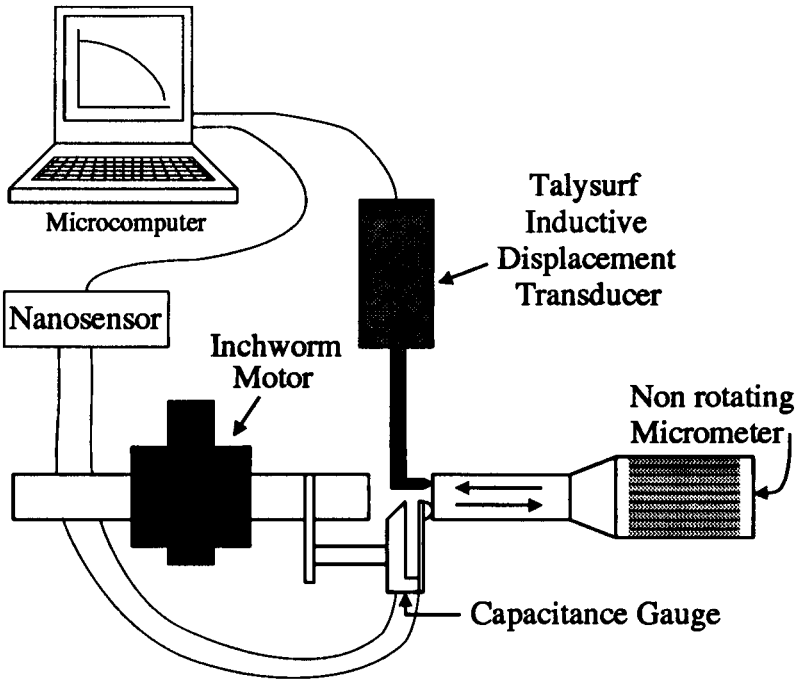

Figure 4.13 Schematic illustration of the apparatus used for calibration of the capacitance displacement gauge.

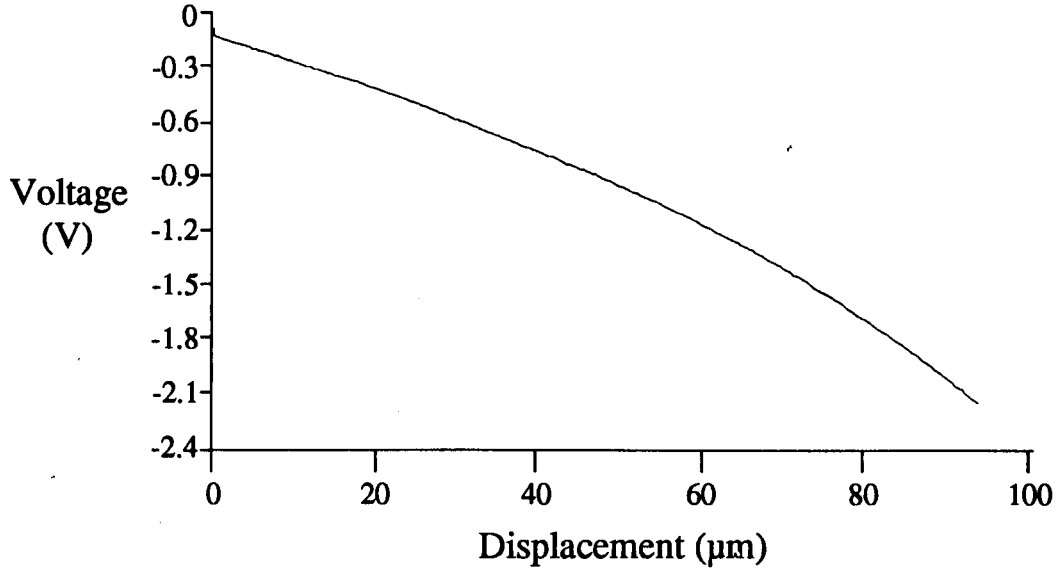

Figure 4.14 Typical displacement gauge calibration data.

calibration at atmospheric pressure is not fully consistent with the normal operation under vacuum, the change in permittivity between atmosphere and vacuum results in a negligible 0.012% change in the output voltage of the sensor [107].

The amplifier was found to provide a resolution of 10nm over the 100μm range of the gauge.

Leads for both the displacement and load transducers connect to vacuum feed throughs machined into a plate on the SEM chamber wall which also serves as the electronic ground plane, see figure 4.19.

4.2.5 Instrumentation

Figures 4.15 - 4.18 are different perspectives and magnifications of the indentor positioned on the *x-y* stage with the SEM door opened.

Figure 4.15 illustrates the Inchworm motor surrounded with μ-metal shield and power cable supplying it from the left. The load cell, displacement gauge, indentor tip and specimen are clearly seen. Figure 4.16 is a higher magnification image of figure 4.15. The specimen protruding 0.86mm above the sample holder is seen and the gap between the electrodes of the capacitance gauge is visible. The sapphire stylus is positioned slightly lower than the diamond indenting tip. A lower magnification perspective is shown in figure 4.17, where the whole stage and indentor are tilted to 47° prior to the SEM chamber door being closed. The sample holder is positioned on the *x-y* stage and the signal leads from the capacitance gauge are trailing in the fore-ground. (Note the reflection of the indentor in the polished specimen surface). Figure 4.18 shows the tilted stage and indentor in the SEM chamber door way, from an opposite angle.

Illustrated in figure 4.19 is the blanking plate with the various feed throughs fitted into it. The 9 way D-type plug is the Inchworm motor control cable feed through, the TNC connector is for the load cell amplifier and the two, co-axial "Lemo" connectors are for the signal lines from the two "plates" of the capacitance gauge.

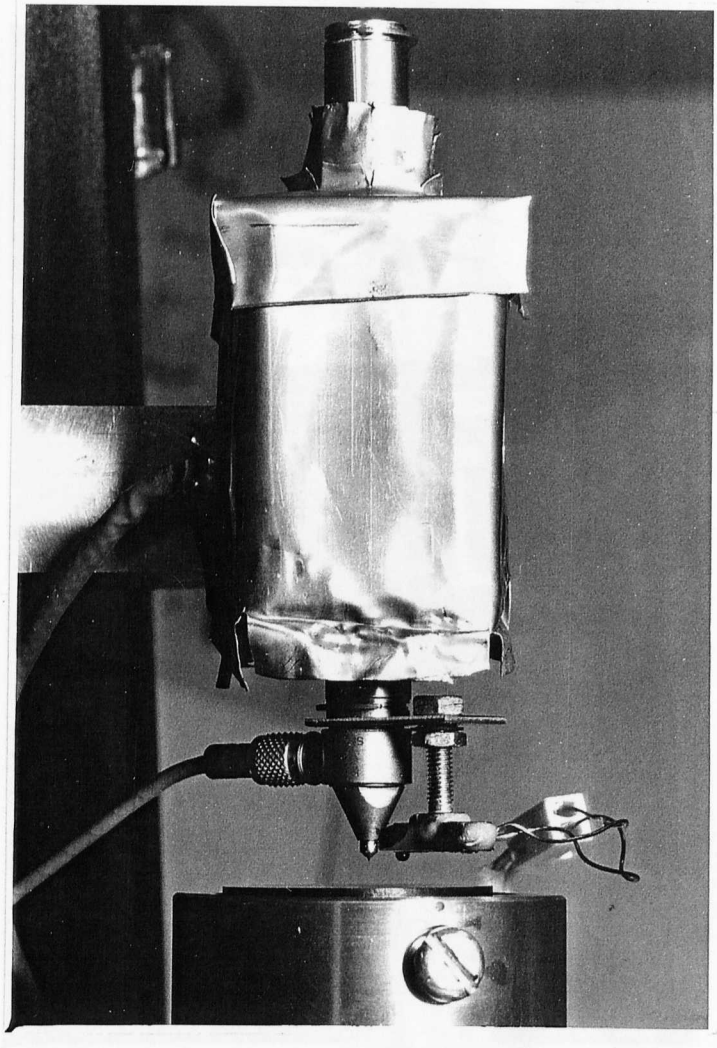

Figure 4.15 Image of the indentor aligned above a specimen. Inchworm motor, μ-metal shield, load cell, capacitance gauge, diamond tip and specimen, are all shown.

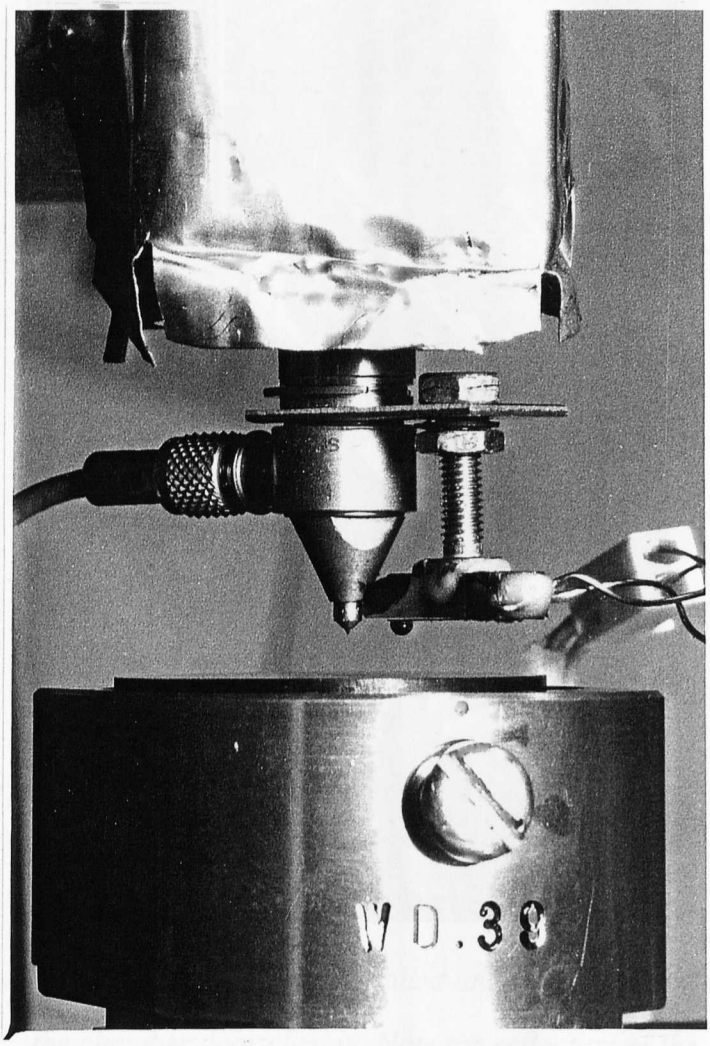

Figure 4.16 Higher magnification image of figure 4.15. Load cell, indentor tip, capacitance gauge are illustrated. Note the gap between the "plates" of the capacitance gauge.

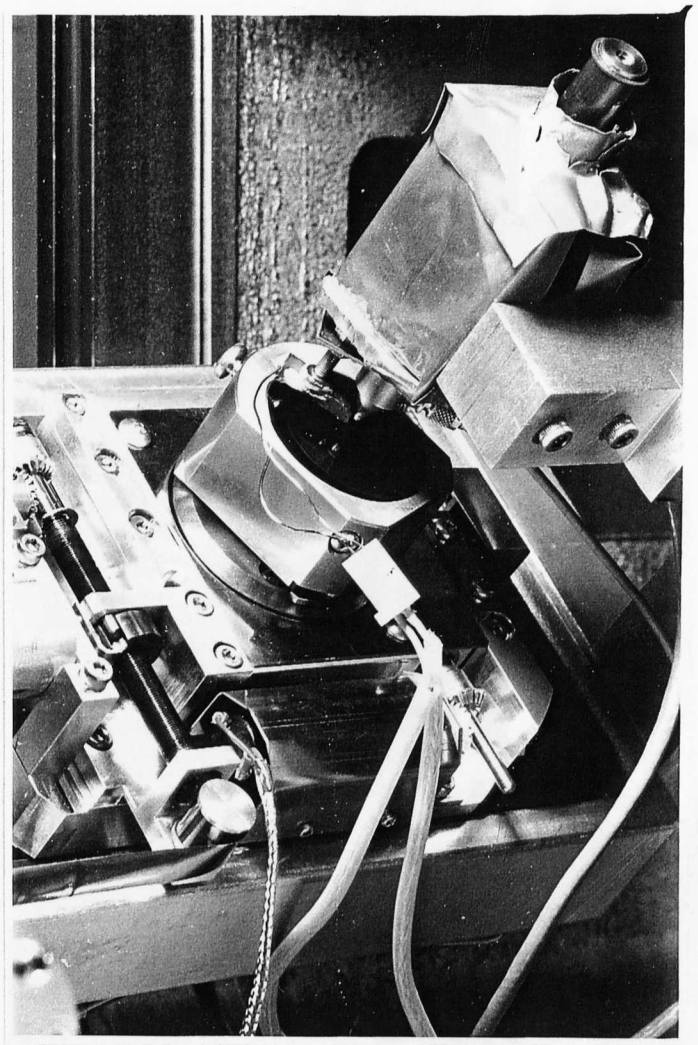

Figure 4.17 Indentor and specimen are installed and the stage is tilted to 47° prior to the chamber door closing. Note the reflection of the indenting tip in the specimen surface.

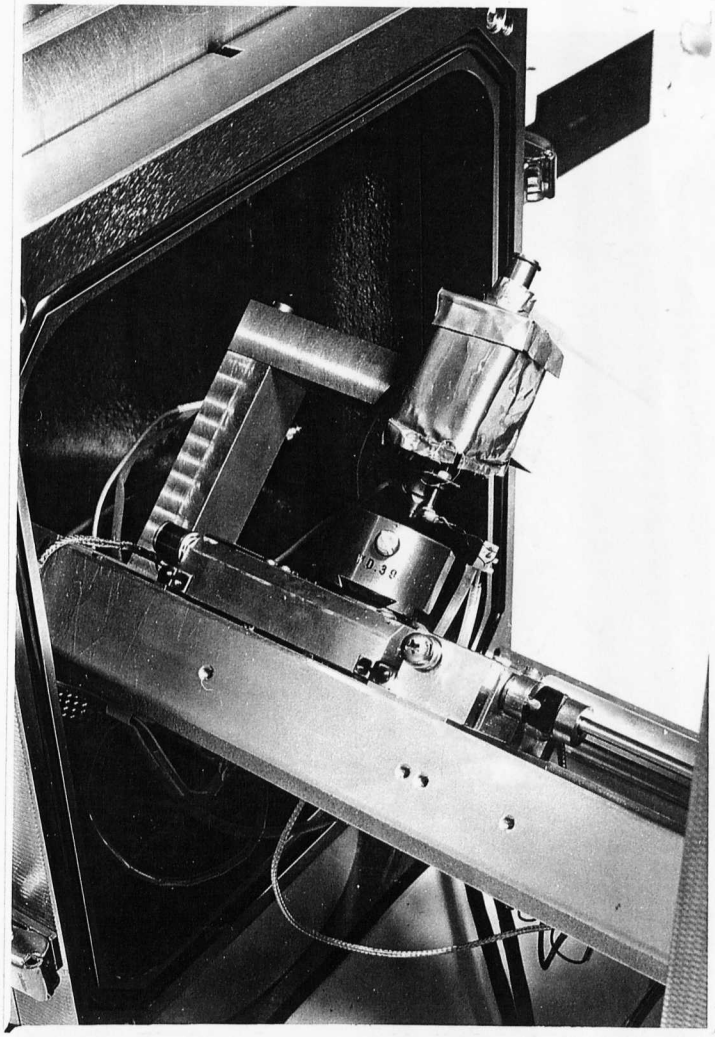

Figure 4.18 Image showing the arrangement in the door way of the SEM chamber, prior to sliding into position and the chamber door closing.

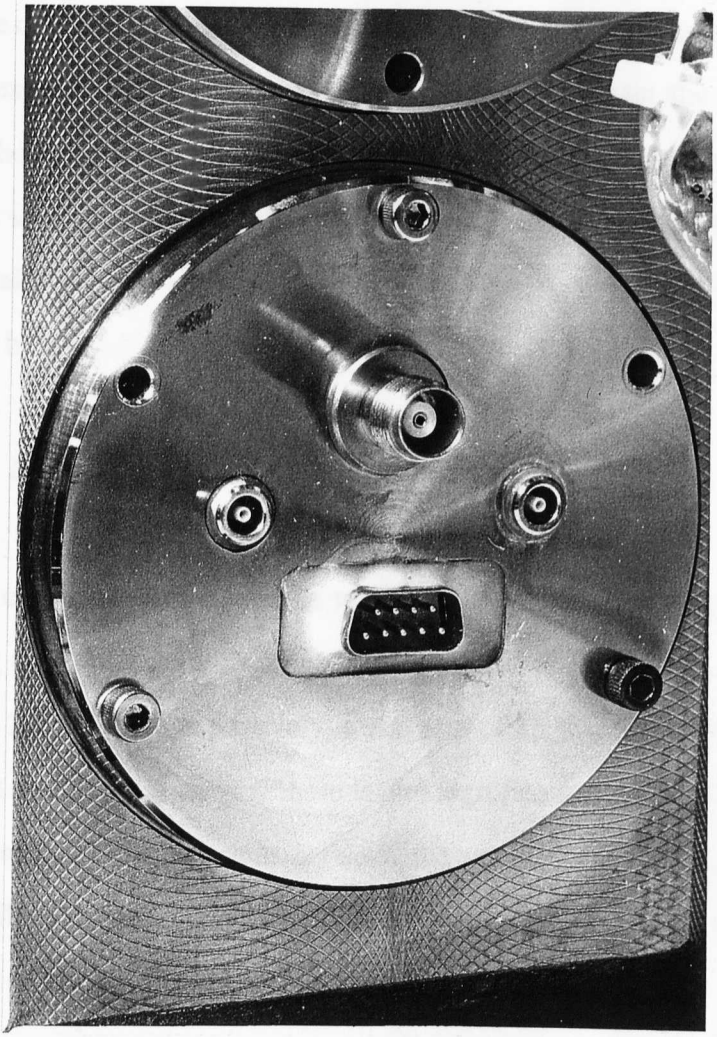

Figure 4.19 Blanking plate incorporating vacuum feed throughs. Note the 9 way D-type plug for Inchworm motor control, the TNC connector for the load cell amplifier and the two Lemo connectors for the capacitance gauge signal lines

4.2.6 Instrument Considerations

The positioning of load cell and displacement gauge is designed to reduce instrument compliance distorting the measured data. The major error source will be lost motion due to compliance in all components around the measurement loop and, in particular those components coincident with the force and measurement loop.

In experiments, the indentor probe does not contact the surface until the cantilever of the sensor has undergone significant deflection and therefore after the sensor contact is under a relatively high applied load. To calculate this load it is necessary to calculate the stiffness of the cantilever, k_c , which from simple beam theory is given by

$$k_c = Ebd^3 / 4L^3 \tag{4.5}$$

where E is the elastic modulus, b is the width, L the length and d the thickness of the beam. Inserting the values corresponding to E,b,L and d of 70 x 10^9 N m^{-2}, 1.5 x 10^{-3}m, 10 x 10^{-3}m and 100 x 10^{-6}m respectively, a stiffness of 26 N m^{-1} is predicted.

Lost motion will occur if there is any significant distortion in the instrument other than the relative displacement between the cantilever and the electrode on the base. One possible distortion would be that due to the contact. From elasticity theory, the stiffness, k_s, of a sphere contacting with a flat surface is

$$k_s = dP/dx_o = 3/2\ P^{1/3} E'^{2/3} R^{2/3} = 2\ x_o^{1/2} R^{1/2} E' \tag{4.6}$$

where

$$\frac{1}{E'} = \left[\frac{1-\nu^2}{E_1} + \frac{1-\nu^2}{E_2} \right] \tag{4.7}$$

and P is the force, x_o is the distortion, R is the radius of the sphere, ν is the Poisson ratio of the material and E_1 and E_2 are the elastic moduli of the sphere and surface respectively. Consider the sapphire stylus contact on a flat steel surface. After the capacitor beam has deflected 1μm - corresponding to an applied force of 26 μN, the stiffness of the contact is already around 200 times greater than that of the beam and so errors due to compliance at the contact are insignificant. This is a conservative estimate as the beam has usually distorted ~ 20 μm before the indentor makes contact with the specimen.

A simple calculation of the stiffness of other components around the measurement loop indicates stiffness considerably higher than those of both the cantilever and the hardness indentation. For example, the highest forces in the measurement loop will be those transmitted from the indentation to the load cell through the brass support. The stiffness of the brass support is difficult to predict but a conservative estimate is given by the product of elastic modulus and average cross sectional area of brass divided by its length, giving a stiffness of 2×10^8 N m^{-1}. The load cell stiffness is quoted as being 10^9 N m^{-1} and the two combined stiffnesses, being in parallel, give a worst case value of 8×10^7 N m^{-1}. This stiffness contributes to the force/ displacement curve and could be subtracted from the plot. However, for a typical indentation this is insignificant and has not been removed from experimental results reported here (typical force / displacement traces have "stiffnesses" of 0.5N/5μm, equivalent to 1×10^5 N m^{-1}, see example in figure 4.28). Taking an upper bound value of an indent's stiffness to be 5×10^5 N m^{-1}, errors of less than 1% are predicted.

Frequency response of the capacitance gauge is limited by the fundamental frequency of the cantilever beam. It can be calculated from the equation [15],

$$\omega_n = \sqrt{(k_c/m_e)} \tag{4.8}$$

where m_e is the equivalent mass of the system given by

$$m_e = 0.24m_c + m_s \tag{4.9}$$

m_c and m_s are the masses of the cantilever and sapphire hemisphere respectively. For the materials and dimensions mentioned above this yields an equivalent mass of 5.5mg which, for the stiffness of 26 Nm^{-1} computed earlier, gives a resonant frequency of 346 Hz. This calculation does not include the added mass of the glue used to bond the hemisphere and, as expected, a slightly lower natural frequency of 320 Hz could be observed by releasing the probe clear of the specimen surface and tapping the sides of the SEM. However, when the sphere is in contact with the specimen surface, the effective stiffness and therefore insensitivity to vibration is considerably increased.

4.2.7 Interfacing to microcomputer

The Inchworm motor was controlled, and the load cell and capacitance gauge monitored, by personal computer interfaced to the instrument. The original computer used was a BBC 'B' that was later superseded by an Acorn A3010 with fitted interface board that had far greater data handling capacity and speed. The control and data acquisition system is illustrated in figure 4.20.

Control of the motor direction and speed required the supply of four TTL signal lines to the Inchworm controller. The controller converted these signals to the high voltages needed to drive the motor. One line was to enable / disable the motor, one to send a stop / go signal, one to set forward / reverse directions and the fourth to set the traverse speed of the shaft. Every time a rising or falling edge was registered on the square wave input of the fourth line, the shaft was moved an approximate 4nm [108]. Thus by varying the frequency of the fourth signal line, shaft speed was controlled.

The 8-bit user port of the Acorn was programmed to output the TTL signals. A clock signal could be adjusted by the timers on the 6522 VIA (Versatile Interface Adapter) and output on the 8th bit of the user port. A maximum frequency of 250 kHz was possible that equated to an approximate speed of 2 mms^{-1}. Frequencies of 1 Hz and

lower were also possible i.e. speed ≤ 8nms^{-1}.

Data logging was achieved using the standard 12-bit ADC (Analogue to Digital Converter) on the input/output board supplied by Acorn. Although circuit protection had to be built to prevent damage from any input voltage dropping below 0V or rising above +1.8V, it was acceptable for this application as its address was easily accessed from BBC BASIC, the programming language used.

For reading the applied load, the 12-bits provided acceptable resolution over the 0 - 1.8V range as the amplifier gain could easily be adjusted (depending on the maximum expected load per experiment) and the zero load point be adjusted to zero

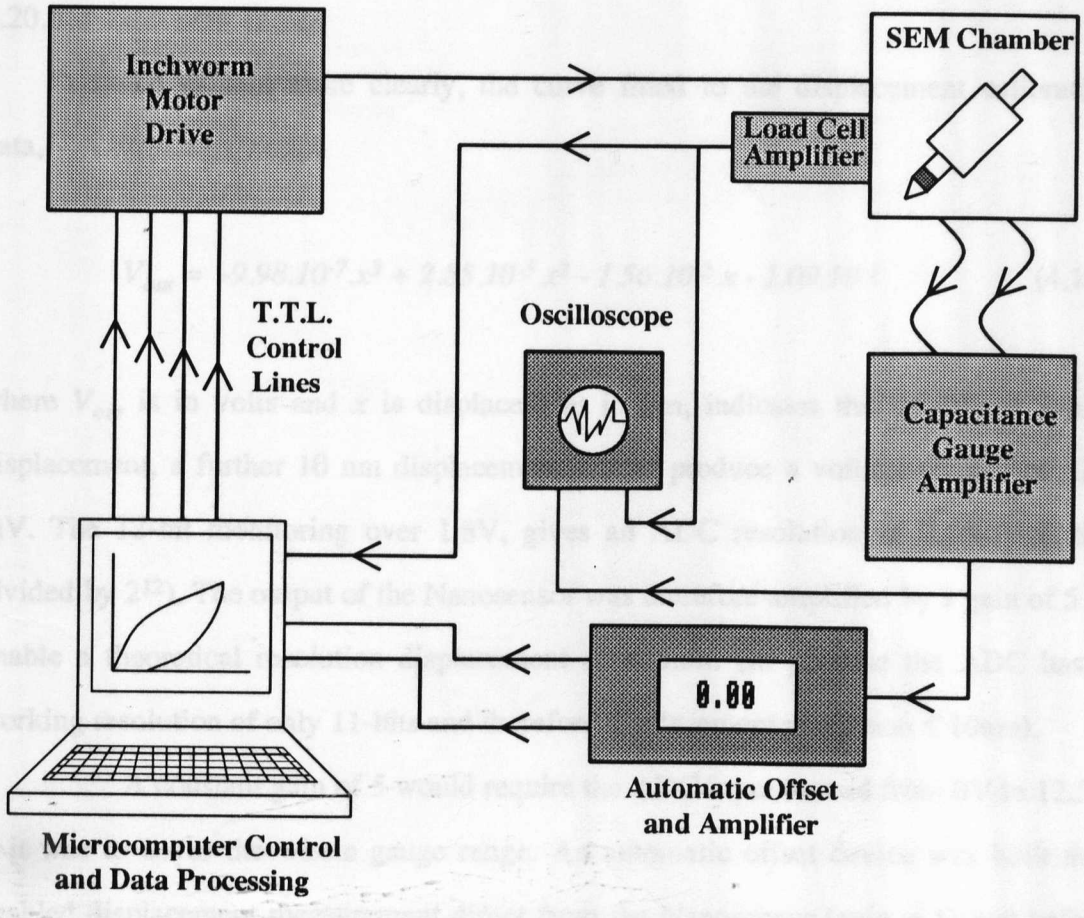

Figure 4.20 Schematic of the control and data acquisition system (arrows show direction of information).

volts output by the potentiometer and short/reset switch (see figure 4.3). The load resolution of ±0.002 N was limited by the noise level on the system's earth.

Interfacing the displacement gauge to the ADC was more complicated. Figure 4.14 shows that the signal from the Nanosensor amplifier approximated to a 2.5V change over 100μm. The capacitance gauge stylus was always positioned 20 - 40μm lower than the actual indenting tip, so it always contacted the specimen surface first. To obtain high resolution measurement, it was necessary to always record the point at which indentation started, directly from the Nanosensor. Knowing this, an offset voltage would then be applied to zero the signal input to the ADC and indentation then proceeded with the signal amplified by a gain of 5. This operation was performed with a specifically built "automatic offset and amplifier" unit, see figure 4.20.

To explain more clearly, the curve fitted to the displacement calibration data,

$$V_{out} = -9.98.10^{-7}x^3 + 2.85.10^{-5}x^2 - 1.56.10^{-2}x - 1.09.10^{-1} \qquad (4.10)$$

where V_{out} is in volts and x is displacement in μm, indicates that at 40 μm initial displacement, a further 10 nm displacement would produce a voltage change of -0.2 mV. The 12-bit monitoring over 1.8V, gives an ADC resolution of 0.44mV (1.8V divided by 2^{12}). The output of the Nanosensor was therefore amplified by a gain of 5 to enable a theoretical resolution displacement of ≤ 5nm. (In practice the ADC has a working resolution of only 11-bits and therefore displacement resolution ≤ 10nm).

A constant gain of 5 would require the ADC input to read from 0V to 12.5V if it was to cover the whole gauge range. An automatic offset device was built that enabled displacement measurement direct from the Nanosensor (gain = 1) just before the start of an indentation and record it in software, apply the required offset voltage to zero the ADC input voltage, then increase gain to 5 and measure to a resolution better than 10 nm during actual indentation.

Figure 4.21 illustrates the procedure. If, for example, indentor tip and specimen contact is just after 40μm displacement of the gauge, then the gauge reads -0.3V at this point (figure 4.21(a)). The voltage is recorded in the software so that all readings during indentation are referred back to the correct point on the calibration curve. Automatic offset then applies +0.3V to the Nanosensor output, resulting in 0V now corresponding to 40μm displacement (4.21(b)). When indentation starts, the signal

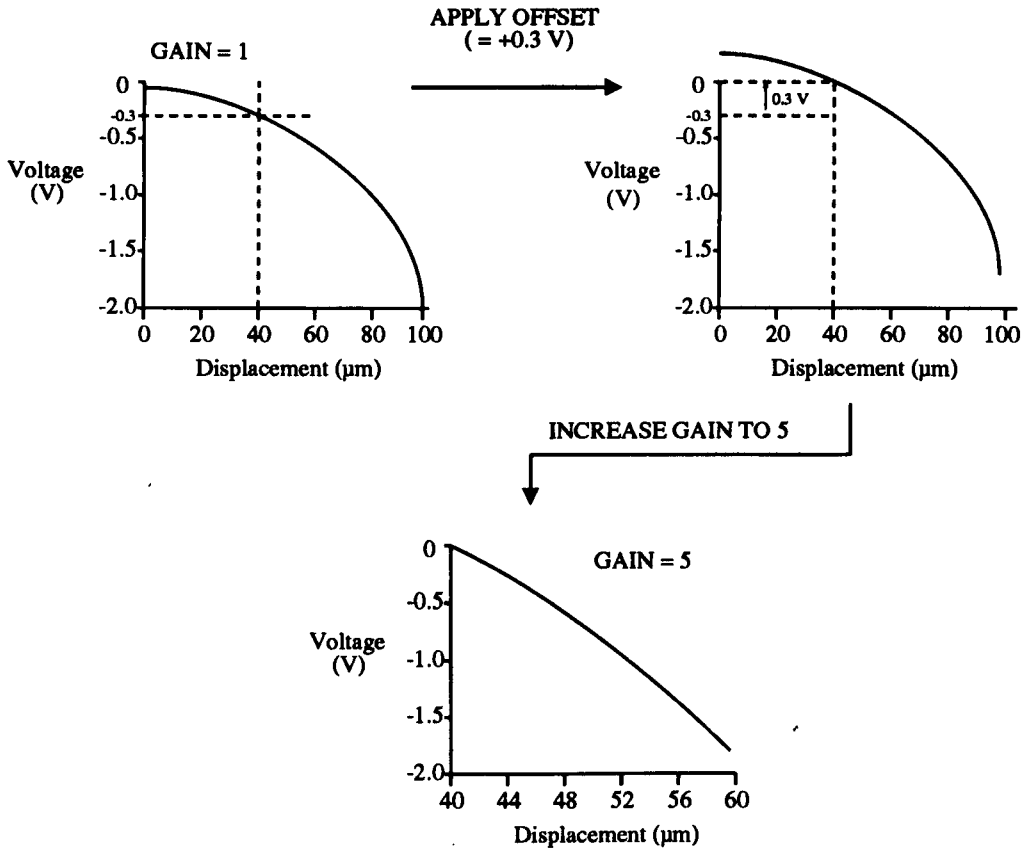

Figure 4.21 Procedure for displacement measurement.

is amplified by a gain of 5 and displacement recorded to a resolution < 10nm (4.21(c)).

The circuit diagram for the automatic offset and amplifier unit is shown in figure 4.22. At all times the Nanosensor signal is at V_{in}. Under normal operation, the indentor would always be raised above the specimen to the point where the capacitance stylus would just lift off the specimen. At this point the signal would be offset to 0V entering the ADC by switching switch C in figure 4.22 to the other position to that

shown, sending the motor driving the potentiometer into motion and offsetting the V_{in} signal to zero. When at zero, C would then be switched back and $V_{out(2)}$ read by the ADC. This "told" the calibration software how far in fact the gauge zero displacement point was from the zero voltage point. The indentor would then be lowered until the diamond tip was just above the specimen surface (about 20-40μm). The switch would be thrown, so that the potentiometer was turned by the motor to offset the voltage, the switch returned, and $V_{out(2)}$ recorded again. This reading corresponds to the 40μm reading in figure 4.21(b). Actual indentation could then proceed with $V_{out(1)}$ continuously recorded. $V_{out(1)}$ is the output of the Nanosensor, offset to the necessary amount and amplified with a gain of 5.

A digital meter was used to monitor the offset operation, see figure 4.20. It read 0.0 mV when the potentiometer had been driven to the correct point. Accuracy of potentiometer positioning was to ±0.5mV.

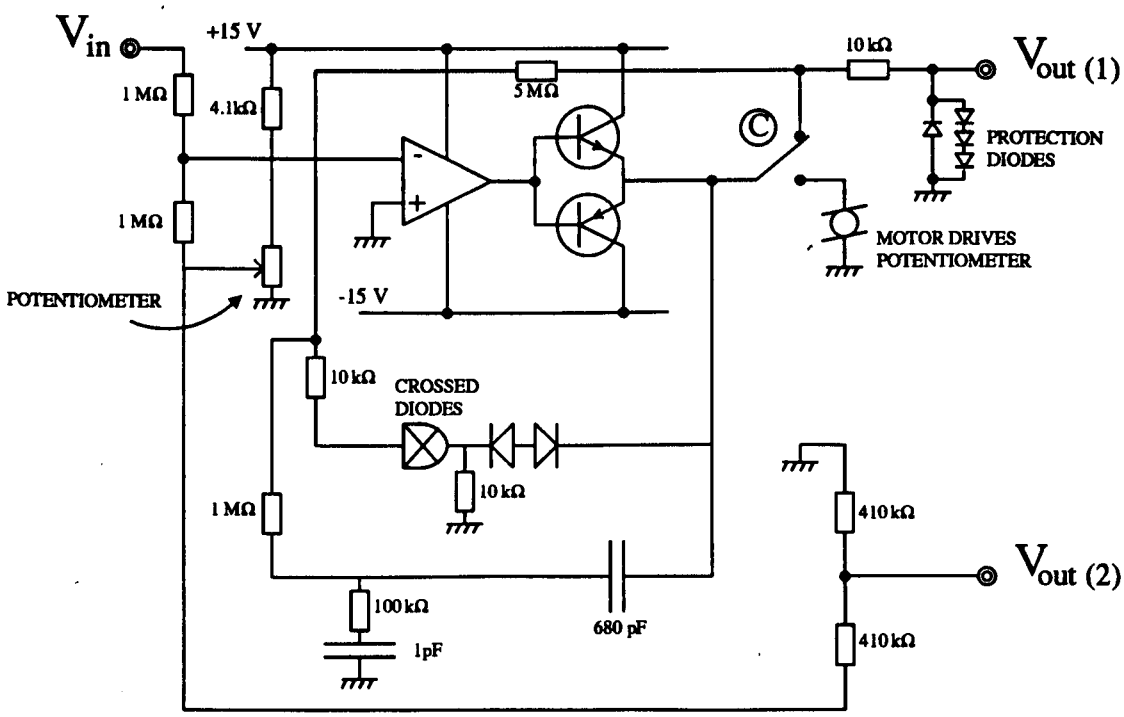

Figure 4.22 Circuit for automatic offset and amplifier unit for displacement gauge.

4.2.8 Software development

The programs required to operate the indentation system were written throughout in BBC BASIC. Various short programs were written and used as tools, an example being the load calibration program that operated the Inchworm motor and recorded the voltage from the load cell as load was applied. These have not been documented in this report. The three main programs used for normal indentor operation were ;

i) To operate the indentor, coarse setting up of the system each time it was used and for actual indenting sequences where "raw" (uncalibrated readings from the ADC) load and displacement data were recorded on floppy disk. Called "ONE".

ii) To read the raw data from each indentation, apply compensation to account for load cell drift and Inchworm non-linearity (see section 4.2.1 and 4.4), and use calibration curves to convert raw data to actual load (N) and displacement (μm) data, and store it on floppy disk. Called "TWO".

iii) To read the load/displacement data and apply the models on fibre push-out tests to the data and determine the values of G_i and τ for the interface of each fibre pushed. Called "THREE".

The code listings are given in Appendix I. Their operation is discussed in sections 4.3.3, 4.4.2 and Chapter 5.

4.3 Instrument Operation

4.3.1 Specimen preparation

For indentation of a specimen, whether for fibre pushing in CMCs or hardness testing of a material, a flat surface had to be available for the displacement gauge stylus to contact and produce acceptable data. This entailed mounting the samples in Bakelite or Metset polymer resin and polishing the surface to be indented to a flat, 1μm diamond finish. Diameter of the bakelite/resin blocks had to be 30mm or less for them to fit in the standard sample holder that was used. Mounting of the samples in the holder is described in section 4.2.3. Grinding and polishing of the samples was carried out with a Beuhler automatic polisher. To prevent charge build up on the specimens when observed in the SEM, they were coated with a thin layer of gold in a standard Emscope gold coating unit. This gold coat was not expected to affect the indentation results as it was typically only tens of nanometres thick.

Great care had to be taken when mounting fibre reinforced CMCs, as it was necessary to ensure the fibre alignment was perpendicular to the polished surface. To help in this, specimens were accurately positioned in spring clips that held them as the bakelite/resin was placed around them. Standard size of CMC specimen for fibre push testing was approximately 3mm x 3mm x 5mm. The 5mm length, that would extend below the prepared sample surface, was set as a minimum dimension for fibre push down tests.

4.3.2 Microindentor installation

Converting the standard SEM into a combined microindentation system was necessary on a day to day basis. It was not feasible to set up the microindentation facility and leave it in for days or weeks at a time as other users needed the SEM for the normal applications. By the end of the project, it was possible to install the system and

be indenting within 30 minutes. However, it was normal to leave the system motionless for 30 - 60 minutes after installation for any difference in SEM chamber and instrument temperatures to reduce and stabilise. This minimised errors in load and displacement data due to thermal drift.

Installation involved clamping the stand (to which the Inchworm motor was permanently attached) to the SEM tray that held the *x-y* stage as in figure 4.2. Locating washers and mounting plates were fabricated to enable quick and correct alignment. The cables connecting the motor, load cell and displacement gauge would then be connected to the respective feed through sockets. The sample holder with mounted specimen would then be placed on the stage and the SEM door closed and the vacuum pumps started. Whilst pumping down, the load cell amplifier and the cables from the displacement amplifier and Inchworm motor would be connected to the feed throughs.

When at the correct vacuum (air pressure $< 10^{-4}$ mbar) the Inchworm motor would be switched on and controlled by running program "ONE" on the microcomputer. An image was obtained on the SEM in the usual way, with all indentation work performed with secondary electron imaging.

4.3.3 Indentation sequence

Once the specimen was in place and an image obtained on the SEM, the indentor could be lowered and raised at various speeds for coarse adjustment. Program "ONE" allowed keyboard control of the motor. Depressing the up and down cursor direction keys would traverse the indenting shaft up and down respectively, and hitting the space bar would stop the motor. Shaft speed was controlled with nine special function keys (F1-F9), setting the speed to 0, 0.117, 0.2, 1, 2, 4, 40, 200, 1000 $\mu m\ s^{-1}$ respectively, when they were depressed.

Once the indentor was lowered to near the specimen surface, a fibre would be aligned beneath the diamond tip with the joystick control of the *x-y* stage. It was possible to observe when the diamond tip was close to the specimen as a shadowing

effect occurred when the tip was less than 15μm away. This was due to the positioning of the secondary electron detector behind the Inchworm support stand.

For each indentation, the procedure described in section 4.2.7 had to be carried out. Practically this meant that once a point had been chosen to indent, the shaft would be raised to the position where the capacitance gauge stylus just lifted off the surface. Using the monitoring oscilloscope, the signal coming directly from the displacement gauge Nanosensor amplifier would be adjusted with the built in potentiometer to be approximately -50 mV. This was necessary to make sure that after inversion and amplification, the signal entering the ADC of the computer did not fall below zero. Similarly, the load cell amplifier offset potentiometer would be adjusted to ensure the signal was approximately +100 mV. (The load cell amplifier signal fed directly to the ADC and was not inverted, hence it was set to a slightly positive voltage). Once these were set, the displacement gauge offset voltage was recorded in the software by depressing "V" on the keyboard and then the indentor lowered to a position where the diamond tip was just above the specimen surface. The automatic offset was then initiated (see 4.2.7) and when complete i.e. the digital display showed 0.0 mV on the offset box, the system was ready to indent.

Indentation was started by depressing key "S" which sent program "ONE" into data recording mode. During indentation, the direction of the motor was controlled by the cursor direction keys and the space bar was the stop. However, speed could not be altered during an indent and for all the work reported in this thesis, it was set at approximately 100 nm s^{-1}. A normal indent would be carried out by depressing the "down" key and letting the tip indent the material. At the point (determined by looking at the process on the SEM screen) where the direction should be reversed, the "up" key would be pressed and the indentor would withdraw. When the diamond tip had lost contact with the specimen, it was usually left to carry on pulling back from the specimen for 5-10 μm so that it completely cleared the surface. The point where tip and specimen lose contact was easily observed by the applied load signal dropping to zero. The load is continuously displayed on the VDU screen during an indentation.

To stop the indentation sequence and data recording, key "S" had to be pressed. At this point a name would be requested for the data file and the fibre diameter entered if interfacial push down tests were being carried out. All data would then be stored on a floppy disk.

The whole procedure was then repeated for each further indent. Each indent would on average take approximately 100 - 200 seconds.

4.3.4 Specimen exchange and system dismantling

Specimen exchange, once the system was installed, was quick and simple. The Inchworm shaft would be retracted to approximately 10mm above the sample surface and the power to the motor then turned off. The SEM chamber would then be vented and the door opened and the sample holder taken off. A new specimen would be put in the holder as described in section 4.2.3 and it put back on the *x-y* stage. The door would then be closed and the chamber pumped down to vacuum.

After an indenting session was over, the system was dismantled by simply following the installation steps of section 4.3.2 in reverse order. This would take approximately 15 minutes.

4.4 Data Analysis

4.4.1 Dynamic, high magnification imaging

Information gained from direct observation of the indentation was recorded either by noting events as they happened in the lab book or by video, using the VCR link to the SEM. For an example of a video recording of fibre push-down tests, the indentor has been featured in the BBC Open University course "Materials Science and Engineering, T203" [109]. Imaging was possible in Back Scattered or Secondary electron modes. A sequence of secondary electron images taken with the SEM camera

is shown in figure 4.23. Typical events in a fibre push-down test are shown. Initial indentor and specimen contact is shown in 4.23(a), the load cell signal starts to rise from this point on. As load increases, the fibre debonds from the matrix. This is clearly seen and is shown in 4.23(b). Further displacement of the indentor tip is observed 4.23(c), until the direction is reversed and the tip eventually loses contact with the specimen, 4.23(d). These events can be correlated to the load / displacement data, the analysis of which is described below.

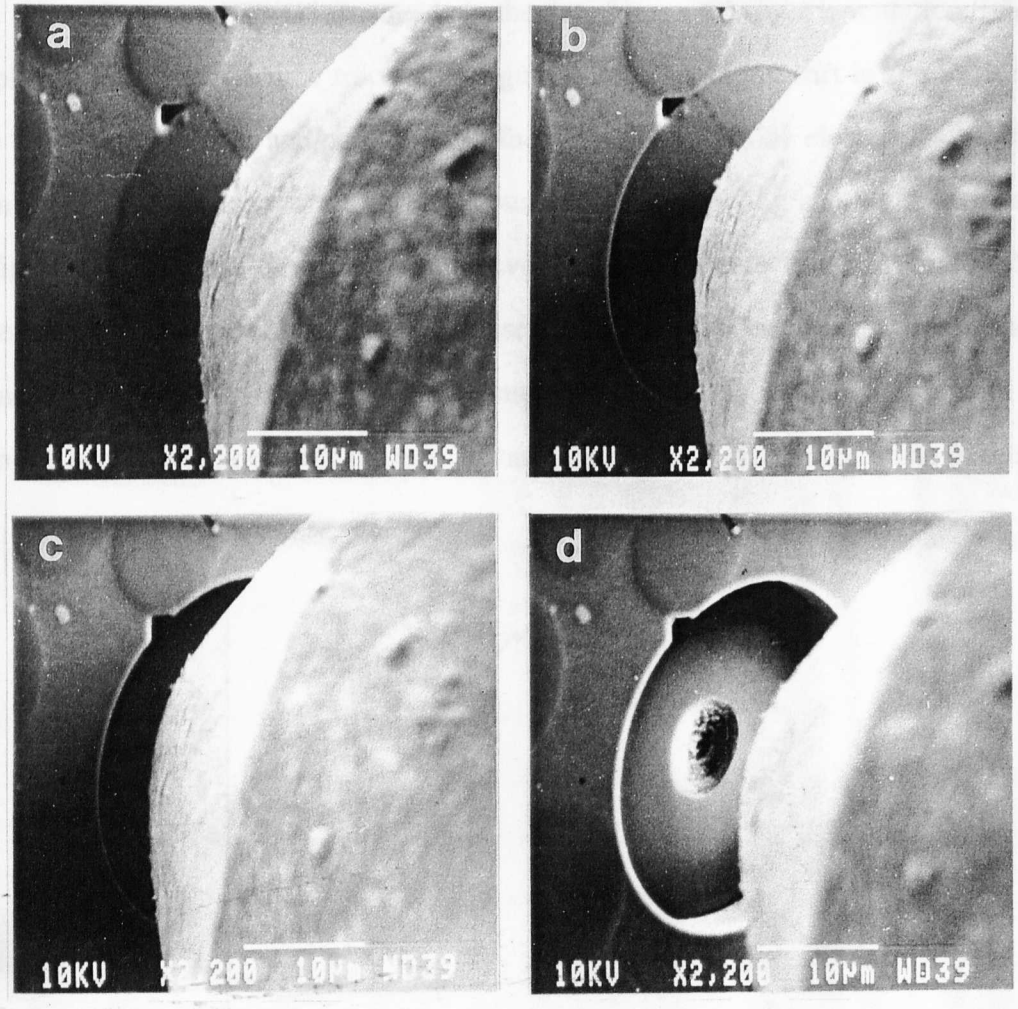

Figure 4.23 Sequence of SEM images taken during a fibre push-down test: a) initial fibre contact, b) fibre / matrix debond, c) fibre pushing and d) indentor withdrawal.

4.4.2 Load and displacement data processing

The raw data recorded during an indentation is converted to load and displacement data using program "TWO". Any drift in the load cell output is first taken account of and then non-linearities due to any piezoelectric clamps (that are clearly seen during indentation) are processed. The data is then converted to load (N) and displacement (μm) using the calibration formulas, the derivation of which were described in sections 4.2.2 and 4.2.4. The above processing steps are described in more detail below.

Program "TWO" first reads in the data from a previous indentation. It is then displayed as a load vs. time trace as in figure 4.24. The slight drift in the load signal, due to charge leakage and/or thermal effects on the amplifier electronics, is clearly seen. In effect it is linear and can be accounted for by applying a straight base line, as in figure 4.25, that can be subtracted to leave data with the effects of drift removed. The base line is located on the trace by mouse control of two cursors that mark the end points of the straight line. It should be emphasised that this is an example with more than the usual amount of drift present. It was normally less pronounced than in this case

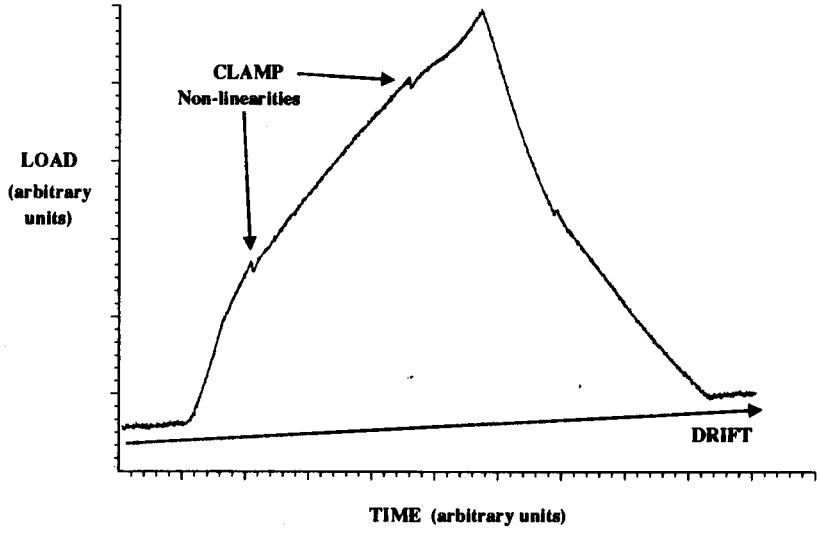

Figure 4.24 Typical raw data plot of load vs. time for a fibre push down indentation. Drift in the applied load signal is seen, as are the discontinuities due to the clamping of piezoelectrics of the motor.

and often not distinguishable.

The discontinuities due to the clamping of piezoelectrics on the Inchworm shaft are clearly seen on the trace. They are identified as such, and not as other material dependent events, by observing the contrast change in the SEM image at the points where they occur. The high voltage changes required to produce the clamping and unclamping cause the contrast on the secondary electron image to change, see section 4.2.1. If an event such as a fibre debond or crack propagation was seen to coincide with

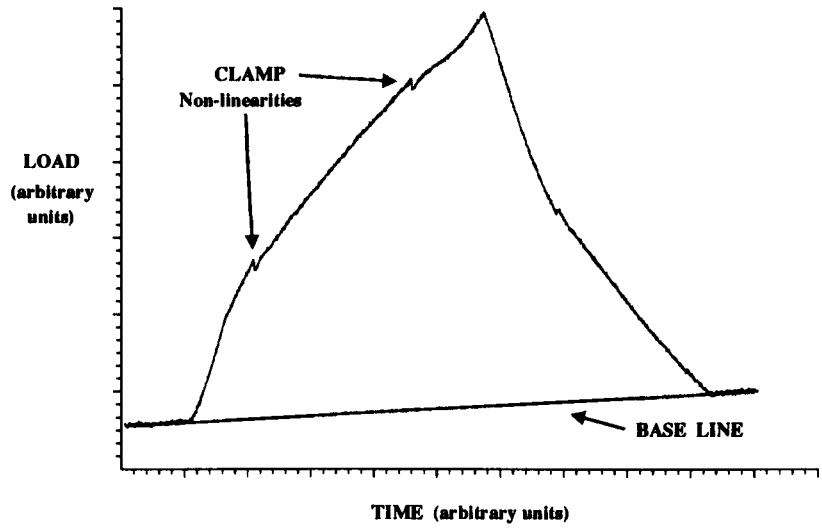

Figure 4.25 Raw data plot of load vs. time for an indentation. Base line is applied to subtract the effects of linear drift in the load data.

a clamp, that indentation would be stopped and the data discarded.

The zero displacement point and the data points where the clamps occurred are then located with mouse controlled cursor and load vs. displacement plotted as in figure 4.26. As can be seen in figure 4.26, the clamps do not cause a simple linear retraction of the shaft for a short distance. The sudden drop in applied load and shift in displacement larger than that expected for linear elastic response of the material suggest that the shaft is tilted slightly at a clamp. The maximum displacement shift measured at a discontinuity was 0.5μm, and with the minimum distance between capacitance gauge probe and indentor tip being 3mm, see figure 4.12 for geometry, the

Missing pages are unavailable

discontinuities by simply moving the data across, in either direction after a clamp, to form a continuous curve. The processing step is shown in figure 4.27, where segment A of data is left untouched and segment B is moved sideways.

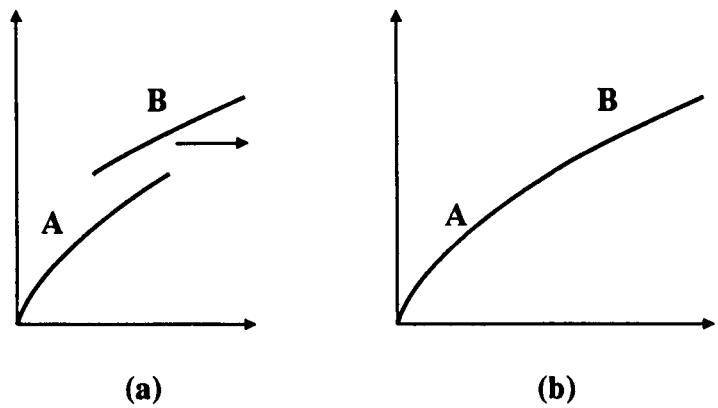

Figure 4.27 Technique for processing out piezoelectric clamp discontinuities, a) before translation of part of curve and (b) after.

This was only performed when there was no other event such as crack initiation occurring at the clamp. As is discussed in Chapter 5, the properties of each trace that are measured to determine interfacial shear stress τ and interface fracture surface energy G_i, are, respectively, the gradient and debond load of a Load^2 vs fibre displacement trace. These are not affected by the above processing of discontinuities.

It may be argued that the tilt of the indentor shaft renders the fibre pushing model invalid as fibre and indentor should be aligned in the same direction. However, this is not the case as only a very small minority of fibres in a typical fibre push-down test sample will be aligned perpendicular to the surface to within a tilt angle of $\pm$ 2x10^{-4} radian.

The clamp discontinuities were not of a consistent size, hence a software algorithm to automatically remove them was not attempted as the operator's eye could do the job more efficiently.

Following the data processing steps above, the final load vs indentor displacement trace for the same example used in the previous figures, is shown in figure 4.28. The conversion of raw data, load into N and displacement into μm, is performed automatically after the discontinuities are removed, using the calibration curves for load cell and displacement gauge, see sections 4.2.2 and 4.2.4, that are incorporated into the software.

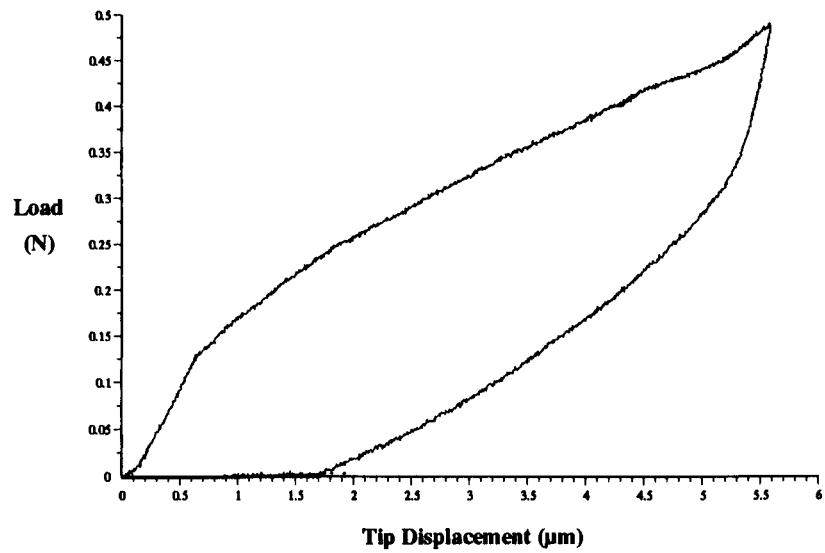

Figure 4.28 Load vs Tip displacement trace calibrated to N and μm.

CHAPTER FIVE

INTERFACE CHARACTERISATION

5.1 Determination of Interface Micromechanical Properties

As discussed in Chapter 3, the techniques of fibre push-down and push-through are currently the only ways to conveniently determine both G_i and τ for small fibre (15 μm diameter) reinforced ceramic matrix composites. Using the SEM based microindentor, these test techniques have been applied to a range of glass-ceramic and glass matrix composite systems. The basic model used in data analysis was that derived by Marshall and Oliver in their original paper describing the push-down technique [89].

The test requires the push-down of an individual fibre until it debonds from the matrix, at the interface, and then further pushing so that the interface crack progresses and the fibre slips relative to the matrix behind the crack front. The analysis for determining G_i and τ from the load / displacement data is discussed below, in the first instance for the case where $G_i = 0$ (i.e. purely frictional shear stress) and then for $G_i > 0$, a bonded fibre and matrix.

5.1.1 Frictional sliding

It is assumed that sliding occurs between the matrix and fibre wherever the shear stress parallel to the interface exceeds a constant value τ . Application of force F to the end of the fibre causes sliding that begins at the surface and extends to a depth l , see figure 5.1(a). With the approximation that only normal, axial stresses exist within the fibre and that shear stress is concentrated at the interface, equilibrium of the fibre at $z < l$ requires

$$d\sigma / dz = 2\tau / r \tag{5.1}$$

where $d\sigma$ is an incremental increase in applied stress ($d\sigma = dF/\pi r^2$), and r is the radius of the fibre. If it is assumed that for $l >> r$ the elastic stresses at $z > l$ can be neglected, then integration of equation (5.1), with the boundary conditions $\sigma(l) = 0$ and $\sigma(0) = F/\pi r^2$, gives

$$l = F / 2 \pi r \tau \tag{5.2}$$

and the strain distribution in the fibre is (see figure 5.1(a)),

$$\varepsilon(z) = (F / \pi r^2 E_f)(1 - z / l) \tag{5.3}$$

where E_f is the fibre elastic modulus in the axial direction. The displacement of the

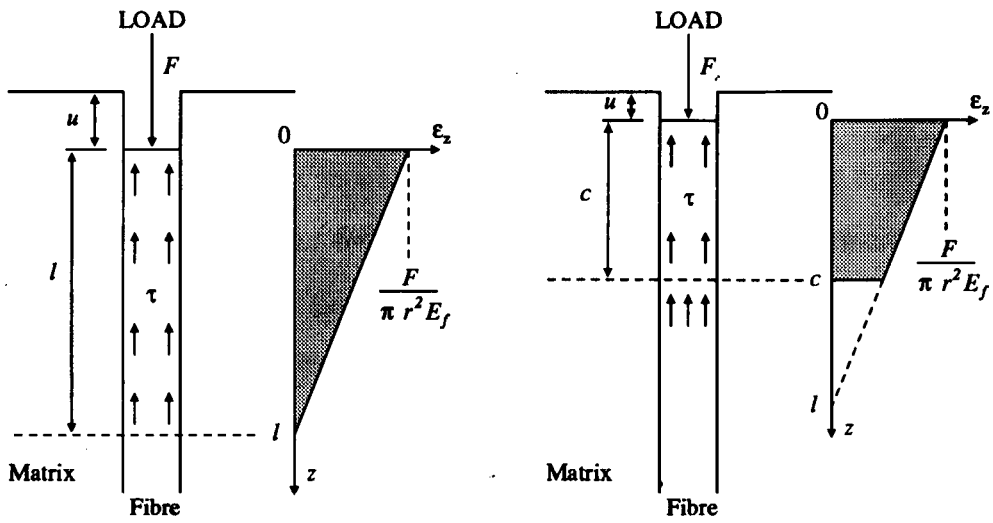

Figure 5.1 Illustration of strain distribution and debond length along the interface for (a) the purely frictional shear stress condition, and (b) the case of bonded fibre and matrix, taken from [89].

fibre surface below the the original specimen surface, obtained by integrating equation (5.3) over the range $z = 0$ to $z = l$ (i.e. the shaded area under the strain-position curve in figure 5.1(a)), is

$$u = F^2 / 4 \pi^2 r^3 \tau E_f \tag{5.4}$$

where u is the fibre surface displacement.

5.1.2 Interface debonding and frictional sliding

However, fibre sliding is generally caused by the propagation of a debonding interface crack followed by frictional sliding over the crack surfaces. In this case, sliding depth is dictated by the length of the debond crack, c, (figure 5.1(b)). For $c >> r$, the strain distribution in the region $z \leq c$ is given by equation (5.3) but the displacement of the fibre surface below the matrix is determined by integration between $z = 0$ and $z = c$, the area shaded in figure 5.1(b) ;

$$u = (F / \pi r^2 E_f) (c - c^2 / 2l) \tag{5.5}$$

and therefore evaluation of u requires knowledge of the debond length c.

This is calculated from an energy balance analysis for incremental crack growth. If the crack extends by dc at constant applied force F, then the strain energy of the specimen increases by dU_E , the potential energy of the loading system changes by dU_L , work dU_F is done against frictional forces, and there is additional energy dU_G associated with the new crack area. For a large debond crack ($c >> r$) these energy changes have been determined, in detail, in reference [89]. They have been derived for pure shear loading on the debond crack and therefore the fracture surface energy G_i below corresponds to that for pure mode 2 loading. From reference [89], the energy

change of the system is,

$$dU = dU_E + dU_L + dU_F + dU_G$$

$$= -(F^2 / 2\pi r^2 E_f)(1 - c/l)^2\, dc + 2\pi r G_i\, dc \qquad (5.6)$$

Assuming the fracture criterion $dU/dc < 0$, equation (5.6) gives,

$$(1 - c/l)^2 = 4\pi^2 r^3 G_i E_f / F^2 \qquad (5.7)$$

which expresses the equilibrium crack length in terms of the applied force and microstructural parameters. It represents stable crack growth with increasing force and therefore implies that debonding does not cause a discontinuity (load drop) in the force-displacement relationship. However, in practice, crack initiation can involve instability which is reflected by a load drop in the force-displacement trace (see section 5.2 for examples). In this case, the analysis applies only when the instability has disappeared, i.e. after the initial instability, the interface crack extends with increasing applied force to $c >> r$, and stable crack growth develops.

The fibre displacement at the surface, derived from equations (5.5) and (5.7) is,

$$u = F^2 / 4\pi^2 r^3 \tau E_f - G_i / \tau \qquad (5.8)$$

Comparing equations (5.4) and (5.8), it is observed that under combined debonding and sliding, the displacement of the fibre surface is reduced by an amount G_i / τ relative to the pure sliding condition.

Marshall and Oliver go on to determine load-displacement relationships for fibre unloading and cyclic loading. However, these have not been studied quantitatively

in this project and so are not discussed here.

For the loading of a fibre, if load and displacement of the fibre surface are measured, then equation (5.8) indicates that a plot of F^2 vs. u, i.e. applied load^2 vs. fibre surface displacement, will give a straight line relationship with the intercept on the F^2 axis giving G_i and the gradient giving τ ;

$$Intercept = F^2 \text{ at } u = 0$$
$$= 4\,\pi^2\, r^3\, E_f G_i \qquad (5.9)$$

$$Gradient = 4\,\pi^2\, r^3\, E_f\, \tau \qquad (5.10)$$

They validated their model using a nanoindentor and an LAS glass ceramic matrix, Nicalon SiC fibre reinforced material. It had a very low debond fracture surface energy of $G_i < 4\text{x}10^{-2}$ Jm^{-2} and frictional shear stress of $\tau \sim 3.5$ MPa. The low load capability of the instrument (0.12N) was therefore enough to push the fibres.

5.1.3 Push-through test

The push-through test analysis is relatively simple. The debond fracture energy is determined, as for push down, by recording the load where the interface crack initiates. On a load-displacement trace, the crack initiation is observed as a change in gradient, but with the SEM based microindentor the crack is actually seen as it nucleates and therefore that point is noted by the operator. Once the crack starts to propagate down the interface with increasing applied load, the load-displacement curve follows the same relationship as in section 5.1.2 above. However, when the crack front reaches the bottom surface of the slice of composite, a load drop appears on the load-displacement curve. This is followed by frictional slipping of the whole fibre through the slice of material. Knowing the depth d, of the slice, the average frictional shear

stress can be calculated from the simple relationship,

$$\tau = F / A \tag{5.11}$$

where A is the surface area over which frictional slip occurs and F is the average applied load after complete fibre debond from the matrix for the duration of fibre pushing. This is equivalent to,

$$\tau = F / (2 \pi r d) \tag{5.12}$$

The value for τ determined using this method is a lower bound to the true value as the actual area of fibre in contact with the interface decreases as the fibre is pushed out from the other side. For this test, a displacement controlled indentor is required as the load drop that accompanies the interface crack reaching the bottom surface would result in a load controlled device instantaneously pushing the indentor tip as far as it would go before contacting the matrix surrounding the fibre at the top surface. Displacement controlled indentation, as with the SEM based microindentor, allows controlled, stable pushing of the fibre through the matrix. The typical shape of load /

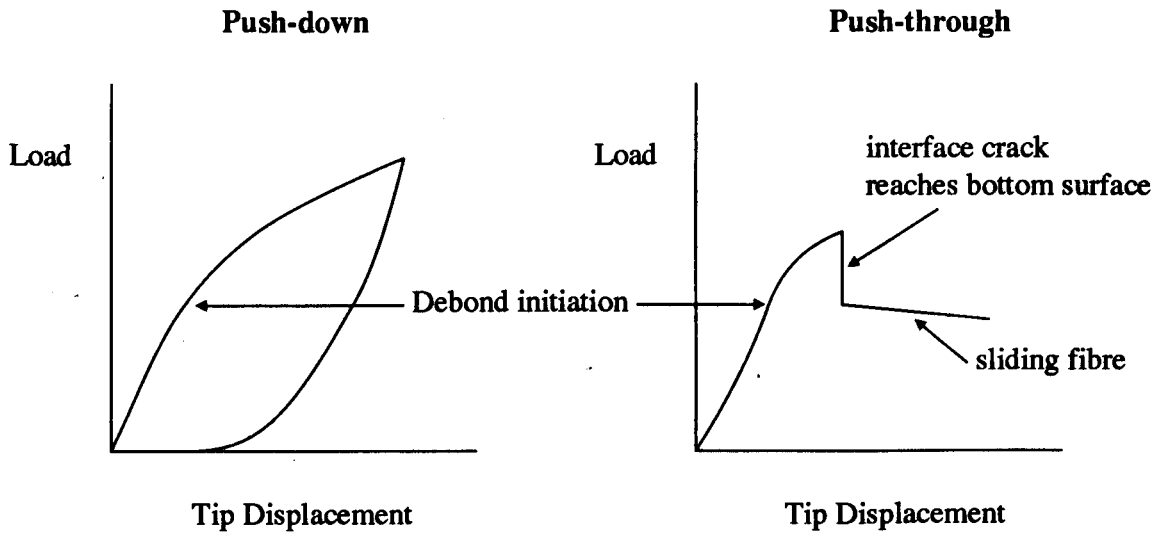

Figure 5.2 Schematic illustrations of typical load-displacement traces for fibre push-down and push-through tests.

indentor tip displacement traces for fibre push-down and push-through tests are shown schematically in figure 5.2.

5.1.4 Experimental procedure

For fibre push-down, the actual fibre displacement needs to be measured to apply the analysis of section 5.1.2. This is derived from load vs. indentor tip displacement traces by subtracting a hardness load-displacement curve recorded from an indentation of the fibre material, i.e. the indentation of a fibre that does not move, so that only the material response is recorded and not any fibre displacement.

For the Nicalon and Tyranno SiC fibres investigated here, their hardness response was determined by sectioning and polishing samples of reinforced composite parallel to the fibre direction. They were mounted in the SEM and load applied by the indentor, on the centre of a fibre, until it fractured. The recorded load-displacement trace described the plastic deformation in the fibre surface, caused by indenting with that particular geometry of diamond tip. A number of indents were performed for each

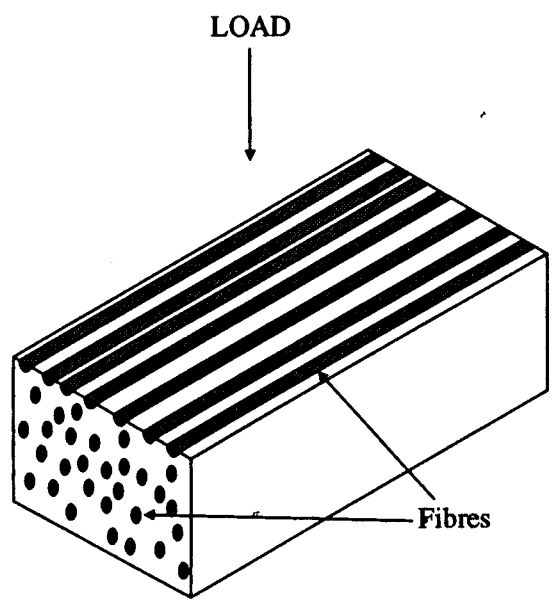

Figure 5.3 Geometry of specimen to measure hardness load-displacement property of fibre material.

fibre type, the data averaged, and a curve fitted to the resultant average trace. The fitted curve was a third order polynomial that was incorporated into data analysis software, program "THREE" (see Appendix I).

The hardness indentation is orthogonal (with respect to fibre direction) to the direction for a push-down test. As Nicalon and Tyranno are both nanocrystalline, there is no structural anisotropy that would lead to different responses for the different indentation directions. If significant structural changes were to occur for different processing and thermal treatments, the hardness response would be expected to change. However, no such effect was noticed in the current work.

Figure 5.4(a) shows the hardness response, for loading only, of an indentation into a Nicalon fibre that was housed in a CAS glass ceramic matrix. The fitted curve is shown and in figure 5.4(b) the difference between actual and fitted curve is plotted to show that at no point was the difference between the two more than ±0.008N for a particular displacement.

Subtracting this load-displacement trace from the data of a fibre push-down test (using the same fibre type and diamond indentor tip) takes into account the extra tip displacement beneath the fibre surface caused by the plastic deformation of the fibre surface, i.e. the conical dimple produced in figure 4.23(d). The resulting trace is the applied load vs. fibre displacement, the data required for application of the Marshall and Oliver model outlined above.

To illustrate, the above procedure and application of the Marshall and Oliver model is performed on the data used in section 4.4.2. The fitted Nicalon hardness curve of figure 5.4 is subtracted from the load-displacement data shown in figure 4.28. This is done by subtracting for the equivalent load values on each curve, the hardness tip displacement from the corresponding push-down tip displacement. This is performed by the software of programme "THREE" and results in data that represents load vs. actual fibre displacement. When the square of load is then plotted against the fibre displacement, as Marshall and Oliver suggest, a straight line relationship exists, the

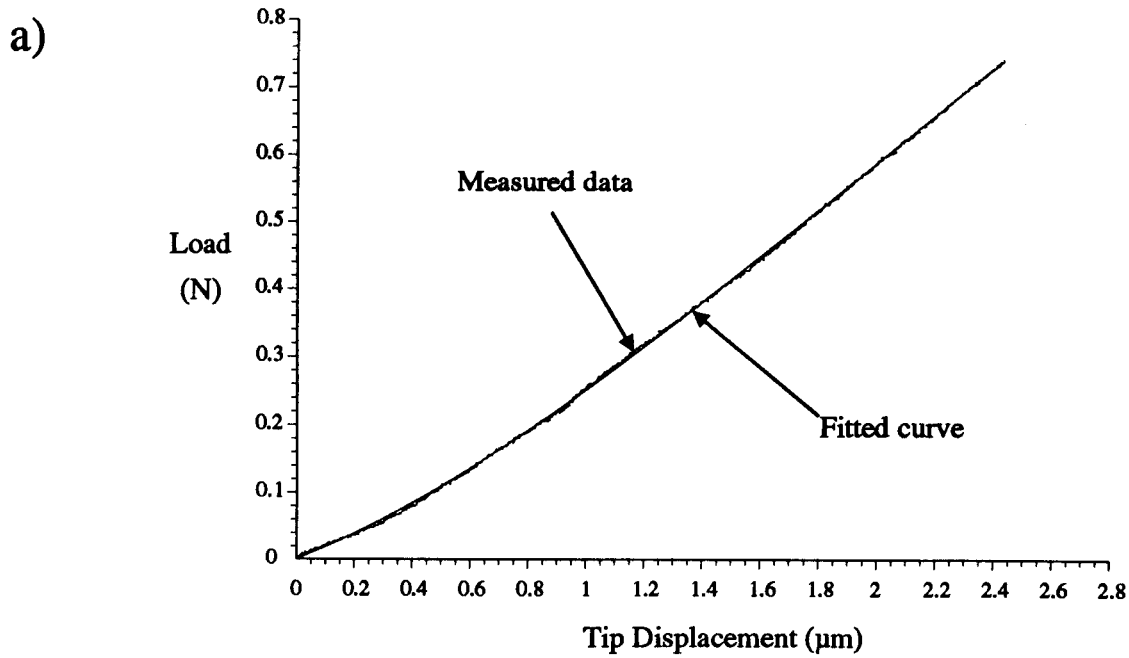

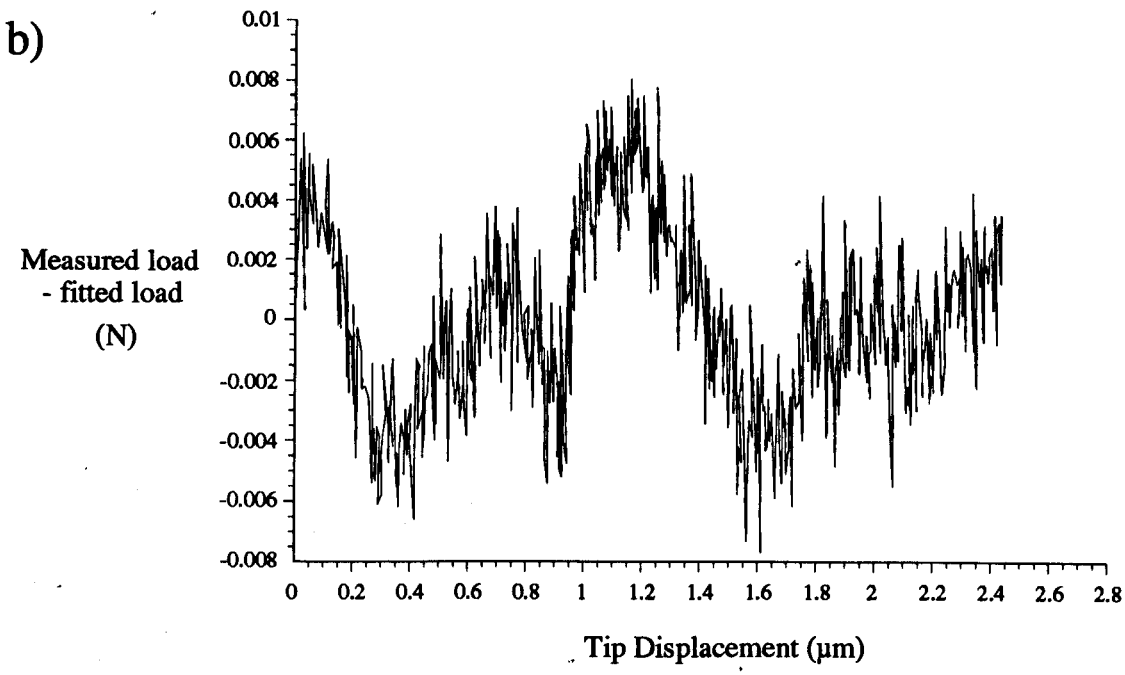

Figure 5.4 (a) Load / tip displacement relationship for the indentation of Nicalon fibre with third order polynomial fitted curve superimposed, and (b) Plot of the difference between measured load data and fitted load curve vs. tip displacement.

intercept and gradient of which are used to determine G_i and τ. The resultant straight line is shown in figure 5.5, the y-axis is shifted back 0.5 μm to illustrate that the fibre does not move until a certain load is applied to initiate debonding, i.e. to clearly illustrate the intercept behaviour. Note that the fibre was pushed over 3.5μm before the diamond tip touched the matrix surrounding the fibre (evidenced by the up-turn in the trace and deviation from straight line behaviour). This large displacement is not possible using an obtuse Vickers diamond. For this 13.2 μm diameter Nicalon fibre, G_i = 8.0 ± 0.4 Jm^{-2} and τ = 24 ± 0.4 MPa. (G_i and τ are determined using mouse controlled software, within program "THREE", to locate and calculate the relevant intercept and gradient).

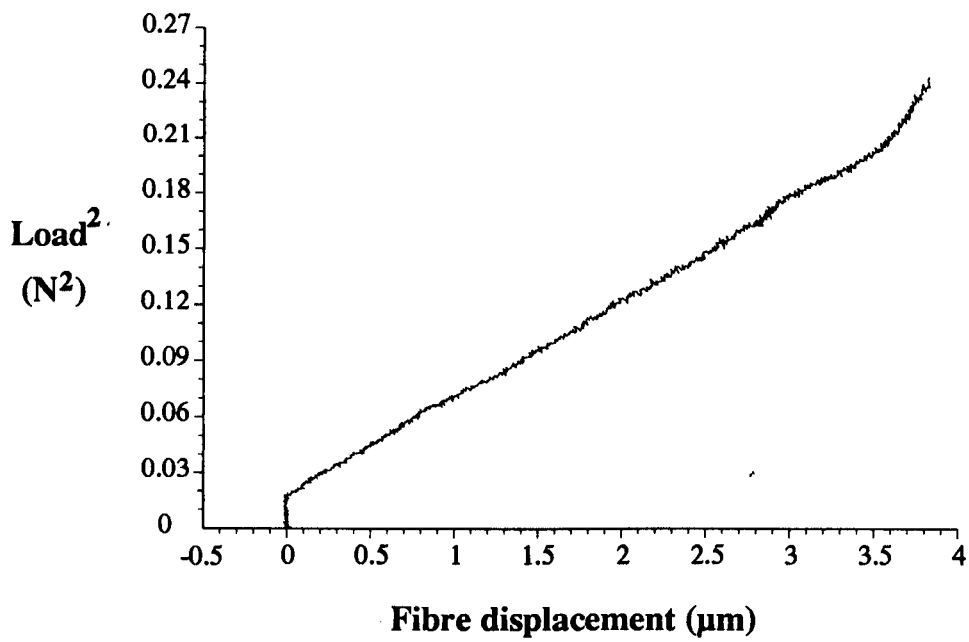

Figure 5.5 Load^2 vs. Fibre displacement relationship for fibre push down from original data shown in figure 4.28. Shows straight line relationship predicted by Marshall and Oliver [89].

For each sample, a minimum of 10 fibres would be pushed to obtain a mean and standard deviation for G_i and τ . For fibre push-down tests, the samples were cut to a depth of at least 5mm. This was to make the samples so deep that interface cracks were unable to extend to the bottom surface, rendering the test invalid. In Nicalon or

Tyranno fibre reinforced material, the maximum debonded lengths possible were of the order 1mm long. For example, using equation (5.2) above and ignoring the interface bonding in the example of figure 5.5, a maximum applied load of 0.45N (square root of $0.2N^2$) and τ of 24MPa would produce a maximum interface sliding length of 450μm. This is approximately 1/10 the depth of the specimen.

5.2 Glass Ceramic Matrix Composites

As discussed in Chapter 2, glass ceramic matrix composites show great potential for the production of tough engineering components. The interfacial micromechanical properties, for a large range of these materials, have been measured with the SEM based microindentor. They were subjected to processing variables, interface modification and pre-synthesis, heat treatments at high temperatures and in oxidising atmospheres, and fatigue load testing. The effects of these procedures on the interface micromechanical behaviour are discussed below.

5.2.1 As processed glass ceramic matrix composites

The procedure for manufacturing fibre reinforced glass ceramic matrix tiles has been outlined in Chapter 2. Although details vary from material to material, such as additional heat treatments after hot pressing to maximise the density of crystalline phases, it is essentially the same for each. From Table 2.1 it is evident that the thermal expansion properties and maximum operating temperature of each vary considerably.

One of the major objectives in using glass ceramic matrices is the reduction of processing temperatures by choosing individual system compositions that lie near a eutectic. Another aim is the tailoring of the matrix thermal expansion coefficient to lower than, near to, or greater than that of the reinforcing fibre. This versatility has been investigated in a parallel project with the aim of optimising mechanical properties

of CAS and MAS glass ceramic matrix composites [110].

In the present study, a range of 6 glass and glass ceramic matrix composites were investigated ;

CAS (Calcium aluminosilicate) reinforced with Nicalon,

MAS (Magnesium aluminosilicate) reinforced with Nicalon,

LAS (Lithium aluminosilicate) reinforced with Nicalon,

BAS (Barium aluminosilicate) reinforced with Nicalon,

BMAS (Barium-Magnesium aluminosilicate) reinforced with Tyranno,

Borosilicate glass reinforced with Nicalon.

The composites were obtained from various sources. The CAS/Nicalon was manufactured by Corning, USA, the BMAS/Tyranno was supplied by AEA Technology, Harwell, UK, one MAS/Nicalon material was produced by Pilkington, UK, and other MAS/Nicalon based CMCs were produced by Rolls Royce plc and by developmental programmes within the Centre for Advanced Materials Technology, Warwick. The LAS and BAS materials were produced at Warwick.

Nicalon and Tyranno SiC fibre reinforced glass ceramic matrices are known, as discussed in Chapter 2, to develop carbon rich interfaces during manufacture. The exact composition and size of interfacial layer varies from system to system. The basic formation of carbon at the interface follows the reaction, $SiC + O_2 \rightarrow SiO_2 + C$, (equation 2.30), but may be supplemented by the indirect path,

$$SiC + CO \rightarrow SiO_2 + 3C \qquad (5.13)$$

following carbon oxidation. Both these reactions are influenced by oxygen content and matrix chemistry, as the thermodynamic activity of SiO_2 depends on the degree of structural polymerisation in the silicate which in turn is controlled by the metallic ion concentration and valency (Li^+, Mg^{2+}, Ca^{2+}, Ba^{2+}). The reaction rates are believed to be controlled by diffusion of O_2 and CO through the carbon-rich layer which comprises

a phase mixture of C + SiO_2. The carbon exists as a precipitated amorphous phase at lower processing temperatures but in the graphitic state at processing temperatures >1200°C [64,75,77,78].

Fabrication temperature also plays an important role in interface development kinetics. This is illustrated by higher hot pressing temperatures producing wider interface layers of C + SiO_2 [75]. Carbon precipitation is preceded by a band of cross diffusion within the fibre, producing a change in phase contrast structure that is detectable within the Transmission Electron Microscope (TEM). The ranges of interface and diffusion layer size commonly observed in glass ceramic matrix systems are illustrated in references [64,75,77,78,95]. The carbon rich layer can vary from approximately 300 nm wide in Nicalon/BAS (that is hot pressed at > 1200°C), to less than 20 nm wide in a Nicalon/Borosilicate glass composite, processed at a lower temperature. The cross-diffusion layer is also wider with higher fabrication temperatures.

With the Tyranno reinforced materials, there is evidence of TiC precipitating within the carbon rich interfacial layer, as a result of the titanium present in the fibre [77,78].

The interfacial micromechanical parameters of the as processed glass-ceramic matrix composites, have been measured using the SEM based microindentor. The results are detailed in Table 5.1.

The fibre push-down response varied considerably across the range of composites tested. Not only were there large differences in the quantitative measurements taken, but also in the nature of respective load vs. displacement traces. To illustrate the extremes of behaviour, the data is compared for LAS/Nicalon, CAS/ Nicalon and MAS/Nicalon (Warwick). They cover the range of behaviour between low G_i and τ to high G_i and τ . Figure 5.6 has typical examples of the load vs. indentor displacement traces recorded for (a) LAS/Nicalon, (b) CAS/Nicalon and (c) MAS/ Nicalon (Warwick). The LAS material has a very low debond load that is hardly

Composite	G_i (Jm^{-2})	τ (MPa)
CAS / Nicalon	5 ± 1	24 ± 2
LAS / Nicalon	2.0 ± 0.8	15 ± 10
BAS / Nicalon	6.0 ± 5.4	99 ± 85
MAS / Nicalon (Warwick / RR)	30 ± 7	239 ± 150
MAS / Nicalon (Pilkington)	1.4 ± 1.6	25 ± 9
BMAS / Tyranno	1.2 ± 1.6	25 ± 7

Table 5.1 Interfacial debond fracture surface energies G_i and frictional shear stress τ for various, as processed, SiC fibre reinforced glass ceramic systems.

distinguishable and low frictional shear stress exemplified by the low loads required for appreciable indentor displacement. Debond and crack growth was stable and so resulted in a continuous curve. CAS/Nicalon had moderate G_i and τ properties that resulted in a continuous curve with higher load at a definite fibre debond and higher loads applied for comparable indentor displacement. The MAS matrix material required a large load to cause debonding of fibre and matrix. This event was sudden and caused rapid and unstable fibre movement and interface crack growth, that was observed visually with the SEM and recorded by the load drop in the load vs. displacement trace. Instability continued as further load was applied, but as the interface crack extended further beneath the specimen surface, the response stabilised, see figure 5.6 (c).

Determination of G_i and τ using the procedure described in section 5.1, required load^2 vs. fibre displacement plotted for the push-down responses. These are shown in figure 5.7, where the examples for the MAS, CAS and LAS push-down

(a) LAS/Nicalon

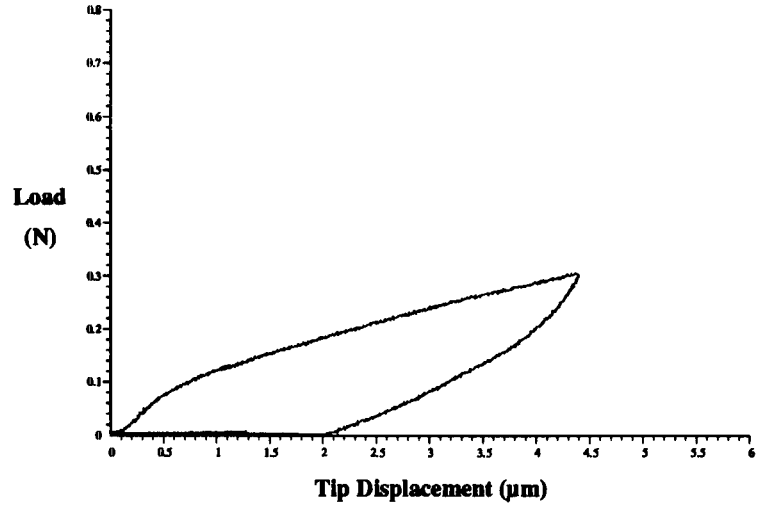

(b) CAS/Nicalon

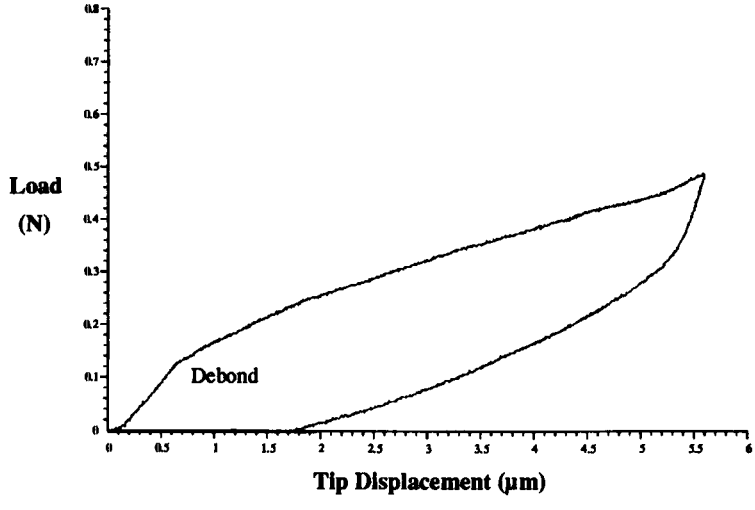

(c) MAS/Nicalon (Warwick)

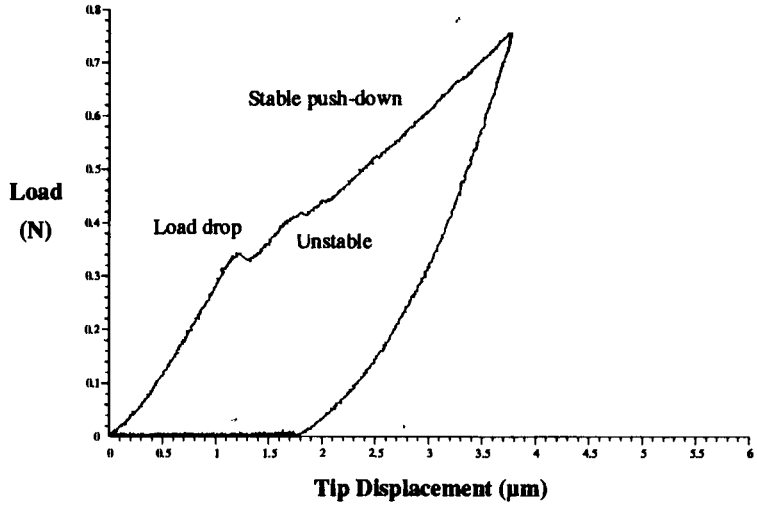

Figure 5.6 Load vs. Tip displacement traces recorded for fibre push-down tests on a) LAS/Nicalon, b) CAS/Nicalon and c) MAS/Nicalon (Warwick). The sudden and unstable debond in the MAS material is illustrated by a load drop.

behaviour are plotted on the same graph to illustrate their differences. The G_i and τ for each particular trace are given (determined by recording debond load and straight line gradient). The diameters of the fibres pushed down in the above examples were similar, i.e. 15.3 μm (MAS), 13.2 μm (CAS) and 14.0 μm (LAS), so their curves can be compared on the same axis.

As can be seen, the MAS material does not follow the straight line model immediately after fibre debond, there is a load drop and unstable crack growth. The gradient that was measured was that of the straight line behaviour that developed at higher applied loads, after the instability in crack growth had disappeared. The Marshall and Oliver model was derived for stable, incremental crack growth with increasing load and assumed that the interface crack length was very much greater than the fibre radius ($c >> r$, see section 5.1, equations 5.6, 5.7, 5.8). The MAS curve tending to a straight line at high applied load, indicates that as the interface crack extends, so that $c >> r$, stable growth develops and the Marshall and Oliver model

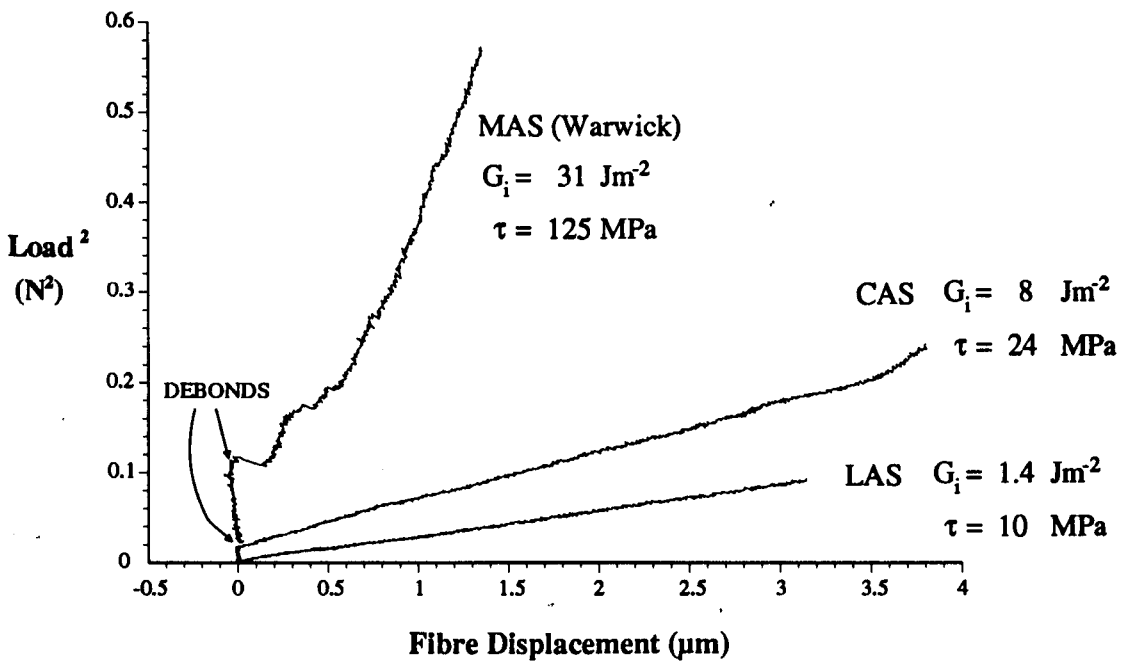

Figure 5.7 Load² vs. Fibre displacement, for increasing load, of the fibre push-down tests in figure 5.6. Note how they obey the straight line relationship predicted by the Marshall and Oliver model [89].

becomes applicable.

All interfaces that had a low debond fracture surface energy (approximately $G_i < 15$ Jm^{-2}) behaved as in figure 5.6 (a) and (b). More strongly bonded interfaces resulted in a crack growth instability and load drop on debond, as in figure 5.6(c).

Looking at Table 5.1, the standard deviations in the mean G_i reported for all but the CAS/Nicalon and MAS/Nicalon(Warwick) CMCs, are greater than or approaching 100% that of the mean. This large scatter is the result of two factors ;

i) In the cases of the BAS, MAS(Pilkington) and BMAS materials, matrix cracks present in the material after fabrication have originated from, or intercepted with, a high proportion of the fibre-matrix interfaces and caused debonding of the interfaces. Thus $G_i = 0$ Jm^{-2} was measured for many of the pushed fibres as there was no interface bond that had to be broken. However a minority of the pushed fibres were not previously debonded and therefore a mean value of $G_i > 0$ Jm^{-2} was derived and accompanied by a large error. The MAS(Pilkington) material was also very porous and this contributed to the low G_i values that were measured. Figure 5.8 shows the presence of the cracks in BAS/Nicalon [111]. There are two cases where the multiphase matrix structure can cause matrix cracking; i) if the different phases have appreciable coefficient of thermal expansion mismatches, then residual stresses developed on cool down from hot pressing may be too great for the matrix to sustain, and ii) if the overall coefficient of thermal expansion for the multiphase matrix is appreciably higher than that of the reinforcing fibres, radial matrix cracking, centered around the fibres, can occur on cool down. An alternative cause is damage from the cutting, grinding and polishing processes used for specimen preparation. However, this is unlikely as the mechanical testing of these materials [113] showed them to be particularly weak, indicating that a large proportion of the bulk material is affected by cracking and porosity.

ii) The LAS/Nicalon composite was the only one in which the matrix thermal expansion coefficient was lower than that of the fibre. Thus on cool down after

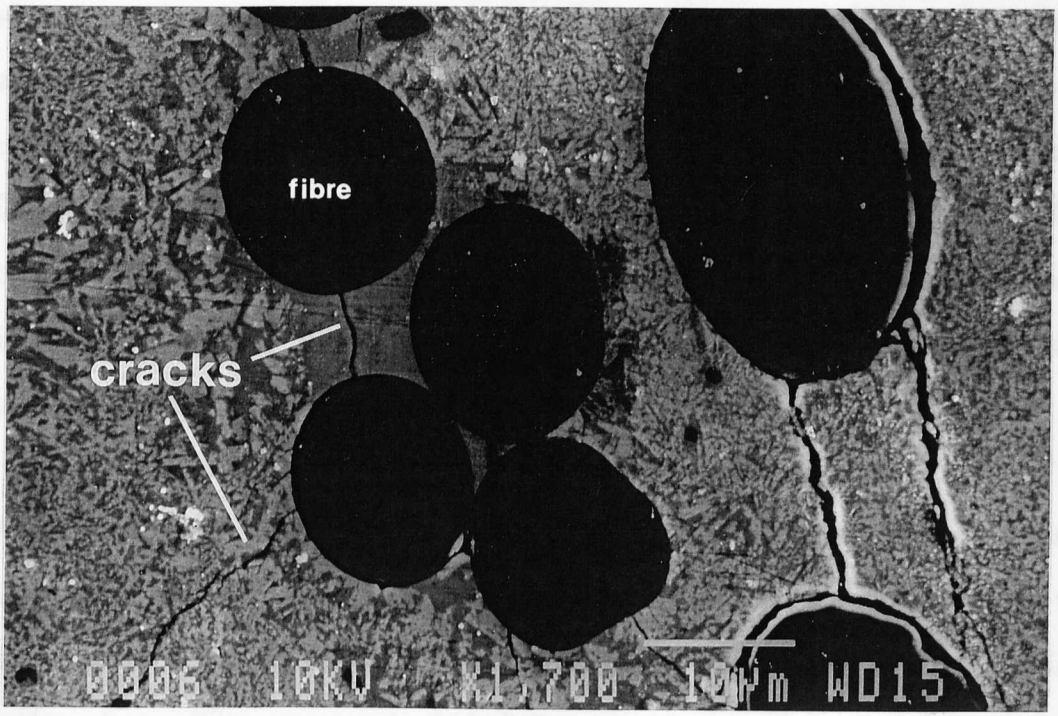

Figure 5.8 SEM micrograph (Back Scattered Electron mode) of the BAS/Nicalon CMC, illustrating matrix cracks impinging with interfaces and causing debonding.

hot pressing, the fibres shrink and pull away from the surrounding matrix, spontaneously debonding the interface. This is illustrated in the push-down data by the low loads that were required to move the fibres. On the load^2 vs. fibre displacement traces it was difficult to determine the load at which debond, if any, occurred and this resulted in a large standard deviation in the mean debond energy reported. A low frictional shear stress τ, again with large standard deviation, is measured because of the presence of gaps at some, but not all, of the fibre-matrix interfaces that were tested. SEM imaging during fibre push down indicated that these gaps were visible, but on preparation of thin slices of material for TEM investigation (cut to 400µm and grinding and polishing to 100µm thick), the specimens degenerated and broke up, thus preventing a TEM study. The negligible bonding and gaps between fibres and matrix

therefore result in a very weak composite, although it must be stated that the cutting and grinding actions may well damage the interfaces further. The LAS/Nicalon material is not that produced by Corning and documented in much of the literature [e.g.29,31,72,73]. It was made at Warwick [112] and reinforced with a grade of Nicalon fibre that was pre-coated with carbon (Nicalon NL-607) to alter the final interfacial characteristics. The measurements made here with the SEM based microindentor are not directly comparable to those for LAS/Nicalon published elsewhere, i.e. $G_i < 4x10^{-2}$ Jm^{-2}, $\tau = 2$ MPa [89].

The most consistently measured interface parameters were those of the CAS/Nicalon composite supplied by Corning. Work was performed on four batches of this material and, with regard to G_i and τ, a relatively high degree of consistency was found between them. For material from other suppliers however, particularly the MAS/ Nicalon from Pilkington and BMAS/Tyranno from AEA Technology, large inconsistencies were found from batch to batch, particularly with regard to more fundamental properties such as porosity [113,114].

The CAS/Nicalon interface structure has a continuous carbon rich layer between fibre and matrix that is approximately 150nm thick [75,95]. BAS/Nicalon has a layer of graphitic crystallites within silica forming a 200nm wide interface [111] and the BMAS/Tyranno composite has a typically 20nm thick, carbon rich interface [113,114]. The carbon rich interfaces of CAS and BMAS give low frictional shear stresses of τ ~25 MPa. The SiO_2 + C phase mixture interface in BAS/Nicalon has a high τ ~ 99 MPa. Thus, when the interphase is a continuous layer of carbon, its thickness does not have a significant effect on τ. The graphitic nature of carbon in CAS/Nicalon suggests the Van der Waals bonding of the graphitic layers does help bestow the low τ that was measured, as the carbon and silica phase mixture interface of BAS/Nicalon had a significantly higher τ. The carbon interfaces also produce more consistent interface frictional shear properties (see Table 5.1).

The many matrix cracks present in the BAS/Nicalon and BMAS/Tyranno

materials confuse the measured data for G_i, for the reason stated above. However, the higher mean G_i = 6 Jm^{-2} for BAS/Nicalon, compared to G_i ~ 1 Jm^{-2} for BMAS/ Tyranno, suggests that those fibres tested that were not previously debonded by matrix cracking, were more strongly bonded to the BAS matrix than the BMAS, i.e. the carbon/silica mixture interface had a higher debond fracture surface energy than the carbon rich interface.

The matrix cracks present in a number of the materials prevent the quantitative observation of a relationship between fibre-matrix thermal expansion mismatch and G_i and τ. However, two examples of it effects are discussed later in section 6.2.1.

5.2.2 Heat treatment of glass ceramic matrix composites

In the gas turbine application for which these glass ceramic matrix composites are being developed, normal operating conditions will be temperatures in excess of 1100°C in aggressive, oxidising environments. The CMCs must retain their mechanical properties under such conditions. However, the Nicalon or Tyranno fibre reinforced glass ceramic matrix composites are known to suffer from thermochemical reactions at elevated temperatures that can seriously degrade their performance [30,76,79,80].

5.2.2.1 Interface modification under oxidising conditions

The major thermochemical effect on glass ceramic matrix composites under oxidising conditions occurs at the interface. At temperatures greater than about 400°C, carbon, in the presence of oxygen, oxidises to gaseous products following either of the reactions;

$$C_{(s)} + O_{2\,(g)} \rightarrow CO_{2\,(g)} \quad (5.13)$$

$$2C_{(s)} + O_{2\,(g)} \rightarrow 2CO_{(g)} \quad (5.14)$$

Thus if oxygen can reach the carbon rich interfaces in these composites, they will be removed at elevated temperatures. There are two diffusion pathways for oxygen, through the matrix and 'channelled' along the interface itself. At higher temperatures (greater than 800°C), oxidation of the exposed SiC fibre surface can occur to produce a SiO_2 surface layer via ;

$$SiC_{(s)} + 2O_{2\,(g)} \rightarrow SiO_{2\,(s,l)} + CO_{2\,(g)} \quad (5.15)$$

Heat treatment experiments have shown with LAS/Nicalon that the above reactions take place at temperatures up to 1100°C [30,76,79,80]. A SiO_2 interphase forms across the gap left by the removed carbon and bonds the fibre to the matrix. This high G_i interface results in the composite becoming brittle.

In collaboration with another ongoing project at Warwick [113], the behaviour of other glass ceramic matrix composites after heat treatment have been studied. A range of heat treatments were applied to samples of CAS/Nicalon (from Corning) and BMAS/Tyranno (from AEA Technology), their interface characteristics measured and mechanical properties determined.

Specimens of unidirectionally reinforced material, approximately 50mm x 3mm x 3mm, were cut, using a diamond saw, from the composite tiles. Batches of three were placed into a furnace, already at temperature, for 100 hours. The temperatures were 450°C, 600°C, 700°C, 750°C, 800°C, 900°C, 1000°C, 1100°C, 1200°C, and the furnace atmosphere was air. Room temperature flexure testing was performed with three point bend apparatus [113]. Interfacial shear properties were measured after each treatment, on a specimen prepared by cross sectioning the centre of a bar not used for

bend testing.

G_i and τ determined from fibre push-down tests and the ultimate bend strengths for both composites across the range of heat treatments, are shown in figures 5.9 and 5.10.

There is a correspondence between the degradation in ultimate strength with increases in interface fracture surface energy and frictional shear stress. In the case of the BMAS/Tyranno CMC (figure 5.9), the correlation between the changes in properties is clear. A fall in bend strength centered around the 700°C heat treatment temperature corresponds to very large increases in G_i and τ that are also centered around 700°C. For CAS/Nicalon, the corresponding maxima and minima are not in such good agreement, but do follow the same approximate trend. In both cases, all the higher strength materials showed graceful, composite like failure under three point bend test (as in figure 2.2(b)), but the specimens subjected to intermediate temperature heat treatments (600°C-800°C) were brittle and weak.

TEM investigations by K. P. Plucknett (BMAS / Tyranno) [115] and M. W. Pharaoh (CAS / Nicalon) [95,75] have shown both interfaces as having very similar structures after similar heat treatments. In the as-fabricated composites, the interfaces are both carbon rich, although their widths are different ; 150 nm for CAS, 20 nm for BMAS. At temperatures 600°C - 800°C, the interface is carbon free and locally bridged along its length by silica, SiO_2. High heat treatment temperatures, 900°C - 1200°C, result in the retention of the carbon rich interphase.

Thus changes in the measured micromechanical response of the interfaces can be explained. The carbon rich interphase that is present in the as-manufactured and the 1000°C and 1200°C heat treated materials produce a low τ and low G_i interface. However, between 600°C and 900°C, the removal of this phase and replacement by silica bridges across the interface, alters the micromechanical behaviour to one with a high level of bonding. High frictional τ is measured due to the shear of SiO_2 asperities (formed on the fibre surface) with the matrix, or from debond debris lodging in any

a) Debond energy BMAS/Tyranno

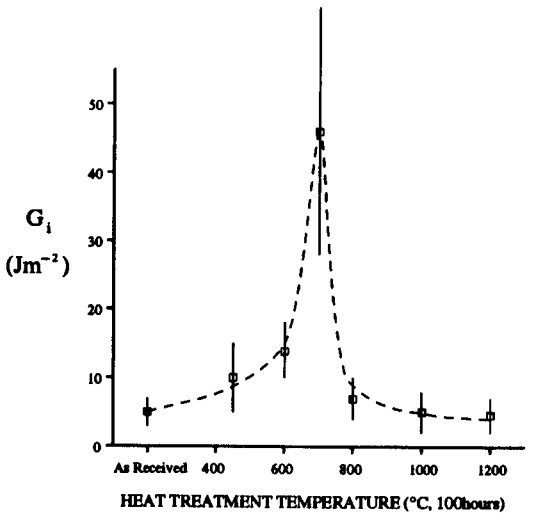

b) Frictional shear BMAS/Tyranno

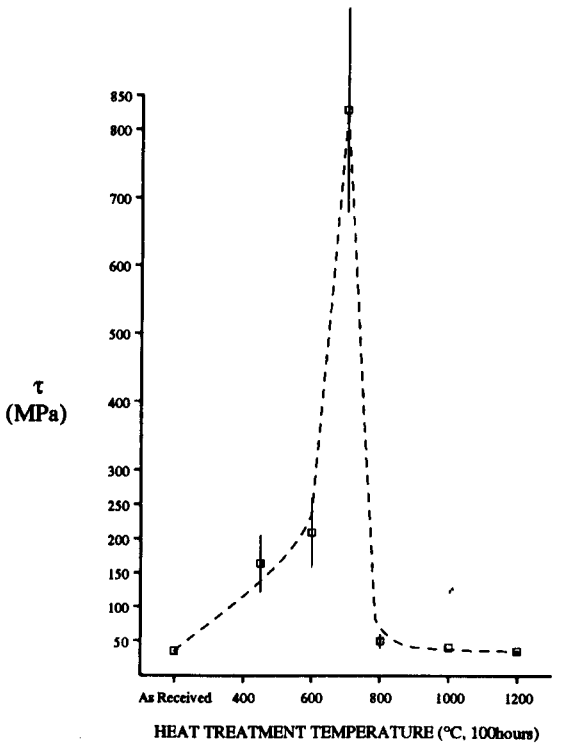

c) Three point bend BMAS/Tyranno

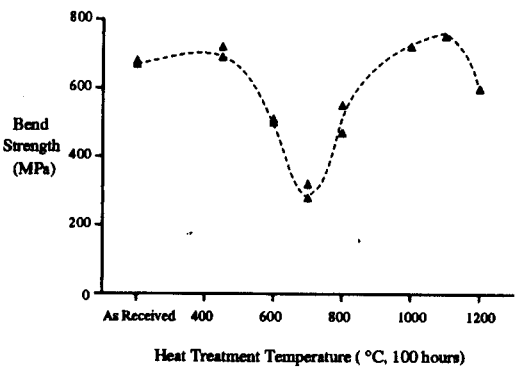

Figure 5.9 BMAS/Tyranno interfacial and mechanical data of heat treated specimens; a) interface debond fracture surface energy, b) interface frictional shear stress, and c) three point bend test ultimate strengths.

a) Debond energy CAS/Nicalon

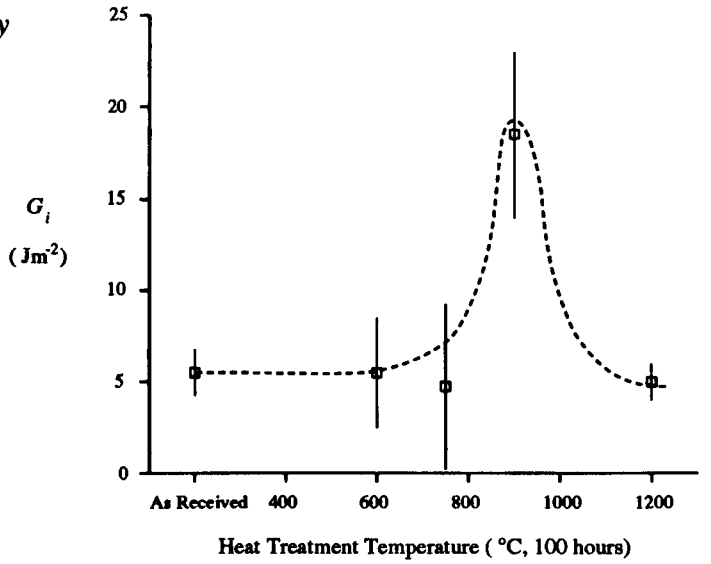

b) Frictional shear CAS/Nicalon

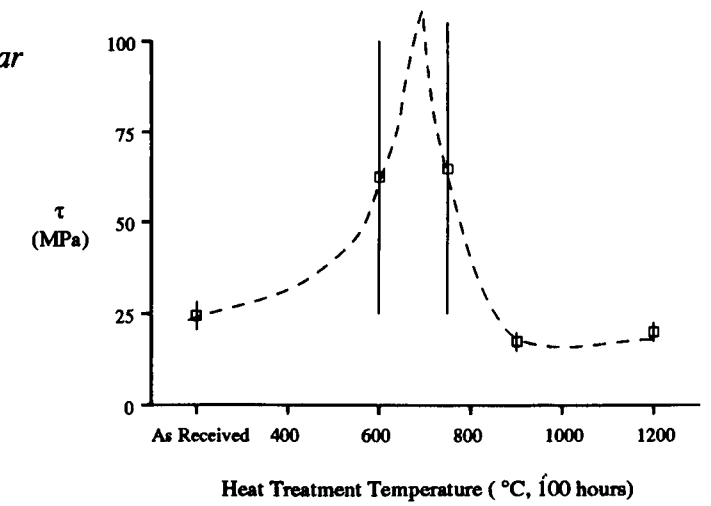

c) Three point bend CAS/Nicalon

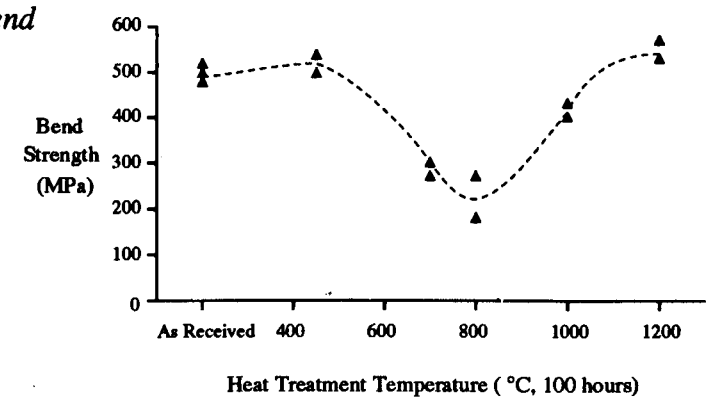

Figure 5.10 CAS / Nicalon interfacial and mechanical data of heat treated specimens; a) interface debond fracture surface energy, b) interface frictional shear stress, and c) three point bend test ultimate strengths.

interface gaps.

In order to understand the formation of these structural changes, the dominant, atmosphere to interface, oxygen diffusion path has to be identified. As stated above this can be either through the matrix from an exterior surface, or 'channelled' along the interface itself, from a fibre end exposed to the atmosphere. In work performed at Warwick [95], cross sections of a CAS/Nicalon test bar that had been heat treated at 1200°C for 100 hours in air, were studied in the SEM. It was observed that within 2 or 3 fibre diameters of the surface (approximately 40μm) the interfaces were silica rich and carbon deficient, indicating oxygen had been present to remove the carbon and form full silica bridges across the interfaces. Further in from the surface however, the carbon interphase remained, indicating that no oxygen had diffused to those depths. Thus it was concluded that oxygen diffusion through the matrix only penetrated approximately 40μm over the temperature and time scales investigated. For interfaces to be affected that were 25mm along from the end of a test bar, and 1.5mm in from the surface, the oxygen must diffuse along the interfaces from exposed fibre ends.

At the intermediate temperatures 600°C - 800°C, the carbon is removed rapidly via reactions (5.13) and (5.14), by oxygen that penetrates the bulk of the material by diffusing down the interface gaps left by the carbon removal. Fibre oxidation, forming SiO_2, then takes place very slowly along the whole length of the interface. Localised areas of silica bridging appear, bonding fibre to matrix.

High temperature heat treated specimens retain the carbon interface because the SiO_2 formation is so rapid at the higher temperatures that once carbon is removed from an interface free end, the gap is quickly plugged by growth of silica, preventing further oxygen transport and therefore carbon removal down the interface. This silica 'plug' is illustrated in reference [95]. For CAS/Nicalon treated at 1200°C, its length was no more than 50μm.

The localised 'pinning' or 'bridging' of the interface at intermediate temperatures has also been detected in TEM studies of CVI fabricated SiC-SiC

composites [116]. Its non-uniform nature accounts for the large standard deviation in the mean values reported for G_i and τ for both BMAS and CAS materials (see figures 5.9, 5.10). Also, for the 750°C heat treated CAS/Nicalon, the debonding of the fibre in the push-down test was not always accompanied by a clean break around the interface. As illustrated by the SEM micrograph in figure 5.11, the fibre often fractured in preference to a well bonded area of interface. An example of clean interface fracture is shown in figure 4.23. A final illustration of the inconsistent properties of the intermediate temperature interfaces comes from push-through tests performed with the indentor prior to the development of its capacitance displacement gauge. Figure 5.12(a) shows a typical load vs. time trace for a push-through test on as-fabricated CAS/

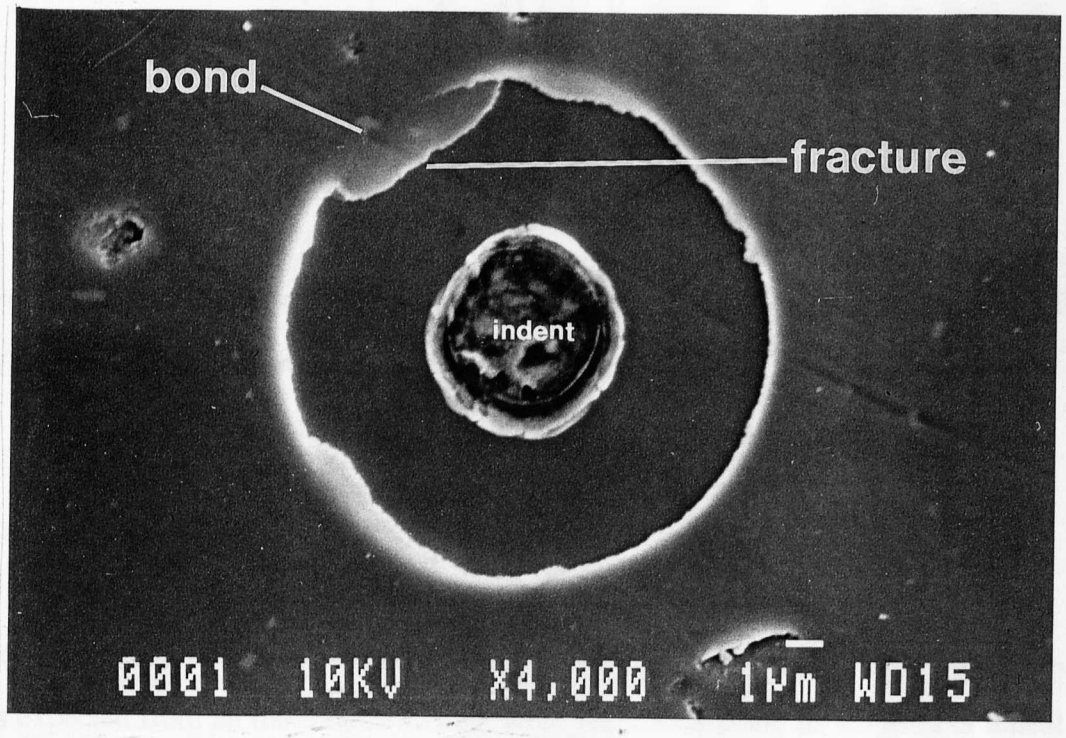

Figure 5.11 SEM micrograph of Nicalon fibre that has been pushed down in a CAS matrix composite after heat treatment in air at 750°C for 100 hours. Localised silica bridging at the interface causes the fibre to fracture and not the interface.

a) As fabricated CAS/Nicalon

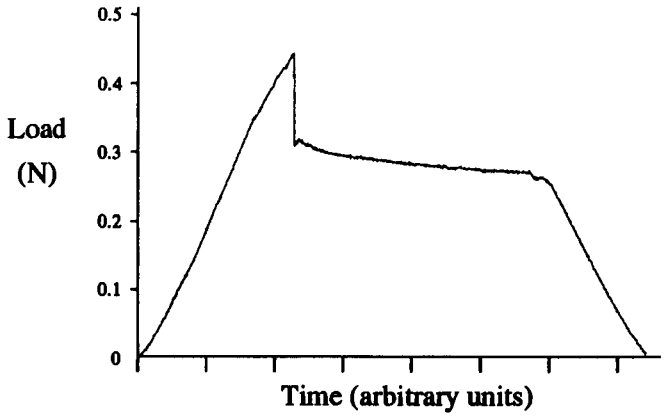

b) 750°C, 100 hrs CAS/Nicalon

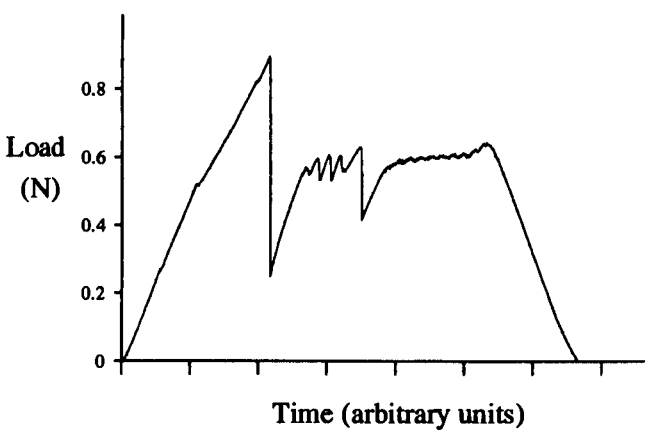

Figure 5.12 Load vs. time traces for push through tests on Nicalon fibre in CAS matrix for (a) the as-fabricated material and (b) heat treated at 750°C for 100 hours in air. The irregular interface consisting of silica bridges and gaps produces a non-continuous, irregular trace in (b).

Nicalon. It has the continuous response, as the fibre is pushed through the thin slice, that is expected from an interface with consistent properties along its length. For a heat treated specimen (750°C), the trace is very irregular, see figure 5.12(b), indicating that the fibre is pushed against an irregular interface formed by thermochemical reaction i.e. localised gaps and silica bridges.

5.2.2.2 Fibre strength degradation

The serious weakening of the composites at the intermediate heat treatment temperatures can only partially be attributed to the change in interfacial properties. The rise in G_i and τ certainly do contribute to the brittleness of the materials, but such a large reduction in ultimate strength is almost certainly dominated by fibre strength degradation within the matrix. The oxidation of the fibre surface that occurs at 600°C-800°C, can considerably weaken the fibre as a whole, due to the development of flaws on the surface. As is indicated in Chapter 2 (equations (2.20), (2.26)), ultimate composite tensile strength is heavily dependent on the strength and statistical distribution of strength, of the reinforcement. Thus any fibre degradation during heat treatment (or during processing, as is discussed later), will cause weakening of the composite.

5.2.3 Interface pre-synthesis via fibre coating

As outlined in section 2.2.4, coatings can be applied to fibres prior to incorporation within a matrix to develop a final fibre-matrix interface with favourable properties. The particular requirements of any coating would be to produce an optimum value for G_i and τ, protect the interface from thermochemical degradation during processing and operation, and if there is a large thermal expansion mismatch between matrix and fibre, to have an intermediate coefficient of thermal expansion to reduce residual stress across the interface. Single coatings cannot perform all three tasks, it may be necessary to deposit two or more on top of each other.

Two types of coated Nicalon fibre have been incorporated within matrices and their effect on interfacial micromechanics investigated.

5.2.3.1 Chemical Vapour Deposition of bi-layer interface

Standard Nicalon fibre was coated with ~1μm thick layers of nanocrystalline silicon carbide on top of carbon by Chemical Vapour Deposition (CVD). For experimental details see reference [117]; material preparation and structural characterisation was performed by M.G.Cain. The deposited carbon was to act as the low G_i and τ interface and the SiC to protect that interface from oxidation during composite fabrication and any subsequent heat treatment. Graphitic carbon is considered an ideal Van der Waals type, low cohesion, low sliding resistance interface and crystalline SiC an ideal oxidation barrier due to its inherent low oxygen mobility. Hot-pressed MAS matrix composites were successfully fabricated with little or no mechanical or chemical damage to the fibres and coatings - the SiC protected the carbon.

The micromechanical properties of the bi-layer interface were measured as having a very high interface fracture toughness, $G_i = 64 \pm 14$ Jm^{-2} , but only a moderate frictional shear stress, $\tau = 57 \pm 27$ MPa. The load^2 vs. fibre displacement response curve is shown in figure 5.13 together with that for the CAS/Nicalon as-fabricated example used above (see figures 5.6(b), 5.7). Debond is sudden and followed by rapid fibre displacement with slight load drop. Fibre slip is stable, unlike that of the MAS/Nicalon example in figure 5.7. This is due to the debond crack extending almost immediately to a length c far greater than that of the fibre radius r (so $c >> r$), resulting in stable fibre slipping as predicted by Marshall and Oliver [89].

In almost all tests, the fibres debonded from the matrix at the C-layer / SiC-layer interface. Figure 5.14(a) shows a typical fibre after it has been pushed. The large indent in the centre is indicative of the high load that was applied in order to achieve debond. The two fibre coatings can clearly be seen on the neighbouring fibre that has not been pushed. The black, inner layer is the carbon and the lighter, outer coating is the silicon carbide. The high magnification image of a section of the interface, in figure

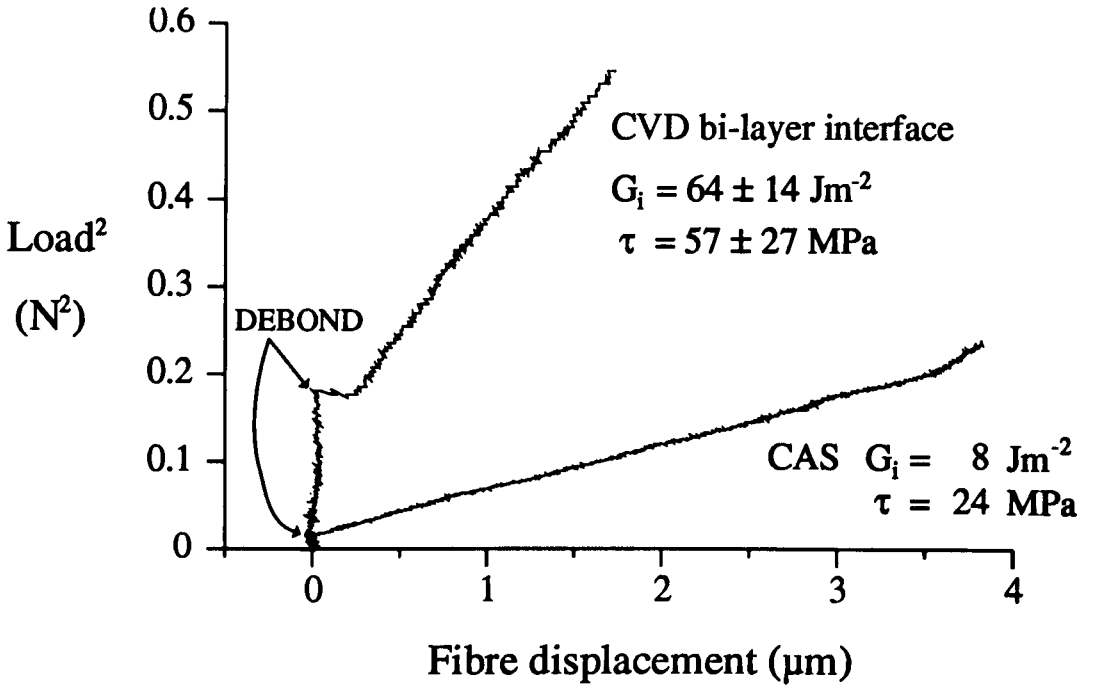

Figure 5.13 Fibre push-down response curve for the CVD bi-layer C and SiC interface for MAS/Nicalon composite. In comparison with the CAS/Nicalon, a very high debond fracture energy is measured.

5.14(b), illustrates that shear occurred along the interface of the C / SiC layers.

Material characterisation [117] showed a 1μm deep reaction zone to be present beneath the surface of the fibre, that developed during both the CVD and hot pressing stages. Together with the above micromechanical observations, this suggests that reaction between Nicalon fibre and the carbon coating during processing, formed a stronger interface than the C/SiC coating interface.

Due to the CVD chamber's restricted size, long continuous fibres could not be coated and therefore composite test specimens long enough for strength testing could not be fabricated. It is not known whether the exceedingly high debond energy that was measured resulted in a brittle material.

The novel combination of high G_i with only a moderate τ, obtained with the pre-synthesised interface is not encountered with the 'in-situ' reaction formed interfaces of the Nicalon reinforced glass-ceramic matrix composites investigated earlier.

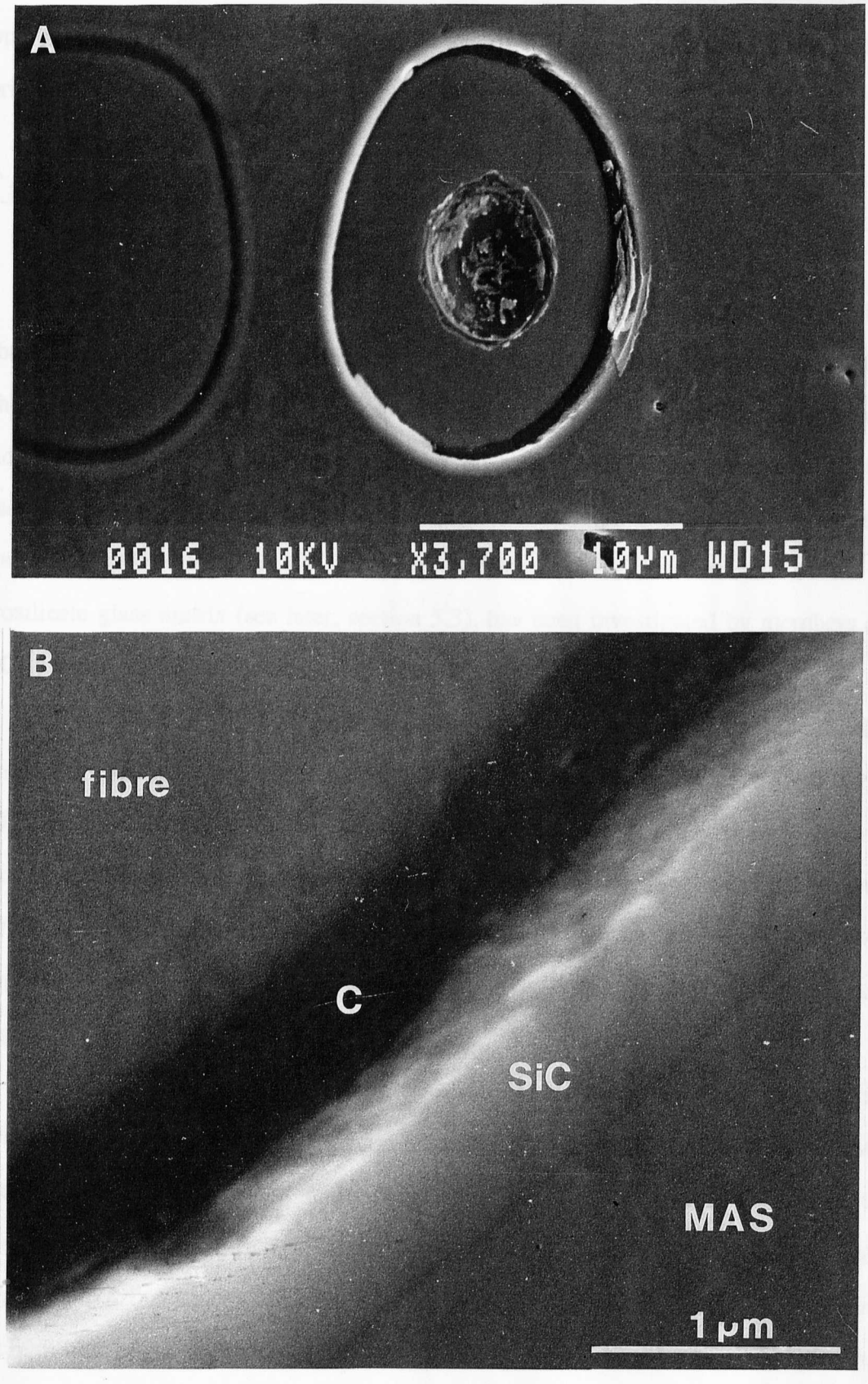

Figure 5.14 (a) Typical image of CVD coated fibre after push-down experiment. (b) High magnification image showing fracture at the interface of the C / SiC coatings.

Interface pre-synthesis via fibre coating can be used to tailor the final micromechanical properties of G_i and τ independently, unlike the 'in-situ' formed interfaces where, after fabrication, G_i and τ are either both high or both low.

5.2.3.2 Carbon coated Nicalon

Nicalon (grade NL-607) can be supplied precoated with a layer of pyrolytic carbon, 10 - 20 nm thick [118]. This is to introduce the carbon rich interface into CMCs without the need for in-situ reactions during processing. Hopefully, the pristine condition of the fibre surface can then be preserved within the composite itself, preserving the strength of the fibres and therefore increasing the strength of the overall material. The incorporation of this fibre within an MAS matrix and within a Borosilicate glass matrix (see later, section 5.3), has been investigated by members of the Centre for Advanced Materials Technology, Warwick [110,112].

A Nicalon NL-607 reinforced MAS matrix composite was identically fabricated to the MAS(Warwick) matrix that was discussed in sections 5.2.1 and 5.2.2 [110], the only differences being that the NL-607 fibre was used, without its sizing removed. Structural characterisation and mechanical flexure testing were carried out [110]. Interfacial micromechanical properties were measured. The properties of the two composite types (standard Nicalon reinforced (NL-201) and NL-607 reinforced) are compared in Table 5.2.

Using the carbon coated Nicalon more than doubles the matrix microcracking stress and ultimate bend strength of the material. Fibre push-down response changes from high debond energy and frictional shear stress for NL-201, to moderate values for NL-607. For the NL-607 cases, debond was controlled and gradual, unlike the sudden debond with load drop of standard Nicalon (see figure 5.6(c)). Width of the carbon interface in NL-607 was larger, on average, than for the NL-201 fibre.

Property	Standard NL-201	Coated NL-607
G_i (Jm^{-2})	30 ± 7	12 ± 5
τ (MPa)	239 ± 150	48 ± 15
Interface width (nm)	20 - 50	40 - 70
Matrix microcracking stress (MPa)	251 ± 17	665 ± 78
Ultimate bend strength (MPa)	504 ± 50	1168 ± 41

Table 5.2 Comparison of interfacial and mechanical properties of NL-201 and NL-607 reinforced MAS composites.

Although the lower and more consistent interface properties of G_i and τ contribute to the improvement in mechanical behaviour with NL-607 reinforcement, they do not account for its superior performance. As mentioned above, the pre-coating of the fibre with a carbon layer protects the pristine, almost flawless surface of the fibre from not only thermochemical damage during hot pressing, but also mechanical damage that may occur in the glass frit impregnation stage, as the fibres are drawn through a glass slurry and wound onto a drum. In the NL-607/MAS case, it is probably the protection afforded against mechanical damage that has increased performance so greatly as, at an interface width of 40-70 nm [110], some in-situ reaction does still occur with the coated fibre as the pre-deposited thickness of carbon is only 10-20 nm. Retention of the sizing on the fibre surface also contributes significantly to this protection.

A range of heat treatments in oxidising atmospheres, similar to those

a) Debond energy MAS/NL-607

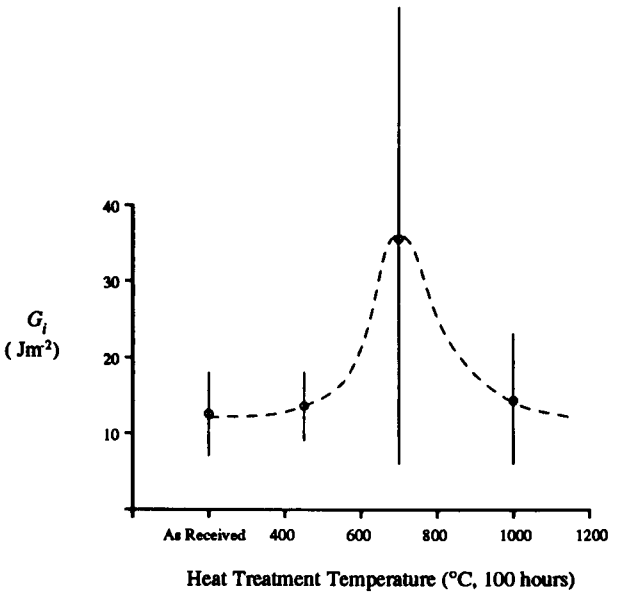

b) Frictional shear MAS/NL-607

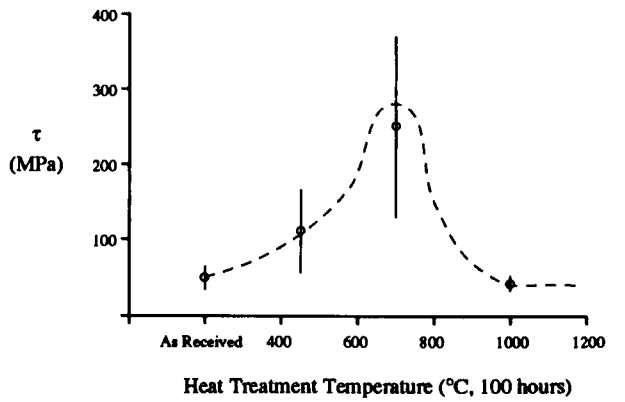

c) Three point bend MAS/NL-607

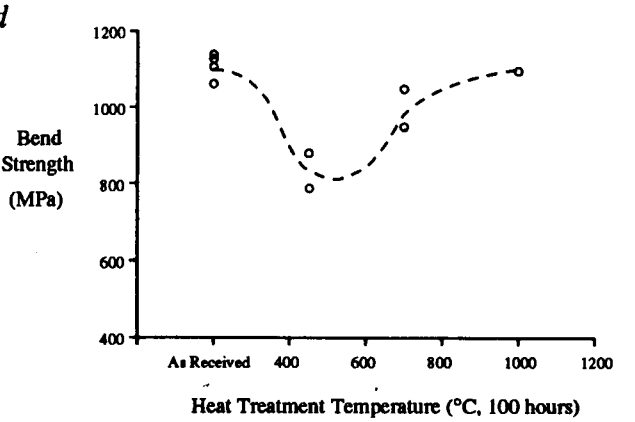

Figure 5.15 MAS/NL-607 (carbon coated Nicalon) interfacial and mechanical data of heat treated specimens; a) interface debond fracture surface energy, b) interface frictional shear stress, and c) three point bend test ultimate strengths.

described for CAS and BMAS, were performed on samples of the NL-607/MAS composite. They were followed by three-point bend and interfacial micromechanical measurements. Figure 5.15 shows the results of these tests. The NL-607/MAS interface behaves in a similar manner to the Nicalon/CAS and Tyranno/BMAS interfaces (see figures 5.9 and 5.10). However, unlike the previous examples where the weakest bend strengths were measured for the 750°C heat treatment, the 450°C treatment produced the weakest material [110]. The cause of this is unclear, but there maybe other factors that have not, as yet, been considered.

One point to note is that the weakest measured bend strength for the NL-607/MAS was just below 800 MPa, much higher than any of the maximum bend strengths recorded for Nicalon/CAS or Tyranno/BMAS. This could indicate that the presence of undamaged fibres within a matrix far outweighs the effects of moderate changes in interfacial micromechanical properties when it comes to overall composite performance.

The influence of G_i and τ on mechanical properties such as matrix microcracking stress are discussed in Chapter 6.

5.2.4 Effects of fatigue on interfacial properties

In collaboration with R.F. Allen of the Interdisciplinary Research Centre in Materials for High Performance Applications, University of Birmingham [119], the effect of fatigue testing on the interfacial micromechanical properties of Nicalon/CAS (supplied by Corning) was investigated. Fatigue testing with three-point bend apparatus of span 40mm and with test bars 5mm wide and 3mm thick, was performed by Allen [119]. Test frequency was 50 Hz and peak stresses between 400 MPa and 700 MPa were possible. Interfacial micromechanical parameters were measured at Warwick using the fibre push-down technique. All fibres tested were located near the tensile face of each test bar. Results were compared to the G_i and τ measured on an untested

specimen cut from the same hot pressed tile as the fatigued specimens.

The results of the fibre push-down tests are shown in Table 5.3. Peak fatigue stresses were kept approximately constant but the cyclic amplitude was varied to give the two different R-ratios (defined as minimum applied stress / maximum applied stress) of 0.1 and 0.5. The number of cycles to test bar failure was recorded.

The interfacial frictional shear stress in the as-received condition is $\tau = 28 \pm 4$ MPa. In all cases, fatigue has resulted in a decrease in τ, to levels as low as 21±4MPa. There is no apparent relationship with regard to R-ratio. The largest decrease in τ was for the specimen subjected to the largest number of load cycles and the smallest decreases to those subjected to the lowest number of cycles.

Debond fracture energies for fatigued specimens are all low compared to the as-received case of $G_i = 7.6 \pm 3.4$. Similar to the values previously reported for as-fabricated LAS, MAS(Pilkington) and BMAS composites (see Table 5.1), the fatigued CAS/Nicalon had $G_i \sim$ 1-2 with a standard deviation of ±1-2. This is indicative of a large proportion of the tested fibres having no interface bonding. In this case they have been debonded by the applied cyclic stresses and the subsequent fibre slipping.

Maximum stress (MPa)	Cyclic stress amplitude (MPa)	R-ratio	Number of cycles	G_i (Jm^{-2})	τ (MPa)
535	482	0.1	24,200	2.4 ± 1.4	23 ± 5
539	485	0.1	46,700	1.8 ± 1.2	22 ± 3
515	257	0.5	24,000	1.2 ± 1.4	23 ± 5
530	265	0.5	38,900	2.2 ± 1.8	23 ± 3
543	270	0.5	1,133,900	1.2 ± 1.4	21 ± 4
N/A	N/A	N/A	0	7.6 ± 3.4	28 ± 4

Table 5.3 Fatigue test conditions and measured micromechanical paramaters.

The G_i dropping to almost zero is caused by the interfaces debonding at the tips of matrix microcracks. The decrease in τ is expected to be due to a wear mechanism between fibre and matrix induced by the application of alternating stresses. The presence of such a mechanism has been deduced elsewhere by measuring the frictional heat produced during fatigue testing of CMCs [125]. It is apparent that the rate of decrease in τ with number of cycles is independent of cyclic stress amplitude. This coincides with the lack of an obvious effect of cyclic stress amplitude on specimen lifetime.

5.3 Glass Matrix Composites

Borosilicate glass is a possible matrix material for potential composites operating in areas of the gas turbine engine that are below 600°C. It has a low coefficient of thermal expansion (3.3×10^{-6} °C^{-1}, similar to that of Nicalon and Tyranno) so thermal mismatch stresses can be reduced, has a low liquidus to enable lower processing temperatures (generally $\leq$ 1100°C), and the vitrified state reduces the damage to fibres and the matrix stress that can be caused by the crystallisation of glass ceramics on cool down after hot pressing.

5.3.1 Structural characterisation of Borosilicate / Nicalon interfaces

Previous fabrication of Nicalon (standard NL-201 grade) reinforced Borosilicate matrix composites at Warwick [64,77,78,120] has resulted in the development of matrix compositions that resist the crystallisation of cristobalite during fabrication which introduces thermal strain mismatching within the matrix and microcracking. The fully vitrified matrix composites obtained have been fully characterised, primarily via electron microscopy [64,77,78,120].

It has been found that the state of the interface can be controlled by the hot

pressing temperature used in fabrication. Ultra-fine precipitated carbon exists along the interface when the CMCs are pressed at 950°C. At 1100°C the interface develops into a semi-continuous carbon layer. Interfacial micromechanics of these interfaces are discussed in section 5.3.2, below.

In an attempt to replicate the excellent mechanical performance obtained using the carbon coated Nicalon (NL-607 grade) reinforcement of MAS matrix material (see section 5.2.3.2), a series of four NL-607 reinforced Borosilicate matrix composites were fabricated [112]. The composites were each processed using a different hot-press temperature and hold time; 950°C for 20 min., 950°C for 60 min., 1100°C for 20 min. and 1100°C for 60 min. Interface characterisation was performed by the author, using TEM to correlate structural information to micromechanical information gained using the SEM based microindentor.

A JEOL 2000FX transmission electron microscope equipped with Oxford Instruments/Link Analytical X-Ray Energy Dispersive Spectroscopy (EDS) elemental analysis apparatus, was used for structural characterisation of the interface. The EDS system had light element analysis capability, that enabled resolution of the characteristic carbon, nitrogen and oxygen, K series X-Ray energy peaks.

TEM specimens were prepared by cutting slices 3mm x 3mm x 0.4mm perpendicular to the fibre direction. They were then ground to a thickness of approximately 100μm and polished on both sides to a 1μm diamond paste finish. Each was then individually glued with araldite to a 3mm diameter, TEM brass ring mount. A very shallow dimple would then be ground in the surface using a dimpler machine, finishing with 0.25μm diamond paste. Each specimen would then be placed in an Ion Tech ion beam thinning apparatus with a 30° beam to specimen surface incidence angle. Thinning would progress until a hole appeared at the centre of the specimen. Carbon coating of the final specimen was avoided as its presence would confuse interpretation of X-Ray EDS measurements. Its absence did not create difficulties with respect to specimen charging within the TEM.

The interface structures of each of the four composites are shown in figures 5.16, 5.17, 5.18 and 5.19.

Both the 950°C processed materials had continuous, carbon rich interfaces approximately 20 nm wide and there were no large diffusion bands visible within the fibres (figures 5.16 and 5.17). Their structures are very similar. EDS showed the interfaces to be carbon rich and to have significant sodium content. Sodium diffused to the interfaces from the Borosilicate matrix where it is present as a minor addition. There was only minor sodium diffusion across interfaces into the fibres. Overall, the interfaces are relatively smooth, the 950°C/60 min. case being slightly more convoluted (figure 5.17). Electron diffraction patterns typical of fibre and matrix are shown in figure 5.17.

The interface width of 20 nm is the same as the depth of carbon coat applied to the fibre by the manufacturer. Its smoothness and the lack of fibre diffusion bands, suggest little or no fibre-matrix reaction has occurred during processing in either of the 950°C fabricated composites. However, high magnification imaging does not indicate a lack of adhesion between matrix and interface and fibre - there are no voids or inclusions present to prevent bonding.

The 1100°C/20 min. hot pressed material consistently showed, throughout specimens from separate batches, a 'double-band' interface. A TEM micrograph of its structure is shown in figure 5.18. There are two carbon rich bands present along the interface. An 'inner' band is in contact with the fibre and is approximately 20 nm thick. The 'outer' band is 10-20 nm thick and separated from the inner by approximately 50 nm of material with a similar phase contrast to the matrix. Each of the bands contains a significant concentration of sodium. The outer band is more convoluted than the inner band and contains a number of voids. EDS shows the material separating the two bands to be deficient in aluminium when compared to matrix composition. This suggests it is silica rich. Large diffusion bands of 200 nm depth that are present within the fibre confirm a significant amount of fibre-matrix cross diffusion and reaction at the higher

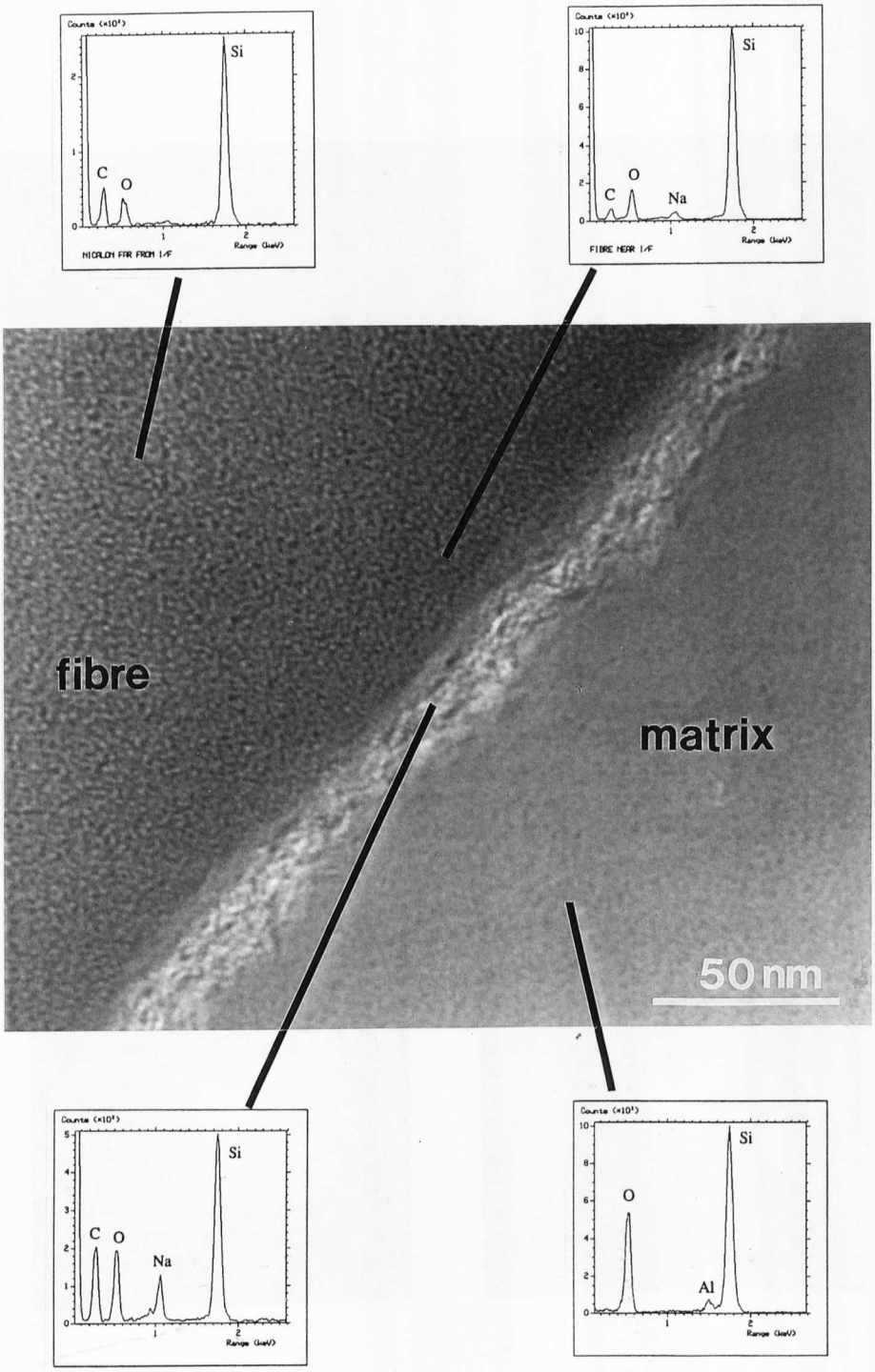

Figure 5.16 TEM micrograph and X-Ray EDS analysis of a typical fibre-matrix interface in Nicalon NL-607 reinforced Borosilicate glass matrix, hot-pressed at 950°C for 20 minutes.

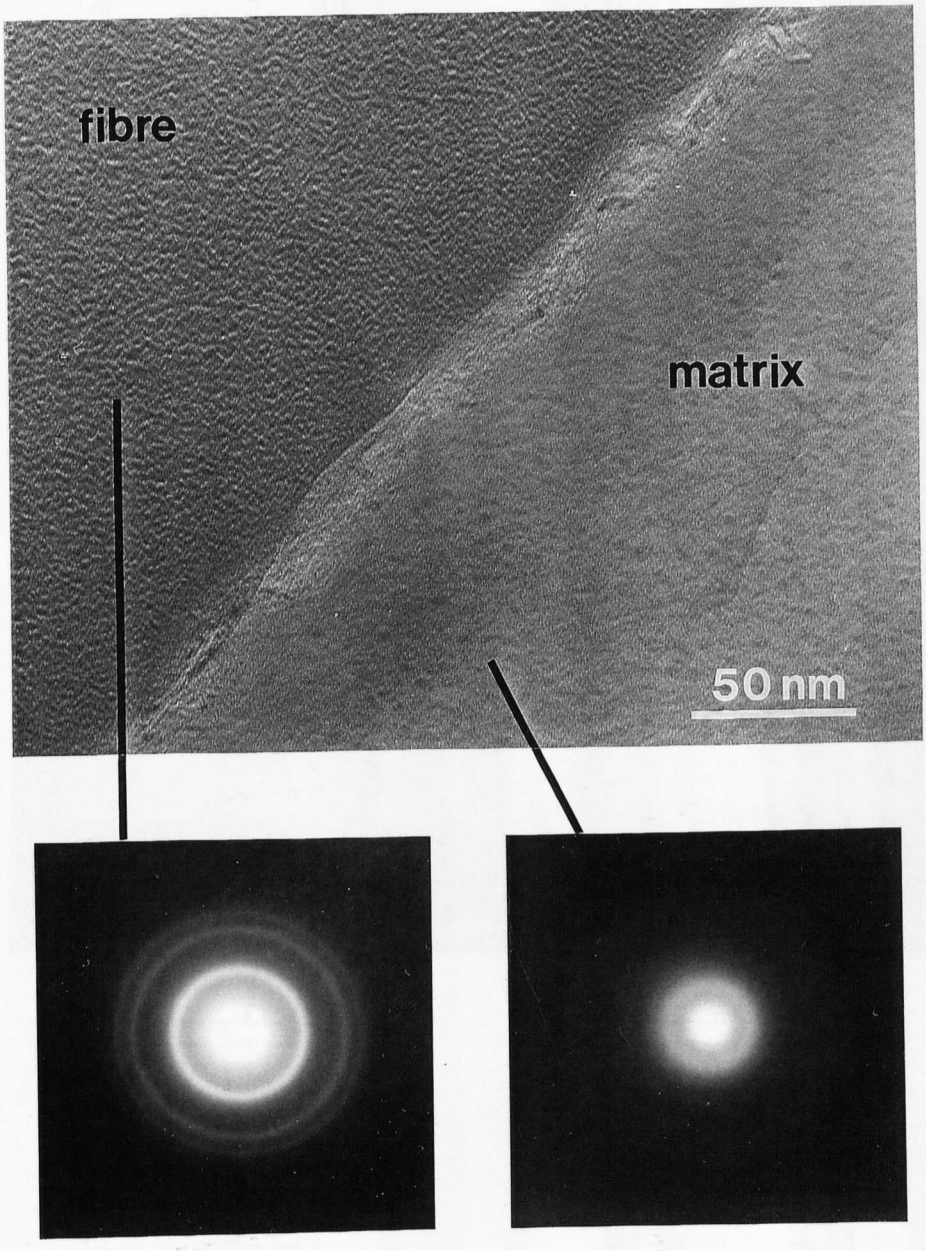

Figure 5.17 TEM micrograph and electron diffraction analysis of a typical fibre-matrix interface in Nicalon NL-607 reinforced Borosilicate glass matrix, hot-pressed at 950°C for 60 minutes.

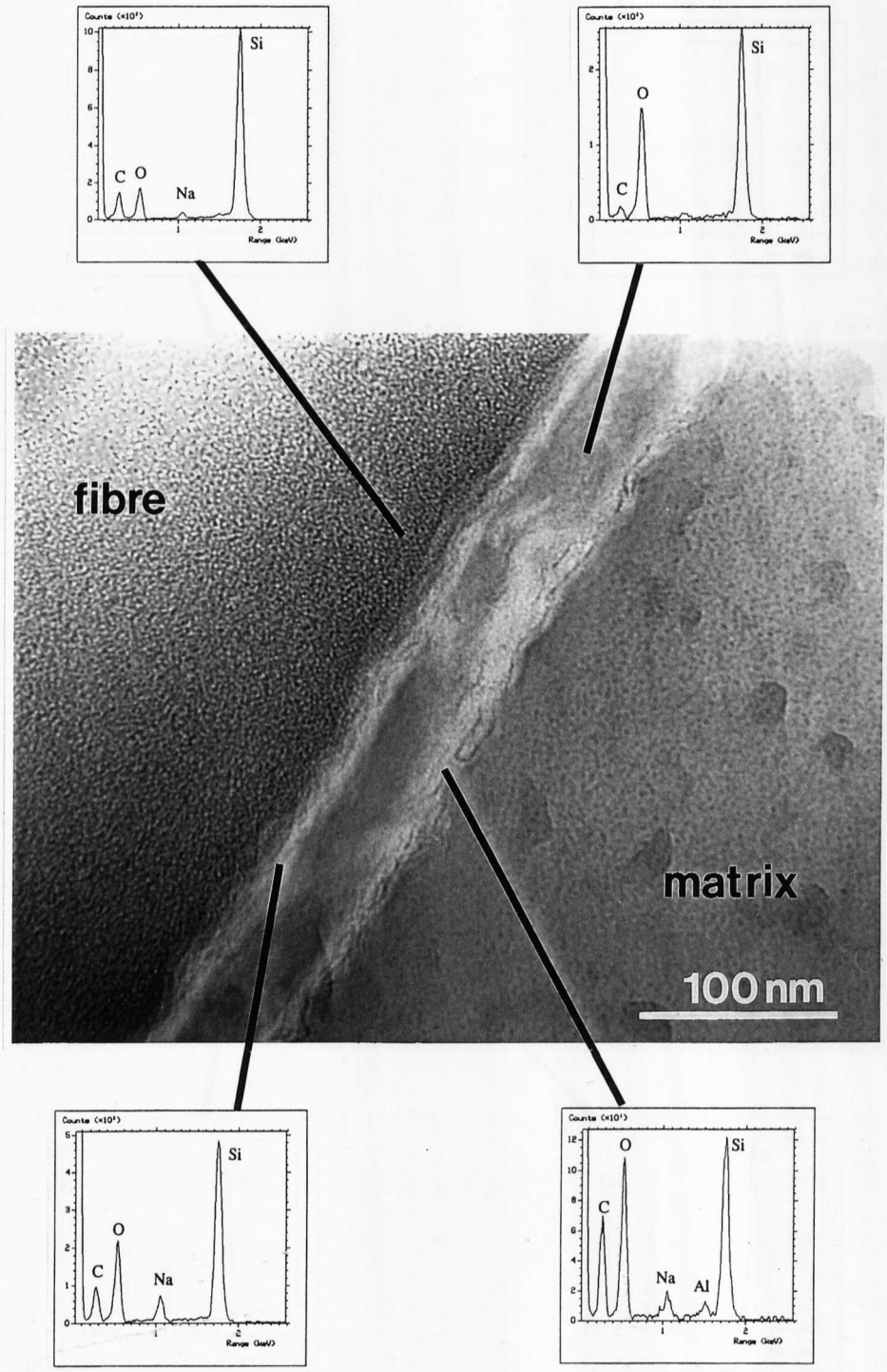

Figure 5.18 TEM micrograph and X-Ray EDS analysis of a typical fibre-matrix interface in Nicalon NL-607 reinforced Borosilicate glass matrix, hot-pressed at 1100°C for 20 minutes.

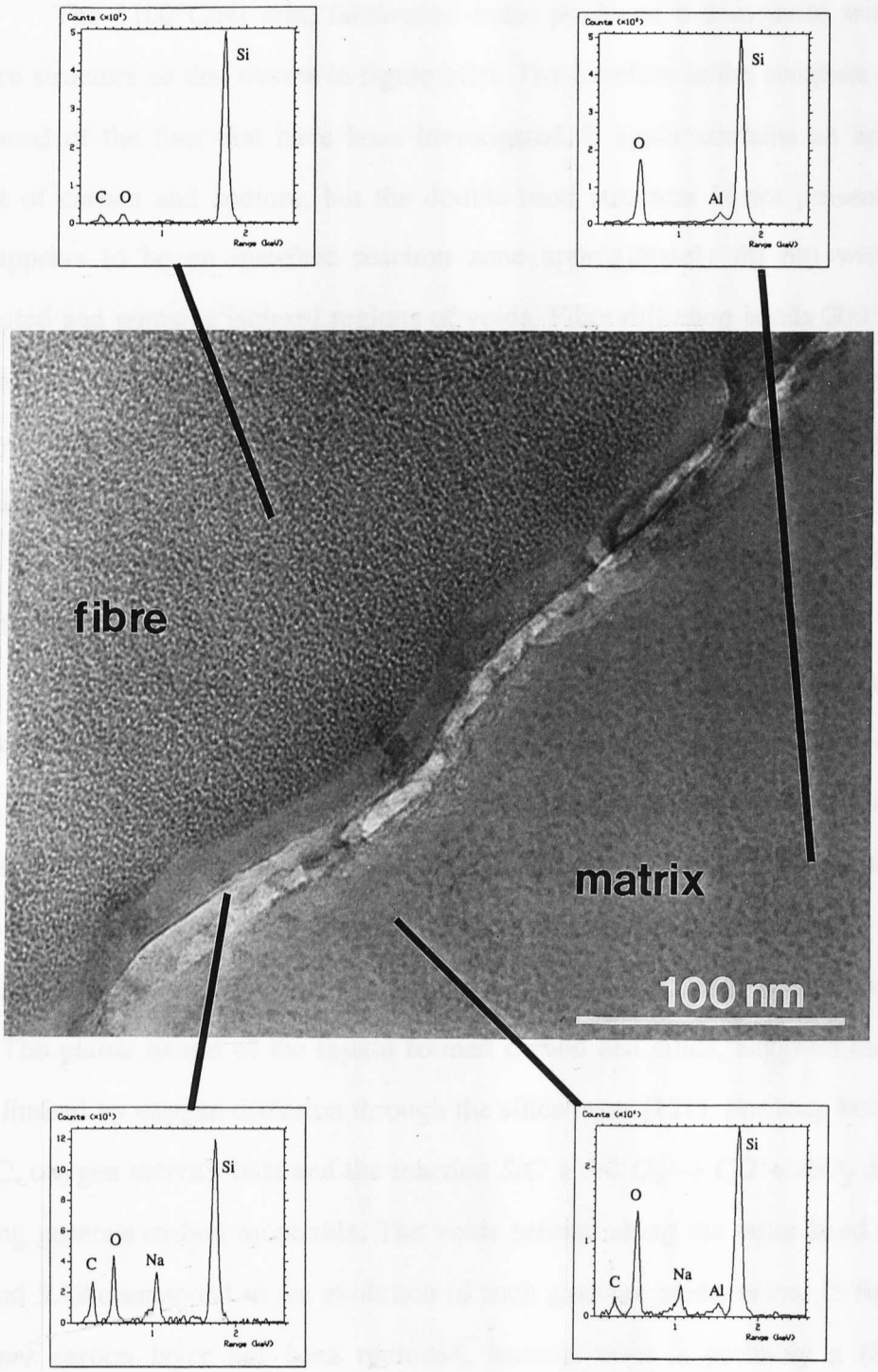

Figure 5.19 TEM micrograph and X-Ray EDS analysis of a typical fibre-matrix interface in Nicalon NL-607 reinforced Borosilicate glass matrix, hot-pressed at 1100°C for 60 minutes.

processing temperature.

The 1100°C/60 min. fabrication route produced a composite with typical interface structure as that shown in figure 5.19. The interface is the roughest and most convoluted of the four that have been investigated. It again contains an appreciable amount of carbon and sodium, but the double-band structure is not present. Instead there appears to be an interface reaction zone approximately 40 nm wide that is convoluted and contains isolated regions of voids. Fibre diffusion bands 200 - 400 nm deep are present. They are rich in silicon and depleted in carbon and oxygen. No carbon rich layer is visible. An unidentified, continuous phase is present on the fibre surface, approximately 20 nm deep.

Fibre-matrix reaction is occurring at 1100°C. Although not yet confirmed by rigorous investigation, a possible interface formation mechanism follows;

At 1100°C the carbon layer on the pre-coated Nicalon does not offer a significant diffusion barrier to oxygen diffusing from the matrix to the fibre. Thus carbon and silica are formed in between the fibre and pre-coated carbon, following the reaction $SiC + O_2 \rightarrow SiO_2 + C$ (reaction (2.30), that is responsible for the in-situ carbon formation in uncoated Nicalon reinforced glass ceramics). Hence the fibre/ carbon/silica/carbon/matrix structure formed in the 20 min. case is observed (figure 5.18). The planar nature of the in-situ formed carbon and silica, suggests the reaction rate is limited by oxygen diffusion through the silica layer [121]. For long hold times at 1100°C, oxygen activity falls and the reaction $SiC + 3/2\ O_2 \rightarrow CO + SiO_2$ dominates, evolving gaseous carbon monoxide. The voids present along the outer band in figures 5.18 and 5.19 correspond to the evolution of such gaseous products and in figure 5.19, the inner carbon layer has been removed, leaving what is probably a fibre/silica/ carbon+CO/matrix interface structure.

5.3.2 Interfacial micromechanics and composite mechanical performance

Interface properties G_i and τ were measured for standard Nicalon reinforced Borosilicate matrix material as well as the four NL-607 composites. The data is shown in Table 5.4.

The Nicalon NL-201 reinforced glass composites had very well bonded interfaces. The majority of fibres in the 950°C fabricated case could not be pushed, applied loads were so high that fibre fracture occurred before fibre movement. As a result, reliable quantitative values for G_i and τ could not be determined. Fibre push-down response for the 1100°C composite was typically a sudden debond at very high applied load with a large load drop and rapid fibre displacement. A very high debond energy (G_i = 104 ± 34 Jm^{-2}) was recorded. Figure 5.20 illustrates one such fibre push-down response. It debonds at an applied load almost double that of the MAS/

Fibre Type	Processing temperature and hold time	G_i (Jm^{-2})	τ (MPa)
NL-201	950°C / 20 min.	Could not push most fibres	
	1100°C / 20 min.	104 ± 34	57 ± 7
NL-607	950°C / 20 min.	20 ± 10	158 ± 74
	950°C / 60 min.	34 ± 22	164 ± 80
	1100°C / 20 min.	20 ± 7	51 ± 9
	1100°C / 60 min.	54 ± 24	229 ± 161

Table 5.4 Interfacial micromechanical information for the Borosilicate glass matrix / Nicalon fibre composites.

Nicalon(Warwick) trace, with G_i = 31 Jm^{-2}, shown in figure 5.6(c). The load drop is large, almost 0.75N. No mechanical three-point bend test data is available for these materials.

Nicalon NL-607 reinforced borosilicate glass showed considerably different micromechanical behaviour to that reinforced with the standard Nicalon. The carbon coating considerably reduces the debond fracture surface energy for 950°C processed materials. The fibres can be pushed without fracturing them and G_i and τ can be measured. Table 5.4 shows that for both the 20 minute and 60 minute hold times at 950°C, the measured G_i and τ were similar (within the considerable standard deviation of the data). This correlates well with the TEM investigation that indicated both these interfaces to be structurally very similar.

The 1100°C, 20 min. composite had a much lower mean frictional shear stress with narrower distribution (τ = 51 ± 9 MPa), than any of the four materials. The G_i = 20 ± 7 Jm^{-2} was comparable to the 950°C, 20 min. composite, but the relative ease of fibre slip after debond must be a consequence of the formation of the double-banded interface (see figure 5.18). It is not known whether debond of the interface occurs at the

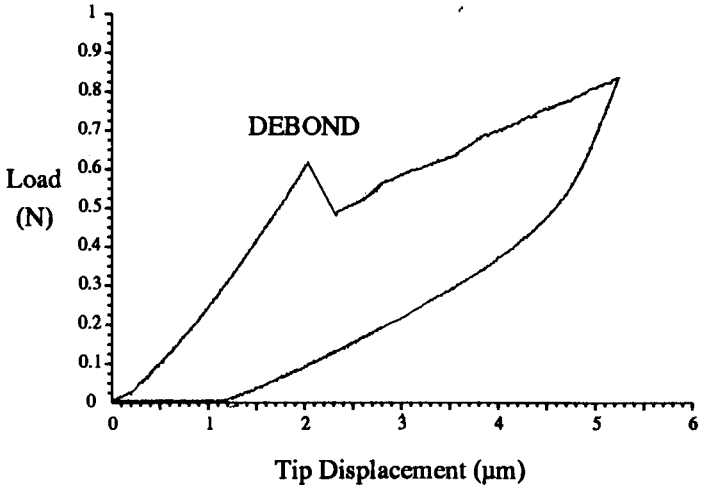

Figure 5.20 Typical load vs tip displacement trace for Borosilicate/Nicalon(NL-201), 950°C/20 min., fibre push-down. Mean G_i = 104 ± 34 Jm^{-2}, τ = 57 ± 7 MPa.

inner or outer band or in between, but as slipping is easier, it may result in a large amount of interface damage, that results in reduction of the frictional shear stress.

TEM investigation suggested an appreciable amount of fibre-matrix reaction occurred during processing of the 1100°C/60 min. composite. Micromechanical measurements showed the average interface in this material to have the highest debond energy (G_i = 54 ± 24 Jm^{-2}) and frictional shear stress (τ = 229 ± 161 MPa) of the four cases. This can be attributed to the very rough, convoluted interface that resulted from the reactions during processing. As opposed to a smooth interface that was present in the 950°C composites, a rough interface will provide a larger frictional resistance against shear. It will also contribute to a measured increase in debond energy, as a larger load will need to be applied to initially push a fibre.

Twenty fibres (compared to the usual ten) in each of the four NL-607 composites were pushed in order to clarify that the considerable standard deviations recorded were a real material effect. It is thought that the high loads used to push the fibres cause damage to the interfaces that is inconsistent from one fibre to the other. Therefore slightly different interface properties are measured from one fibre to another. This is an explanation for the lower G_i and τ having smaller standard deviations. When other factors such as interface variability within a specimen occurs, such as with the 1100°C/60 min. material that has various diffusion band widths and varying degrees of roughness of interface, this effects the measured micromechanical response.

Mechanical three-point bend testing was performed on each of the NL-607 composites [112]. Each was fabricated with a fibre volume fraction of ~44%. Table 5.5 gives the measured microcracking stresses and ultimate strengths. They all showed exceptional performance. Ultimate strengths were at least 50% higher than the strongest of the commercially available CAS/Nicalon and BMAS/Tyranno studied earlier (refer to figures 5.9(c) and 5.10(c)). With regard to toughness and graceful composite like fracture, they all had microcracking stresses at a level of 0.4-0.68 σ_{ubs} (σ_{ubs} is ultimate bend strength), except for the 950°C/20min. case that behaved in a

Fibre Type	Processing temperature and hold time	Matrix microcracking stress σ_{mm}(MPa)	Ultimate bend strength σ_{ubs} (MPa)
NL-201	950°C / 20 min. 1100°C / 20 min.	NOT AVAILABLE	NOT AVAILABLE
NL-607	950°C / 20 min.	> 1000	1290 ± 30
	950°C / 60 min.	~ 800	1270 ± 40
	1100°C / 20 min.	~ 600	1380 ± 50
	1100°C / 60 min.	~ 570	1360 ± 50

Table 5.5 Borosilicate/Nicalon mechanical three-point bend test data [112].

more brittle manner. There is no clear relationship between the measured interface properties and interface structure (that do correlate), and the overall mechanical behaviour of the material. For example, the two 1100°C processed composites have very different G_i and τ (see Table 5.4), different interface structure (see figures 5.18, 5.19), but very similar mechanical performance (Table 5.5). The same conclusion has to be drawn as for the case of NL-607 reinforced MAS (section 5.2.3.2), in that the sizing and carbon coating protect the fibre against mechanical damage during processing, and thus the fibre maintains high strength within the matrix. It is thought any thermochemical damage present does not effect strength greatly because where it is present in the 1100°C/60 min. case (see figure 5.19), it does not significantly alter mechanical performance. Other factors such as lack of porosity and matrix cracks in the fabricated composite, obtained by the perfected processing route [112], give these materials their superior performance.

5.4 Large diameter fibre reinforcements

As discussed in Chapters 3 and 4, the high load capability of the SEM based microindentor was designed to enable fibre pushing tests of large diameter fibres. The instrument has been used to measure the interfacial properties of Textron® SCS-6 SiC fibre reinforced sintered reaction-bonded silicon nitride (SRBSN) matrix composites [122]. The fibres are fabricated by CVD of SiC onto a carbon core, producing a 150 μm diameter fibre. Carbon is deposited onto the surface to help develop favourable interfacial properties.

Specimens 5 mm thick were cut and polished for fibre push-through testing. The diamond tip geometry used for pushing the smaller Nicalon fibres was not suitable for this application. It was replaced with a standard Vickers diamond. This meant that the actual fibre push-down was not visible, and the *x-y* stage co-ordinates and SEM screen cross-hairs had to be used to position fibres centrally under the indentor tip. However, because of their large diameter, fibre displacements of more than 10 μm were still possible. The gain of the load cell amplifier had to be adjusted to enable the analogue to digital converter of the Acorn microcomputer to record the higher applied loads (see section 4.2.2). Displacement measurement is not required to determine τ in push-through tests. The capacitance gauge was not used and approximate displacement (for plotting of illustrative load vs. displacement traces only) was estimated by counting the TTL pulses applied to the Inchworm motor controller (see Chapter 4 for information).

Figure 5.21 shows the load vs. tip displacement trace for a fibre push-through test. The fibre is pictured in figure 5.22, after the test, showing its relative displacement to the matrix. There are three zones, A, B, C, on the upward, load application response curve of figure 5.21. Zone A, is the shallow gradient at low loads where the indentor is contacting and pushing the carbon core relative to the SiC surrounding it. Zone B is a steeper gradient where the indentor is pressing against the

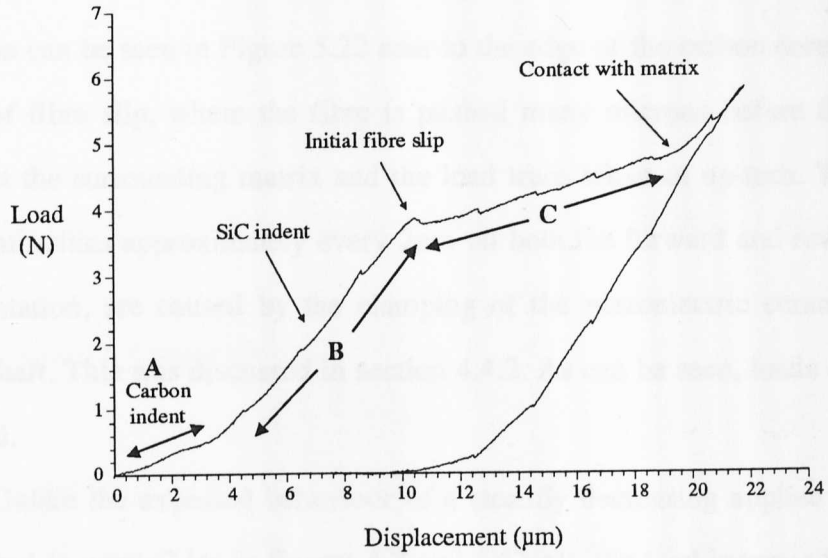

Figure 5.21 Load vs. displacement trace for the push-through test of 150 μm diameter Textron SCS-6 fibre within silicon nitride matrix.

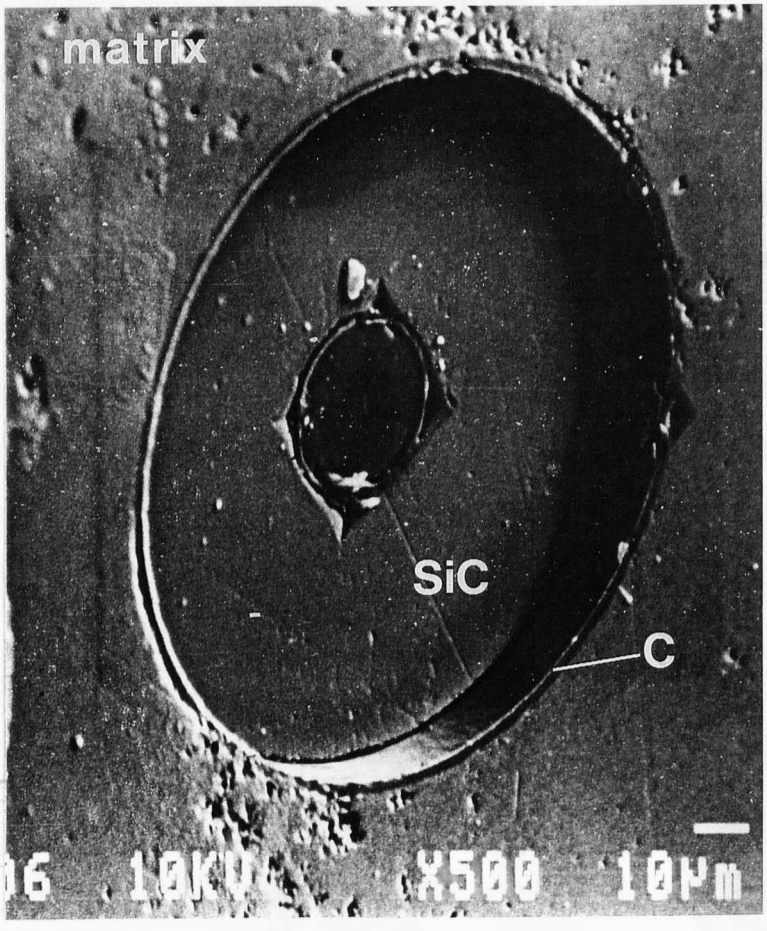

Figure 5.22 Textron SCS-6 silicon carbide fibre in silicon nitride matrix after push-through test of figure 5.21.

SiC bulk of the fibre, but the fibre is not moving. The indentations formed during zone B indentation can be seen in Figure 5.22 near to the edge of the carbon core. Zone C is the region of fibre slip, where the fibre is pushed many microns before the indentor sides contact the surrounding matrix and the load trace takes an up-turn. The regular, slight discontinuities approximately every 2μm on both the forward and reverse cycles of the indentation, are caused by the clamping of the piezoelectric ceramics on the Inchworm shaft. This was discussed in section 4.4.2. As can be seen, loads of up to 6N were applied.

Unlike the expected behaviour of a steadily decreasing applied load as the fibre is pushed in zone C (as in figures 5.2 and 5.12(a)), the load increased the further the fibre was pushed. This effective increase in friction could be caused by the presence of debris between fibre and matrix that is dislodged during the sliding action and also by asperities on the fibre surface preventing smooth fibre slip [123].

Figure 5.22 shows clearly that the carbon coating deposited on the SiC surface remained attached to the surrounding matrix after the fibre was pushed. Using equation 5.12 to determine the average frictional shear stress for a number of these push-through tests, it was found the carbon coating produced a very low shear stress interface of τ = 2-4 MPa [122,124].

Even for such low shear stresses, loads in excess of 5N were required to push the fibres, indicating the range of application of the SEM based indentor to fibre push testing of many types of CMC.

CHAPTER SIX

DISCUSSION ON INTERFACE CHARACTERISATION

6.1 Modelling of fibre push-down

As stated in Chapter 3, the reasons for development of an SEM based microindentor for the measurement of interfacial micromechanics of ceramic matrix composites, were based on the versatility of the fibre push-down test. It does not require very specialised specimen preparation, and as long as a device with acceptable load range, resolution, and dynamic imaging (such as the SEM microindentor) is available, it is applicable to a wide range of composite types. The work performed on the large range of interfaces described in Chapter 5 shows that this is the case.

Application of the Marshall and Oliver model [89] has been a success, with the large majority of fibre push-down tests fitting the predicted behaviour. However, the model is a simplification of the push-down mechanism and ignores other important factors. These factors effect both frictional shear stress and debond fracture energy measurements.

6.1.1 Frictional shear stress τ

The major assumption when modelling frictional shear stress is that it is discrete and does not follow the Coulombic friction law, $\tau = \mu p$, where μ is the coefficient of friction and p is the residual stress normal to the interface (see section 2.1.2.6). This means that the effects of residual stresses on the measured τ (caused by fibre-matrix thermal expansion mismatch) are not taken into account. This becomes an issue due to the fact that fibre pushing causes Poisson expansion of the fibre and

increases any compression across the interface, effectively increasing τ. In any real application, fibre reinforcements will undergo tensile stresses and will be pulled, not pushed, causing fibre Poisson contraction and reduction of any compressive stress at the interface. Thus to accurately determine τ for tensile stresses from fibre push-down tests, the residual stress across the interface and the fibre Poisson expansion must be known. The extent to which Coulombic friction contributes to τ is also determined by the morphology of the interface. If it is rough with many asperities, then the effect of residual stress diminishes [39,42].

Many models have been formulated that incorporate residual stresses, interfacial roughness, and Poisson expansion of the fibre during push-down [126-132]. The detailed analysis and implementation of these models has proved beyond the scope of the current work. As stated in Chapter 3, the only material that has been extensively studied via fibre push-down testing with nanoindentors has been the Nicalon/LAS III composite supplied by Corning, USA. There has been very little work performed on other glass ceramic matrix composites reinforced with small fibres that the current work can be compared to.

However, a small study has been performed on CAS/Nicalon (Corning) [133,134]. Using a nanoindentor, fibre push-down tests were attempted. The majority of fibres did not move when the maximum load was applied (0.11N). Many of the pushed fibres showed non-linear F^2 *vs* u behaviour and were only displaced 50-150 nm. Application of the Marshall and Oliver model [89] to the fibres that did move, gave τ = 25 MPa, G_i = 0.32 Jm^{-2}. The frictional shear stress is the same as that measured in the present study (see Chapter 5), but the interface fracture surface energy is more than an order of magnitude lower. The much lower debond energy recorded with the nanoindentor (G_i = 0.32 Jm^{-2}) cannot be considered to be a representative value. Most fibres were not moved by the maximum applied load of 0.11N, suggesting those that did had damaged interfaces that were already debonded, as they only needed ~0.16 mN applied to initiate fibre slip [133,134]. It was also stated that the linear F^2 *vs* u

relationship was not always followed. This is expected to be due to the debond crack not propagating to a length c, much greater than the fibre radius r, as fibre displacement was only 50 - 150 nm at maximum. Thus the necessary condition for Marshall and Oliver to apply, $c >> r$, was not reached.

When the Shetty [126] model was applied, taking into account Poisson expansion of the fibres, a shear stress of τ = 16 MPa was determined [133,134]. Other work [83,66] has determined τ = 10-30 MPa for CAS/Nicalon by measurement techniques other than fibre push-down.

If the effect of Poisson expansion of the fibre was very significant, then one would expect the effective value of τ to increase as the fibre is pushed and its sides expand and compress against the matrix. This would result in the gradient of the F^2 *vs* u plot increasing with higher loads, i.e. deviating from the straight line of the Marshall and Oliver model. Such a deviation was recorded only in a small number of cases, an example is shown in figure 6.1. The composites that showed examples of this behaviour were Borosilicate/Nicalon NL-607 (950°C processing), as-fabricated BMAS/ Tyranno and MAS/Nicalon NL-607. It is noticeable that each of these composites had thin carbon rich interfaces of 20 nm, 20 nm and 55 nm respectively.

Poisson ratio ν, is defined as the ratio of lateral strain ε_{lat} to axial strain ε_{ax} of a rod when it is put under axial tension or compression,

$$\nu = \varepsilon_{lat} / \varepsilon_{ax} \tag{6.1}$$

From integration of equation (5.3) for fibre push down with G_i = 0, the average compressive strain along the sliding fibre is given by,

$$\varepsilon = u / l = F / (2 \pi r^2 E_f) \tag{6.2}$$

where u is the fibre displacement from the surface, l the interface crack length, F the

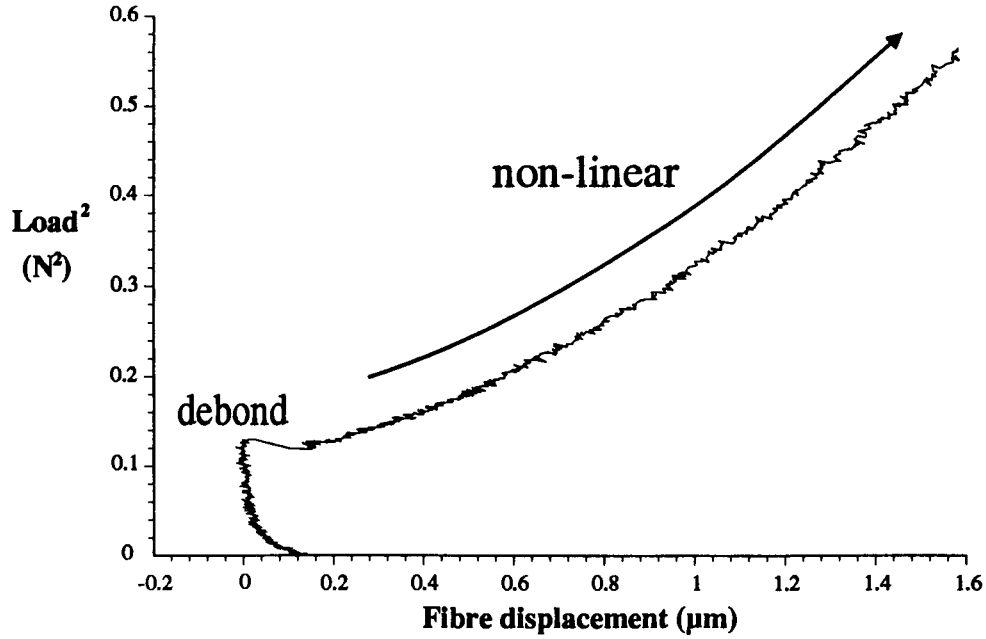

Figure 6.1 F^2 vs u plot for push-down of Nicalon fibre in Borosilicate matrix. An example of fibre push-down test that did not follow the straight line model of Marshall and Oliver [89].

applied load, r the fibre radius and E_f the fibre modulus. Poisson ratio for Nicalon fibre is given as $\nu = 0.2$, and this gives, for the example of figure 6.1, an average increase in the radius of the fibre of approximately 15 nm (as r = 7.7 μm). This is approximately the same dimension as the interface width. It is possible that the contribution of Poisson expansion to τ, is higher for thinner interfaces as the compliance of the thin interface is too low to prevent the build up of large stresses across the interface - it cannot "cushion" the expanding fibre sides. It has been hypothesised in other work that thicker interfaces can accommodate clamping stresses across the fibre-matrix interface [135,136].

6.1.2 Debond fracture surface energy G_i

Measurement of debond fracture surface energy G_i with the Marshall and Oliver model has resulted in values that appear too high. As stated in Chapter 2, the theoretical condition for debond at the interface to occur in preference to crack propagation through the reinforcing fibre is $G_i < 1/4 \rightarrow 1/2\ G_f$, where G_f is the fracture energy of the fibre. The G_f for Nicalon within glass ceramic matrices has been measured via fracture mirror sizes to be ~5 Jm^{-2} [81]. In the present study however, G_i has been measured for some mechanically excellent composites, and found to be greater than 10 Jm^{-2} and even approaching 60 Jm^{-2} (see Tables 5.1, 5.2 and 5.3). Therefore either the measured G_i are wrong or the G_f of Nicalon is incorrect.

6.1.2.1 Models to determine G_i

There are a number of models detailed in the literature that can be used to determine the level of bonding between fibre and matrix. Work that has focussed on push-through tests on monofilament reinforcements, considers a debond stress τ_{db} that has to be overcome at the interface before sliding of the fibre can occur [137,138]. After this stress has been applied, fibre slip is then governed by the frictional shear stress τ_f. However, the majority of modelling has taken the approach used in Marshall and Oliver [89], that debond is a condition of the fracture surface energy of the interface G_i.

There are short-comings in both approaches, as pointed out by Steif and Dollar [139,140]. The debond shear stress approach considers the stress field at the tip of a propagating crack approaching τ_{db}, whilst immediately behind the tip the stress is equal to τ_f . This discontinuity in the stress field is impossible in a linear elastic solid. The critical debond energy approach is well suited to the analysis of a propagating crack, but for actual debond initiation the model fails as it predicts an initial debond

crack length of zero which would require an infinite load to initiate debonding. This failure of classical fracture mechanics to include crack initiation is well known (see Chapter 2, equations (2.2)-(2.6), where an initial crack length is required for analysis of fracture). One method of avoiding the problem is to assume the presence of an initial debond length so that the load for debond initiation will then be finite. This has been used in some of the more complex analyses for fibre-pushing [130,131,132].

To determine the most applicable debond parameter, either τ_{db} or G_i, the approach used by Rouby and Osmani [141] was employed. They analysed both the critical stress condition and the critical energy release rate condition and derived formulas for each that gave the applied load at debond F_d, as a function of the fibre radius r.

For the critical stress condition,

$$F_d = 2\,\pi\,\beta\,\tau_{db}\,(E_f / 2\,G_m)^{1/2}\,r^2 \tag{6.3}$$

where β is a structural constant and G_m is the shear modulus of the matrix.

For the critical energy condition,

$$F_d = (4\pi^2\,E_f G_i)^{1/2}\,r^{3/2} \tag{6.4}$$

the same as equation (5.9). To determine which of the two models is more applicable to a particular composite, a plot of $\log(F_d)$ vs. $\log(r)$ for a number of push-down tests is required. In equation (6.3), F_d is proportional to r^2, and in equation (6.4), F_d is proportional to $r^{3/2}$, so the gradient of $\log(F_d)$ vs. $\log(r)$ will be either 2 or 3/2, depending on which condition applies. Nicalon reinforced composites are ideal for performing such an analysis as the fibres have a wide diameter distribution.

The reliability of as-fabricated CAS/Nicalon (Corning) and consistency in micromechanical properties (see Table 5.1), was used to bring together the push-down

data from four separate samples. A total of 36 fibre push-downs was analysed and a plot of $\log(F_d)$ vs. $\log(r)$ was made, see figure 6.2. Linear regression was performed, the gradient was measured to be 1.52 ± 0.35, and therefore the critical debond fracture energy condition was deduced as applicable.

Rouby and Osmani performed the same analysis on a Nicalon reinforced Mullite matrix composite and found the same condition to apply [141].

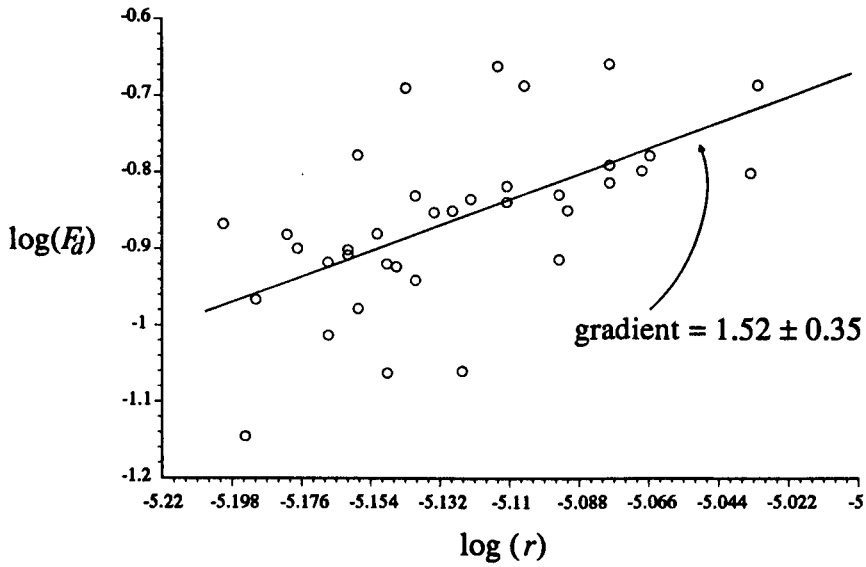

Figure 6.2 Plot of $\log(F_d)$ vs. $\log(r)$ for Nicalon fibre push-down tests within CAS glass ceramic matrix. Gradient of ~3/2 indicates the critical energy condition applies to debond.

Other debond models that take the fracture surface energy approach, all derive similar expressions to Marshall and Oliver [89] for G_i, see equation (5.9). The original debond model of Outwater and Murphy [142], that also ignored residual thermal stress and Poisson expansion as it was applied to polymer matrix composites, is identical to that of [89]. More recent studies have taken these parameters into account, including the residual axial stress within the fibre [129]. Kerans and Parthasarathy [127] and Liang and Hutchinson [131] derive complicated expressions that include all relevant factors and when assumptions are made that residual stress, fibre roughness

and frictional stress are all negligible, the debond energy simplifies to essentially that of the Marshall and Oliver case. Further work by Marshall [132], developing the Hutchinson and Jensen model [130], can relate the load at debond to a debond energy that takes into account axial and normal residual stresses and relative fibre and matrix elastic response, and without the need for curve fitting data analysis. Brief investigation of CAS/Nicalon response has been carried out with this model, using the example test data illustrated in figures 4.28, 5.5, 5.6(b), see Appendix II. The derived debond energy was G_i = 4.6 Jm^{-2}. It is lower than that derived with the Marshall and Oliver model, where G_i = 8 Jm^{-2}, but is still approximately the same as the fracture energy of Nicalon (G_f~ 5 Jm^{-2}), and therefore the debond condition $G_i < 1/2\ G_f$, is still not satisfied.

6.1.2.2 Mixed mode crack deflection

As discussed in Chapter 2, deflection of a crack at an interface is necessarily a mixed mode mechanism, whereas the fibre push-down test measures only the mode 2 debond energy of the interface. This means during a push-down test, the phase angle loading ψ (see section 2.1.2.1, equation (2.13)) on the interface is approaching 90°, i.e. theoretically there is no mode 1 contribution. However, as can be seen in figure 2.5, the phase angle for a deflecting matrix crack at an interface can vary from ~ 40°-15° (as α_E varies from 0 - 1), indicating that mode 1 contributes significantly more to crack deflection than mode 2.

Experimental data measuring the interface fracture energy G_i of a glass/ epoxy system as a function of ψ [143,144], has shown that measured G_i increases more than four-fold from ~ 5 Jm^{-2} to ~ 22 Jm^{-2} as ψ tends from 0 to 70°, see figure 6.3. This clearly illustrates that G_i is a function of the relative mode 1 and mode 2 contributions.

Detailed analysis of the fracture criteria [143] of crack deflection, suggests that the ratio of the mode 1 critical fracture energy G_{i1} of the interface, to the mode 2 critical fracture energy G_{i2} , is

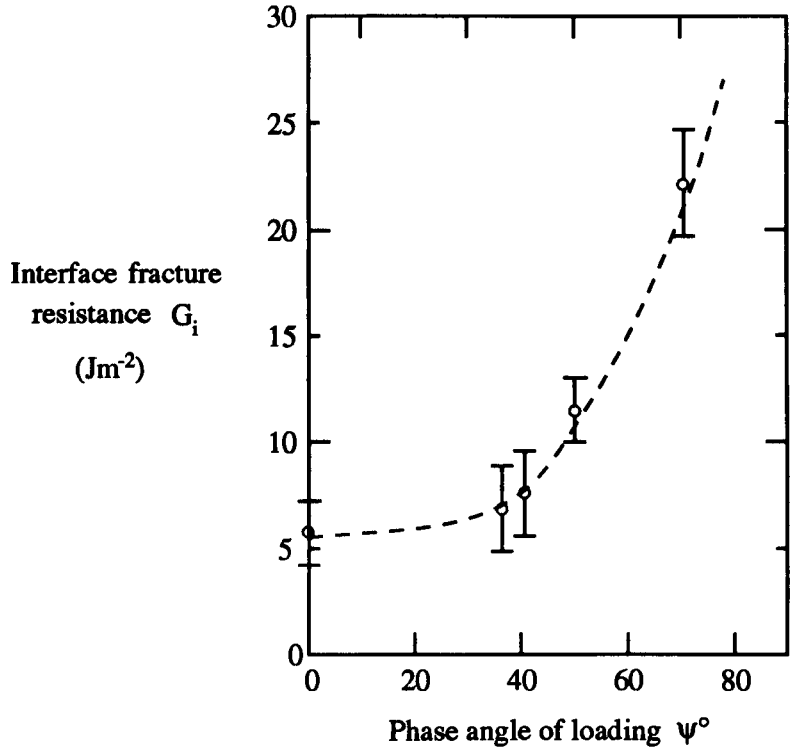

Figure 6.3 Fracture toughness of an epoxy/glass interface G_i as a function of the phase angle of loading $\psi = \tan^{-1}(K_2 / K_1)$, taken from [143].

$$G_{i1} / G_{i2} = \lambda \tag{6.5}$$

where λ is a material constant, generally $\lambda = 0.1 \rightarrow 0.2$. Equation (6.5) indicates that pure mode 2 fracture energy of an interface can be up to ten times greater ($1/\lambda$) than the pure mode 1 fracture energy for a matrix crack deflecting along the interface, i.e. when $\psi = 0°$, $G_i = G_{i1}$, and when $\psi = 90°$, $G_i = G_{i2}$, with up to a factor of ten difference between them. In the case of $\psi = 0°$, fracture energy can be regarded as being due to purely "chemical" bonding but as $\psi \rightarrow 90°$, fracture energy increases rapidly due to an additional "mechanical" component comprising of both a crack tip shielding mechanism and an interface roughness effect [143,145].

For the condition of composite toughening by matrix crack deflection at an interface, at the point of deflection mode 1 failure mechanism dominates over mode 2. Therefore if $G_{i1} = \lambda G_{i2}$, the majority of values for G_i measured by push-down tests in this work are reasonable and correspond to interfaces that satisfy $G_i < 1/2\ G_f$. For example, if $G_{i2} \sim 10 Jm^{-2}$, a typical value measured with the fibre push-down test, this can reasonably expect to correspond to $G_{i1} \sim 1\text{-}2\ Jm^{-2}$, as $\lambda = 0.1 - 0.2$.

The analysis has not yet been rigorously applied to ceramic matrix composites and therefore a quantifiable G_{i1} for mode 1 failure cannot be derived from the experimental mode 2 G_{i2} that have been determined in this study. Further development is required and the interface roughness has to be quantified.

6.1.2.3 Fracture energy of fibre reinforcement

When analysing the debond energies measured via fibre push-down, and comparing them to the crack deflection condition for toughening, the fracture energy of the fibre reinforcement is required.

For single fibres, this can be found by performing individual tensile tests and measuring strength S. It has been shown with Nicalon fibres that were previously heat treated in air [41], that

$$K_f \sim S\sqrt{a_m} / 3.5 \tag{6.6}$$

where a_m is the fracture mirror radius, K_f is the fracture toughness (mode 1). Therefore, fracture toughness of the fibre was determined by measuring individual fracture mirror radii and tensile strengths, and found to be $K_f \sim 1$ MPa $m^{1/2}$ [41]. This relates simply, using equation (2.9) to a $G_f \sim 5\ Jm^{-2}$ [81].

This value for G_f appears low as recognised fracture energies for glass and glass ceramic monolithics can range from 10-30 Jm^{-2} [81,146]. The practice of heat

treating the fibres in air prior to tensile testing, is not a satisfactory replication of thermochemical conditions during composite fabrication. Work has shown (see Chapter 5), particularly with the carbon pre-coated Nicalon NL-607, that the amount of fibre-matrix reaction during processing can be small. Therefore the heat treatment of fibres in air which causes severe oxidation and modification of surface composition, results in the crack nucleating surface flaws sitting in material that has a different composition to that of normal Nicalon. Therefore the measured G_f does not accurately relate to true G_f of Nicalon.

6.1.2.4 Summary

It is clear that the Marshall and Oliver [89] model applied to determine the debond energy of the fibre matrix interface from push-down tests does not take account of all the influential parameters. The derived G_i are too high because they do not consider residual stress and interface roughness. They are not however, orders of magnitude out as application of the revised Hutchinson and Jensen [130,132] model produced values for CAS/Nicalon that were less than 50% lower. The measured G_i are for pure mode 2 loading of the interface and it has been shown, theoretically, that this may be up to 10 times greater than the mode 1 fracture energy of an interface in the presence of a deflecting crack. The crack deflection condition can therefore be satisfied. The fibre $G_f \sim 5$ Jm^{-2} could be inaccurate as it was measured for Nicalon fibres that would have undergone serious surface modification.

Therefore the G_i reported in Chapter 5 are not unreasonably high. With further analysis and development of the models, G_i as a function of ψ should be able to be determined from push-down tests, interface roughness measurement and fibre and matrix properties. The validity of the crack deflection condition $G_i < 1/4 \rightarrow 1/2\, G_f$, can then be determined for particular composites.

As it currently stands, the push-down test using the SEM based

microindentor, can assess the micromechanical properties of a wide range of CMC interfaces. From this study, a whole range of glass and glass ceramic interfaces have been "ranked" with respect to their bond strength and frictional shear characteristics. This has not been possible before as instrumentation has not been available to do it. Experimentally, the push-down test is one of the simplest techniques available for determination of G_i and τ because of ease of specimen fabrication.

6.2 Correlation of micromechanical behaviour to macromechanical performance

As stated in section 3.3, it was an objective to relate structural characterisation of fibre-matrix interfaces to the recorded micromechanical properties. The work performed on glass and glass ceramic matrix composites is summarised below. Another objective was to correlate G_i and τ to the debond condition and the matrix microcracking stresses and ultimate bend strengths. Using the theoretical relationships of Chapter 2, this was attempted for some of the composites studied.

6.2.1 Comparison of interface structure to micromechanical behaviour

A major objective was to correlate micromechanical behaviour to the in-situ formed interface structure in glass ceramic matrix composites. This proved difficult as the quality of material supplied by some sources was not good enough to provide consistent data, even across a single specimen. High proportions of porosity and matrix cracking affected the recorded micromechanical behaviour. However, from the CAS/ Nicalon, BMAS/Tyranno and BAS/Nicalon data, it was observed that the thickness of a continuous carbon interface did not have a significant effect on τ and that such interfaces had considerably lower G_i and τ in comparison to interfaces comprising phase mixtures of silica and carbon crystallites.

The considerable effect that residual stress has on micromechanical

properties can be demonstrated. The CAS/Nicalon interface is structurally similar to the interface of the LAS III/Nicalon composite that has been the subject of intensive study within the literature. They have similar composition and width, being carbon rich and approximately 100-200 nm wide [75,76,95]. However, their different matrix coefficients of thermal expansion result in residual stresses across each interface that are opposite in direction. CAS/Nicalon has a compressive stress, whilst LAS/Nicalon has a tensile stress that can result in gaps being present at the interface [76]. Using Marshall and Oliver [89] to analyse the fibre push-down data for these materials, they are seen to have very different G_i and τ. For CAS/Nicalon; $G_i \sim 5$ Jm^{-2} and $\tau \sim 25$ MPa (Table 5.1), and for LAS/Nicalon; $G_i \sim 4\text{x}10^{-2}$ Jm^{-2} , $\tau \sim 2$ MPa [89].

Another example of this is the comparison of the LAS and MAS matrix materials reinforced with Nicalon NL-607, that were prepared at Warwick [110,112]. The carbon coated fibre was incorporated within LAS and MAS matrices, with the processing conditions being similar [110,112]. As the presence of the carbon reduces the amount of interface reaction during processing [110], the structure and composition of the interfaces would be expected to be similar. However, micromechanical properties are again different; MAS $G_i \sim 12$ Jm^{-2} and MAS $\tau \sim 30$ MPa, and LAS $G_i \sim 2$ Jm^{-2} and LAS $\tau \sim 15$ MPa, (see Tables 5.1 and 5.2). Such large differences almost certainly arise from the opposite directions of stress across the two types of interface.

The effect of interface modification via oxidation and its influence on micromechanical behaviour was measured successfully. For Nicalon reinforced CAS and MAS matrices and Tyranno reinforced BMAS, the changes in interface structure characterised by other workers were seen to correlate with changes in G_i and τ. The formation of localised, strongly bonding silica bridges across the interfaces was recorded as increases in G_i and τ that had large statistical distributions. This was due to the irregularity of the formation of bridges along an interface. The embrittlement of interfaces via this mechanism coincided with overall embrittlement of the composites, as measured by three-point bend testing [110,113]. (As stated in Chapter 5, degradation

in composite performance is due in a large part to degradation in strength of the reinforcing fibres due to the oxidation of their surfaces, not only to the change in interface G_i and τ).

There is a relationship between the relative increase in G_i and τ caused by the silica bridging, and the thickness of the carbon rich interphase originally present in

Composite	Carbon interface width (nm)	$\frac{G_i (750°C)}{G_i (as\text{-}fab.)}$
CAS/Nicalon	150	4.8 / 5.4 ~ 1
MAS/Nicalon NL-607	55	36 / 12 = 3
BMAS/Tyranno	20	46 / 5 ~ 9

Table 6.1 Comparison of carbon rich interface widths with relative increases in measured debond fracture energies.

the heat treated specimens. If G_i for the 750°C heat treatment, divided by the as-fabricated G_i, is plotted against the interface thickness, an inverse relationship is observed. The thinner the carbon layer, the greater the relative increase in G_i when bridged by silica, see Table 6.1 and figure 6.4.

The silica bridging material is essentially the same across these interfaces. Therefore, the differences in bonding strengths, as measured via fibre push-down, could possibly be due to the thickness of interface. The thinner the interface, the shorter the silica bridge that spans it, and therefore the less "leverage" is applied to the bridge

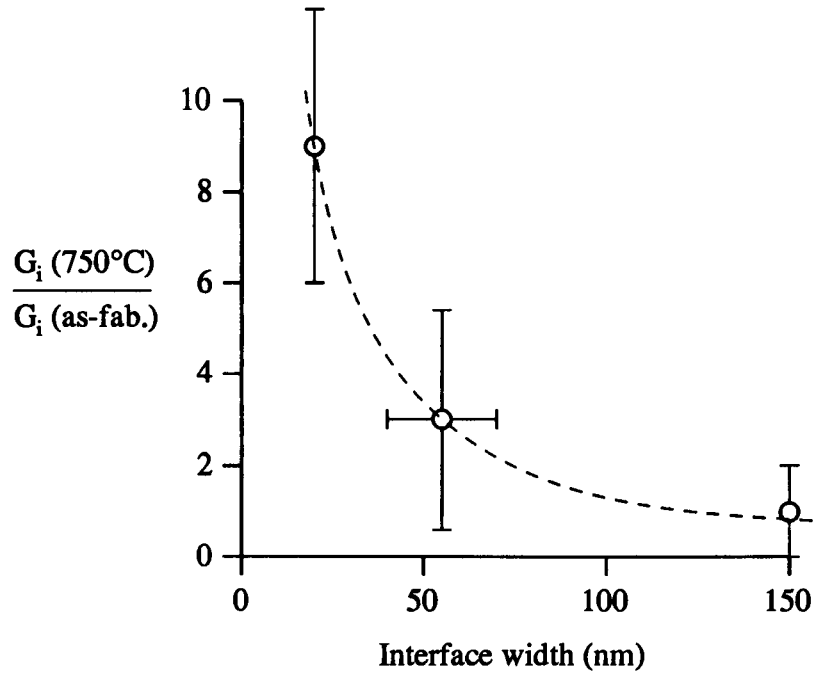

Figure 6.4 Relative increase in debond energy vs. original carbon rich interphase width for oxidised interfaces of BMAS/Tyranno, MAS/Nicalon NL-607 and CAS/Nicalon.

when load is applied to the fibre. Longer spans, in wider interfaces, undergo a higher leverage at the same load and so will break at lower loads. Therefore it is possible thin carbon interfaces, when replaced by localised silica bridges, have larger increases in measured G_i because interface thickness and the leverage it undergoes are not accounted for in any push-down model.

This is only a tentative hypothesis and needs further investigation as there are other possible reasons for the different increases in G_i that are not interface width dependent, such as differences in volume fraction of the interface gap occupied by silica.

The pre-synthesis of interfaces via fibre coating has been shown to significantly alter interface response. The CVD bi-layer coating of Nicalon illustrated how an extra coating can be applied to protect the original one, deposited to introduce

the desirable interface behaviour. It also illustrated the potential to tailor G_i and τ independently, i.e. achieve a high G_i with a low or moderate τ. The use of Nicalon NL-607 showed the improvement in mechanical properties that can be achieved by tailoring interface properties but also by reducing mechanical and thermochemical damage to fibres during processing.

Micromechanical measurements of fatigue tested material has shown that G_i and τ change with operating conditions, over time. The fall of G_i to zero once cyclic testing has started, indicates that for a real component in service, τ may well be the most important parameter to tailor as it is that which will dominate the CMC behaviour over its lifetime (especially if applied stresses are regularly higher than the matrix microcracking stress). When the wear mechanism that reduces τ over time is identified, interfaces can be tailored by fibre pre-coating to minimise the wear and so keep τ as constant as possible over the service lifetime.

Interface roughness has been discussed above with respect to the effect it has on G_i measured in mode 2 loading. It also effects τ significantly. The work performed on Borosilicate glass reinforced with NL-607 (section 5.3), illustrates how the roughness can effect both parameters. Residual stress considerations are not required as the matrix and fibre have the same thermal expansion coefficient. The very rough interface of the 1100°C/60 min. processed material gave rise to the highest debond energy, $G_i = 54 \pm 24$ Jm^{-2}, of the four composites, even though voids were present along the interface. This was double the G_i of the 950°C materials. (It must be noted however, that the extensive reaction during processing that produced the rough interface could also cause a significant amount of "chemical" bonding between fibre and matrix). Increase in frictional shear to $\tau = 229 \pm 160$ MPa compared to the 950°C composites where $\tau = 160 \pm 80$ MPa, suggests that roughness contributes significantly to the micromechanical behaviour of the 1100°C/60 min. Borosilicate composite.

6.2.2 Matrix microcracking dependence on τ

The ultimate goal for CMC material designers is to tailor G_i and τ to optimise the composite mechanical properties. To do this, the optimum ranges for G_i and τ need to be quantified for individual composite systems and particular applications, by experimental verification of theoretical considerations relating the interface properties to the overall mechanical performance. An attempt has been made to correlate the models describing mechanical properties (outlined in section 2.1.2) with the interface data recorded earlier.

Assuming G_i is low enough to enable crack deflection toughening at an interface, it is interfacial τ that governs the matrix microcracking stress σ_m, see equations (2.19) and (2.27). For three of the composites studied earlier, the τ measured with the SEM microindentor was incorporated into equations (2.19) and (2.27) in an attempt to correlate theoretical and experimental σ_m. Lists of the fibre, matrix and composite properties used in the equations for the three composites CAS/Nicalon, MAS/Nicalon NL-607 and Borosilicate/Nicalon NL-607, are given in Appendix III(a).

Moderate agreement between σ_m and τ has been obtained (see Table 6.2). Microcracking stresses were estimated from thresholds for significant acoustic emission from 3-point bend specimens ; this is considered more reliable than detection of the non-linearity in stress / strain curves. Figure 6.5 is an example from a MAS/ Nicalon NL-607 bend test with acoustic emission and stress / strain curve superposed. It is the uncertainty in determining the exact microcracking stress that inhibits the precise correlation between σ_m and τ. Pure tensile testing would give more marked differences in both stress / strain curves and acoustic emission levels at matrix cracking, and so make its detection easier because of the larger specimen volume actually under tension. The coefficients of thermal expansion of the matrices (α_m) are given to indicate thermal expansion mismatch. For Nicalon, $\alpha = 3.2\times10^{-6}\ °C^{-1}$, equal to that for Borosilicate glass.

Composite	G_i / Jm^{-2}	τ / MPa	α_m / $10^{-6}°C^{-1}$	σ_m / MPa	Theoretical σ_m / MPa
CAS/Nicalon (Corning)	5 ± 1	24 ± 2	4.5	390 ± 30	450
MAS/Nicalon NL-607	12 ± 5	48 ± 15	5.5	640 ± 50	690
Borosilicate/Nicalon NL-607	20 ± 7	51 ± 9	3.2	600 ± 100	510

Table 6.2 Interfacial debond energy and frictional shear stress for various glass and glass ceramic matrix composites together with experimental and theoretical matrix microcracking stresses.

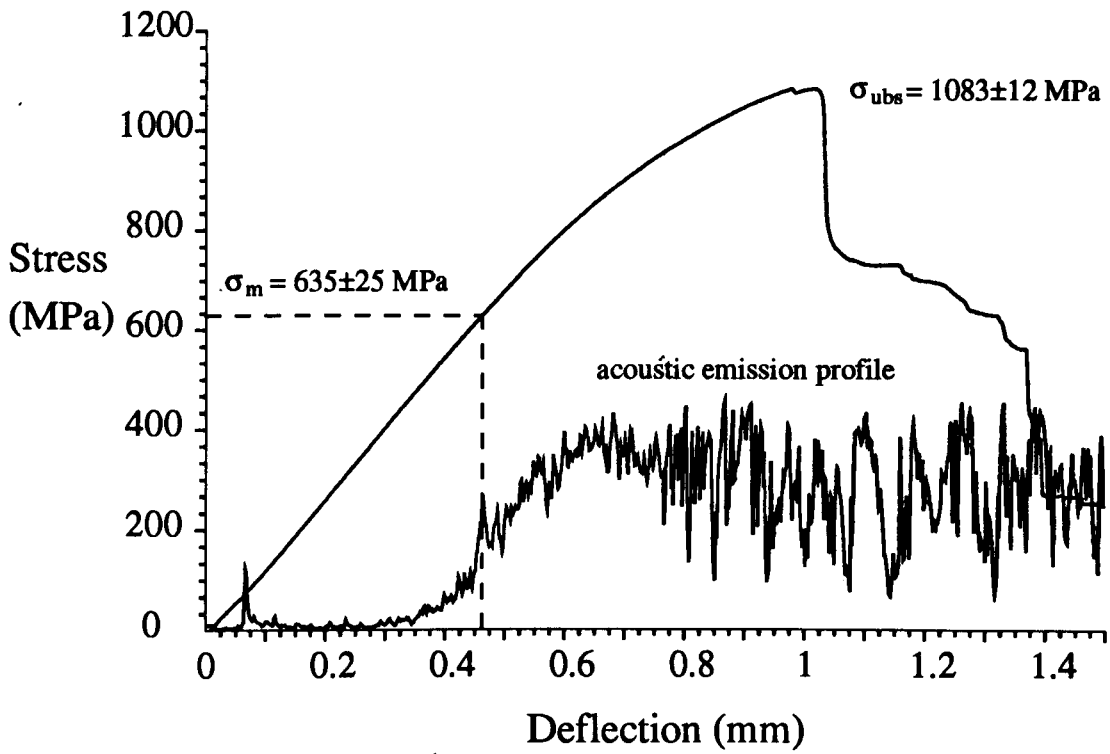

Figure 6.5 Three-point bend stress-deflection plot for high strength Nicalon NL-607 reinforced MAS matrix. Acoustic emission from composite recorded to indicate initiation of matrix cracking (taken from [110]).

6.2.3 Transition to brittle failure

As the frictional shear τ of a particular system is increased, the σ_m increases and the σ_u decreases, as long as $m > 2$ (m is Weibull modulus of fibre strength, see section 2.1.2). At the point where $\sigma_m = \sigma_u$, brittle failure occurs. An upper bound to τ for tough fracture can be obtained by equating the microcracking stress to the ultimate strength of the composite for the case where $m = \infty$, i.e. by equating equations (2.27) and (2.20) as ;

$$V_f S = \left[\frac{6 \tau G_m E_f E_c^2 V_f^2}{r (1-V_f) E_m^2}\right]^{1/3} - q\frac{E_c}{E_m} \tag{6.7}$$

For the glass ceramic matrices of CAS and MAS, the upper bound for τ is 180 MPa and 130 MPa respectively. The residual stress free composite of Borosilicate matrix reinforced Nicalon has an upper bound of $\tau \sim 280$ MPa. The calculation of these limits is described in Appendix III(b).

In this project, the τ that were recorded for these real composites that showed tough behaviour, were never higher than these limits. In particular, some of the Borosilicate matrix materials with $\tau \sim 150 - 230$ MPa (Table 5.4), satisfied the above condition and showed tough, composite like mechanical behaviour under 3-point bend test (Table 5.5). These high τ, that approach the upper limit of 280 MPa and yet still produce toughness, are possible because the coated fibres (Nicalon NL-607) retain much of their pristine condition within the matrix, and therefore a high value of m. Thus the actual σ_u is closer to the expression for its upper bound (σ_u for $m = \infty$), and so equation (2.20) is more applicable.

For the CAS and MAS interfaces that were heat treated (sections 5.2.2 and 5.2.3.2), brittleness occurred when for the MAS, τ increased to a higher level than the above limit of 130 MPa (see figure 5.15), and for CAS, τ increased but did not approach the limit of 180 MPa (see figure 5.10). The CAS material did not have a

carbon coating deposited on the fibres prior to composite fabrication.

Thus it is clear the theoretical upper limit for τ obtained from equation (2.20), can be approached with a composite retaining its toughness, if the fibres do not undergo significant mechanical or thermochemical damage during processing or subsequent heat treatment.

The evidence above suggests the statement that the necessary condition for a tough ceramic matrix composite is 2 MPa $< \tau <$ 40 MPa (from [41]), is incorrect (as suggested in Chapter 3, section 3.1). The existence of high frictional shear stresses, i.e. in tough composites where $\tau >$ 40 MPa, is further illustrated with a tough Nicalon reinforced silicon carbide matrix that has been reported to have τ = 100-150 MPa [83].

6.2.4 Summary

Although rigorous, quantitative analysis has not been achieved, correlation of interface structure with the measured micromechanical properties has been possible. Effects on the interface properties of residual stresses, oxidation, fatigue testing and roughness, have all been measured.

Moderate agreement of mechanical properties with the micromechanical measurements has been obtained, using the descriptions of CMC behaviour in Chapter 2. Both the predicted dependencies of matrix microcracking stress and transition to brittle behaviour with τ have been demonstrated.

CHAPTER SEVEN

ALTERNATIVE INDENTOR APPLICATIONS AND FURTHER DEVELOPMENT

An objective of the project was to explore alternative applications of the SEM based microindentor. Examples that have been investigated take advantage of one or all of the SEM indentor's capabilities of high spatial resolution, dynamic imaging of the indentor-specimen contact zone, or continuous load and displacement measurement during indentation.

7.1 Controlled crack propagation

Fracture-mechanics studies that enable direct observation of crack/ microstructure interaction are possible with the SEM microindentor. Controlled crack growth that can be observed at high magnification, offers great potential to the researcher investigating crack tip/interface interactions within ceramic composites of all types. There is the possibility of observing directly the microstructure dependent mechanisms in the crack wake that give rise to "rising resistance" or R-curve behaviour present in transformation toughened, particulate reinforced and fibre reinforced composites.

A short study has been performed on two fibre reinforced glass ceramic composites, CAS/Nicalon (as fabricated) and BMAS/Tyranno (oxidised interfaces - fully silica bridged). Cracks were introduced by indenting a fibre on the specimen surface until radial cracks were nucleated that progressed into the matrix. With increasing applied load, the cracks were propagated in a controlled manner and observed directly at high magnification. The crack front interaction at the fibre-matrix

interface was observed as it happened. Illustrative images, taken after indentation, are shown in figures 7.1 and 7.2.

The CAS/Nicalon showed typical tough composite behaviour in that matrix cracks were deflected around the fibre-matrix interfaces and not through the reinforcing fibres (see figure 7.1). It is a clear illustration of the crack deflection mechanism introduced by low G_i. Note that all crack/interface interactions result in deflection, whatever the angle of incidence between crack and interface.

Figure 7.2 shows the typical behaviour of a brittle fibre reinforced composite caused by an extremely high G_i. This particular material was oxidised for 500 hours at 1100°C [113]. The interfaces were taken from near the end of a specimen so that they were fully silica bridged. Fibre push-down tests were not possible as the fibres were so well bonded to the matrix, they fractured under the high applied loads

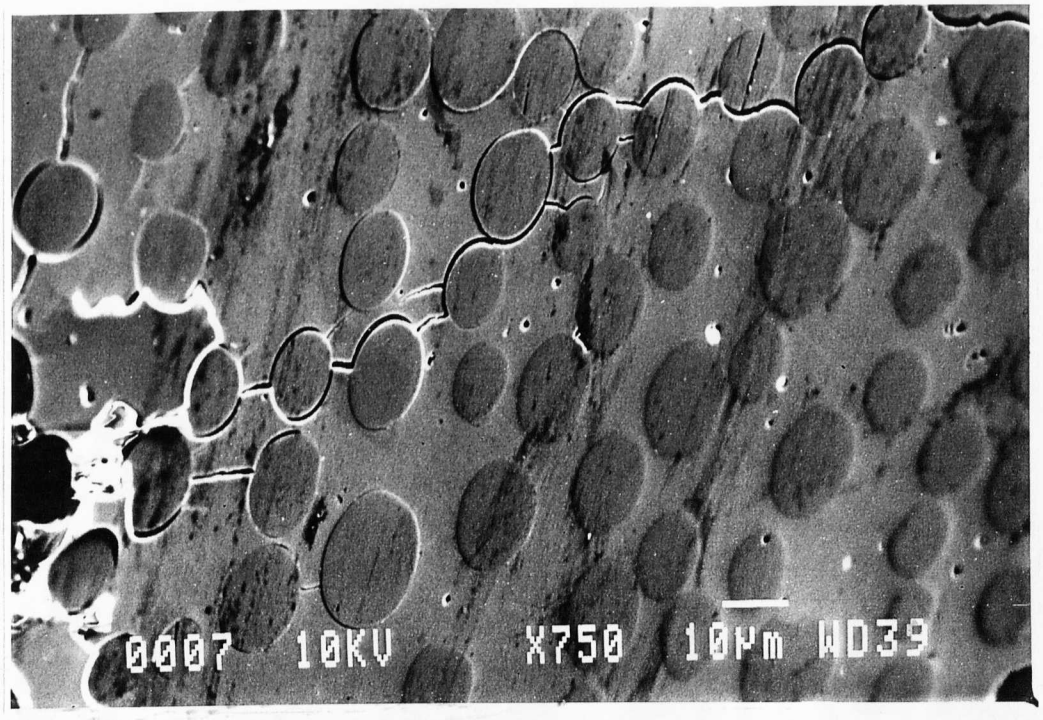

Figure 7.1 SEM secondary electron image of controlled crack growth experiment in CAS/Nicalon composite, showing tough crack deflection mechanism at the fibre-matrix interface.

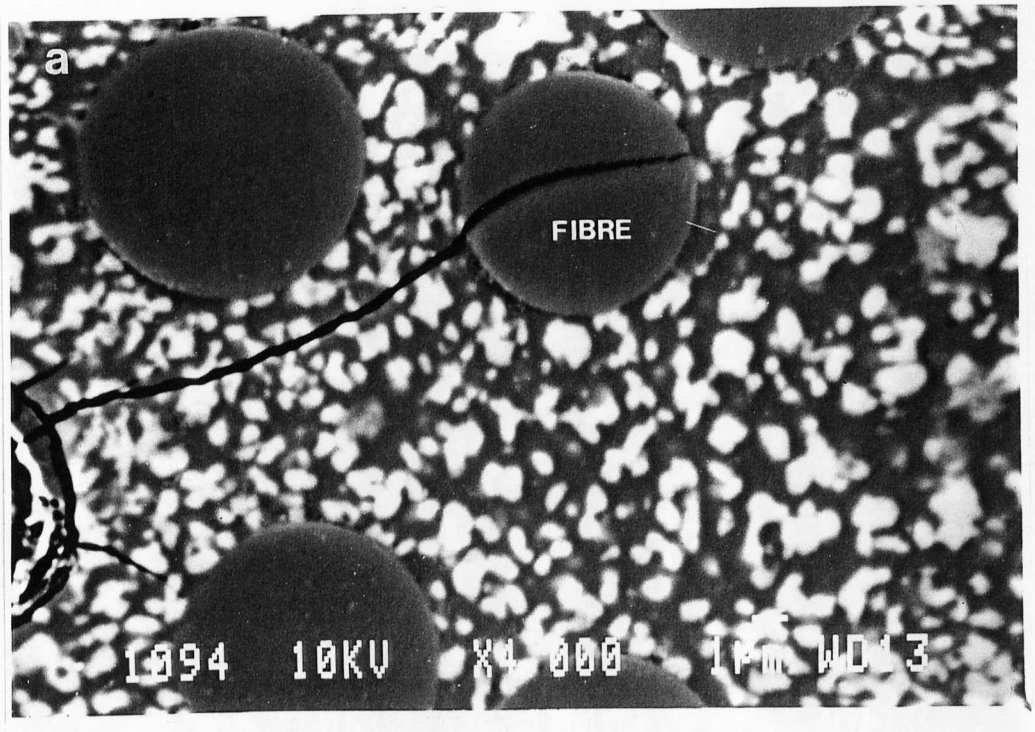

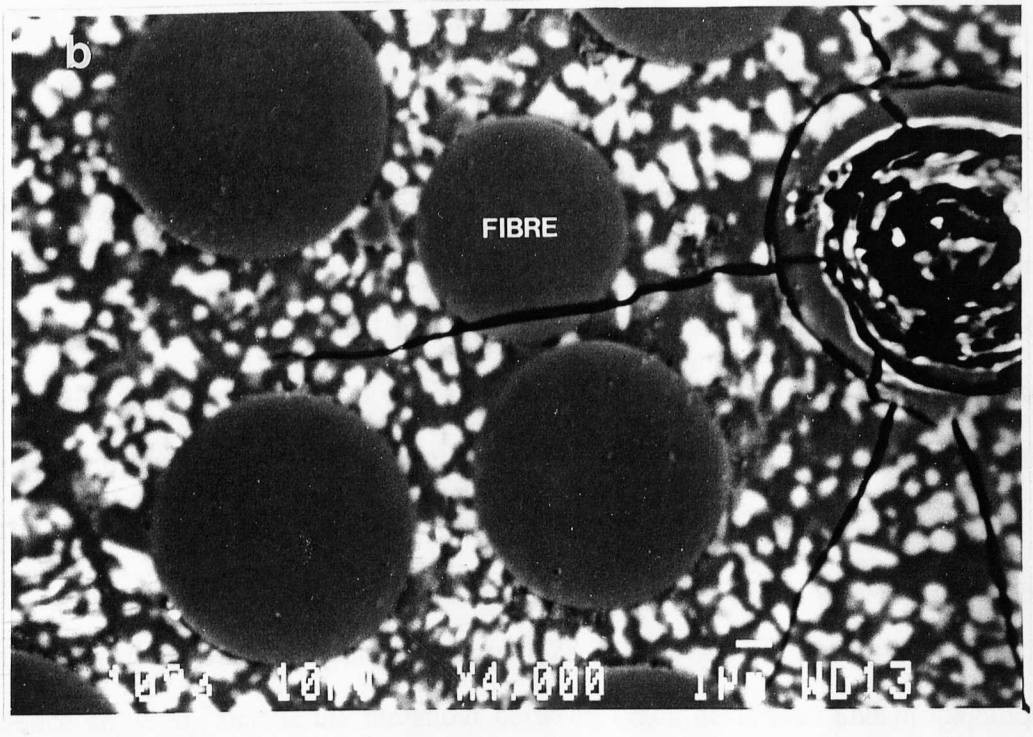

Figure 7.2 (a),(b) SEM back scattered electron images illustrating no crack deflection at the fibre-matrix interface of BMAS/Tyranno composite.

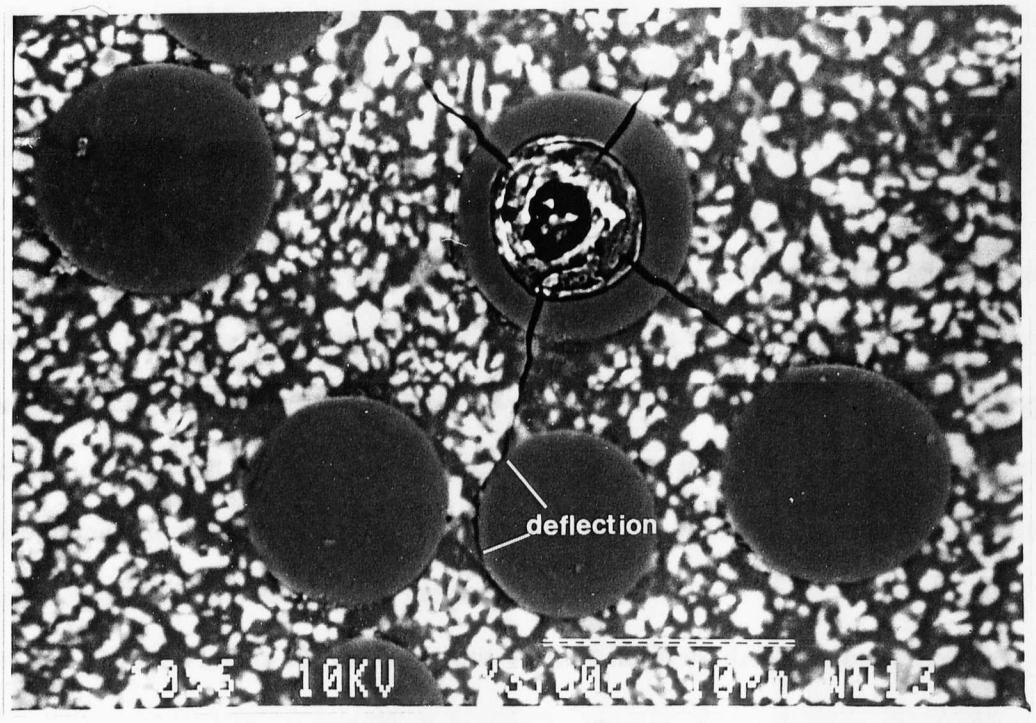

Figure 7.2 (c) SEM back scattered electron image showing crack deflection at the interface in BMAS/Tyranno for a shallow incident angle.

before they were debonded. In the majority of cases, cracks were not deflected by the fibre-matrix interface. As can be seen in figure 7.2(a,b), matrix crack propagation continued through the fibres and into the matrix on the other side. Examples of both high (ω ~85°) and moderate (ω ~40°) angles of crack/interface incidence are shown, both resulting in no crack deflection. However, crack deflection was observed at an interface with a lower angle of incidence ($\omega \sim 30°$, see figure 7.2(c)).

As stated in Chapter 2, the lower the angle of crack/interface incidence, the more likely that crack deflection occurs ([28,38]). With further investigation the incidence angle ω_c, that is the threshold between crack deflection and propagation at the interface, could be measured and the ratio G_i / G_f for the interface be determined. It

is expected to be very high, $G_i / G_f > 1$ (see reference [38]).

7.2 Hardness and Modulus measurement

7.2.1 Hardness testing

The hardness of a material is determined by indenting a flat surface with a known load and measuring the area of the indentation that is left in the surface. The geometry of the indentor tip must be known. The definition of area is dependent on the type of hardness test being used. For Vickers hardness, the area is the total surface area of the indentation, whereas for Knoop hardness it is the area of the elongated diamond shape that is left in the surface i.e. the projected area.

For a Vickers diamond tip, the Vickers hardness (H_V) is determined by

$$H_V = F / A \tag{7.1}$$

where F is the applied load and A is the surface area of the indentation. For experimental ease, the surface area of the pyramidal geometry of the Vickers diamond with standard apex angle of 136° can be calculated for an indent diagonal length d. Hardness then becomes,

$$H_V = 1854\, F / d^2 \tag{7.2}$$

for H_V in GPa, F measured in N and d measured in μm. H_V is determined by first optically aligning an area to be indented with x-y stage control, precisely traversing the stage to beneath the indenting tip, performing the indentation, traversing the stage back to beneath the optical microscope, and measuring the diagonal length of the projected square on the surface.

This procedure is laborious and for small indentations (d< 5μm) in localised areas on a specimen, the x-y stage resolution of a microindentor (typically ± 5μm) may not be good enough for precise location and indentation. Such small indents are also difficult to measure accurately with optical imaging techniques.

The SEM microindentor was used to perform hardness tests. Its capability of simultaneous imaging, and measurement of load and displacement, its ease of use and high spatial resolution was demonstrated.

To image an indentation throughout the cycle, a Vickers diamond could not be used (at an SEM stage angle of 45°) as its apex angle of 136° is far greater than the maximum allowable of 90° (see Chapter 4). The diamond used for the fibre push-down tests was therefore used (see figure 4.8). To determine hardness, the surface area of the diamond tip was required as a function of its length i.e. as it was conical, its surface of revolution had to be determined. This was performed by taking a high contrast SEM image of the tip in profile, printing it at A4 size and plotting its profile on graph paper placed over it. The coordinates of the curve describing the surface profile were then read off the graph paper and used with PC based curve fitting software ("Sigmaplot") to derive a polynomial expression for the radius of the tip as a function of its length. The image used is shown in figure 7.3 (at smaller print size). The profile is illustrated in figure 7.4, with half the data mirrored in the symmetrical axis, and the fitted curve shown. The fitted curve is only applicable to indent depths of less than 4μm. Tip length (or depth) δ for the radius of the cone ρ was,

$$\delta = -3.524\text{x}10^{-3}\,\rho^4 + 3.038\text{x}10^{-2}\,\rho^3 + 4.383\text{x}10^{-2}\,\rho^2 + 6.267\text{x}10^{-2}\,\rho \qquad (7.3)$$

with δ and ρ in μm.

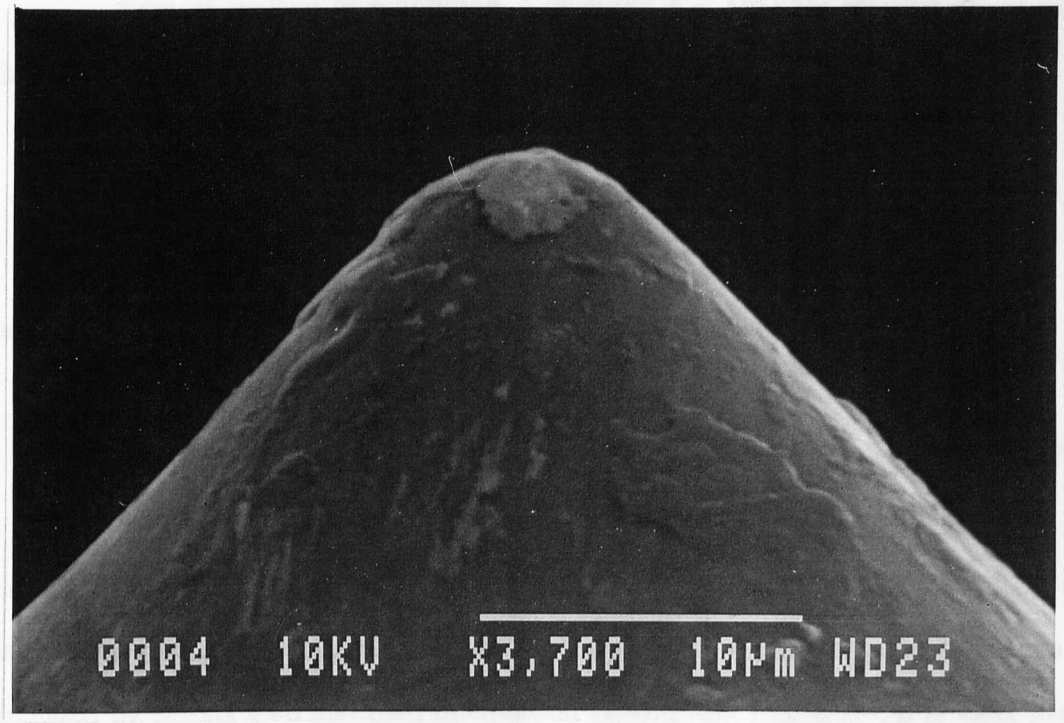

Figure 7.3 High magnification SEM image showing profile of diamond indenting tip.

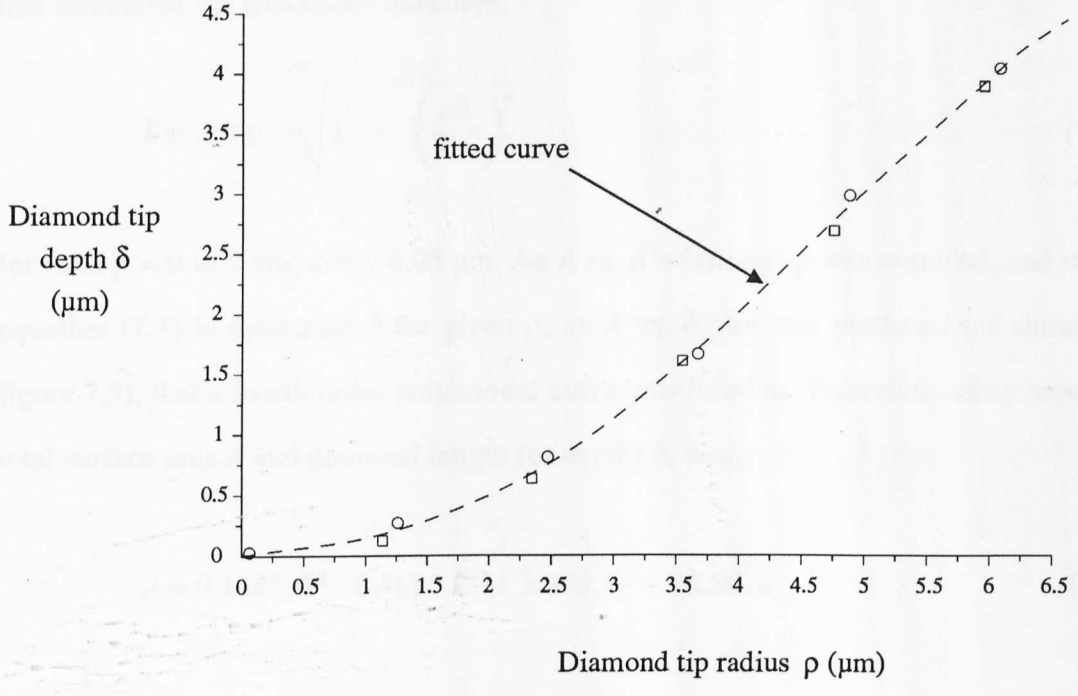

Figure 7.4 Diamond tip length or depth δ vs. radius ρ trace. Both left hand side and right hand side of profile are plotted together to aid fitting of polynomial curve, as shown.

Area of surface of revolution A of curve $\delta = f(\rho)$ for rotation about the δ axis is given by,

$$A = \int_a^b 2\,\pi\,\rho.\,ds \tag{7.4}$$

where,

$$ds = \sqrt{1 + \left(\frac{d\delta}{d\rho}\right)^2}\; d\rho \tag{7.5}$$

ds is the incremental arc length of the curve. Combining equations (7.3, 7.4, 7.5), the total surface area of the diamond between the very tip and 4 μm along the δ axis can be calculated by setting a=0 and b=6 in equation (7.4). From figure 7.4, it is clear that a depth of 4 μm, corresponds to a radius of approximately 6 μm, and therefore b=6 in equation (7.4). The integration was performed empirically by writing a short program that calculated the area under the curve,

$$\delta = 2\,\pi\,\rho\,\sqrt{1 + \left(\frac{d\delta}{d\rho}\right)^2} \tag{7.6}$$

for radii ρ = 0 to 6 μm, every 0.05 μm. An A *vs.* ρ relationship was obtained, and using equation (7.3) to determine δ for given ρ, an A vs. δ plot was produced (as shown in figure 7.5), that a fourth order polynomial curve was fitted to. The relationship between total surface area A and diamond length (or depth) δ, was,

$$A = 0.1185.\,\delta^4 - 0.4654.\,\delta^3 + 3.059.\,\delta^2 + 25.56.\,\delta \tag{7.7}$$

Thus, for an indentation of depth δ, its surface area is given by A.

It was then possible to perform hardness tests on materials that did not require post-indentation observation to measure the indent size, as the area was

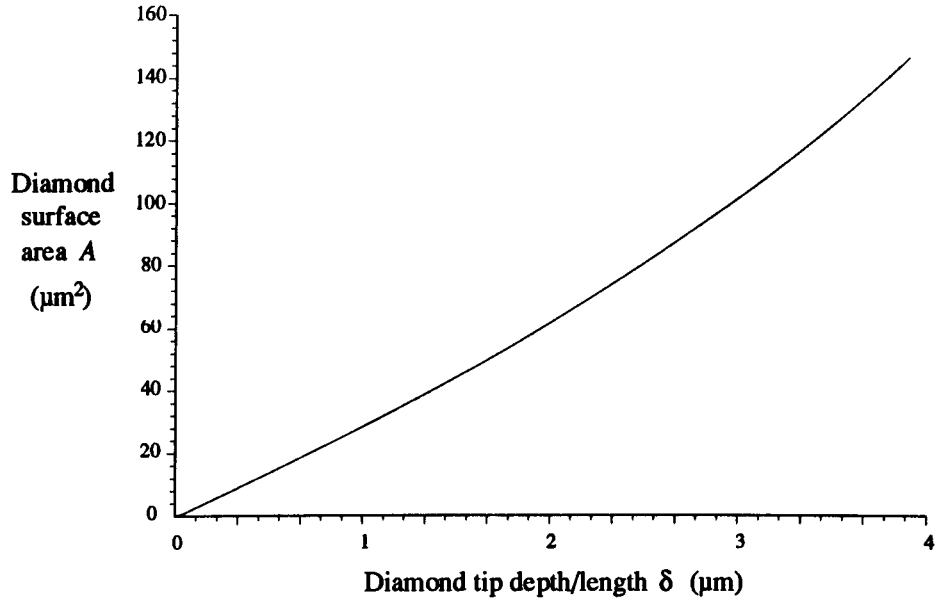

Figure 7.5 Relationship between surface area of diamond and distance along from its tip. Equation (7.7) describes the curve.

determined by measuring the indent depth from the load/displacement data (using equation (7.7)). To determine hardness, load was taken as the maximum applied load F_{max}, and indent depth was taken as the tip displacement where the load dropped to zero on unloading δ_{ind} (see figure 7.6). Thus,

$$H_{SEM} = F_{max} / A \tag{7.8}$$

where H_{SEM} is the hardness determined with the diamond in figure 7.3, and A is determined using δ_{ind} in equation (7.7).

7.2.2 Measurement of elastic modulus

The measurement of elastic modulus E from a microindentation experiment is based on the original analysis of Sneddon [147] for the load F vs displacement δ

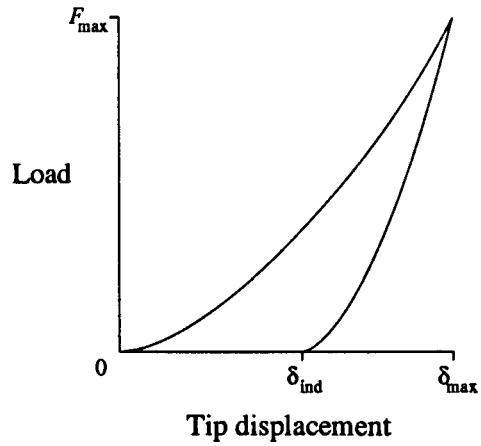

Figure 7.6 Schematic of typical load/displacement trace for indentation of a ceramic material. Indent area is calculated by recording indent depth δ_{ind} *and using equation* (7.7).

relationship of a flat cylindrical punch indenting a surface. Recent analyses indicate the method is valid for most contact geometries [148]. For various tip geometries, the following differential expression was derived,

$$\frac{dF}{d\delta} = \beta \frac{2}{\sqrt{\pi}} \sqrt{A_p}\, E_r \tag{7.9}$$

where $dF/d\delta$ is the experimentally measured stiffness of the upper portion of the unloading curve (see figure 7.8), β is a geometrical constant, A_p is the projected area of the contact and E_r is the reduced modulus defined as,

$$\frac{1}{E_r} = \frac{(1 - \nu^2)}{E} + \frac{(1 - \nu_i^2)}{E_i} \tag{7.10}$$

with E, ν the elastic modulus and Poisson ratio of the material being studied and E_i, ν_i those of the indenting tip. For Vickers and Berkovich geometries, $\beta = 1.012$ and $\beta = 1.034$ respectively. For a geometry described by a surface of revolution, as in the

current investigation, $\beta = 1$.

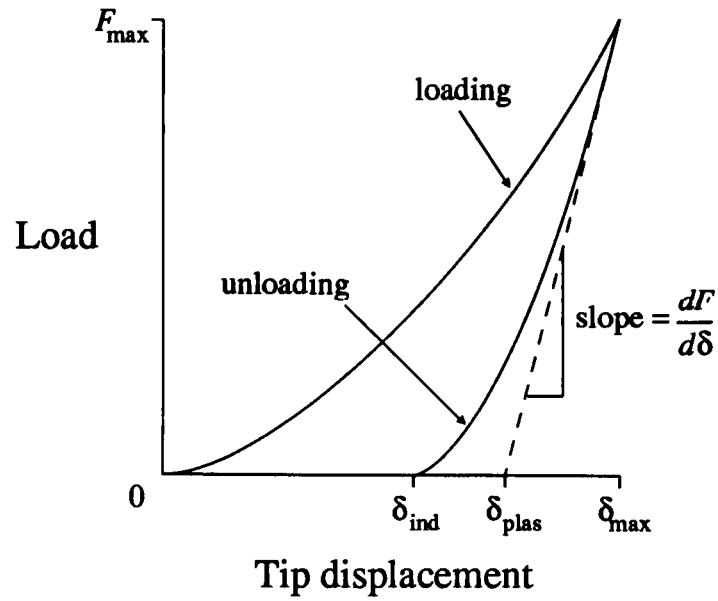

Figure 7.8 Schematic load vs. displacement curve for an indent in a ceramic material. Measurement of the initial unloading slope enables determination of elastic modulus.

The projected contact area A_p, is not that of the final indentation after tip withdrawal, but that of the circle with radius a in figure 7.9, i.e. the contact radius at maximum applied load F_{max}. It is given by the x-axis intercept δ_{plas} of the tangent to the initial unloading slope [149] (see figures 7.8, 7.9).

Two short studies were undertaken, measuring the hardness and modulus of two ceramic composite materials, Syalon 101 and TiB_2 particulate reinforced Si_3N_4.

7.2.3 Syalon 101

Syalon 101 was studied to compare measurements taken with the SEM indentor with previous work performed on a conventional Vickers hardness tester

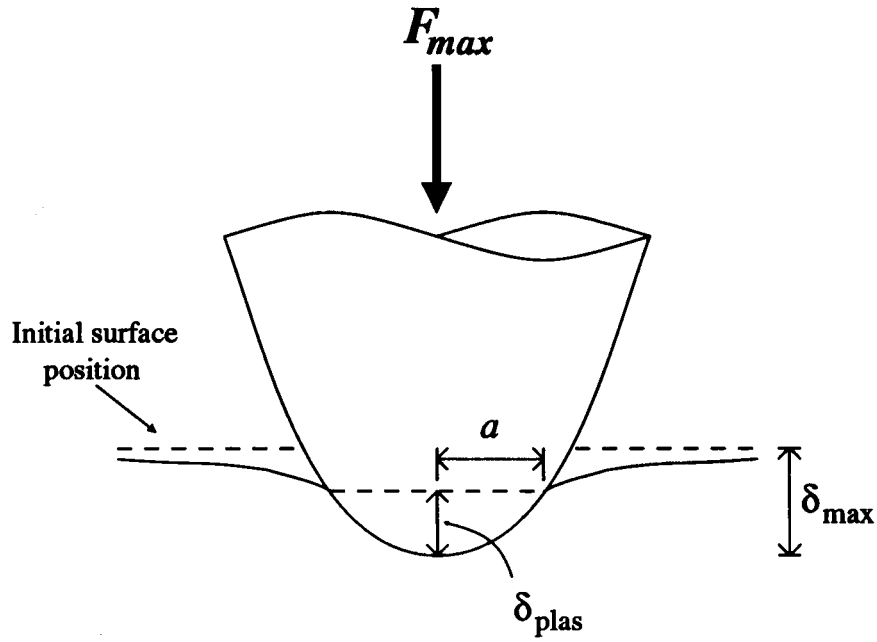

Figure 7.9 Schematic geometry of indentation at maximum applied load, taken from [148].

[150]. A number of indentations were made in a specimen polished to a 0.25μm diamond polish finish [150]. An applied load range of 0.07N to 1 N was chosen to illustrate the capability of the instrument to bridge the resolution gap between nano- and micro-indentation. The hardness measurements for each indentation are shown in figure 7.11. Mean hardness was H_{SEM} = 26 ± 3 GPa. There was no noticeable indentation size effect - the often observed increase in measured hardness with lower indentation loads (for information see [151]).

Typical indentation traces are shown in figures 7.11 and 7.12, with maximum applied loads of 0.277 N and 0.079 N respectively. The low load indentation is almost at the resolution limit of the instrument. It should be noted however that no signal averaging or curve smoothing procedures were carried out in obtaining the data. If signal averaging were to be carried out, resolution would be improved. The loading and unloading curve superimposed on the data in figure 7.12 was drawn in to aid illustration.

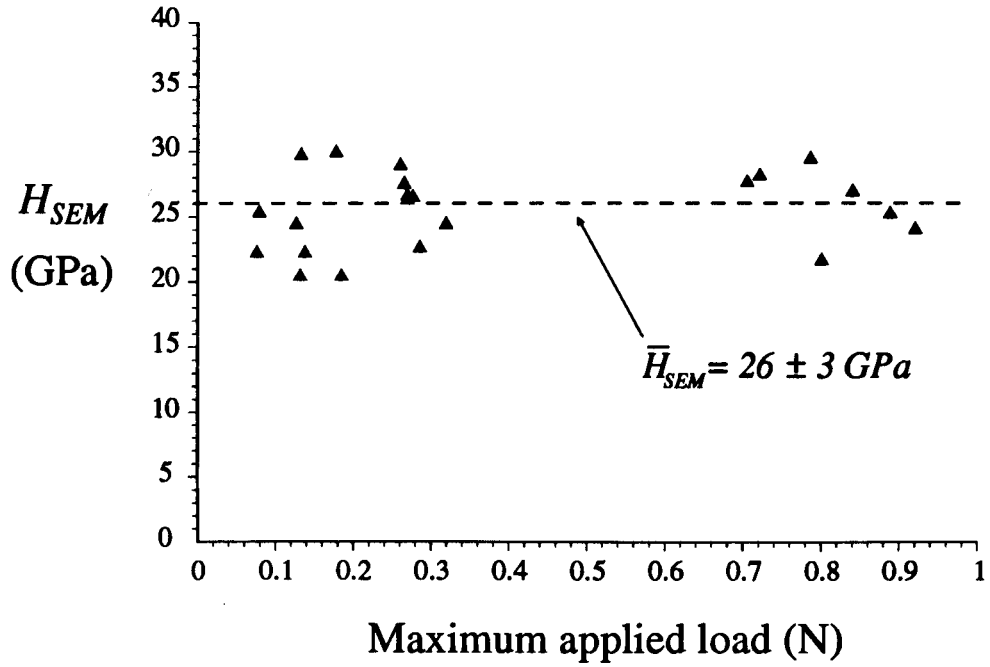

Figure 7.10 Hardness vs. applied load plot for sub 1N indentations in Sialon 101. Average H_{SEM} = 26 ± 3 GPa.

Elastic modulus was determined by writing a small program in BBC BASIC that measured all relevant gradients and axis intercepts (this has not been documented). Modulus and Poisson ratio of diamond were taken as E_i = 960 GPa and ν_i = 0.20, the Poisson ratio of sialon was ν = 0.27, (all from reference [152]). The elastic modulus determined for Syalon 101 for sub 1N indentation was E = 270 ± 40 GPa.

These values compare to Vickers hardness for Syalon 101 of H_V=13-17 GPa for indent loads from 100 - 20 N respectively [153,154], that increase to H_V > 30 GPa as indent load reduces to less than 2N [150,153], due to the indentation size effect. The H_{SEM} values are therefore of the correct magnitude, but not directly comparable with the Vickers hardness measurements taken at different applied loads. For a direct comparison between hardness measurements made with the two different tip geometries, a Vickers diamond with an accurately known surface area profile (particularly with respect to the bluntness of the very tip, see below) needs to be used with similar applied loads that were used in the above experiment. This can be

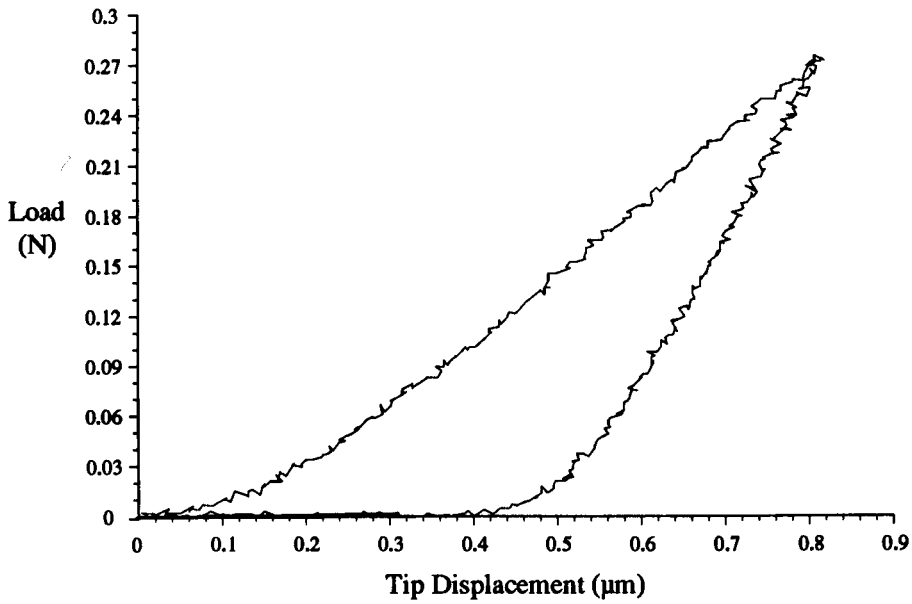

Figure 7.11 Load vs. displacement trace for an indentation, maximum applied load of 0.28 N, in Syalon 101.

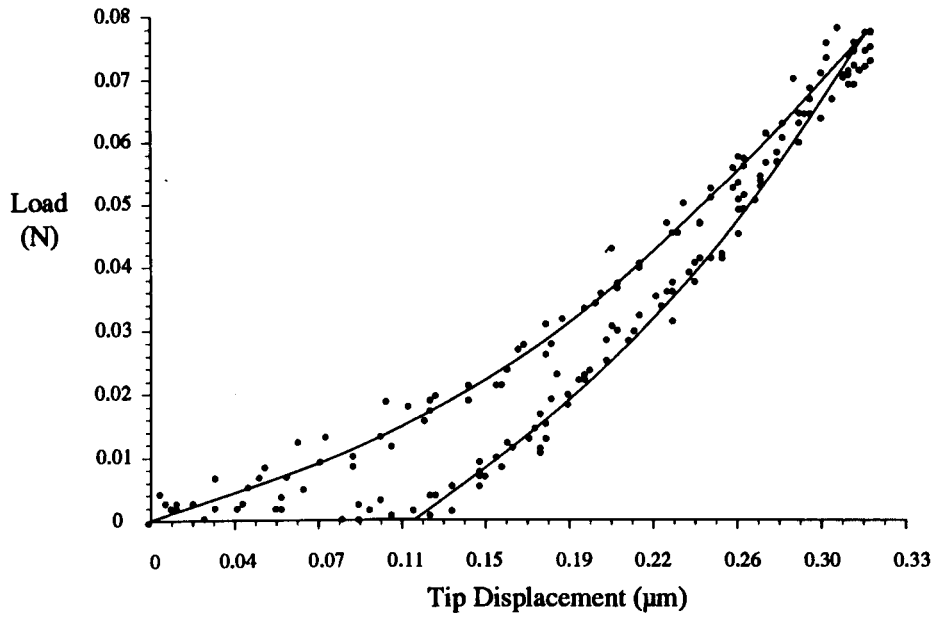

Figure 7.12 Load vs. displacement trace for indentation, maximum applied load of 0.08N, in Syalon 101.

performed on the SEM indentor by simply attaching a Vickers diamond to the apparatus.

The lack of a noticeable indentation size effect on hardness, across the indentations in figure 7.10, may be attributable to the fact that the area of the tip is known accurately as a function of its depth. Doerner and Nix [149] showed that the use of blunt Vickers or Berkovich diamond tips results in an indentation size effect for shallow indents ($\delta_{ind} < 0.5$ μm), due to the tip's actual surface area being inaccurately described by the particular geometrical relationship for that indentor.

Elastic modulus for Syalon 101, measured by tensile testing of bulk material is given as E = 300 GPa [152], and therefore the measurement made by indentation compares well.

7.2.4 TiB_2 particulate reinforced sialon

The high magnification imaging of a surface immediately prior to and during indentation, enables precise location of the actual indentation zone. Finely dispersed secondary phases within a matrix can be indented and their hardness and modulus measured. An in-situ reaction sintered TiB_2 particulate reinforced sialon [154,155] has been studied to test the viability of indenting secondary phases. The typical TiB_2 particle size was less than 5μm. Examples of small indentations (approximately 2μm diameter) in both matrix and particulate, are shown in figure 7.13(a,b).

Six indentations (with $F_{max} < 0.3$N) were made in each of the sialon and TiB_2, and hardness and modulus determined for each material. Table 7.1 gives the derived H_{SEM} and E, and figure 7.14 compares typical load-displacement traces for both sialon and TiB_2 on the same axes.

For the sialon matrix, $H_{SEM} = 29 \pm 4$ GPa and $E = 315 \pm 20$ GPa. These are consistent with those for Syalon 101 above, taken with similar applied loads. TiB_2

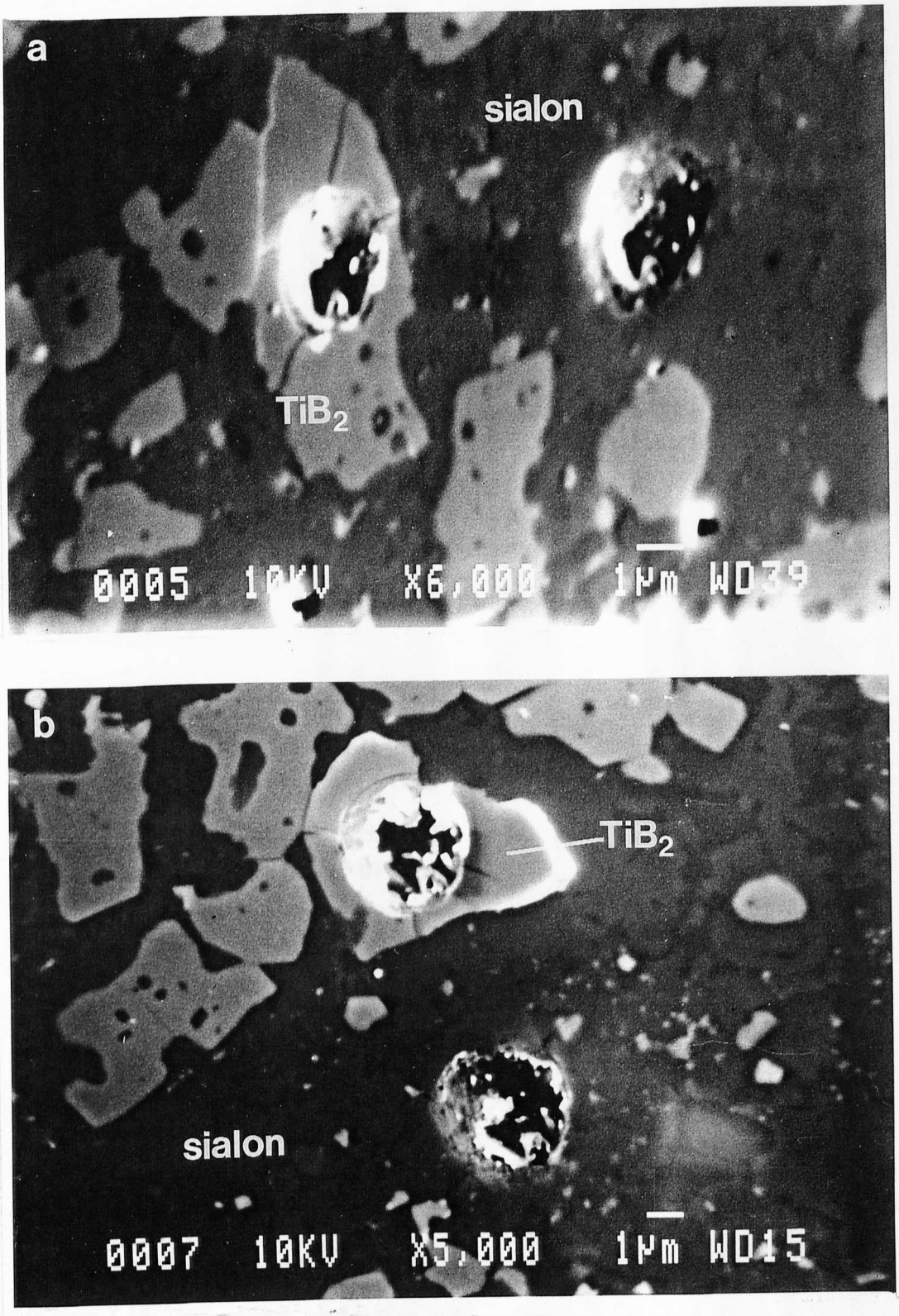

Figure 7.13 (a,b) Indentations in TiB_2 reinforced sialon composite, illustrating the ability to indent individual phases in a material.

Material	ν	E (GPa)	H_{SEM} (GPa)
TiB_2	0.24	407 ± 40	41 ± 4
sialon	0.27	315 ± 20	29 ± 4

Table 7.1 Elastic modulus and hardness determined by indentation for TiB_2 particles and sialon matrix.

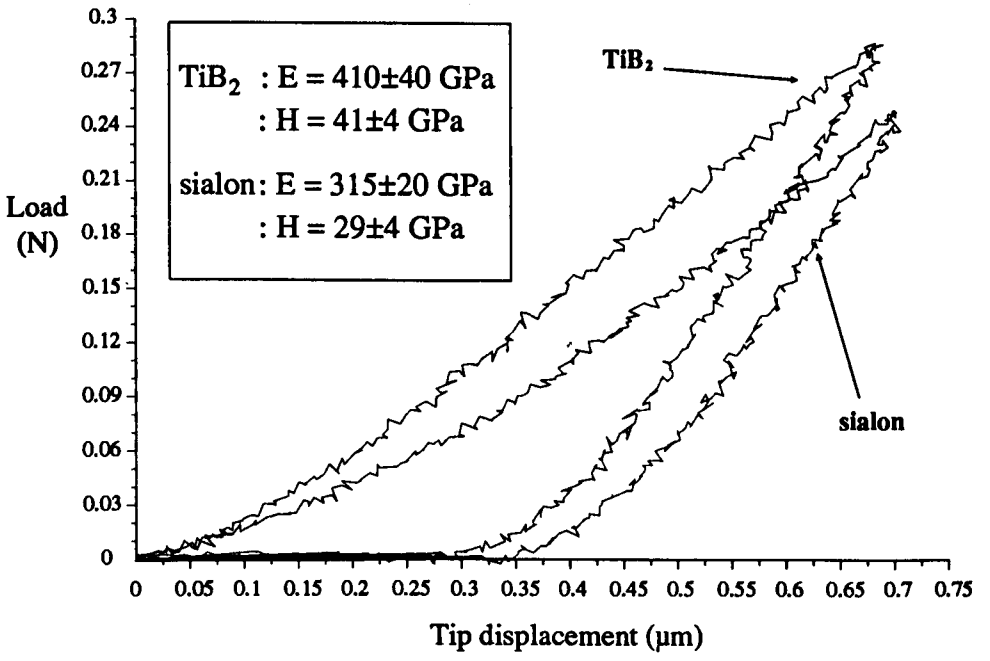

Figure 7.14 Typical TiB_2 and sialon indentations compared on the same axis, illustrating their different response.

hardness and modulus, H_{SEM} = 41 ± 4 GPa and E = 410 ± 40 GPa, are consistent with Vickers hardness of H_V = 35 GPa and modulus E ~ 400 GPa for the bulk material [154,155].

Properties of secondary phases can therefore be measured with the SEM indentor, at indent depths small enough to reduce the influence of the surrounding matrix on the measured property.

7.2.5 Summary

The brief studies on Syalon 101 and TiB_2/sialon, show that the novel geometry of the indentor tip can be used to gain useful hardness and modulus data from indentations that span the nano- and micro-indentor load ranges (0.01N - 1N). Higher applied loads are possible (up to 20N) and with further development, the resolution in both load and displacement measurement could be improved to lower the minimum measurable load and displacement.

Hardness measurements using the conical tip need to be directly compared with Vickers hardness tests on the same material at similar loads, and so quantify the relationship between the two tip geometries.

Elastic modulus measurements are comparable with those made with other, non-indentation based, techniques.

The high resolution in location of indentor tip - specimen surface contact point, enables indentation of small areas of secondary phases in heterogeneous material. Indents can be controlled to shallow depths and low loads, to reduce the influence of surrounding matrix material or substrate.

7.3 Future development and applications

Application of the SEM microindentation system has identified a number of

instrument refinements and further development that are required to increase its overall performance and versatility as a research tool.

7.3.1 Improvement in indentation performance

To increase the capability of the SEM based indentor, particularly with respect to improving its operation at nano- as well as micro-indentation load ranges, various modifications are required.

The major disadvantage of the system is the small discontinuity in the Inchworm shaft's translation, approximately every 2μm, caused by the sudden clamping of the piezoelectric ceramics onto the shaft (see Chapter 4). Although the discontinuities can, in the majority of cases, be taken account of with data processing, this is undesirable. Investigation into alternative, possibly high resolution mechanical drive systems, is required. However, the Inchworm motor's high applied load, compactness, high mechanical resolution and wide range of approach velocity, will be hard to beat.

Resolution in measurement of load needs to be increased. To enable measurement over the full nanoindentor range, resolutions in the region of at least ±1μN are required. The use of a piezoelectric load cell should be retained as its negligible compliance is critical in relation to precision of tip displacement measurement (see figure 4.12 for configuration). The reduction of signal drift from the load cell must therefore be addressed. This can be achieved by shortening the length of cable from the load cell to the charge amplifier, over which charge leakage can occur. One way this can be done is by placing the amplifier inside the SEM vacuum chamber with the instrument. This would have the added benefit of reducing charge leakage within the amplifier that could be effected by humidity when at atmospheric pressure. Charge amplifier design should be updated to take advantage of the latest, low-noise and high impedance amplifiers that become available. The investigation of other

piezoelectric load cells should be carried out. The currently used design is primarily aimed at an industrial market for measurement of loads up to 1 tonne [105].

A load signal "feedback loop" should be incorporated within the Inchworm motor control software to provide a load controlled test option.

Alternatives for measurement of displacement should be explored, but it is not expected that any would supersede the capacitance gauge approach. The short measurement loop that is possible by measuring displacement with respect to the specimen surface, is effective in reducing error from instrument compliance. The actual design of the gauge should be investigated to allow, for example, quick and easy dismantling and attachment. The resolution limit of the current device is governed by the accuracy with which the calibration curve is fitted to the non-linear response and also the resolution of the 12-bit analogue to digital converter used (ADC, see below). If a gauge with a linear response can be built, resolution could be improved and operation made simpler. Large improvements would need constant and accurate determination of the relative permittivity ε_r of the atmosphere between the capacitor plates, as this effects the gauge's capacitance (see section 4.2.4). Incorporation of a reference capacitor, comprising two parallel plates separated by an "air" gap, located near to the actual gauge, should give information on changes in ε_r that could then be used to determine displacement more precisely.

To permit maximum marketability of the instrument at a later stage, all computer control and software development should be carried out on an IBM compatible personal computer (PC). User friendly software (preferably Microsoft Windows based) should be developed to permit the highest sales potential via reduced costs as there would be no need to supply computer hardware with the instrument (PCs are widely available and inexpensive).

In any future computer interface, a higher performance ADC should be used. The current 12-bit ADC has a working accuracy of only 11-bits and limits the recorded displacement resolution to ±10nm. To increase resolution, and also negate the

need for the complicated "offset" hardware and procedure described in section 4.2.7, an improved ADC is required. For example, to achieve the current displacement resolution (10nm) over the full 100μm range of the capacitance gauge (and so bypass the need for the offset procedure), an accurate 14-bit ADC is required. To achieve 1nm resolution over 100μm, a 17-bit ADC is required.

The current design of mounting for the instrument is not optimised. As described in Chapter 4, the mounting initially fabricated to test the feasibility of using the Inchworm motor was used throughout, and had not been developed further. A more rigid design would be favourable, made out of non-magnetic stainless steel for SEM installation. It would be beneficial to include an x-y stage on any new mounting, so that the whole device could be installed as a complete module into more than one model of SEM. Such a module could also be used outside of the SEM, for applications where high magnification imaging is not required. In such cases, coupling to an optical microscope on a laboratory bench may be possible.

An ability to perform indentations at high temperature would be useful in measuring the effects of residual stress due to thermal expansion mismatch within heterogeneous materials (and in ceramic matrix composites). SEM based "hot stages" are commercially available [96,156] and could possibly be included in future modifications.

Finally, attachment of an acoustic emission probe to the specimen or stage would aid detection of sub-surface micro-cracking events during indentation that would be correlated to load/displacement discontinuities.

7.3.2 Possible applications

The SEM microindentation system has great potential for use in a wide range of applications. With further development of the system, the total range of properties that could be investigated include, (list taken from [157]) ;

i) elastic modulus, hardness, microplasticity and creep of individual phases in heterogeneous solids

ii) hardness, modulus and interface cohesion of thin films, coatings or surface-modified layers

iii) tribological response (friction and wear mechanisms, surface profile) with reference to in-situ observation of microstructure

iv) adhesion and fragmentation stresses in particle agglomerates (ceramics, pharmaceuticals)

v) fracture mechanisms in brittle solids (with reference to fracture toughness and R-curve response)

vi) interface debond and shear stresses in ceramic and metal matrix composites.

Many of the above studies require test procedures other than indentation. To achieve them, redesign of the instrument is required. A modular based system is envisaged that would operate in either indentation mode, tribological mode or fracture mechanics mode.

Indentation experiments include the modulus and hardness measurement, crack/interface interaction studies and fibre debond and shear studies, that have been demonstrated in the previous chapters. There is large scope for investigation of hardness, modulus and adhesion of surface coatings. The displacement control of the indentor should provide the capability to study these properties at different indent depths and so measure the effect of substrate property for different coating thicknesses [158]. Coating to substrate adhesion measurements can be performed using a spherical indentor to initiate lateral cracks parallel to the interface and detect the applied load for initiation [159].

Tribological investigations centre on the development of "scratch" tests to measure friction coefficients, wear parameters and identify wear mechanisms [160].

Specimen translation normal to the axis of the probe is required with monitoring of the normal applied load as well as constant probe applied load control via load cell signal "feedback". The capacitance gauge design could be adapted to measure surface topography and determine wear rates. It would be a great advantage to dynamically image the wear mechanisms within the SEM and perform elemental analyses (EDS) on debris and wear tracks.

Scratch tests are also used to determine coating adhesion. The critical probe load for de-adhesion of the coating under a sliding contact may be quickly identified under SEM imaging. Coupled with the x-y stage translation, large areas of inhomogeneous coating could be investigated with rapid correlation of coating adhesion to structural information.

An x-y stage development is envisaged with precise translation over a wide range, possibly driven by two orthogonal piezoelectric Inchworm motors. Monitoring of load normal to the probe axis needs to be investigated. However, piezoelectric load cells similar to that used in the current study do offer this capability [105].

Fracture mechanics studies will take advantage of the high load capability of the current instrument. Interchangeable, mini-test fixtures could be manufactured to perform bend tests, double torsion or compact tension tests to monitor stress intensity K_1-crack size relationships and derive R-curve data that relates to direct observation of crack/microstructure interaction. Similar SEM based instruments have been developed elsewhere, but without the capability for other applications [161].

A compression test module is envisaged to study particulate crushing and interparticle forces of brittle agglomerates. Such information is useful in the powder processing industries such as colloidal processing and compaction of pharmaceuticals [162].

CHAPTER EIGHT

CONCLUSIONS

The primary objective of the project, to study the interfacial properties of ceramic matrix composites by developing instrumentation to measure interfacial micromechanical response, has been successful. Correlation of experimentally determined interface parameters (G_i and τ) with structural information has been achieved and shown to agree with mechanical data and fracture mechanics models for fibre reinforced ceramic matrix composites.

8.1 The SEM based Microindentation System

The SEM based microindentor has great potential for many applications as it enables high magnification imaging of the indentor tip - specimen contact zone during indentation. The mechanical processes occurring at the loading point, such as crack nucleation or plastic deformation, are observed and so correlated to the continuously measured applied load and tip displacement data. Unlike conventional hardness testing instruments in the same load range (nano- and micro-indentors), the indentation cycle is displacement controlled and not load controlled.

The successful implementation of the device within the limited volume of the SEM chamber is due to the combination of compact piezo-electric motor, piezo-electric load cell mounted behind the indentor tip and novel capacitance displacement sensor. Specimens are not greatly restricted in size as the load cell is not mounted beneath them. The tight measurement loop enables accurate displacement measurement without introducing significant errors due to instrument compliance. It eliminates the need for a massive instrument frame, making it a compact device that can be positioned

within a SEM. The indentor is capable of working in high vacuum. Normal operation involves indentation cycle times of less than two minutes.

The high load capability of the instrument is achieved by the use of the Inchworm motor. It is controllable to a 4 nm mechanical resolution over a total possible traverse of 25 mm. Indentor speed can be controlled over the range $4nms^{-1}$ to $2mms^{-1}$, and so rate dependent effects may be studied. Further development of the indentor may however require an alternative load application device as the displacement translation is not truly linear. The contraction and expansion of piezo-electric components within the motor cause a slight discontinuity in the indentor shaft displacement every 2-3 μm. This causes a discontinuity in the load/displacement data that is due to the shaft tilting an estimated maximum $2x10^{-4}$ radians. It is easily compensated for with data processing as it is known exactly where the discontinuities occur during an indentation. With the fibre pushing experiments, this has not introduced errors to data interpretation.

Current areas of potential use are, for example, the surface engineering applications of ceramic coating adhesion and fracture investigations, tribological response, grain to grain microhardness of heterogeneous materials and elastic modulus measurements. With further development, an instrument is envisaged that could be used both on the laboratory bench with optical microscope attachment or within the SEM. With the incorporation of a reference capacitance positioned close to the displacement sensor, it should be possible to increase the resolution of displacement measurement to that of current nanoindentors, i.e. of the order 0.2 nm. Combined with an enhanced load measurement resolution to the 1μN level, nanoindentor applications such as nucleation of plasticity stress investigations should be possible [163].

8.2 Fibre Reinforced Ceramic Matrix Composite Interface Properties

The development of the SEM microindentor enabled a previously impossible, wide ranging and comprehensive investigation into the interface

micromechanics of silicon carbide fibre reinforced glass and glass ceramic matrix composites.

The data collected has been correlated with interface structural information obtained via transmission and scanning electron microscopies. Effects on interface behaviour of residual stress, oxidation, fatigue testing and interface pre-synthesis via fibre coating, have been measured. Fibres with diameters ranging from 7μm to 150μm have been tested to demonstrate the versatility of the device for interfacial property measurement across the full range of modern ceramic matrix composites. No other experimental technique is currently available that can measure both interface debond fracture surface energy G_i and frictional shear stress τ, over such a wide range of composites, and so easily.

Application of the original Marshall and Oliver model [89] describing the fibre push-down test has proved successful. Correlation of changes in G_i and τ with changes in overall composite mechanical behaviour, was possible.

The theoretical requirement of $G_i < 1/4 \rightarrow 1/2\ G_f$ (G_f, the surface fracture energy of the fibre), for toughness to be exhibited by a composite, has been experimentally investigated. The pure mode 2 loading of the interface in the fibre push-down test gives G_i that are high due to factors other than the purely chemical bonding between fibre and matrix, e.g. interface roughness effects. Theoretical models that take these into consideration when describing the push-down test have yet to be implemented. The variation of τ, within and across different composite systems, has been measured. Its effect on matrix micro-cracking stress and the tough/brittle property transition of a composite, has been experimentally demonstrated to agree with theoretical considerations.

8.3 Future Developments

With regard to measurement of interfacial micromechanics of composites, use of the SEM microindentor for the fibre push-down test is the most versatile technique available today. It can be applied to developmental samples or to slices of actual component in service lifetime investigations, as specimen preparation is simple. Imaging of interface debond as it happens provides invaluable information when environmental effects have modified the original interface structure or when multi-coated fibres are investigated. Its wide load range means it can test CMCs reinforced with the whole range of commercially available fibres.

Therefore developmental effort should be focussed on suitable models that consider other material parameters such as fibre Poisson expansion, residual stress and interface roughness, to derive accurate G_i and τ. The system is available to perform the test for the relevant parameters, now a model is required to accurately describe it.

Development of the SEM microindentation system should be focussed on the ultimate goal of producing a commercially available, modular, multi-functional, nano/micro-load scale, mechanical test facility. Such a device, that could operate under vacuum in the SEM, or at atmospheric pressure on the laboratory bench, at elevated temperature with the incorporation of a hot stage, and able to measure all of the material properties discussed earlier, would prove an invaluable tool for a research laboratory investigating the engineering potential of new materials. Cost should not prove prohibitive - the system described in this thesis was developed for a capital cost of less than half the price of a standard Vickers microhardness unit.

REFERENCES

[1] E.G. Butler, M.H.Lewis in *'Ceramic Materials and Components for Engines'* ed. R. Carlsson, Elsevier, p 32, (1992).

[2] L.M. Sheppard. Cer. Bull., **71**, 4, p632, (1992).

[3] J.E. Hove, M.A.Rigdon. 17th Annual Conference on Composites and Advanced Ceramic Materials, January 10-15, 1993, Cocoa Beach, FL. (unpublished).

[4] W. Krenkel. AGARD-R-**795**, ref 13, (1993). DRIC, 65 Brown Street, Glasgow.

[5] M. Percival. Rolls Royce plc, private communication.

[6] S.M. Weiderhorn. Ann Rev Mat Sci, **14**, p373, (1984).

[7] D. Cratchley, A.A. Baker. Ceram Bull, **46**, p191, (1967).

[8] W.B. Hillig. J Appl Physics, **32**, p 741, (1961).

[9] S.S. Brenner in *'Growth and Perfection of Crystals'* ed. R.H.Doremus, B.W.Robes, D.Turnbull, Wiley, New York, p160, (1958).

[10] I.W. Donald, P.W. McMillan. J Mater Sci, **11**, p949, (1976).

[11] I. Crivelli-Visconti, G.A. Cooper. Nature, **221**, p754, (1969).

[12] R.A.J. Sambell, D.H. Bowen, D.C. Phillips. J Mater Sci, **7**, p663, (1972).

[13] R.A.J. Sambell, A.Briggs, D.C. Phillips, D.H. Bowen. J Mater Sci, **7**, p676, (1972).

[14] D.C. Phillips, R.A.J. Sambell, D.H. Bowen. J Mater Sci, **7**, p1454, (1972).

[15] D.C. Phillips. J Mater Sci, **9**, p1847, (1974).

[16] J. Aveston. *Proc. Conference on the Properties of Fibre Composites*, November 4, 1971, NPL, Teddington, UK. Paper 2. IPC Science and Technical Press, Guildford, UK.

[17] J. Aveston, G.A. Cooper, A. Kelly. *Proc. Conference on the Properties of Fibre Composites*, November 4, 1971, NPL, Teddington, UK. Paper 2. IPC Science and Technical Press, Guildford, UK.

[18] M.H. Lewis, R.J. Lumby. Powder Metallurgy, **26**, 2, p73, (1983).

[19] R.J. Lumby, P. Hodgson, N.E. Cother, A. Szweda. SAE Tech. Paper Series, International Congress, Febuary 25-March 1, 1985.

[20] K.H. Jack. Ceramics and Civilisation Vol III, High Tech Ceramics - Past,

Present and Future, p259, (1985).

[21] G. Ziegler, J. Henrich, G. Watting. J Mat Sci, **22**, p3041, (1987).

[22] T. Eckström, M. Nygren. J Am Ceram Soc, **75**, 2, p259, (1992).

[23] P.D. Shalek, J.J. Petrovic, G.F. Hurley, F.D. Gac. Ceram Bull, **65**, 2, p351, (1986).

[24] J.G. Lee, I.B. Cutler. Ceram Bull, **54**, 2, p195, (1975).

[25] S. Yajima, K. Okamura, J. Hayashi, M. Omuri. J Am Ceram Soc, **59**, p324, (1976).

[26] T.N. Tiegs, P.F. Becher. Ceram Bull, **66**, 2, p339, (1987).

[27] G.C. Wei, P.F. Becher. Ceram Bull, **64**, 2, p298, (1985).

[28] K.T. Faber, A.G. Evans. Acta Metall, **34**, p565, (1983).

[29] K.M. Prewo, J.J. Brennan, G.K. Layden. Ceram Bull, **65**, 2, p305, (1986).

[30] J.J. Brennan in *Tailoring Multiphase and Composite Ceramics* ed. Tressler, Messing, Pantano, Newham. Plenum Press, New York. p549, (1986).

[31] K.M. Prewo in *Glasses and Glass Ceramics* ed. M.H.Lewis. Chapman and Hall, p336, (1989).

[32] R.F Cooper, K. Chyung. J Mater Sci, **22**, p3148, (1987).

[33] J.E.Gordon.*The New Science of Strong Materials* Penguin Books, (1968).

[34] C.E. Inglis. Trans Inst Naval Archit, **55**, p219, (1913).

[35] A.A. Griffith. Philos Trans R Soc London, **A221**, p163, (1920).

[36] G.R.Irwin. J Appl Mech, **24**, p361, (1957).

[37] W.Weibull. J Appl Mech, **18**, p293, (1951).

[38] M.Y. He, J.W. Hutchinson. Int J Solids Structures, **25**, 9, p1053, (1989).

[39] A.G. Evans, D.B. Marshall. Acta Metall, **37**, 10, p2567, (1989).

[40] M.D. Thouless, A.G. Evans. Acta Metall, **36**, 3, p517, (1988).

[41] M.D. Thouless, O. Sbaizero, L.S. Sigl, A.G. Evans. J Am Ceram Soc, **72**, 4, p525, (1989).

[42] B. Budiansky, J.W. Hutchinson, A.G. Evans. J Mech Phys Solids, **34**, 2, p167, (1986).

[43] D.B. Marshall, B.N. Cox, A.G. Evans. Acta Metall, **33**, 11, p2013, (1985).

[44] L.N. McCartney. Proc R Soc London, **A409**, p329, (1987).

[45] J.F. Stohr. AGARD-R-**795**, ref 1, (1993).DRIC, 65 Brown Street, Glasgow.

[46] F.K. Ko. Cer Bull, **68**, 2, p401, (1989).

[47] K.M. Prewo, J.A. Batt. J Mater Sci, **23**, p523, (1988).

[48] K.S. Goto, K.H. Han, G.R. St Pierre. Trans ISIJ, **26**, p597, (1986).

[49] E. Fitzer. Carbon, **25**, 2, p163, (1987).

[50] J.R. Strife, J.A. Sheehan. Cer Bull, **67**, 2, p369, (1988).

[51] A.R. Bunsell. J Appl Polym Sci, **47**, p87, (1991).

[52] A.G. Razzell, M.H. Lewis. Ceram Eng Sci Proc, **12**, 7-8, p1304, (1991).

[53] J. Hellmann. Pennsylvania State University, private communication.

[54] P.J. Lamiq, G.A. Bernhart, M.M. Dauchier, J.G. Mace. Ceram Bull, **65**, 2, p336, (1986).

[55] D.P. Stinton, A.J. Caputo, R.A. Lowden. Ceram Bull, **65**, 2, p347, (1986).

[56] E. Fitzer, R.Gadow. Ceram Bull, **65**, 2, p326, (1986).

[57] R.A. Lowden, D.P. Stinton. Ceram Eng Sci Proc, **9**, 7-8, p705, (1988).

[58] R.A. Lowden, K.L. More. Proc MRS convention, November 1989.

[59] R.T. Bhatt. NASA Tech Memorandum 101356, **N89-10130**, (1988). NASA Lewis Research Centre, Cleveland, Ohio.

[60] D.K. Shetty, M.R. Pasucci, B.C. Mustuddy, R.A. Willis. Ceram Eng Sci Proc, **6**, p632, (1985).

[61] A.G. Razzell, M.H. Lewis. J Microscopy, **169**, 2, p215, (1993).

[62] E. Fitzer, R.Gadow. Materials Science Research Vol 20, Plenum, New York. p571, (1985).

[63] K.L. Luthra. J Am Ceram Soc, **71**, 12, p1114, (1988).

[64] M.H. Lewis, V.S.R. Murthy. Comp Sci Tech, **42**, p221, (1991).

[65] A.G. Evans, F.W. Zok, J. Davies. Comp Sci Tech, **42**, p3, (1991).

[66] A.G.Evans. Presented at IPCM'93, Cambridge, UK, September 1993. (Not published).

[67] R.S.Hay. Ceram Eng Sci Proc, **14**, 9-10, p922, (1993)

[68] J.B.Davis, A.G.Evans. J Am Ceram Soc, submitted, (1993).

[69] W.A. Bryant. J Mat Sci, **12**, p1285, (1977).

[70] D.P. Stinton, T.M. Bessmann, R.A. Lowden. Ceram Bull, **67**, 2, p350,(1988)

[71] U.S. Björkert. MSc Thesis, University of Warwick, Coventry, UK / KTH, Stockholm, Sweden, (1994).

[72] K.M. Prewo. Mat Res Soc Symp Proc, **120**, p145, (1988).

[73] J.J. Brennan, K.M. Prewo. J Mat Sci, **17**, p2371, (1982).

[74] A.Chamberlain, M.W.Pharaoh, M.H.Lewis. Ceram Eng Sci Proc, **14**, 9-10, p939, (1993)

[75] M.H. Lewis, A.M. Daniel, A. Chamberlain, M.W. Pharaoh, M.G.Cain. J Microscopy, **169**, 2, p109, (1993).

[76] E. Bischoff, M. Ruhle, O. Sbaizero, A.G. Evans. J Am Ceram Soc, **72**, 5, p741, (1989).

[77] V.S.R. Murthy, M.H. Lewis. J Mat Sci Lett, **8**, p571, (1989).

[78] V.S.R. Murthy, Li Jie, M.H. Lewis. Ceram Eng Sci Proc, **10**, p938, (1989).

[79] J.J. Brennan in *Ceramic microstructures '86 : The Role of Interfaces.* ed. J.A. Pask, A.G. Evans. Plenum Press, p387, (1987).

[80] E.Y. Luh, A.G. Evans. J Am Ceram Soc, **70**, p466, (1987).

[81] H.C. Cao, E. Bischoff, O. Sbaizero, M. Ruhle, A.G. Evans, D.B. Marshall, J.J. Brennan. J Am Ceram Soc, **73**, 6, p1691, (1990).

[82] D.B. Marshall, A.G. Evans. J Am Ceram Soc, **68**, p225, (1985).

[83] A.G. Evans. AGARD-R-**795**, ref 2, (1993).

[84] N. Shafry, D.G. Brandon, M.Terasaki. Presented at 1st Eurpean Ceramic Society Conference, Maastricht, Netherlands. June 1989 (not published).

[85] G.P. Pearson, S.M. Bleay, R.G. Cooke. Brit Ceram Trans, **92**, 4, p141, (1993).

[86] B. Derby, C.W. Lawrence, S. Kooner. Presented at IPCM'93, Cambridge, UK, September 1993. (Not published).

[87] C.W. Griffin, D.K. Shetty, S.Y. Limaye, D.W. Richardson. Ceram Eng Sci Proc, **12**, p671, (1988).

[88] D.B. Marshall. J Am Ceram Soc, **67**, 12, C259, (1984).

[89] D.B. Marshall, W.C. Oliver. J Am Ceram Soc, **70**, 8, p542, (1987).

[90] T.P. Weihs, W.D. Nix. Scripta Metall et Mat, **22**, p271, (1988).

[91] T.A. Parthasarathy, P.D. Jero, R.J. Kerans. Scripta Metall et Mat, **25**, p2457, (1991).

[92] J.D. Bright, S. Danchaivijit, D.S. Shetty. J Am Ceram Soc, **74**, 1, p115, (1991).

[93] G. Morscher, P. Pirouz, A.H. Heuer. J Am Ceram Soc, **73**, 3, p713, (1990).

[94] Nanoindenter, Nano Instruments Inc, PO Box 14211, Knoxville, TN 37914, USA.

[95] M.W. Pharaoh, A.M. Daniel, M.H. Lewis. J Mat Sci Lett, **12**, p998, (1993).

[96] S. Kooner, C.W. Lawrence, B. Derby. Ceram Eng Sci Proc, **14**, 7-8, p229, (1993).

[97] B.W. Mott. *Microindentation Hardness Testing*, Butterworths Scientific Publications, London (1956).

[98] N. Gane. Proc Roy Soc London, **A317**, p367, (1970).

[99] N. Gane, J.M. Cox. Phil Mag, **22**, p881, (1970).

[100] J.B. Pethica, R. Hutchings, W.C. Oliver. Phil Mag, **48**, 4, p593, (1983).

[101] Nanoindenter, Nano Instruments Inc, PO Box 14211, Knoxville, TN 37914, USA.

[102] Fisherscope H100V, Fischer Instrumentation (GB) Ltd, Gordleton Industrial Park, Pennington, Hampshire SO41 8JD.

[103] Queensgate Instruments Ltd, Silwood Park, Ascot, Berkshire SL5 7PW.

[104] Burleigh Instruments (UK) Ltd, Nine, Allied Business Centre, Coldharbour Lane, Harpenden, Hertfordshire AL5 4UT.

[105] Kistler Instruments Ltd, The Grove, Hartley Wintney, Hants. U.K.

[106] I. Miyamoto, S.T. Davies. Annals of the CIRP, **37**, 1, p171, (1988).

[107] Nanosensor 2000 application notes. Queensgate Instruments [103].

[108] Inchworm motor application notes. Burleigh Instruments [104].

[109] *Materials Science and Engineering*, course **T203**, BBC Open University, Milton Keynes, UK. (1994).

[110] A. Chamberlain. PhD Thesis, Physics Dept, University of Warwick, (1994).

[111] N. Frety, M.H. Lewis. Final report, Brite-Euram B/BREU-913004, University of Warwick, (1993).

[112] M.W. Pharaoh, M.H.Lewis, University of Warwick, (1989-1993). (Not published).

[113] K.P.Plucknett, S. Sutherland, M.H.Lewis. University of Warwick, Brite-Euram Conract #4610-09, (1992-95).

[114] K.P.Plucknett, G.West, D.M.R. Taplin, A.M.Daniel, S.Sutherland, R.L.Cain, M.H.Lewis. Proc. 8th Int. Conf. on Fracture, Kiev, Ukrane. June 1993. Published in *"Advances in Fracture and Structural Integrity"* Pergamon Press, Oxford. (1994).

[115] K.P. Plucknett, S.Sutherland, A.M.Daniel, R.L.Cain, G.West,D.M.R.Taplin, M.H.Lewis. J. Microscopy. (submitted June 1994).

[116] N. Frety. PhD Thesis, Ecole des Mines, Paris, France. (1992).

[117] M.G. Cain, A.M. Daniel, M.H. Lewis. Mater Lett, **17**, p246, (1993).

[118] Product information on Nicalon NL-607, supplied by Dow Corning, Midland, Michigan, USA.

[119] R.F. Allen. PhD Thesis, University of Birmingham. (1994).

[120] M.W.Pharaoh, V.S.R.Murthy, M.H.Lewis. Rolls Royce report (1989).

[121] L.A.Bonney, R.F.Cooper. J Am Ceram Soc, **73**, 10, p2916, (1990).

[122] A.G.Razzell. PhD Thesis, Physics Dept, University of Warwick, (1993).

[123] J.I.Eldridge, R.T.Bhatt, J.D.Kiser. Ceram Eng Sci Proc, **12**, 7-8, p1152, (1991).

[124] M.H.Lewis, A.Chamberlain, A.M. Daniel, M.W.Pharaoh, A.G. Razzell and S.Sutherland. AGARD-R-**795**, ref. 10, (1993).

[125] C.Cho, J.W.Holmes, J.R.Barber. J Am Ceram Soc, **74**, p2802, (1991)

[126] D.K.Shetty. J Am Ceram Soc, **71**, C107, (1988).

[127] R.J.Kerans, T.A.Parthasarathy. J Am Ceram Soc, **74**, p1585, (1991).

[128] T.P.Weihs, W.D.Nix. J Am Ceram Soc, **74**, p524, (1991).

[129] D.B.Marshall, W.C.Oliver. Mat Sci Eng, **A126**, p95, (1990).

[130] J.W.Hutchinson, H.M.Jensen. Mech of Mat, **9**, p139, (1990).

[131] C.Liang, J.W.Hutchinson. Mech of Mat, **14**, p207, (1993).

[132] D.B.Marshall. Acta metall mater, **40**, p427, (1992).

[133] C.W.Lawrence, B.Derby. Ceram Eng Sci Proc, **14**, 7-8, p139, (1993).

[134] C.W.Lawrence. Dept. of Materials, University of Oxford, Parks Road, Oxford. Private communication (1993).

[135] R.A.Lowden, O.J.Schwatrz, K.L.Moore. Ceram Eng Sci Proc, **14**, 7-8, p375, (1993).

[136] C.H.Hseuh, P.F.Becher, P.Angelini. J Am Ceram Soc, **71**, 11, p929, (1988).

[137] D.H.Grande, J.F.Mandell, K.C.C.Hong. J Mater Sci, **23**, p311, (1988).

[138] M.K.Brun, R.N.Singh. Adv Ceram Mater, **3**, p506, (1988).

[139] P.S.Steif, A.Dollar. J Am Ceram Soc, **75**, 6, p1694, (1992).

[140] A.Dollar, P.S.Steif. J Am Ceram Soc, **76**, 4, p897, (1993).

[141] D.Rouby, H.Osmani. J Mat Sci Lett, **7**, p1154, (1988).

[142] J.O.Outwater, M.C.Murphy. Mod Plast, **47**, p160, (1970).

[143] H.M.Jensen. Acta metall mater, **38**, 12, p2637, (1990).

[144] H.C.Cao, A.G.Evans. Mech Mater, **7**, p295, (1989).

[145] A.G.Evans, M.Ruhle, B.J.Dalgleish, P.G.Charalambides. Metall Trans A, **21A**, p2419, (1990).

[146] D.S.Beyerle, S.M.Spearing, F.W.Zok, A.G.Evans. J Am Ceram Soc, **75**, 10, p2719, (1992).

[147] I.N.Sneddon. Int J Eng Sci, **3**, p47, (1965).

[148] G.M.Pharr, W.C.Oliver, F.R.Brotzen. J Mater Res, **7**, 3, p613, (1992).

[149] M.F.Doerner, W.D.Nix. J Mater Res, **1**, 4, p601, (1986).

[150] R.J.Lumby. University of Warwick, unpublished work (1989-94).

[151] I.J.McColme. *Ceramic Hardness*, Plenum Press, (1990).

[152] R.Morrell. *Handbook of properties of technical and engineering ceramics*, HMSO : London. (1987).

[153] R.J.Lumby.*"Hardness Measurements on Ceramic Materials."* Internal report, Physics Dept., University of Warwick, (1992).

[154] F.Hong, M.H.Lewis. Ceram Eng Sci Proc, **14**, 9-10, p699, (1993).

[155] F.Hong. University of Warwick, private communication.

[156] Oxford Instruments, Eynsham, Oxford, OX8 1TL. U.K.

[157] M.H.Lewis. TAPM, DTI/LINK application, (1994).

[158] B.D.Fabes, W.C.Oliver, R.A.McKee, F.J.Walker. J Mater Res, **7**, p3057, (1992).

[159] J.B.Davis, H.C.Cao, G.Baa, A.G.Evans. Acta metall mater, **39**, p1019, (1991).

[160] S.J.Sharp, M.F.Ashby, N.A.Fleck. Acta metall mater, **41**, p685, (1993).

[161] J.Rodel, J.F.Kelly, B.R.Lawn. J Am Ceram Soc, **73**, 11, p3313, (1990).

[162] K.Kendall, T.P.Weihs. J Phys D : Appl Phys, **25**, A3, (1992).

[163] T.F.Page, W.C.Oliver, C.J.McHargue. J Mater Res, **7**, 2, p450, (1992).

APPENDIX I

The three major programs used for operation of the SEM microindentation system and data analysis are listed below. They were written in BBC BASIC on an Acorn A3010 microcomputer. Copies on floppy disc can be obtained from the author.

Program "ONE"

```
 10 DIM data(20000):DIM dist(20000):DIM cap(20000):DIM event(10)
 20 MODE0
 30 *FX151,&60,1
 40 *FX151,&62,223
 50 *FX151,&6B,0
 60 *FX225,199
 70 *KEY 10
 80 *FX4,1
 90 DISP=0
100 flag=1
110 SP=32
120 REM INCHWORM SPEED PROGRAM
130 CLS
140 PRINT"        INCHWORM CONTROL"
150 PRINT
160 PRINT
170 PRINT
180 PRINT"YOU CAN CHOOSE 10 DIFFERENT SPEEDS FOR"
190 PRINT"THE SHAFT.THE RED FUNCTION KEYS"
200 PRINT"CONTROL THE SPEED FROM STATIONARY AT"
210 PRINT"F0 TO MAX SPEED OF 1.0 mm per sec AT F9."
220 PRINT"SEE THE GUIDE ON THE KEYBOARD.","
230 PROCproc
240 GOTO230
250END
260
270DEFPROCproc
280 PRINT TAB(0,16)"                              "
290 PRINT TAB(0,16)"PRESS THE REQUIRED KEY"
300 PRINTTAB(0,28)"PRESS V TO READ THE CAP. GAUGE VOLTAGE BEFORE STARTING."
310 PROCdisp
320 PRINT TAB(0,23)"Speed is ",DISP," Microns per sec.          "
330 IF SP=83 THEN PROCload
340 IF SP=138 THEN *FX151,&60,2
350 IF SP=139 THEN *FX151,&60,0
360 IF SP=32 THEN *FX151,&60,1
370 IF SP=200 THEN *FX151,&6B,0
```

```
380 IF SP=201 THEN PROCspeed(255,255)
390 IF SP=202 THEN PROCspeed(255,150)
400 IF SP=203 THEN PROCspeed(255,31)
410 IF SP=204 THEN PROCspeed(255,15)
420 IF SP=205 THEN PROCspeed(255,7)
430 IF SP=206 THEN PROCspeed(186,0)
440 IF SP=207 THEN PROCspeed(38,0)
450 IF SP=208 THEN PROCspeed(7,0)
460 IF SP=209 THEN PROCspeed(1,0)
470 IF SP=138 THEN PRINT TAB(0,21)"GOING DOWN      "
480 IF SP=139 THEN PRINT TAB(0,21)"GOING UP        "
490 IF SP=32 THEN PRINT TAB(0,21)"STOPPED          "
500 SP=GET
510ENDPROC
520DEFPROCdisp
530 IF SP=200 THEN DISP=0
540 IF SP=201 THEN DISP=0.117
550 IF SP=202 THEN DISP=0.2
560 IF SP=203 THEN DISP=1
570 IF SP=204 THEN DISP=2
580 IF SP=205 THEN DISP=4
590 IF SP=206 THEN DISP=40
600 IF SP=207 THEN DISP=200
610 IF SP=208 THEN DISP=1000
620 IF SP=86 THEN V%=ADVAL(3)
625 vstart=V%
630ENDPROC
640DEFPROCspeed(X,Y)
650 *FX151,&6B,224
660 OSCLI("FX151,&64,"+STR$(X)):OSCLI("FX151,&66,"+STR$(X))
670 OSCLI("FX151,&65,"+STR$(Y)):OSCLI("FX151,&67,"+STR$(Y))
680 IF X=1 THEN *FX151,&66,0
690ENDPROC
700DEFPROCload
710 *FX151,&62,255
720 *FX151,&6B,0
730 *FX151,&60,1
740 CLS
750 flag=11
760 ev=1
770 *FX16,3
780 D=0:E=1:H=0
790 PRINTTAB(0,0);"PRESS THE LEFT HAND MOUSE BUTTON AT AN EVENT."
800 vzero=ADVAL(3)
805 t1=0
810 REPEAT
820 S=E+(H*128)
830 OSCLI("FX151,&60,"+STR$(S))
840 TIME=0:REPEAT UNTIL TIME>2
850 data(flag)=ADVAL(1)
860 cap(flag)=ADVAL(2)
870 dist(flag)=dist(flag-1)+D
880 MOUSEx,y,z,t: IF t<t1+50 THEN 890
882 IF z=4 THEN event(ev)=flag: ev=ev+1:t1=t
890 z=0
900 plot=flag MOD 3600
```

```
910 IF plot=0 THEN CLG
920 PLOT69,plot/3,data(flag)/32
930 up=INKEY(-58):IF up=-1 THEN D=-1:E=0
940 down=INKEY(-42):IF down=-1 THEN D=1:E=2
950 stop=INKEY(-99):IF stop=-1 THEN D=0:E=1
960 flag=flag+1
970 IF H=0 THEN H=1:GOTO990
980 H=0
990 UNTIL INKEY(1)=83
1000 *FX151,&60,1
1010 maxdist=0:maxcap=0
1020 FOR N=2 TO flag
1030 IF dist(N)>maxdist THEN maxdist=dist(N)
1035 IF cap(N)>maxcap THEN maxcap=cap(N)
1040 NEXT N
1050 PROCdraw
1060 PRINT"DO YOU WANT TO PERFORM ANOTHER INDENTATION?"
1070 ANSW=GET
1080 IF ANSW=89 THEN 20
1090 *FX151,&60,1
1100 CHAIN"TWO"
1110 END
1120ENDPROC
1130DEFPROCdraw
1140 CLS
1150 FOR N= 1 TO flag
1151 PLOT69,N*1200/flag,data(N)/32
1152 NEXT N
1153 CONT=GET
1154 IF CONT=32 THEN 1160 ELSE 1154
1160 FOR N=1 TO flag
1161 PLOT69,N*1200/flag,dist(N)
1162 NEXT N
1163 CONT=GET
1164 IF CONT=32 THEN 1170 ELSE 1164
1170 FOR N=1 TO flag
1171 PLOT69,dist(N)*1200/maxdist,data(N)/20
1172 NEXT N
1173 CONT=GET
1174 IF CONT=32 THEN 1179 ELSE 1174
1179 CLS
1180 FOR N=1 TO flag
1181 PLOT69,cap(N)*1200/maxcap,data(N)/20
1190 NEXT N
1200 PROCsave
1210ENDPROC
1220DEFPROCsave
1230 PRINT"DO YOU WANT TO SAVE THIS DATA ?"
1240 ANS=GET
1250 IF ANS<>89 THEN ENDPROC
1260 INPUT"FIBRE DIAMETER",rad
1270 INPUT"ENTER FILENAME",name$
1280 data(0)=rad
1290 dist(0)=maxdist
1295 FOR B=1 TO 10:dist(B)=event(B):NEXT B
1297 cap(0)=vstart: cap(1)=vzero:cap(2)=maxcap
```

```
1300 X=OPENOUT(name$)
1310 FOR Y=0 TO flag
1320 PRINT#X,data(Y),dist(Y),cap(Y)
1330 NEXT Y
1340 CLOSE#X
1350ENDPROC
```

Program "TWO"

```
 10 DIM data(20000):DIM dist(20000):DIM cap(20000)
 20 *DIR :0
 25 *CAT
 30 INPUT"Filename ";NME$
 40 F%=OPENIN(NME$)
 50 flag=0
 60 REPEAT
 70 INPUT#F%,data(flag),dist(flag),cap(flag)
 80  flag=flag+1
 90 UNTIL EOF#F%
100 CLOSE#0
110 IF NME$="ALL1" THEN cap(0)=0
120 maxcap=0:maxdat=0
130 FOR N =11 TO flag
140 IF cap(N)>maxcap THEN maxcap=cap(N)
150 IF data(N)>maxdat THEN maxdat=data(N)
160 NEXT
170 PROCplot
180 PROCbase
190 PROCplot
200 CLS
210 PROCmassa
220 PROCzero
230 PROCplot1
240 PROCcut
250 PROCreal
260 PROCsave
270 END
280 DEFPROCplot
290 CLS
300 FOR N= 11 TO flag
310 PLOT69,N/flag*1280,data(N)*1024/maxdat
320 NEXT N
330 ENDPROC
340 DEFPROCbase
350 *FX4,1
360 MOUSE ON
370 TIME=0
380 IF TIME<50 THEN 380
390 PRINTTAB(31,8);"MOVE THE BASE LINE"
400 MOUSEx,y,z:IF z=4 THEN 410 ELSE 400
410 X1=x:Y1=y
420 MOVE x-20,y:PLOT6,x+20,y:MOVE x,y+20:PLOT6,x,y-20
430 TIME=0
440 IF TIME<50 THEN 440 ELSE 450
450 MOUSEx,y,z:IF z=4 THEN 460 ELSE 450
```

```
460 X2=x:Y2=y
470 MOVE x-20,y:PLOT6,x+20,y:MOVE x,y+20:PLOT6,x,y-20
480 MOVE X1,Y1:PLOT6,X2,Y2
490 PRINTTAB(35,10);"IS THIS BASE LINE OK?"
500 PRINTTAB(35,12);"IF SO CLICK R.H. BUTTON"
510 TIME=0
520 IF TIME<50 THEN 520 ELSE 530
530 REPEAT
540 MOUSEx,y,z
550 UNTIL z=1 OR z=4
560 IF z=1 THEN 580
570 IF z=4 THEN PLOT6,X1,Y1:GOTO 370
580 PRINT"DONE IT"
590 PRINTTAB(35,10);"PLEASE WAIT"
600 M=(Y2-Y1)/(X2-X1):C=Y1-M*X1
610 FOR N=11 TO flag-1
620 YN=M*1280/(flag-1)*N+C
630 data(N)=data(N)-(YN*maxdat/1024)
640 NEXT N
650 ENDPROC
660 DEFPROCplot1
670 CLS
680 FOR N= 11 TO flag
690 PLOT69,cap(N)*1280/maxcap,data(N)*1024/maxdat
700 NEXT N
710 ENDPROC
720 DEFPROCmassa
730 FOR N =11 TO flag
740 PLOT69,N*1200/flag,cap(N)*960/maxcap
750 PLOT69,N*1200/flag,data(N)*750/maxdat
760 NEXT N
770 MOUSE ON
780 REPEAT
790 MOUSE x,y,z
800 IF z=4 THEN MOUSE TO x,cap(INT(x*flag/1200+0.5))*960/maxcap:PRINTTAB(0,0)
    cap(INT(x*flag/1200+0.5))/16:PRINTTAB(20,0) (INT(x*flag/1200 +0.5))
810 UNTIL z=2 OR z=1
820 IF z=2THEN 830:IF z=1 THEN 850
830 CLS
840 PROCplot1
850 INPUT"THE FLAG VALUE"FL
860 INPUT"THE INCREMENT IN CAP"INC
870 CLS
880 FOR N=FL TO flag
890 cap(N)=cap(N)+INC*16
900 NEXT N
910 maxcap=maxcap+16*INC
920 FOR N =11 TO flag
930 PLOT69,cap(N)*1280/maxcap,data(N)*1024/maxdat
940 NEXT N
950 INPUT"DONE?"DONE$
960 IF DONE$="Y" THEN ENDPROC ELSE 850
970 DEFPROCzero
980 PRINTTAB(0,0)"PLEASE SET THE ZERO DISPLACEMENT POINT"
990 PRINT"PRESS THE LEFT HAND MOUSE BUTTON TO SET"
1000 REPEAT
```

```
1010 MOUSEx,y,z
1020 TIME=0
1030 IF TIME<25 THEN 1030
1040 UNTIL z=4
1050 XZERO=x*maxcap/1280
1060 FOR N=11 TO flag
1070 cap(N)=cap(N)-XZERO
1080 NEXT N
1090 maxcap=maxcap-XZERO
1100 ENDPROC
1110 DEFPROCcut
1120 FOR N=11 TO flag
1130 IF cap(N)<0 OR data(N)<0 THEN cap(N)=0:data(N)=0
1140 NEXT N
1150 ENDPROC
1160 DEFPROCreal
1170 vind=(17.4/8.5)*(cap(1)-cap(0))/65520*1.273
1180 VZERO=XZERO*1.273/(4.915*65520)
1190 dind=0.868027*(vind+VZERO)^3-13.7655*(vind+VZERO)^2 +70.574*(vind+VZERO)
1200 FOR N=11 TO flag
1210 cap(N)=(cap(N)+XZERO)*1.273/(4.915*65520)
1220 cap(N)=cap(N)+vind
1230 cap(N)=0.868027*cap(N)^3-13.7655*cap(N)^2+70.5741*cap(N)
1240 cap(N)=cap(N)-dind
1250 IF data(N)<2896 THEN 1270
1260 data(N)=(data(N)+134.4)/207.52*9.807E-3:GOTO 1280
1270 data(N)=(data(N)+15.2)/199.28*9.807E-3
1280 NEXT N
1290 maxcap=0:maxdat=0
1300 FOR N=11 TO flag
1310 IF cap(N)>maxcap THEN maxcap=cap(N)
1320 IF data(N)>maxdat THEN maxdat=data(N)
1330 NEXT N
1340 PROCplot1
1350 ENDPROC
1360 DEFPROCsave
1370 PRINT"DO YOU WANT TO SAVE THIS FOR GRAPH?"
1380 ANS=GET
1390 IF ANS<>89 THEN END
1400 G%=OPENOUT(NME$+"GR")
1410 T$="Title,"+NME$+"      "+STR$(data(0))+CHR$(181)+"m  Diameter"
1420 X$="xaxis,Tip Displacement / microns"
1430 Y$="yaxis,Load / N"
1440 L$="line,1"
1445 F$="0,"+STR$(data(0))
1450 BPUT#G%,T$
1460 BPUT#G%,X$
1470 BPUT#G%,Y$
1480 BPUT#G%,L$
1485 BPUT#G%,F$
1490 FOR N= 11 TO flag
1500 D$=STR$(cap(N))+","+STR$(data(N))
1510 BPUT#G%,D$
1520 NEXT N
1530 CLOSE#0
1540 ENDPROC
```

Program "THREE"

```
 10 DIM cap1(10000):DIM cap2(10000):DIM data1(10000):DIM data2(10000):DIMdisp(10000)
 14 MODE0
 16 *DIR:0
 18 *CAT
 20 INPUT"THE FIBRE TYPE PUSHED, N OR T", NME$
 25 IF NME$="N" THEN PROCnic3
 26 IF NME$="T" THEN PROCtyr2
 35 comma$=","
 50 offy=0
100 INPUT"THE FILENAME OF THE FIBRE PUSH DOWN",PD$
110 H%=OPENIN(PD$)
120 B=1
130 REPEAT
140 E$=GET$#H%
150 IF B<5 THEN 190
160 comma=INSTR(E$,comma$)
170 cap2(B)=VAL(LEFT$(E$,comma-1))
180 data2(B)=VAL(RIGHT$(E$,(LEN(E$)-comma)))
190 B=B+1
200 UNTIL EOF#H%
202 CLOSE#H%
205 flag2=B
250 PROCzero
270 PROCload
300 PROCmovement
330 PROCresult
350 PROCsave
400 END
500 DEFPROCzero
530 B=5
550 B=B+1
560 IF cap2(B)>0 THEN 570 ELSE 550
570 st2=B
580 ENDPROC
600 DEFPROCload
605 maxdat1=0
635 maxdat=0
640 FOR B=st2 TO flag2
660 IF data2(B)>maxdat THEN maxdat=data2(B):maxB=B
670 NEXT B
675 IF maxdat>ML THEN maxdat=ML
680 ENDPROC
700 DEFPROCmovement
705 maxdisp=0
710 refdisp=100
739 CLS
740 FOR B=st2 TO maxB
742 IF NME$="T" AND data2(B)<0.077 THEN PROCtyrlow
750 disp(B)=cap2(B)-(AA*(data2(B)^4)+BB*(data2(B)^3)+CC*(data2(B)^2)+DD*data2(B))
755 IF disp(B)>maxdisp THEN maxdisp=disp(B)
757 ROUNDED=INT((data2(B)*200)+0.5)/200
758 IF ROUNDED=ML THEN refdisp=disp(B)
759 IF NME$="T" THEN PROCtyr2
760 NEXT B
```

```
763 IF refdisp<maxdisp THEN maxdisp=refdisp
765 CLS
770 FOR B=st2 TO maxB
780 PLOT69,disp(B)*1280/maxdisp,data2(B)*data2(B)*1024/(maxdat*maxdat)
790 NEXT B
795 ENDPROC
800 DEFPROCsave
810 PRINT"DO YOU WANT TO SAVE THIS AS AN ASCII FILE?"
820 ANS=GET
830 IF ANS<>89 THEN ENDPROC
840 INPUT"WHAT FILENAME?",RES$
850 I%=OPENOUT(RES$)
860 T$="Title,"+RES$
870 X$="xaxis,Fibre Displacement  "+CHR$(181)+"m"
880 Y$="yaxis,Load*Load   N*N"
900 F$=STR$(data2(5))
910 BPUT#I%,T$
920 BPUT#I%,X$
930 BPUT#I%,Y$
940 BPUT#I%,F$
950 FOR B=6 TO maxB
960 J$=STR$(disp(B))+","+STR$(data2(B)*data2(B))
970 BPUT#I%,J$
980 NEXT B
990 CLOSE#I%
1000 ENDPROC
1500 DEFPROCresult
2020 MOUSE ON
2030 TIME=0
2040 IF TIME<50 THEN 2040
2050 PRINTTAB(0,0);"FIT A STRAIGHT LINE TO THE DATA"
2060 MOUSEx,y,z:IF z=4 THEN 2070 ELSE 2060
2070 X1=x:Y1=y
2080 MOVE x-20,y:PLOT6,x+20,y:MOVE x,y+20:PLOT6,x,y-20
2090 TIME=0
2100 IF TIME<50 THEN 2100 ELSE 2110
2110 MOUSEx,y,z:IF z=4 THEN 2120 ELSE 2110
2120 X2=x:Y2=y
2130 MOVE x-20,y:PLOT6,x+20,y:MOVE x,y+20:PLOT6,x,y-20
2140 MOVE X1,Y1:PLOT6,X2,Y2
2150 PRINTTAB(0,0);"IS THIS FIT O.K.?                    "
2160 PRINTTAB(0,2);"IF SO CLICK R.H. BUTTON                    "
2170 TIME=0
2180 IF TIME<50 THEN 2180 ELSE 2190
2190 REPEAT
2200 MOUSEx,y,z
2210 UNTIL z=1 OR z=4
2220 IF z=1 THEN 2250
2230 IF z=4 THEN PLOT6,X1,Y1:GOTO 2030
2250 PRINTTAB(0,2);"PLEASE WAIT"
2260 M=(((Y2-Y1)/1024)*maxdat*maxdat)/(((X2-X1)/1280)*maxdisp*1E-6)
2270 C=((Y1/1024)*maxdat^2)-(M*(X1/1280)*maxdisp*1E-6)
2300 gdt=M
2310 intcpt=C
2315 rad=data2(5)/2*1E-6
2320 fact=4*PI*PI*rad^3*190E9
```

```
2330 tau=gdt/fact
2340 gamma=intcpt/(2*fact)
2350 PRINTTAB(0,2);"                                    "
2351 PRINTTAB(0,0);"                                    "
2352 PRINTTAB(0,1);"                                    "
2360 PRINTTAB(0,2);"DEBOND SURFACE ENERGY ";gamma;" J/m^2"
2370 PRINTTAB(0,4);"FRICTIONAL SHEAR STRESS ";tau/1E6;" MPa"
2380 PRINTTAB(0,6);"ANOTHER LINE? Y/N"
2390 ANS=GET
2400 IF ANS=89 THEN 2030 ELSE 2410
2410 PRINTTAB(0,6);"APPLY AN OFFSET? Y/N"
2420 ANS=GET
2430 IF ANS<>89 THEN ENDPROC
2440 CLS
2445 offy=offy+1
2450 FOR B=st2 TO maxB
2460 PLOT69,disp(B)*1280/maxdisp+(100*offy),data2(B)*data2(B)*1024/(maxdat*maxdat)
2470 NEXT B
2480 GOTO 2030
2500 ENDPROC
2600 DEFPROCnic3
2610 AA=-6.916:BB=12.43:CC=-8.293:DD=5.402
2615 ML=0.74
2620 ENDPROC
2630 DEFPROCtyr2
2635 AA=-108.37:BB=101.04:CC=-33.93:DD=8.8077
2640 ML=0.4
2650 ENDPROC
2660 DEFPROCtyrlow
2670 AA=-4748.76:BB=1330.5:CC=-145.97:DD=12.061
2680 ENDPROC
```

APPENDIX II

Analysis of debond surface fracture energy G_i

The analysis described by Marshall [132] was performed on the CAS/ Nicalon fibre push-down data illustrated in figures 4.28, 5.5, 5.6(b). For detailed descriptions of the model, see references [130,132].

The analysis is based on a concentric cylinder model representing the composite reinforced with a volume fraction f of aligned, continuous fibres (see figure II.1), that was developed by Hutchinson and Jensen [130]. A typographical mistake has

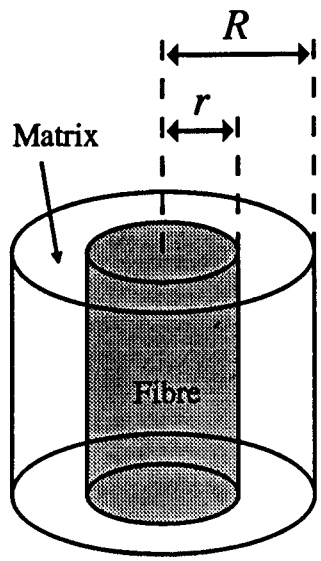

Figure II.1 Concentric cylinder representing the fibre and matrix composite, volume fraction of fibres f given by $f = (r/R)^2$.

been noticed with Marshall's definition of fibre volume fraction as $f = r/R$. For the cylinder shown, fibre volume fraction is actually $f = (r/R)^2$, as correctly stated in Hutchinson and Jensen [130].

The model characterises (in terms of stress) a normalised, debond surface

fracture energy γ to be,

$$\gamma = \frac{-(1 - f)}{f\, c_1\, c_3} \left(\frac{E_m\, G_i}{r} \right)^{1/2} \qquad \text{(II.1)}$$

where E_m is the matrix elastic modulus, c_1 and c_3 are dimensionless and defined in equation (II.8) and G_i is the interface mode 2 fracture surface energy. The experimentally characterised and normalised debond energy Γ is,

$$|\Gamma| = |\gamma| + |\sigma_{f0}^{+}| \qquad \text{(II.2)}$$

where σ_{f0}^{+} is the axial residual stress in the fibre arising from thermal expansion mismatch of matrix and fibre defined as,

$$\sigma_{f0}^{+} = -a_2\, E_m\, \varepsilon \qquad \text{(II.3)}$$

and thermal mismatch strain ε is

$$\varepsilon = (\alpha_f - \alpha_m)\, \Delta T \qquad \text{(II.4)}$$

and

$$a_2 = \frac{(1 - f)\, E_f}{(1 + \nu)(E_f + (1 - 2\nu)E_c)} (2\nu + 1 - \nu + (1 + \nu)(E_f/E_c)) \qquad \text{(II.5)}$$

The stress applied to the fibre at debond σ_{db} (applied load $F_d / \pi r^2$), is equated to

$$\sigma_{db} = \frac{\Gamma}{1 - a_1 f} \qquad \text{(II.6)}$$

where

$$a_1 = E_f / E_c \qquad \text{(II.7)}$$

E_f is the fibre elastic modulus and E_c is the composite modulus given by the rule of mixtures (see equation 2.11).

The b_i, c_i are dimensionless functions of the fibre and matrix elastic properties. For the fibre push-down test, with the simplification $\nu_f = \nu_m = \nu$, they are related by

$$c_1 = \frac{(1 - fa_1)(b_2 + b_3)^{1/2}}{2f} \quad , \quad c_3 = \frac{(1 - f)}{(1 - fa_1)} \qquad \text{(II.8 a,b)}$$

and so equation (II.1) becomes

$$\gamma = \frac{-2}{(b_2 + b_3)^{1/2}} \left(\frac{E_m \; G_i}{r}\right)^{1/2} \qquad \text{(II.9)}$$

where

$$b_2 = \frac{(1 + \nu)E_m \, (E_f + (1 - 2\nu)E_c)}{E_f((1 + \nu)E_f + (1 - \nu)E_c)} \qquad \text{(II.10 a)}$$

$$b_3 = \frac{f(1 + \nu)(E_f + (1 - 2\nu)E_c)}{(1 - f)((1 + \nu)E_f + (1 - \nu)E_c)} \qquad \text{(II.10 b)}$$

For CAS/Nicalon, the material parameters used were;

$f = 0.4 \; (=V_f)$	$\nu=\nu_m=\nu_f= 0.25$
$E_m = 80$ GPa	$\alpha_m = 4.5\text{x}10^{-6}$ °C^{-1}
$E_f = 190$ GPa	$\alpha_f = 3.2\text{x}10^{-6}$ °C^{-1}
$E_c = 124$ GPa	$\Delta T = -800$ °C

which give material properties of a_1=1.53, a_2=1.15, b_2=0.401, b_3=0.636, $(1-a_1 f) = 0.39$ and residual axial stress in fibre $\sigma_{f0}^{+} = -95.7$ MPa.

Measuring the applied load at debond F_d and fibre radius r, gives σ_{db}. Combining equations (II.6), (II.2) and (II.9) then gives G_i.

For the example push down test of figures 4.28, 5.5, 5.6(b), the applied load

at debond F_d = 0.13N, and the fibre radius r = 6.6x10^{-6}m. This gives σ_{db}= -950 MPa. So equation (II.6) gives $\Gamma = 0.39\ \sigma_{db}$, so equation (II.2) gives

$$|\gamma| = -0.39\ \sigma_{db} - \sigma_{f0}^{+} \tag{II.11}$$

when equated to (II.9) gives

$$0.39\sigma_{db} + \sigma_{f0}^{+} = \frac{-2}{(1.037)^{1/2}} \left(\frac{80.10^{9}\ G_i}{r} \right)^{1/2} \tag{II.12}$$

that re-arranges to,

$$G_i = \frac{r}{80.10^{9}} \left[\left(\frac{-1.018}{2} \right) (0.39(-950.10^{6}) - 95.7.10^{6}) \right]^{2} \tag{II.13}$$

and finally results in,

$$G_i = 4.6\ \text{Jm}^{-2}$$

which compares to G_i = 8 Jm^{-2} determined with the same data and the original Marshall and Oliver [89] model.

APPENDIX III

a) Properties of Nicalon reinforced glass ceramic matrix composites

Fibre properties consistent for all three composites :

E_f = 200 GPa r = 7.1 μm α_f =3.2x10^{-6} °C^{-1}

ν_f = 0.2

CAS/Nicalon (Corning) :

E_m = 90 GPa ν_m = 0.3 G_m = 20 Jm^{-2}

V_f = 0.4 τ = 25 MPa α_m = 4.5x10^{-6} °C^{-1}

ΔT = -720 °C

MAS/Nicalon NL-607 :

E_m = 90 GPa ν_m = 0.3 G_m = 20 Jm^{-2}

V_f = 0.45 τ = 48 MPa α_m = 5.5x10^{-6} °C^{-1}

ΔT = -720 °C

Borosilicate/Nicalon NL-607 :

E_m = 70 GPa ν_m = 0.3 G_m = 12.5 Jm^{-2}

V_f = 0.45 τ = 51 MPa α_m = 3.2x10^{-6} °C^{-1}

ΔT ; Not applicable (as $\alpha_m = \alpha_f$)

E is elastic modulus, r the average radius of Nicalon, ν the Poisson ratio, G fracture surface energy, V volume fraction, τ the interface frictional shear stress, α coefficient of thermal expansion, and ΔT is the temperature difference between ambient and the

glass transition point. Subscript *f* refers to the fibre, *m* to the matrix properties.

Matrix microcracking stress is given by [81],

$$\sigma_m = \left[\frac{6\,\tau\, G_m E_f E_c^2 V_f^2}{r\,(1-V_f)\,E_m^2}\right]^{1/3} - q\frac{E_c}{E_m} \qquad \text{(III.1)}$$

where

$$\frac{q}{E_m} = \frac{\lambda_2}{\lambda_1}\left(\frac{E_f}{E_c}\right)\left(\frac{V_f}{1-\nu_m}\right)\varepsilon \qquad \text{(III.2)}$$

ε is the thermal mismatch strain, $\varepsilon = (\alpha_f - \alpha_m)\Delta T$, and

$$\lambda_1 = \{1-(1-E_c/E_f)(1-\nu_f)/2+(1-V_f)(\nu_m-\nu_f)/2-(E_c/E_f)[\nu_f + (\nu_m - \nu_f)\,V_f E_f/E_c]^2\}/$$
$$\{(1-\nu_m)[1+\nu_f+(\nu_m-\nu_f)\,V_f E_f/E_c]\}$$

$$\lambda_2 = \{1-(1-E_c/E_f)/2(1+\nu_f)+(1+V_f)(\nu_m-\nu_f)/2\} \,/\, [1+\nu_f+(\nu_m-\nu_f)V_f E_f/E_c]$$

The matrix microcracking stresses given by the above relationships are ;

CAS/Nicalon ..... σ_m = 450 MPa

MAS/Nicalon NL-607..... σ_m = 690 MPa

Borosilicate/Nicalon NL-607..... σ_m = 510 MPa

b) The brittle / tough property transition

Upper bounds to the possible frictional shear stress τ can be estimated from equating (III.1) to the product of fibre strength and fibre volume fraction, (see equation (6,7), repeated here as (III.3));

$$V_f S = \left[\frac{6\tau G_m E_f E_c^2 V_f^2}{r(1-V_f) E_m^2}\right]^{1/3} - q\frac{E_c}{E_m} \qquad \text{(III.3)}$$

where S is fibre strength within the matrix (~ 2GPa). Hence the maximum τ possible for tough behaviour,

$$\tau = \frac{r(1-V_f) E_m^2}{6 G_m E_f E_c^2 V_f^2} \left[V_f S + q\frac{E_c}{E_m}\right]^3 \qquad \text{(III.4)}$$

For the three composites listed above in section III(a), the calculated upper bounds are;

CAS/Nicalon .....τ = 184 MPa

MAS/Nicalon NL-607.....τ = 133 MPa

Borosilicate/Nicalon NL-607..... τ = 278 MPa